Study of the Hydro-Morpho-Sedimentary Dynamics on Pebble Beaches

Antoine Soloy

Normandie Université

THÈSE

Pour obtenir le diplôme de doctorat

Spécialité SCIENCES DE L'UNIVERS

Préparée au sein de l'Université de Rouen Normandie

Etude de la dynamique hydro-morpho-sédimentaire sur les plages de galets

Présentée et soutenue par
ANTOINE SOLOY

Thèse soutenue le 06/06/2022 devant le jury composé de		
M. FRANCOIS SCHMITT	DIRECTEUR DE RECHERCHE, UNIVERSITE LILLE 1 SCIENCES ET TECHNOLOGIE	Rapporteur du jury
MME MARISSA YATES	CHARGE DE RECHERCHE, Ecole des Ponts ParisTech	Rapporteur du jury
M. BRUNO CASTELLE	DIRECTEUR DE RECHERCHE, UNIVERSITE DE BORDEAUX	Membre du jury
M. STEPHANE COSTA	PROFESSEUR DES UNIVERSITES, Université de Caen Normandie	Membre du jury
M. PIERRE STEPHAN	CHARGE DE RECHERCHE, UNIVERSITE BRET. OCCIDENTALE UBO	Membre du jury
MME EMMA TURKI	MAITRE DE CONFERENCES, Université de Rouen Normandie	Membre du jury
M. BENOIT LAIGNEL	PROFESSEUR DES UNIVERSITES, Université de Rouen Normandie	Président du jury
M. NICOLAS LECOQ	MAITRE DE CONFERENCES HDR, Université de Rouen Normandie	Directeur de thèse

Thèse dirigée par NICOLAS LECOQ (Morphodynamique continentale et côtière)

UNIVERSITÉ DE ROUEN NORMANDIE

ED 497 NBISE
Normande de Biologie Intégrative, Santé, Environnement

M2C

REMERCIEMENTS

Pour commencer, je tiens à remercier profondément mes directeurs de thèse Imen Turki et Nicolas Lecoq, qui ont été de véritables mentors, toujours présents, bienveillants et à l'écoute. Imen, tu es une super-héroïne : enseignement, recherche, administration & supervision de projets, boulot de maman à temps complet et pourtant toujours là quand a besoin de toi, même depuis l'autre bout de la planète, peu importe le jour et l'heure ! Et Nico, tu es un vrai capitaine de navire, toujours capable de prendre et de faire prendre le recul nécessaire, et toujours volontaire pour une bonne grosse journée de terrain sous la pluie normande. J'ai vraiment passé de supers années sous votre supervision, et je vous en remercie sincèrement. Je veux également remercier Benoit Laignel, qui m'a suivi, aiguillé, soutenu et encouragé depuis mon tout premier stage de licence au M2C, jusqu'à ma soutenance de thèse. Ton influence a été considérable : grâce à toi, j'ai eu l'opportunité d'effectuer un stage passionnant outre Atlantique, au cours duquel j'ai vraiment décidé de faire une thèse, où j'ai découvert les questions côtières et la télédétection, mais aussi où j'ai appris l'anglais et rencontré celle qui partage ma vie, ce n'est pas rien !

Mes remerciements s'adressent ensuite à la Région Normandie, à l'Université de Rouen-Normandie, au laboratoire M2C, aux membres de mon jury de soutenance et à toutes les personnes et structures qui ont concouru de quelque façon à mon projet de thèse. Dans de nombreux pays, le coût de l'éducation est prohibitif, et c'est une véritable chance d'avoir pu réaliser des études jusqu'au diplôme de doctorat avec le soutien de ces entités.

Ce troisième paragraphe s'adresse à mes proches, qui ont toujours été un soutien inconditionnel, en particulier durant la thèse. Merci Papa, Maman, Mamie et William pour votre présence, votre aide et votre dévouement (surtout lorsqu'il a fallu détourer des galets et des traits de côte en photo) ! Et évidemment merci à ma chérie Jackie, qui a eu le courage de quitter sa Californie natale pour me rejoindre en France, d'apprendre la langue et la culture, de reprendre des études et de décrocher un master, de trouver du travail… A côté de tout ça tu as toujours trouvé le temps de m'encourager, de me conseiller, de me relire, de me corriger, et surtout de me supporter pendant ces 3 années intenses. Il va sans dire que cette thèse n'aurait pas été la même sans toi, et je te suis éternellement reconnaissant d'avoir été un pilier aussi solide pour m'aider à la réaliser. J'en profite pour faire un clin d'œil à tes parents, thank you so much Mary & John for your love and support as well, you guys are awesome ! J'ai aussi une petite pensée pour Téo, Filou, McGhee, Hooper, et Quint, les meilleurs amis du monde.

Les résultats obtenus au cours de ma thèse l'ont été en grande partie grâce à la collaboration avec des personnes fantastiques rencontrées sur le chemin, que je suis heureux pouvoir appeler des

amis. Je cite leur nom par ordre alphabétique : Duccio Bertoni, Stéphane Costa, Ángel David Gutiérrez Barceló, Edoardo Grottoli, Mark Lorang, Pierre Stéphan et Yves Soufflet. Cela n'aurait pas été possible non plus sans la contribution des nombreux stagiaires (Benjamin Bazin, Jérémy Courtois, Sami Helis, Audrey Hunt, Tom Nebel, Abderrahim Ourabah, Hassan Shafiei et Zainab Sif Eddine), ainsi que du personnel de l'université, notamment les techniciens du M2C Michel Simon et Romain Levaillant, et l'équipe du département audiovisuel, en particulier Philippe Rouxin, Florian Lebaillif et Anne Langlois.

Enfin, j'aimerais terminer en remerciant tous ceux que je n'ai pas eu l'occasion de citer plus haut : Lisa Baulon, Florian Bellanger, Mehdi Carmeille, Christophe Coupeur, Mariam Fares, Eugénie Féron, Thomas & Marie-Alix Gardes, Maxime & Juliette Gosselin, Ervan Kassarian, Elisa Lecoeur, Carlos Lopez Solano, Sandy Maarouf, Ernesto (Tona) Mendoza, Lise Monfray, Emilie Morlaine, Bastien Peuziat, Edward Salameh, Charlie Soloy, Anjana Timilsina, Gabriela (Gabi) Tolentino de Sá, Eva Torfeh, Tom Van der Stocken, Arnaud & Derya Venin et tous ceux que j'aurais malencontreusement omis dans cette liste.

ABSTRACT

Français

Les plages de galets sont des environnements côtiers très répandus sur les côtes de la Manche. Elles offrent une protection efficace aux structures côtières contre lesquelles elles reposent en absorbant une part significative de l'énergie des vagues, et sont par conséquent des environnements particulièrement dynamiques. Cependant, bien que la dynamique des plages de sable soit aujourd'hui bien comprise, celle des plages de galets reste à ce jour relativement peu documentée. Le consensus scientifique actuel décrit la dynamique complexe des plages de galets comme étant le résultat d'interactions rétroactives entre la morphodynamique, l'hydrodynamique et la dynamique sédimentaire. Plus particulièrement, il est admis que les variabilités spatiale et temporelle de la granulométrie jouent un rôle important dans la régulation de ces interactions. Ainsi, notre manque de compréhension vis-à-vis de la dynamique des plages de galet serait en grande partie dû à la difficulté de mesurer ces trois aspects simultanément.

Le présent manuscrit rapporte le travail réalisé dans l'objectif d'étudier la dynamique hydro-morpho-sédimentaire des plages de galets à des échelles multiples, en analysant un couplage de données provenant de plateforme multiple : drone (Unmaned Aerial Vehicle, UAV), et Système de surveillance par caméras vidéo (Video Monitoring System, VMS). Pour ce faire, deux méthodes innovantes basées sur des techniques de deep learning ont été développées afin de (1) cartographier la taille, la forme et l'orientation des galets à la surface d'une plage à partir d'une ortho-image drone, et (2) de produire un ensemble de Modèles Numériques de Terrain (MNT, ou DEM pour Digital Elevation Model) journaliers de plages à partir d'images VMS. A cet effet, deux sites comportant chacun une plage de galets ont été instrumentés et sont surveillés de façon continue depuis 2018 en Normandie. Les deux plages sont situées sur les côtes de la Manche, à proximité l'une de l'autre (64 km), et rencontrent des conditions de marée et de vagues considérées comme similaires. Cependant leur organisation spatiale et leurs caractéristiques granulométriques diffèrent : Etretat est une plage de galets pure située dans le creux d'une baie, et Hautot-sur-Mer est une plage composite de sable et galets située sur une côte semi-ouverte.

Les données recueillies ont permis l'analyse la dynamique morphologique des plages en réponse aux forçages marins entre les échelles journalière et biannuelle. Différents mécanismes du mouvement des plages ont été mis en évidence (e.g. translation, rotation, rollover and breathing), et certains ont pu être reliés à des processus physiques. Les résultats concernant la variabilité de la granulométrie ont également mis en évidence la présence de motifs sédimentaires spatiaux en lien avec l'altitude comme un gradient cross-shore systématique, et avec la présence d'épis comme la périodicité des assemblages de clastes triés par taille. Enfin, l'évolution temporelle de la perméabilité

au cours d'évènements de tempêtes a été analysée en utilisant une stratégie de calibration du modèle numérique XBeach-G, lui-même nourrit avec les données de morphologie et de granulométrie mesurées depuis les plateformes VMS et UAV, respectivement.

English

Gravel beaches are very common coastal environments on the English Channel coasts. They offer an effective protection to the coastal structures against which they rest by absorbing a significant part of the wave energy and are therefore particularly dynamic environments. However, although the dynamics of sandy beaches are well documented, the dynamics of gravel beaches remain relatively poorly understood. The current scientific consensus describes the complex dynamics of gravel beaches as the result of feedback interactions between morphodynamics, hydrodynamics and sediment dynamics. Spatial and temporal variabilities in grain size are expected to play an important role in these interactions. Thus, the lack of understanding of pebble beach dynamics is related to the difficulty of measuring these three aspects simultaneously.

The present manuscript reports the work done with the aim to investigate the hydro-morpho-sedimentary dynamics of gravel beaches at multiple timescales, by coupling data from multiple platforms: Unmanned Aerial Vehicle (UAV) and Video Monitoring System (VMS). For this purpose, two innovative methods based on deep learning techniques were developed (1) to map the size, shape and orientation of gravel on the surface of a beach using UAV-derived ortho-imagery, and (2) to produce a dataset of daily digital elevation models (DEM) of a beach morphology using VMS images. For this purpose, two pebble beach sites have been instrumented and monitored since 2018 in Normandy, France: Etretat and Hautot-sur-Mer. Both beaches are located on the French coasts of the English Channel, they are close to each other (64 km), and thus face tidal and wave conditions that are considered similar. However, they differ in their spatial organization and granulometric characteristics: Etretat is a pure gravel beach located in the hollow of a bay, and Hautot-sur-Mer is a composite sand and gravel beach located on a semi-open coast.

The data collected allowed the analysis of the morphological dynamics of the beaches in response to marine forcing from daily to biannual scales. Different mechanisms of shoreline movement were highlighted (e.g., translation, rotation, rollover and breathing), some of which were linked to physical processes. The results on grain size variability also highlighted the presence of spatial sedimentary patterns related to elevation such as a systematic cross-shore gradient, and to the presence of groin structures such as the periodic repetition of size-sorted clast assemblages. Finally, the temporal evolution of permeability during storm events was analyzed with a calibration strategy using the XBeach-G numerical model that was fed with measured morphology and gravel size data.

SUMMARY

LIST OF FIGURES

LIST OF TABLES

LIST OF ABBREVIATIONS

Abbreviation	Meaning
ANN	Artificial Neural Network
BOA	Beach Orientation Angle (deg)
BS	Beach Slope (tan β)
BW	Beach Width (m)
c	Wave celerity
CCD	Color Chanel Divergence
Cg	Wave group celerity
Ck	EOF temporal eigenfunction
CNN	Convolutional Neural Network
CS	Current Velocity
CSG	Composite Sand-Gravel beach
DEM	Digital Elevation Model
dGNSS	differential Global Navigation Satellite System
Dn	Percentile grain size (m), with n from 0 to 100 (e.g., D50 is the median grain size)
E or WE	Wave Energy
EF	Wave Energy Flux
Ek	EOF spatial eigenfunction
EOF	Empirical Orthogonal Function
FCN	Fully Convolutional Network
FPN	Feature Pyramid Network
g	Acceleration of gravity (m/s^2)

GSD	Ground Sampling Distance (m/px)
GWS	Global Wavelet Spectrum
h	Water depth (m)
Hs	Wave Significant Height (m)
HT	High Tide
IBM	Intertidal Beach Mapper
Ifremer	Institut Français de Recherche pour l'Exploitation de la Mer *French Research Institute for Exploitation of the Sea*
k	Wave number
L	Wavelength (m)
LCHF	Laboratoire Central d'Hydraulique de France *Central Hydraulic Laboratory of France*
LT	Low Tide
Mask R-CNN	Mask Regional Convolutional Neural Network
MSG	Mixed Sand-Gravel beach
PC	[EOF] Principal Component
PG	Pure Gravel beach
PIC	Pixel Intensity Clustering
(R)BNE	(Reverse) Brazil Nut Effect
R^2	Coefficient of Determination
RGB	Red-Green-Blue image channels
RMSE	Root Mean Square Error
ROI	Region Of Interest
SDM	Shoreline Detection Model
SFM	Surface From Motion

SHOM	Service Hydrographique et Océanographique de la Marine *Naval Hyrographic and Oceaographic Service*
SLIM	ShoreLine Intensity Maximum
Std	Standard Deviation
Tp	Wave Peak Period (sec)
TR	Tidal Range
UAV	Unmanned Aerial Vehicle
VMS	Video Monitoring System
ρ	Density (kg/m^3)

RESUME SUBSTANTIEL

A l'échelle mondiale, la surface de la Terre est couverte par un total de 1 634 701 km de côtes, ce qui équivaut à 402 fois le périmètre de la planète à l'équateur (Burke et al., 2005). Les populations vivant dans les zones côtières représentaient environ un quart de l'humanité en 1990 avec des densités plusieurs fois supérieures au reste des zones continentales (Small et Nicholls, 2003), et cette part a vraisemblablement augmenté durant les 30 dernières années. L'attractivité des zones côtières tient à leur richesse en ressources combinée à leur accès direct à la mer, qui favorisent le développement d'activités économiques (ex : pêche, production d'énergie, tourisme, etc.), et facilitent la navigation et le commerce (Neumann et al., 2015). Les zones côtières abritent également une large biodiversité, dont les services écosystémiques ont été estimés à 47,4 trillions de dollars internationaux par an, soit près de la moitié des services écosystémiques fournis par l'ensemble des biomes de la planète (Davidson et al., 2019). Le statut de rôle majeur des zones côtières est soutenu par le fait qu'elles sont très dynamiques et en constante évolution en réponse à différents forçages internes et externes.

Dans ce contexte, les zones côtières sont soumises à divers aléas exposant les populations et les enjeux environnementaux et économiques à des risques spécifiques à la côte tels que les tempêtes, les submersions marines, les inondations, les tsunamis, l'érosion côtière, et plus encore (Meur-Férec et al., 2008 ; Strunz et al., 2011). En outre, les zones côtières sont parmi les premières à faire face aux conséquences du changement climatique, notamment l'élévation du niveau de la mer et le recul du trait de côte (Cazenave et Llovel, 2010), l'augmentation de l'intensité des événements extrêmes les plus puissants (Wolf et al., 2020), et bien d'autres. Comprendre la dynamique des zones côtières est donc un enjeu crucial, notamment dans le contexte actuel de changement global.

Les plages et barrières de galets constituent une protection naturelle précieuse pour de nombreux environnements littoraux. Les galets peuvent également être utilisés dans le cadre de systèmes de défense côtière artificiels. Ils agissent comme des moyens de protection des côtes grâce à leur capacité à dissiper une grande partie de l'énergie des vagues incidentes dans des conditions de vagues très énergétiques (Buscombe et Masselink, 2006). Notez que dans le contexte de cette thèse, le mot galet (en anglais, gravel ou pebble) fait référence à tous les types de sédiments dont la taille est supérieure à celle du sable (c'est-à-dire 2 mm, Wentwort (1922)). Au cours des 50 dernières années, et plus particulièrement au cours de la dernière décennie, de nombreuses études ont été menées pour comprendre la dynamique des systèmes côtiers de type plage.

Parmi les différents types de systèmes côtiers, les plages de galets ont probablement reçu le moins d'attention de la part des scientifiques, ce qui explique que la connaissance et la compréhension de la dynamique de ce type d'environnement restent très limitées (Buscombe et Masselink, 2006 ; Orford et Anthony, 2022). La difficulté de déployer des équipements de mesure coûteux et sensibles

dans des conditions aussi dynamiques avec des galets lourds et mobiles susceptibles d'endommager les instruments explique probablement en grande partie cette lacune, malgré un intérêt scientifique significatif (Almeida et al., 2015 ; Mason et Coates, 2001 ; Orford et Anthony, 2022 ; Orford, 2020). Cependant, les différentes études menées ont montré que les plages de galets répondent différemment aux forçages marins, par rapport aux plages de sable, et leur évolution est à l'heure actuelle difficile à modéliser.

L'un des principaux facteurs expliquant ces différences est la perméabilité. Sur une plage de sable, la perméabilité limitée des sédiments (typiquement inférieure à 1 mm/s) ne permet qu'à un faible volume d'eau de s'infiltrer pendant un cycle de swash (la période de swash dure généralement entre 5 et 20 secondes). Par conséquent, l'asymétrie entre les volumes du run-up et du rundown est négligeable. Sur une plage de sédiments grossiers, la perméabilité plus élevée (entre 1 mm/s et 1 m/s) (Bear, 1972 ; McCall, 2015) entraîne une asymétrie de swash significative. Le volume d'eau lors du run-up (ou uprush) étant significativement plus important que celui du rundown (ou backwash), l'asymétrie du swash génère un transport de sédiments principalement vers la côte et conduit à un gradient topographique réflectif (Masselink et Li, 2001). Cependant, bien que granulométrie des galets soit un paramètre de contrôle majeur sur la perméabilité, les méthodes permettant d'en mesurer la variabilité sont relativement limitées.

Plus généralement, le consensus scientifique actuel considère la dynamique des plages de galet comme le résultat d'un ensemble complexe de boucles de rétroaction positives et négatives entre les variabilités morphologiques, hydrauliques et sédimentaires (Buscombe et Masselink, 2006 ; McCall, 2015 ; Orford et Anthony, 2022). Cette idée est à la base du concept de dynamique hydro-morpho-sédimentaire, qui suppose que l'hétérogénéité des sédiments est un facteur de contrôle fondamental de la morphodynamique des plages de galet, cette dernière étant elle-même en équilibre dynamique avec les forçages marins variables. Pour comprendre la dynamique complexe des plages de galets, il est nécessaire de suivre indépendamment et simultanément ces variabilités spatio-temporelles avec précision.

L'utilisation de Systèmes de Video Surveillance (en anglais Video Monitoring System ou VMS) pour le suivi haute fréquence (journalier) de la morphologie côtière est une approche éprouvée pour les systèmes sableux (Aarninkhof et al., 2003 ; Holman et al., 1991 ; Kingston, 2003 ; Osorio et al., 2012 ; Plant et al., 2007 ; Turner et al., 2004 ; Valentini et al., 2017). Les VMS sont particulièrement bien adaptés aux contraintes spécifiques des systèmes de galet, car ils peuvent être déployés à une distance sûre du littoral actif et exploités directement depuis le laboratoire, à une fréquence élevée (de quelques minutes à quelques heures) pendant de longues périodes (années). Les techniques de Surface par Mouvement (en anglais Surface From Motion, ou SFM), en particulier la photogrammétrie par image de drone, deviennent également de plus en plus populaires pour les applications de science côtière, car elles permettent de mesurer la morphologie des plages avec

précision et à moindre coût (Burdziakowski et al., 2020 ; Gonçalves et Henriques, 2015 ; Laporte-Fauret et al., 2019 ; Medjkane et al., 2018).

Dans ce contexte, ce travail de thèse propose d'utiliser ces méthodes pour aborder la question de la dynamique hydro-morpho-sédimentaire des plages de galet à court-moyen terme (jours à années), à une fréquence élevée (journalière), notamment en période de tempête. Cette tâche est réalisée en couplant les informations extraites à l'aide de techniques de télédétection appliquées aux données d'imagerie côtière acquises à partir de plateformes multiples (VMS et UAV). Cette recherche est axée sur la réponse aux cinq questions scientifiques suivantes :

1. Comment quantifier de manière fiable la variabilité spatio-temporelle de la morphométrie des galets ?
2. Comment suivre de manière fiable la morphodynamique des plages de galet ?
3. Comment la morphodynamique des plages répond-elle aux forçages marins ?
4. Quelle est la variabilité spatio-temporelle de la taille des galets sur la surface des plages ?
5. Quel est l'effet des tempêtes sur la perméabilité de la plage et sa morphologie ?

Pour répondre à ces questions, des VMS ont été installés sur trois plages de Normandie à Etretat, Hautot-sur-Mer et Villers-sur-Mer. Parallèlement, des vols de drone ont été effectués à différentes dates afin de recueillir des images de la surface des plages. Les informations extraites de ces données multi-plateformes sont analysées au moyen de différentes méthodes de traitement numérique afin d'apporter des éléments de réponses aux questions scientifiques posées, et les résultats sont présentés et discutés au cours des différents chapitres de la thèse.

Chapitre 1

Le premier chapitre est une introduction aux processus impliqués dans la dynamique des plages. Il commence par décrire les forçages impliqués dans l'hydrodynamique côtière tels que les ondes de marée et de gravité et caractérise les différents éléments qui composent la morphologie générale d'une plage. Des détails sur la morphologie et la dynamique spécifique des plages de galets sont ensuite fournis, notamment la description des bermes, du step, des cusps, et des spécificités liées à l'écoulement des eaux souterraines et au transport sédimentaire. Enfin, l'ensemble des tâches à réaliser afin de répondre aux questions de recherche auxquelles cette thèse s'intéresse sont énoncées.

Pour résumer, les plages de galets offrent une protection importante aux côtes sur lesquelles elles reposent, et constituent donc un enjeu important, notamment dans le contexte du changement climatique. Leur morphodynamique est singulière sous plusieurs aspects. Cela est notamment dû à la zone de surf relativement courte voire inexistante, qui ne peut pas dissiper une quantité d'énergie aussi importante que sur les systèmes sableux où elle est plus large, ce qui conduit à une zone de swash particulièrement énergique. L'absorption de l'énergie des vagues se fait par infiltration dans le sédiment. La perméabilité du sédiment est d'autant plus élevée que la taille des grains est grande, ce qui fait de la granulométrie un important paramètre de contrôle de la perméabilité, et par extension de

la morphodynamique des plages de galets. En outre, la position et l'amplitude de la zone de swash sont modulées par les oscillations de la marée. Le profile transversal d'une plage de galets comporte des éléments typiquement associés à la combinaison de ces facteurs comme une pente réflective, la présence de bermes et d'un step. Les conditions énergétiques associées rendent les mesures difficiles notamment dans la zone de swash, limitant ainsi notre connaissance de la dynamique de ces systèmes.

Cette thèse représente un effort de recherche visant à mieux comprendre la dynamique des plages de galet. A cette fin, elle propose d'investiguer sur différentes questions scientifiques visant (1) à proposer des solutions de mesure innovantes et adaptées aux conditions de mesure difficiles de ces environnements, (2) à utiliser ces solutions pour observer la dynamique morpho-sédimentaire des plages de galet à différentes échelles de temps, et (3) à investiguer sur les relations entre les dynamiques hydrauliques, morphologiques et sédimentaires alors observées.

Chapitre 2

Après la description des processus hydro- et morphodynamiques pertinents pour l'étude des plages de galets dans le chapitre 1, le chapitre 2 vise d'abord à décrire le contexte spécifique de la Normandie. La géomorphologie côtière est présentée ainsi que l'origine et le transport des particules de galets, puis un aperçu global sur les établissements humains et la défense côtière de la région est donné avant de présenter les aspects climatiques, les vagues et les marées de la Manche.

La Normandie est décrite comme une région côtière située au nord-ouest de la France, en bordure du côté sud-est de la Manche. Sa localisation au sein du bassin sédimentaire parisien est à l'origine de la présence de falaises crayeuses et des plages de galets de silex typiques de cette région balnéaire touristique. La forme en entonnoir de la Manche est responsable de ses marées d'amplitudes extrêmes (5 à 10 m) et des directions préférentielles de propagation des vagues vers l'est et le sud, observées près des côtes normandes. Ces caractéristiques conduisent à une dérive sédimentaire principalement orientée vers l'est le long du littoral, laquelle est modulée par la présence d'obstacles naturels et anthropiques suscitant la formation de cordons de galets.

Dans une deuxième section du chapitre, les trois sites d'étude initialement sélectionnés sont présentés : Etretat, Hautot-sur-Mer et Villers-sur-Mer, puis une description des VMS est apportée.

La plage d'Etretat est un système enfermé dans une baie, elle s'étend sur 1000 m de long, et est encadrée par de hautes falaises de calcaire plus induré (recul moyen de 14 à 17 cm/an (Costa et al., 2019)). Les caps fermant la baie bloquent la dérive littorale, ainsi le stock de galets est ancien, et les éléments sont de taille réduite en comparaison d'autres sites Normands (D50 = 5.99 cm). Ce stock s'accumule sous la forme d'un cordon de galets purs (Jennings and Shulmeister, 2002) (pente de 10%) installé contre un perré bordé par quatre épis, avec une extension cross-shore pouvant atteindre 150 m aux marées les plus basses.

Hautot-sur-Mer est un système semi-ouvert de 1000 m de long situé à l'embouchure de la vallée de la Scie. Les falaises de craie qui l'entourent présentent un recul moyen de 20 à 50 cm par an (Costa et al., 2019), renouvelant régulièrement le stock de galets. Le cordon de galets est formé de clastes plus grossiers (D50 = 7.44 cm), piégés entre sept épis transversaux. Selon la classification de Jennings and Shulmeister (2002), le site correspond à la définition d'une plage composite : le cordon (pente > 10%) repose sur un substrat sableux (pente 1,3%) qui laisse émerger une terrasse intertidale sur plus de 210 m à marée basse.

La plage de Villers-sur-Mer est un système sableux ouvert de 4250 m de long situé au sud-ouest de l'estuaire de la Seine. La plage se trouve au pied d'un petit perré et est traversé par 15 grands épis. Sa faible pente (< 1%) permet à la zone intertidale de se découvrir sur plus de 310 m dans le sens transversal aux marées basses les plus basses, tout en développant de petites mares et des couloirs.

Les trois sites ont été équipés entre mi-2018 et début 2019, mais le site de Villers-sur-Mer a été abandonné à la suite d'une série de dysfonctionnements importants et n'est pas considéré dans la suite de ce travail de thèse. Ces systèmes enregistrent des images à partir desquelles il est possible d'extraire la position du trait de côte toutes les heures et de produire des Modèles Numériques d'Elévation (MNE, ou DEM pour Digital Elevation Model en anglais) journaliers de la morphologie des plages.

Pour finir, la troisième et dernière section de ce chapitre détaille les différentes méthodologies utilisées pour traiter les images (photogrammétrie et segmentation d'images), pour analyser la dynamique observée (Fonctions Orthogonales Empiriques, corrélation et analyse en ondelettes) et pour la modéliser à l'aide du modèle numérique 1D XBeach-G.

Chapitre 3

Ce chapitre s'attache à répondre à la première question scientifique de cette thèse, « *Comment quantifier de manière fiable la variabilité spatio-temporelle de la morphométrie des galets ?* ». Comme nous l'avons vu dans les chapitres 1 et 2, la perméabilité est un facteur clé contrôlant la morphodynamique des plages de galets. Par conséquent, la taille, la forme et le tri spatial des grains sont des informations importantes à connaître pour comprendre et éventuellement prévoir l'évolution morphologique des plages de galets.

Cependant, la mesure de ces paramètres est souvent une tâche coûteuse et fastidieuse, ce qui tend à limiter les études observationnelles et par extension le développement de modèles descriptifs et prédictifs. En effet, d'une part les méthodes d'échantillonnage physique nécessitent des échantillons lourds et nombreux pour atteindre la significativité statistique (de l'ordre de la tonne(s) par échantillon : plus le sédiment est grossier, plus la masse à échantillonner est lourde), et sont souvent destructives. D'autre part, les méthodes alternatives basées sur la photographie sont souvent

compliquées et difficiles à automatiser car elles nécessitent une expertise importante et un temps de traitement long, bien qu'elles présentent l'avantage d'être non-destructives.

Il existe donc un besoin de solutions automatiques de cartographie des caractéristiques des galets. La première partie de ce chapitre présente une méthode basée sur l'algorithme d'apprentissage profond Mask R-CNN qui a été développée dans le but de répondre à cette demande en surmontant les contraintes précédemment évoquées. Cette partie fait également l'objet d'un article scientifique publié dans la revue Remote Sensing (MDPI) : ***Soloy, A., Turki, I., Fournier, M., Costa, S., Peuziat, B., Lecoq, N., 2020. A deep learning-based method for quantifying and mapping the grain size on pebble beaches. Remote Sens. 12, 1–23. https://doi.org/10.3390/rs12213659***

Mask-RCNN signifie Mask Regional Convolutional Neural Network (en français : réseau neuronal convolutif de masque régional). C'est un méta-algorithme développé par He et al. (2017) qui permet l'identification d'instances d'objets (c'est-à-dire qu'il est capable de distinguer plusieurs objets appartenant à une même classe, même s'ils se chevauchent) et la délinéation de leurs contours. Après un apprentissage sur des données étiquetées manuellement, le modèle est capable d'effectuer la détection automatique, la classification et la délinéation des galets non-chevauchants visibles sur les images, et finalement de quantifier leur taille, leur forme, leur position et leur orientation. La méthodologie développée a été validée avec une incertitude de ±8 pixels (±4 mm pour une distance d'échantillonnage au sol (en anglais Ground Sampling Distance ou GSD) de 0,5 mm/pixel) par rapport à un ensemble de données mesurées manuellement.

Cette méthodologie a été appliquée sur les plages d'Etretat et Hautot-sur-Mer en utilisant deux types de données différents : des photographies terrestres en vue de dessus à une hauteur d'environ 2 m sans trépied, avec une structure quadra pour l'échelle, et des ortho-images produites par traitement SFM à l'issue d'un vol de drone. Les résultats obtenus sont cohérents avec les observations de la littérature scientifique, et permettent d'analyser la variabilité spatio-temporelle granulométrique des plages Normandes. Nos observations mettent en évidence l'hétérogénéité spatiale du tri granulométrique et son évolution au cours du temps. L'apparition de changements de taille concomitants à la présence de conditions hydrodynamiques spécifiques suggère que la responsabilité du tri des clastes grossiers est partagée par une combinaison de plusieurs facteurs tels que la hauteur significative des vagues et l'amplitude de la marée.

La méthode a également été appliquée avec succès sur différents sites d'étude en Europe et aux Etats-Unis, dans le cadre d'une collaboration internationale de recherche qui a été initiée par ce travail et qui est présentée en deuxième partie de ce chapitre. L'application de la méthode à ces nouveaux sites est un défi visant à déterminer les capacités de généralisation du modèle, c'est-à-dire son abilité à fonctionner efficacement sur des données différentes de celles du jeu d'entrainement initial. Ces sites incluent une plage mixte sable-galets (Irlande), deux plages artificielles de galets pures sur un lac

(Montana), les berges rocailleuses d'une rivière alpine (Suisse) et une plage de galets volcaniques très grossiers (Islande). Les résultats montrent que le modèle est capable de détecter les clastes sur ces sites avec la même efficacité qu'en Normandie. La comparaison montre la capacité du modèle à déterminer l'hétérogénéité spatiale du sédiment et ses changements temporels.

Une partie des résultats de cette collaboration a été présentée à la réunion d'automne de l'American Geophysical Union de décembre 2021, à la Nouvelle-Orléans, aux États-Unis : ***Soloy, A., Grottoli, E., Lorang, M.S., De Graffenried, B., Pascal, I., Bertoni, D., Turki, I., Lecoq, N., Jackson, D.W., Guisado-Pintado, E., Ancey, C., Trembanis, A.C., Laignel, B., 2021. Mapping the size and shape of coarse clasts using Mask R-CNN: spatial and temporal variability over six different study sites including sea shores, and lake and river banks, in: EP34A - Grains to Satellites: Sediment and Hydrological Processes Across Scales II Oral. New Orleans, USA.*** ***https://agu.confex.com/agu/fm21/meetingapp.cgi/Paper/861821***

Le modèle a été mis à disposition dans un dépôt public. Dans le futur, l'outil pourrait être amélioré afin de fournir des informations supplémentaires sur la composition géologique la plus probable de chaque objet, ou la distribution les éléments fraichement cassés et ceux plus longuement arrondis par l'action de l'eau.

Chapitre 4

Ce dernier chapitre s'intéresse aux quatre dernières questions scientifiques posées pour ce travail de thèse. Dans une première partie, nous présentons une méthodologie développée dans le but de répondre à la première d'entre elles, *« Comment suivre de manière fiable la morphodynamique des plages de galet ? »*. Ce travail a fait l'objet d'une publication dans le journal Coastal Engineering (Elsevier) : ***Soloy, A., Turki, I., Lecoq, N., Gutiérrez Barceló, Á.D., Costa, S., Laignel, B., Bazin, B., Soufflet, Y., Le Louargant, L., Maquaire, O., 2021. A fully automated method for monitoring the intertidal topography using Video Monitoring Systems. Coast. Eng. 103894.*** ***https://doi.org/10.1016/j.coastaleng.2021.103894***

Parmi les différentes méthodes couramment utilisées pour le suivi de la morphologie côtière, les VMS permettent de mesurer la morphologie d'un site avec une résolution spatiale de quelques centimètres et une résolution temporelle d'une journée ou moins. En effet, la morphologie du littoral peut être estimée en identifiant et en délinéant le trait de côte visible sur des images côtières photographiée à des instants successifs. Les traits de côte d'un même cycle de marée sont utilisés comme lignes de contour de la morphologie intertidale et peuvent potentiellement permettre de constituer un MNE par transition entre basse mer et pleine mer ou inversement.

Cependant, l'extraction de la position de la ligne de côte à partir d'images VMS reste une tâche longue et souvent fastidieuse. Comme les VMS enregistrent continuellement des images par intervalles de 10 minutes, le poids de l'ensemble de données cumulées et les conditions d'imagerie

variables rendent difficile l'automatisation de la détection du littoral. Historiquement, il a d'abord fallu délimiter manuellement le trait de côte (Holman et al., 1991), puis cette tâche a été facilitée par le développement de plusieurs méthodes de détection paramétriques (Plant et al., 2007).

Bien que ces méthodes aient considérablement amélioré le temps de traitement des données, leur application est limitée par la variabilité de la qualité des données et nécessite une grande expertise (Osorio et al., 2012). La plupart des algorithmes restent fortement contraints par les multiples variabilités environnementales (luminosité, contraste, pluie, brouillard, présence d'utilisateurs, de bateaux, objectifs de caméra poussiéreux, etc.) et nécessitent donc l'action d'un opérateur humain pour affiner les paramètres avant d'être appliqués à un nouveau site.

Pour surmonter ces limitations, la première partie du chapitre 4 propose une nouvelle méthode basée sur le modèle de segmentation en instance Mask R-CNN. S'il est entraîné sur une quantité de données suffisante, et présentant suffisamment de variabilité, Mask R-CNN peut détecter et délinéer des concepts aussi abstraits que des étendues d'eau délimitées par un trait de côte et une ligne d'horizon, sur des images côtières. La versatilité et les capacités de généralisation du modèle sont des atouts précieux dans cet exercice en lui permettant de s'affranchir d'une partie des limitations posées par la variabilité des conditions d'imagerie.

Après un entrainement sur plus de 1000 images issues des VMS normands labélisées manuellement, Mask R-CNN peut ainsi effectuer l'extraction en quelques heures du trait de côte visible sur plusieurs dizaines de milliers d'images côtières, avec un taux de succès évalué entre 67% et 97%, selon le site d'étude considéré. Il est possible de mettre à profit de ce fort taux de succès pour filtrer les éventuels faux positifs. En effet, ces derniers adoptent souvent une forme peu conventionnelle, alors que les traits de côte successifs ne sont pas censés se croiser. On peut identifier et filtrer la grande majorité des détections insatisfaisantes en fonction du nombre d'intersections entre traits de côtes successifs. Une fois nettoyé, le nuage de points regroupant les mesures faites au cours d'un même cycle de marée peut être interpolé sur une grille fixe, ce qui permet de construire une série temporelle de MNE côtiers, avec un RMSE vertical moyen mesuré de 28 cm, tous sites confondus. La combinaison de ces caractéristiques fait de cette approche une méthode entièrement automatisée de surveillance de la morphologie côtière par VMS.

La seconde partie de ce chapitre s'intéresse à la variabilité morpho-sédimentaire et cherche à répondre aux deux questions « *Comment la morphodynamique des plages répond-elle aux forçages marins ?* » et *« Quelle est la variabilité spatio-temporelle de la taille des galets sur la surface des plages ?»*. Cette section a également fait l'objet d'une publication dans le journal Marine Geology (Elsevier) : ***Soloy, A., Turki, I., Lecoq, N., Solano, C.L., Laignel, B., 2022. Spatiotemporal variability of the morpho-sedimentary dynamics observed on two gravel beaches in response to hydrodynamic forcing. Mar. Geol. 106796. https://doi.org/10.1016/j.margeo.2022.106796***

Pour répondre à ces questions, nous avons combiné et analysé les informations extraites depuis les plateformes VMS et les vols de drone. L'approche présentée en partie 1 du chapitre 4 a été appliquée à un jeu de données de plus de 2 ans d'imagerie côtière afin d'obtenir la topographie quotidienne et d'évaluer la dynamique morphologique des plages d'Etretat et de Hautot-sur-Mer en réponse aux forçages marins. Les aspects sédimentaires de surface ont également été étudiés à l'aide de mesures effectuées selon le protocole détaillé dans la section 1 du chapitre 3. Ces informations nous aideront à répondre à différentes questions plus précises concernant la morphodynamique et la variabilité sédimentaire des plages de galets de Normandie, notamment : (1) Comment la forme du littoral évolue-t-elle au cours du temps ? (2) Les changements sont-ils homogènes à toutes les altitudes ? (3) Existe-t-il des mécanismes morphodynamiques spécifiquement identifiables, et quelle est leur période de variabilité temporelle typique ? (4) Quels phénomènes physiques sont responsables des changements morphologiques observés ? (5) Quelle est la variabilité spatio-temporelle de la granulométrie des plages étudiées ? (6) Comment les propriétés de ce sédiment varient-elles dans le temps ? (7) Peut-on relier la variabilité morphologique à la variabilité sédimentaire avec les informations reccueillies ?

L'évolution morphologique des deux plages a été étudiée à l'aide d'une analyse par fonction orthogonale empirique (en anglais Empirical Orthogonal Function, ou EOF) appliquée à des séries temporelles position du trait de côte à différentes altitudes. Les composantes principales (en anglais Principal Components, ou PC) de l'EOF ont mis en évidence l'existence d'au moins quatre mécanismes de changement du littoral, à savoir la rotation, la translation cross-shore, le renversement (en anglais rollover) et la respiration (en anglais breathing). Malgré leur proximité relative, les deux plages présentent des ensembles de modes de variabilité différents : 88,5 % de la variabilité de la position du trait de côte à d'Etretat est expliquée par la combinaison entre translation cross-shore, renversement, respiration, rotation à large échelle et rotation des cellules de plage (c'est-à-dire entre les épis), par ordre d'importance décroissante. La variabilité de la position du trait de côte de Hautot-sur-Mer est expliquée à 72,2% par la combinaison entre rotation centrée à droite (entre les épis), rotation centrée à gauche, rotation à grande échelle, et renversement, par ordre d'importance décroissante également. L'interprétation de la plupart des PC a été confirmée lors du calcul du coefficient de corrélation entre les PC et les paramètres morphologiques, notamment la largeur de la plage (en anglais Beach Width, ou BW), l'angle d'orientation de la plage (en anglais Beach Orientation Angle, ou BOA) et la pente de la plage (en anglais Beach Slope, ou BS). De plus, l'analyse a montré que l'élévation joue un rôle significatif dans tous les mécanismes de changement de position du littoral, et que l'influence des structures d'épis est plus importante à Hautot-sur-Mer, où elle joue un rôle dans chaque PC, qu'à Etretat, où elle n'est visible que dans la PC5.

L'analyse en ondelettes des signaux morphologiques (BW, BOA et BS) a révélé que la variabilité du trait de côte s'exprime à des périodes similaires pour tous les paramètres : 2, 3, 5 et 8+

mois à Etretat, et 2 et 6 mois à Hautot-sur-Mer. Des périodes similaires ont été trouvées en appliquant l'analyse en ondelettes aux signaux d'énergie des vagues. Bien qu'aucune corrélation linéaire significative n'ait été trouvée entre l'évolution des paramètres hydro- et morphologiques, ces résultats tendent à montrer que le facteur hydrodynamique ayant le plus d'influence sur la dynamique morphologique est l'énergie des vagues.

La dispersion spatiale de la granulométrie des galets de surface a été cartographiée sur les deux sites. Le jeu de données reste limité temporellement et ne comporte qu'une seule date à Etretat (2020/06/10) et trois dates à Hautot-sur-Mer (2019/04/09, 2019/06/04 et 2020/06/09). Néanmoins, ces données nous ont permis de formuler une première estimation de la variabilité temporelle sur ce dernier site, en conditions estivales. De manière générale, les deux sites présentent des tailles de galets différentes avec des valeurs de longueur des clastes moyennes de 5,2 cm à Etretat et de 7,0 cm à Hautot-sur-Mer (moyenne temporelle). La dispersion spatiale a généralement révélé des motifs tels qu'un gradient cross-shore systématique, des cusps et des assemblages de clastes dont la périodicité d'une cellule de plage à ses voisines démontre l'influence des épis sur la dynamique sédimentaire. L'analyse temporelle a révélé des différences à la fois dans la taille moyenne des grains (jusqu'à -1 cm entre avril et juin 2019 à Hautot-sur-Mer) et dans la présence et la position des assemblages de clastes. Des explications sont proposées sur la variabilité temporelle observée (par exemple, abrasion, percolation, processus liés à la rotation), mais la quantité de données limite l'analyse à des spéculations. Cependant, le besoin d'une meilleure connaissance et compréhension de la variabilité spatio-temporelle granulométrique est largement reconnu par la communauté scientifique côtière, et ces résultats sont prometteurs à cet égard.

Enfin, la troisième partie de ce chapitre porte sur la dernière question scientifique posée lors de ce travail de thèse : *« Quel est l'effet des tempêtes sur la perméabilité de la plage et sa morphologie ? »*. Pour y répondre, l'impact de trois des tempêtes les plus intenses de la période 2018 - 2020 a été simulé à l'aide du modèle XBeach-G, sur la plage d'Etretat. Le modèle XBeach a été développé par Roelvink et al. (2009) dans le but de de prédire la dynamique morphologique des plages de sable lors d'événements extrêmes. La version -G correspond à une évolution mise au point par McCall et al. (2014) pour simuler la dynamique des barrières de galets dans des conditions énergétiques similaires. Elle permet de tenir compte de deux paramètres généralement négligés pour les systèmes sableux mais essentiels pour la dynamique des environnements de galets : (1) la pression non-hydrostatique pour propager les vagues une par une afin d'assurer une résolution précise des processus de transformation des vagues, et (2) l'écoulement des eaux souterraines, c'est-à-dire les échanges par infiltration et exfiltration entre la surface libre et la nappe phréatique de la plage, pour lesquels la perméabilité est importante.

Le modèle a été implémenté en utilisant la morphologie de la plage estimée à partir d'images VMS à Etretat, et la taille moyenne des graviers mesurée lors d'une campagne de drones. Des données

de bathymétrie subtidale et d'hydrodynamique provenant de différentes sources ont été utilisées en complément pour alimenter le modèle. Les trois tempêtes sélectionnées ont été simulées avec une mise à jour quotidienne des données de bathymétrie, et une stratégie de calibration de la perméabilité utilisant un ensemble de valeurs sélectionnées variant de 0 à 0.6 m/s.

De manière générale, les changements morphologiques associés à l'impact d'une tempête sur le profil varient d'un événement à l'autre mais sont toujours sensibles à la valeur de la perméabilité : une valeur plus élevée favorise la construction de la berme, et une valeur plus faible conduit à son érosion. Sur les trois événements modélisés, seule une tempête (tempête 2) a montré une performance satisfaisante du modèle. Les résultats des scénarios relatifs à cet évènement montrent que la perméabilité a été réduite d'un facteur 4 dans les 24 premières heures de la tempête. Une telle diminution tend à indiquer des changements dans la porosité, avec potentiellement un mélange de sable et de gravier se produisant dans des conditions énergiques. La perméabilité étant considérée comme un paramètre constant et homogène dans le temps dans XBeach-G, une variation aussi importante et rapide montre les limites des simplifications imposées par le modèle. Plus particulièrement, l'hypothèse de l’uniformité spatiale et temporelle de la perméabilité, ainsi que d'autres facteurs connexes tels que la taille des grains et la porosité, constituent des limites importantes à la modélisation de la réponse des plages de galets lors de l'impact de tempêtes. En l'absence de mesures fiables de ces paramètres, ces simplifications restent toutefois nécessaires à des fins de modélisation.

INTRODUCTION

1. General context

On a global scale, the Earth's surface is covered by a total of 1,634,701 km of coastline, which is equivalent to 402 times the planet's perimeter at the equator (Burke et al., 2005). The population living in the near coastal zone represented approximately one quarter of humanity in 1990 with densities several times higher than the rest of the continental areas (Small and Nicholls, 2003), and has likely increased since. The attractiveness of the coastal zone stems from their wealth of resources combined with their direct access to the sea, which promote the development of economic activities (e.g., fishing, energy production, tourism, etc.), and facilitate navigation and trade (Neumann et al., 2015). Coastal areas also host a wide biodiversity, whose ecosystem services have been estimated at 47.4 trillion international dollars per year, or nearly half of the ecosystem services provided by all biomes on the planet (Davidson et al., 2019). The key role of coastal areas is mainly reinforced by the fact that they are dynamic and constantly changing in response to several internal and external forcings.

In this context, coastal areas are subject to various hazards exposing populations, and environmental and economic issues to risks specific to the coast such as storms, marine submersions, floods, tsunamis, coastal erosion, and more (e.g., Meur-Férec et al., 2008; Strunz et al., 2011). In addition, coastal areas are among the first ones facing the consequences of climate change, including sea level rise and retreat of the coastline (Cazenave and Llovel, 2010), the increase in intensity of the most powerful extreme events (Wolf et al., 2020), and many others. Understanding coastal zone dynamics is therefore a crucial issue, especially in the current context of global change.

Gravel beaches and barriers form a valuable natural protection for many shorelines. They can also be used as part of a coastal defense system. They act as natural means of coast protection and are able to dissipate a large portion of incident wave energy under highly energetic wave conditions (e.g., Buscombe and Masselink, 2006). Note that in the context of this thesis, the word gravel refers to all types of clastic sediment larger than sand (i.e., 2 mm), and other terms such as pebble, cobble and boulder designate specific ranges of size according to Wentwort (1922): from 2 to 64 mm, 64 to 256 mm and more than 256 mm, respectively. Over the past 50 years and the last 10 in particular, extensive understanding was gained regarding the dynamics of beaches (Figure 1). However, this gain was disproportionately in favor of sandy systems, and the dynamics of gravel systems remains to this day relatively incomplete (Buscombe and Masselink, 2006; Hayes et al., 2010; Orford and Anthony, 2022).

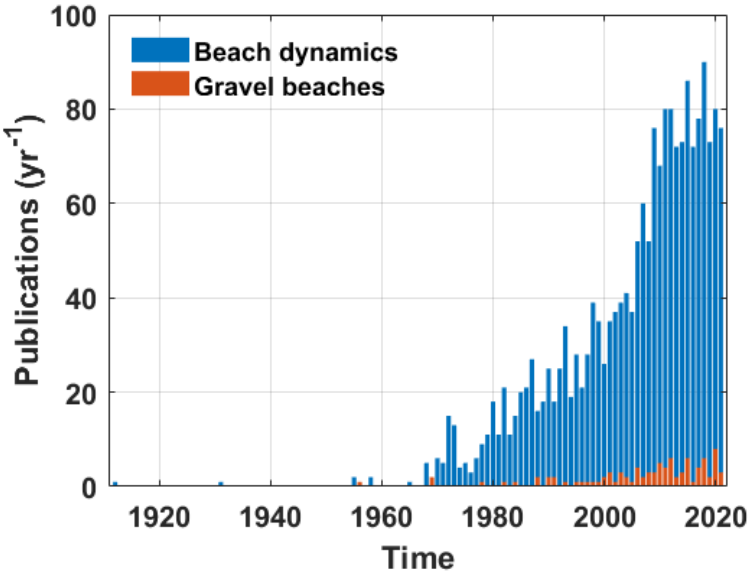

Figure 1 - Temporal evolution of the number of publications including the words "beach dynamics" (blue) and "gravel beaches" (orange). Alternative words were also considered

In the South English Channel, barrier morphodynamics are the most important systems for Normandy coastal defense. In the global context of climate change, the Normandy stakeholders, including water authorities and governments in coastal areas, have given a special interest to these areas that are subject to large perturbations induced by extreme events. Hence, this PhD project was funded and supported by the region of Normandy to investigate the dynamics of pebble systems and their response to extreme events. The achievement of this project was carried out in close interaction with the different stakeholders including actors in municipalities and environmental agencies as well as the coastal users (Syndicat mixte de la Seine Maritime), and the councils of Etretat and Hautot-sur-mer.

2. Thesis outline

The first chapter of this thesis provides information related to coastal dynamics, including a first part dedicated to hydrodynamics, followed by a second part about generalities on beach morphology. Details on the specific characteristics of gravel beach morphology and dynamics are provided in part 3, then the scientific questions to be addressed in the present research work are stated in part 4.

The second chapter presents in a first part the regional context, including (1) the geomorphology of Normandy, (2) the origin and transport of its pebbles, (3) the distribution and consequence of human settlements on the coast, (4) some climatic aspects, and (5) wave and tidal conditions. The second part of this chapter is dedicated to the study sites: Hautot-sur-Mer, Etretat and Villers-sur-Mer, and to the video monitoring systems installed on each of these sites at the beginning of this thesis. Finally, a third and last part describes the different research methods used during this

work, including photogrammetry, image segmentation, principal component analysis, correlation and wavelet signal processing tools, and finally the XBeach-G numerical model.

The third chapter focuses on the measurement of surface grain size variability on gravel beaches. A method specifically developed for this purpose in the framework of this thesis and published in a research paper is presented in the first part (Soloy et al., 2020). The application of this method on multiple other sites in Europe and the USA is the subject of the second and last part of this chapter, some results of which were presented in an international scientific conference (Soloy et al., 2021a).

The fourth and final chapter aims to analyze the morphological dynamics of pebble beaches of Normandy after 2+ years of VMS observation. It is divided into three parts. The first part describes a method to model the daily 3D morphology of beaches in an automatic way. The development of this approach was the subject of a published article (Soloy et al., 2021b). The second part presents the results obtained when applying this method to the VMS data from Hautot-sur-Mer and Etretat, which were also described in a scientific publication (Soloy et al., 2022). An analysis of the coastline mechanisms of movement is carried out, and the forcings that cause them are investigated. A first evaluation of the spatiotemporal variability of the beaches is also performed, and hypotheses are formulated concerning the hydro-morpho-sedimentary dynamics.

Concluding remarks and perspectives are provided in a dedicated section following Chapter 4.

– CHAPTER 1 –

NEARSHORE DYNAMICS AND GRAVEL BEACHES

This first chapter is an introduction to the processes involved in beach dynamics. It begins by describing the forcings involved in coastal hydrodynamics such as tide and gravity waves and characterizes the different elements that make up the general morphology of a beach. Details on the morphology and specific dynamics of gravel beaches are then provided, including description of the berms, the beach step, the cusps, and specificities related to groundwater flow and sediment transport, all of which will have an important role in our reflection. Finally, the research questions that this thesis aims to address will be stated as well as the set of tasks to be achieved in order to answer them.

1. Coastal hydrodynamics

The terms “coastal hydrodynamics” refer to the processes responsible for energy propagation in the coastal domain, mainly through free surface oscillations (i.e., waves) and currents (i.e., rivers and gradient- or wave- induced discharges). These processes interact with each other and with the coastal morphology, often in a non-linear manner, and are responsible for most of the coastal sediment transport and associated morphological changes.

Ocean waves can be characterized according to their period, in a similar fashion to the way electromagnetic waves are divided into different ray bands. Munk (1950) defined seven categories of waves based on their relative amplitude and related them to different forcing (Figure 2). Wave categories include capillary waves (period < 0.1 sec), ultra-gravity waves (period from 0.1 to 1 sec), ordinary gravity waves (period from 1 to 30 sec), infra-gravity waves (period from 30 sec to 5 min), long-period waves (period from 5 min to 12 h), ordinary tides (period from 12h to 24h), and trans-tidal waves (period > 24h).

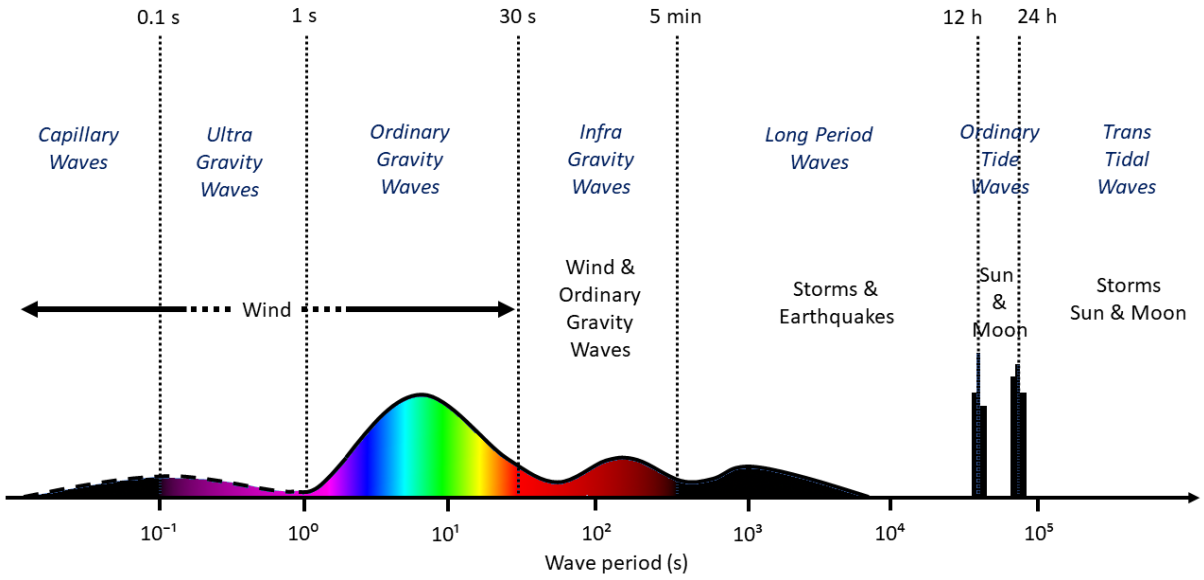

Figure 2 - Classification spectrum of ocean waves (modified after Munk (1950)*. The rainbow curve represents the relative arbitrary wave energy (vertical axis) of each type of wave according to their period (horizontal axis), colors are only meant to highlight the analogy with the spectrum of electromagnetic waves.*

Waves are expected to be the main forcing responsible for shoreline change, especially semi-diurnal to diurnal tides and wind ordinary gravity waves, which carry most of the amplitude. Therefore, we described these processes in more details in the following parts.

1.1.1. Tides

Tide is a quasi-periodic oscillation of the sea level of astronomical origin, propagated in the form of a semi-diurnal to diurnal wave. It is the result of the action of the joint gravitational forces

from the Moon and the Sun on the water masses of a given basin, and of the centrifugal force exerted on the Earth by the rotation of the Earth-Moon system (Simon, 2007). This variation can range from a few centimeters to several meters at a daily or sub-daily timescale. As it approaches the coast, the tidal wave becomes more complex due to interactions with the shape of the basin and with other forcings specific to the coast, for example the flow of rivers in estuarine areas.

In general, the tidal range can vary from a few decimeters to more than ten meters, depending on the location. Thus, Davies (1980) proposed a classification of tides according to their amplitude (TR**)**, later modified by Levoy et al. (2000) :

- **TR < 2 m** : Microtidal range
- **2 m < TR < 4 m** : Mesotidal range
- **4 m < TR < 8 m** : Macrotidal range
- **TR > 8 m** : Megatidal range

In the coastal domain, tidal waves are constrained by the rise of the bathymetry and begin to interact significantly with the basin. These interactions result in the appearance of new harmonic components of higher frequency (e.g. quarter-diurnal components, eighth-diurnal components, etc.), and may amplify the tidal amplitude. In some cases, the shape of the basin subjects the waves to a resonance phenomenon allowing tidal ranges of more than 10 to 12 m, as seen in the Bay of Mont Saint Michel, France.

However, the observed water level at a given location is not only due to the tidal forcing, especially near the coast. Indeed, additional phenomena can be added to the tidal forcing and amplify or attenuate it, such as surge and wave setup. These phenomena are less periodic and may constitute a risk in coastal environments during concomitant extreme events. For example, a storm can generate a large surge at the time of a spring tide, which is likely to cause overtopping and flooding. Hence, they remain important to consider for water elevation prediction applications.

In addition, tide is also responsible for currents occurring during ebb and flood phases. Their intensity depends on the tidal range and the bathymetry, their direction is controlled by the tidal phase (raising or lowering).

1.1.2. Ordinary gravity waves

Ordinary gravity waves are generated by the friction of wind on the sea surface. The height, direction, and period of the waves depend on the intensity of the wind, its direction, the extent of the surface to which it is applied (fetch), and the depth of water in the generation area. At any moment, the instantaneous state of the sea results from the combination of two components called the wind sea and the swell. The wind sea corresponds to the irregular waves generated by the local wind. The swell corresponds to waves that are unrelated to the local wind. They were generated and propagated from a distant region and are regular.

During their transfer, waves are subjected to different types of transformation, mainly due to interactions with the seafloor and hard structures. Like any wave phenomenon, ocean waves can be subject to refraction, diffraction, and reflection effects. Refraction tends to align the wave front with the coastline due to the slowing down of the waves when the depth is reduced as the coast approaches. Diffraction corresponds to the radiation of waves in the shadow of an obstacle (e.g., breakwater, islands, etc.). Reflection is the seaward rebound of part of the wave energy when it hits a non-dissipative structure.

The motion of water particles under a wave field can be described as a rotational displacement in a vertical plane (i.e., an orbit) perpendicular to the direction of propagation, whose radius decreases with depth until it becomes zero. The interaction between the waves and the bathymetry occurs when the water depth falls below a threshold called the closure depth (Figure 3). Above this depth, the orbital trajectory of water particles is influenced by the bottom and becomes elliptical. The wave parameters are then modified: the wave height increases, while velocity and period decrease. This process occurs in 3 steps, namely shoaling, surfing, and swash. The closure depth marks the limit of the active coastal profile where the speed of the water particles is sufficient to transport sediment. Its position varies in time depending on the tidal level and the wave period.

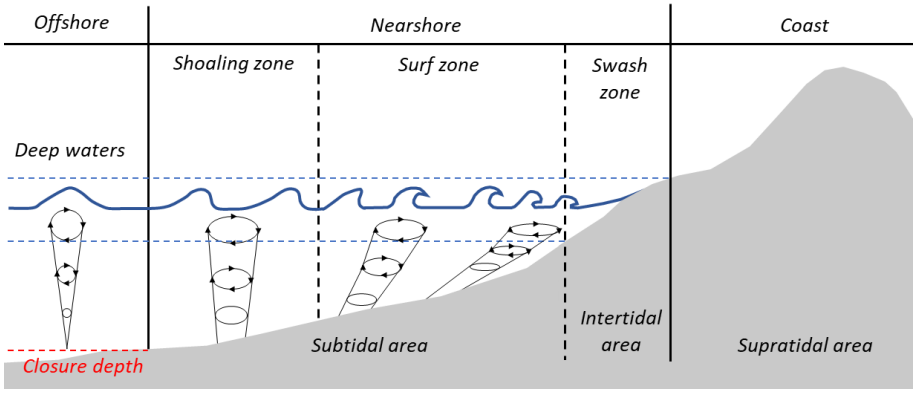

Figure 3 - Idealized cross-section of a wave-dominated beach system presenting the transformation of waves through the nearshore area (modified after Andriolo (2018)*).*

2. Beach morphology

Beaches are sediment accumulations along the shoreline that have been deposited by waves. They lay on bedrock foundation and are shaped by the action of waves. They require a source of sediment to form them, and most are affected by tides. The beach stretches from the wave base, where waves begin to interact with the bottom and shoal, through the nearshore zone, and into the surf zone, until it reaches the upper limit of wave swash (Figure 4). Processes of shoaling, breaking, and swash transform the ocean waves in the coastal zone, and modify the sea bed morphology. (Short, 2012).

The subaerial beach is generally composed of a wide berm whose seaward slope (beach face) varies according to hydrodynamic conditions and granulometry (Bujan et al., 2019). It results from the action of the swash of storm waves, which gives it its name (storm berm). Depending on site

conditions and sediment availability, it can be backed by a larger dune or by a lagoon in natural environments, or by a seawall in managed ones. Smaller berms called high tide berms are superimposed on the storm berm by the combined action of the waves and the tide. They are more mobile than storm berms as their scale is smaller. In the surf zone, the slope becomes gentler and sandy bars and channels appear, the number (between 0 and 2) and dimensions (order of magnitude of a hundred meters) of which vary according to hydrodynamic and sedimentary conditions. Bars are responsible for wave breaking in the surf zone. Their position can be deduced by observing where wave breaking happens on the sea surface, which can help estimating the underwater nearshore bathymetry (Holman et al., 2013; Román-Rivera and Ellis, 2019). However, gravel beaches often have a relatively steeper and therefore narrower surf zone. Instead of bars, a feature called the beach step forms at the bottom of the beach face, under the lowest tide level and provides a focus point for wave breaking (Buscombe and Masselink, 2006; Orford and Anthony, 2022). Further downslope, the slope increases again in the nearshore zone until the closure depth, which marks the threshold where the interaction between the bathymetric bottom and waves stops, and the boundary of the beach system.

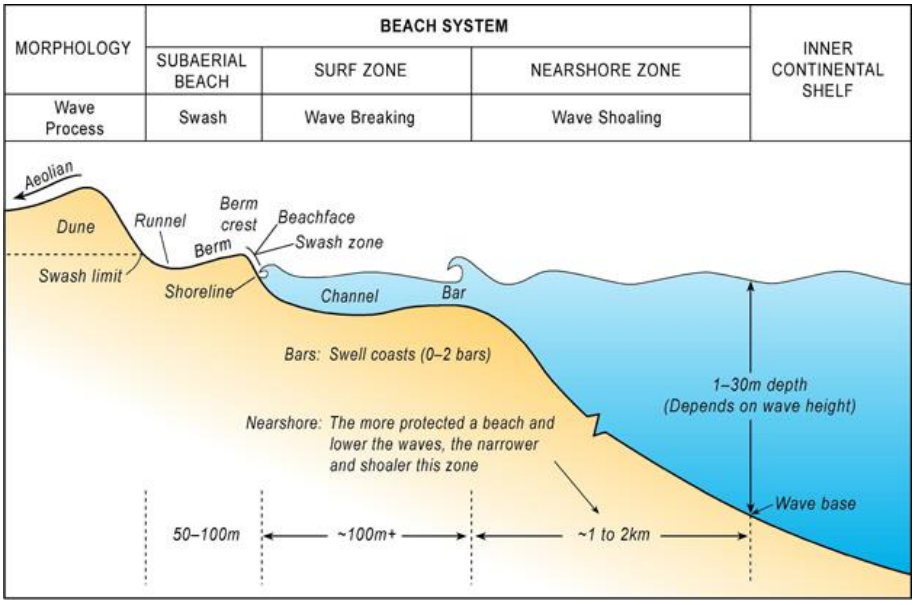

Figure 4 - Idealized cross-section of a wave-dominated beach system presenting the beach morphology (Short and Woodroffe, 2009).

3. Specific characteristics of gravel beach

3.1. Gravel Beach Classification

While the overall morphology of gravel beaches is similar to that of sandy beaches, some specific characteristics allow us to distinguish different types of gravel shorelines. Although gravel beaches are generally considered reflective with regards to wave propagation due to their steep slope (Bujan et al., 2019; López de San Román-Blanco et al., 2006; Masselink and Short, 1993; Orford and Anthony, 2022; Short, 1999), the different beach types also discriminate different wave dissipation/reflection behaviors. Jennings and Shulmeister (2002) proposed a classification according to the beach composition. The authors identified 3 types of profiles:

- Pure gravel beaches (PG, Figure 5a), with a steep reflective slope (8 to 24%). The gravel accumulation extends from the top of the storm berm into the subtidal zone. Of the three beach types, this is the one that was the subject of the first historical studies (Carr and Blackley, 1974; Orford and Anthony, 2022; Steers, 1965).
- Mixed sand-gravel beaches (MSG, Figure 5b) represent beaches with a mixed bimodal granulometry, their slope reflective varies from 4 to 13%. The sand component is very important in the characterization of this type of beach, indeed Holmes et al. (1997) showed that the finest 10% controls the hydraulic conductivity, which is a key factor of MSG beaches morphodynamics, and Mason et al. (1997) evidenced that a beach containing more than 25% of sand in its first meter of depth behaves more like a sandy beach than a gravel beach. This is probably the beach type that now focuses most of the research effort about gravel beaches (Atkinson and Esteves, 2018; Buscombe and Masselink, 2006; Guest and Hay, 2021; Horn and Walton, 2007; Orford and Anthony, 2022; Pitman et al., 2019; Roberts et al., 2013).
- Composite sand and gravel beaches (CSG, Figure 5c) are beaches consisting of two tiered compartments: a steeply sloping reflective upper beach made of gravel and a dissipative gently sloping sandy low-tide terrace (overall average slope between 5 and 14%)

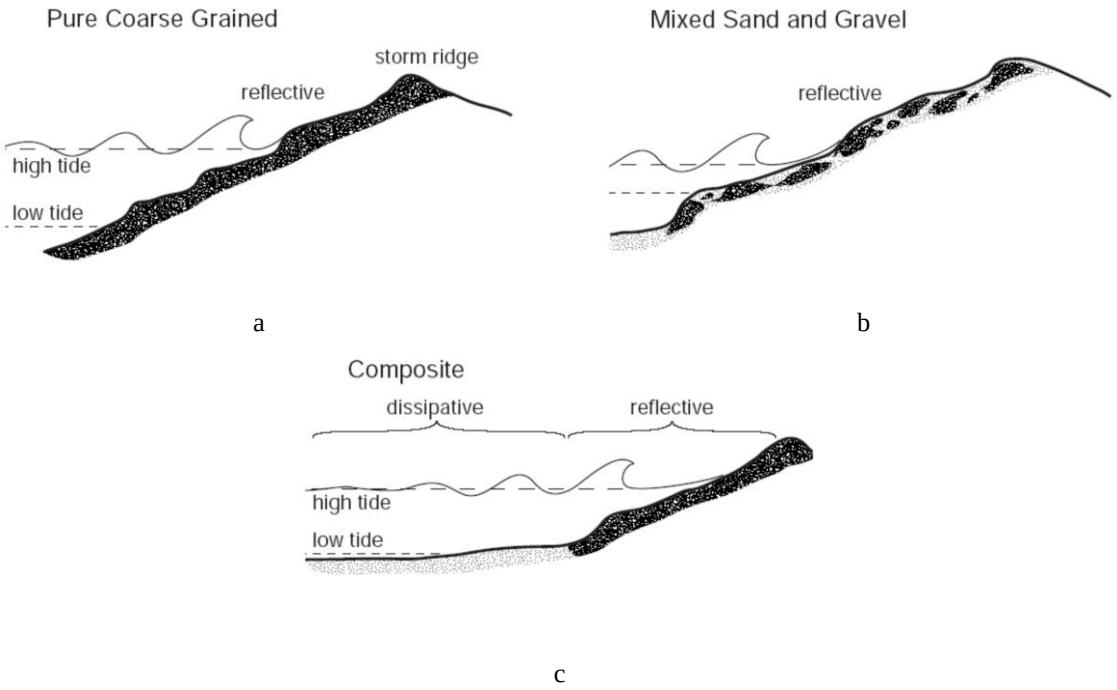

Figure 5 – Main types of gravel beaches according to the classification of Jennings and Shulmeister (2002) *modified after* Napier City Concil (2007)

3.2. Morphological features

3.2.1.Berms

Berms are discontinuities in the cross-shore topographic profile in the shape of a staircase with a flat top that may have a slightly positive seaward slope and a steeper face (Figure 6). Their existence is related to the asymmetry of the force exerted by the water on the sediment between runup (or

uprush) and rundown (or backwash). Indeed, swash lenses tend to seep more or less rapidly into the porosity of the swash zone, losing some of their ability to transport surface sediment, resulting in residual onshore sediment movement. For the same reasons, the elevation of the water table partly controls the elevation of the berm, as it limits the volume of water able to infiltrate during a swash cycle and thus the extent of the runup/rundown asymmetry. The berm tends to grow during the rising tide by a rollover landward mechanism generated by swash overtopping. The magnitude of this phenomenon depends on the tidal range: on a macrotidal beach the berm is a one-block construction, whereas on micro- to mesotidal beaches the berm is an accumulation of smaller independent bars (Pontee et al., 2004). This mechanism tends to increase the beach face slope and thus maintain a reflective beach profile. The position of the berm on the profile depends on the tidal cycle: the berm ridge settles at the highest elevations reached by the swash during a tidal period, hence their name: high tide berms. Therefore, neap berms are located at lower, onshore elevations than spring berms (Austin and Masselink, 2006a; Hine, 1979). The final geometric characteristics of the berm also depend on the size and shape of the available sediment. For example, the presence of disc-shaped and blade-shaped clasts generates an increase in beach face slope (Bluck, 1967; Orford et al., 2001; Orford, 1975).

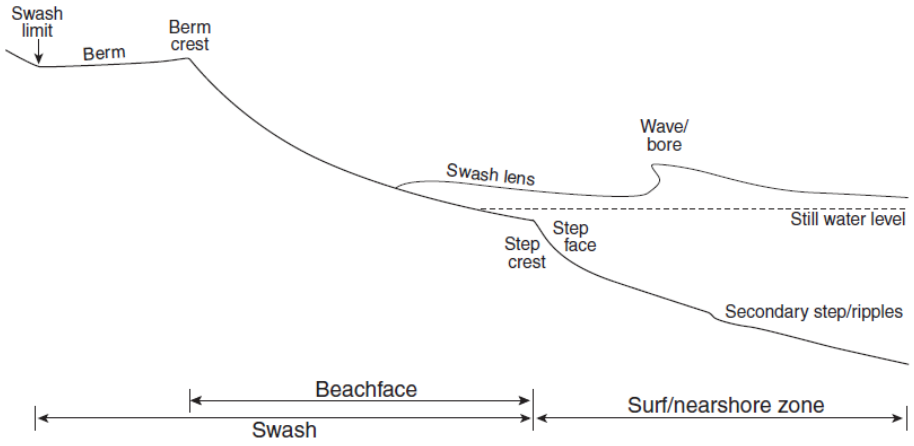

a

b

Figure 6 – a: Conceptual model of the nearshore profile of a stepped gravel beach (Austin and Buscombe, 2008) *; b: Example of a berm in Hautot-sur-Mer (Credit: A. Soloy, 2020).*

3.2.2.Beach step

The step is a submerged sedimentary accumulation forming a break in the slope at the foot of the beach face (Figure 6a). It plays a similar role to sand bars in the surf zone – which is often narrow or absent on gravel beaches - in forcing wave breaking, though much closer to the beach face (Hughes and Cowell, 1987; Orford and Anthony, 2022). Although it is not directly located within the swash zone, it is strongly linked to it through hydro-morpho-sedimentary feedback processes (Buscombe and Masselink, 2006; Orford and Anthony, 2022). Its position and dimensions may vary over time, but its mobility appears to remain relatively limited compared to the frequency and amplitude of tidal oscillations (Masselink et al., 2010). For this reason, the magnitude of its influence on wave transformation varies between low tide, where the step's ability to filter waves is maximal, and high tide, where it is less significant (Ivamy and Kench, 2006; Orford and Anthony, 2022). Thus, the step plays an important role in filtering and modulating the type of wave energy that can propagate to the beach face over time. The step rises with incident wave height, which can be understood as a positive

feedback process leading the reflectivity to a dynamic equilibrium (Austin and Masselink, 2006b; Buscombe and Masselink, 2006). More specifically, the type of breaker seems to matter significantly in the step's morphological variability: plunging breakers are expected to increase the step's slope, while surging ones will likely flatten it. Finally, the step often seems to select the largest and most spherical clasts available locally, therefore playing an active role in sediment sorting (Bluck, 1967; Orford and Anthony, 2022; Orford, 1975; Williams and Caldwell, 1988).

3.2.3.Cusps

Beach cusps are quasi periodic morphological longshore oscillations of the beach face (Figure 7). The intersection between a cuspate shoreline slope and the horizontal water surface creates a typical crescent shape. In addition, cusps are also involved in spatial sediment sorting as their horns (i.e., cusp top) are made of coarser material than their bays (Buscombe and Masselink, 2006; Masselink et al., 2014a). Cusps can grow on all types of beaches but are most prevalent on reflective beaches with low longshore transport rates, and are therefore a common feature of gravel shorelines (Kuenen, 1948). The cycle of generation to destruction happens rapidly, in a matter of hours. The process of cusp generation remains unknown, but there is one main theory: Random initial depressions on the beach face could concentrate more wave energy than their flatter surrounding, which would locally increase the erosion rate and eventually lead to digging bays and forming horns. The lower wave energy on top of horns would also tend to gather the bigger clasts there, while bays would be left with finer sediment. This explanation therefore sees cusp generation as a positive feedback loop process which would corelate the cusp wavelength to the height of runup (Durnkerley et al., 2016; Masselink et al., 2014a).

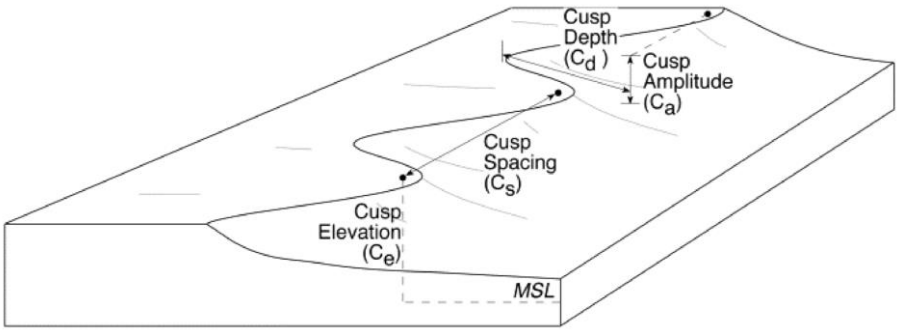

Figure 7 – 3D Scheme of the horizontal and cross-shore vertical profiles of beach cusps (Nolan et al., 1999)

In their classification of cobble beaches, Jennings and Shulmeister (2002) identified different types of cusps whose distribution varies according to beach type (Figure 8). Cusp types are categorized by wavelength: storm cusps are of the order of magnitude of 10 m or more and are located on the storm berm, high tide cusps are around 5 to 10 m and are found on the high tide berm, and swash cusps are features of metric dimension located in the swash zone but only occur on pure gravel beaches.

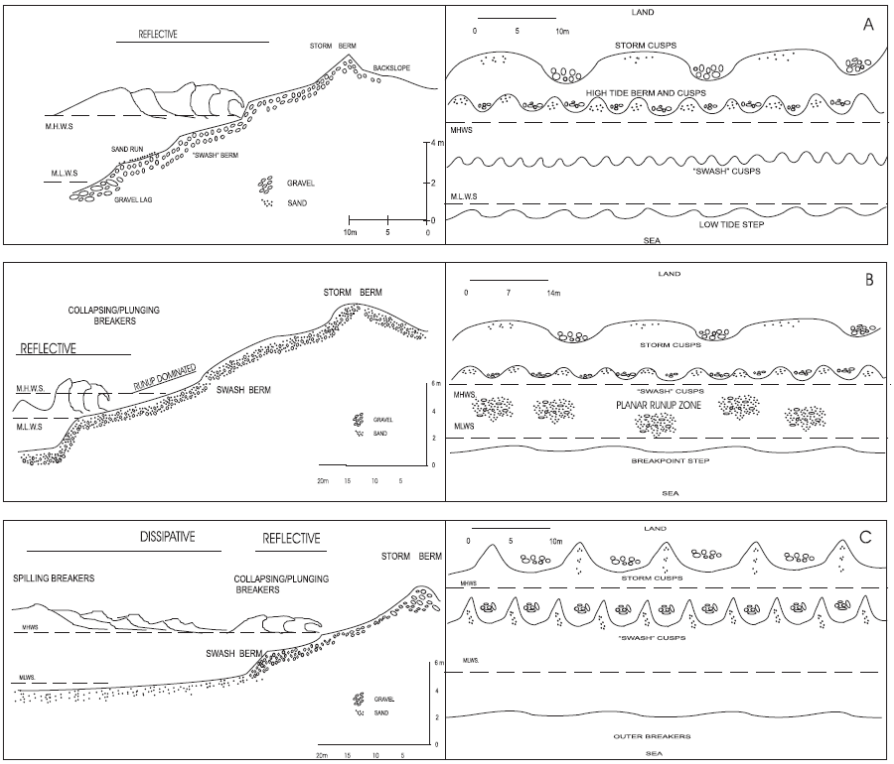

Figure 8 – Schematic representation of the three gravel beach types, in cross-section and plan view. The scale for each beach is different:(A) pure gravel beach characterized by a steep slope and plunging waves ; several sets of cusps are often present and a lag of coarse gravels forms at the toe of the beach ;(B) mixed sand and gravel (MSG) beach characterized by run-up over a planar swash zone and cusp development at the landward limit of run-up ; sand and gravel are entirely intermixed, although some surficial sorting may develop ;(C) composite sand and gravel (CSG) beach, characterized by a sandy intertidal zone on the lower profile, with a low slope ; the change from sand to gravel is often marked by a distinct breaking slope ; spilling breakers form at low tide and during storms. Adapted from Jennings and Shulmeister (2002), with permission from Elsevier. (Anthony 2008)

3.3. Groundwater flow

The swash zone is the most dynamic area of hydro-morphological activity on a gravel beach. The imbalance between swash lens volumes during runup and during rundown is responsible for the morphological dynamics of the swash zone (Bagnold, 1940; Carter and Orford, 1993; Grant, 1948; McCall, 2015). This imbalance is controlled by the infiltration process through the sediment, and the most critical sediment property regarding infiltration is permeability or hydraulic conductivity (Masselink and Li, 2001). The infiltration rate is maximal at the arrival of the swash lens, and then gradually decreases, sometimes down to zero during the backwash (Kikkert et al., 2013).

On a sandy beach, the limited sediment permeability (typically lower than 1 mm/s) allows only a small volume of water to infiltrate during a swash cycle (swash period ranges around 5 to 20 sec). Consequently, the volume asymmetry between runup and rundown is negligible. On a coarse sediment beach, the highest permeability (between 1 mm/s and 1 m/s) (Bear, 1972; McCall, 2015) results in significant swash asymmetry. Kikkert et al. (2013) measured a 35-50% reduction in water volume between uprush and backwash on two beaches including one of coarse sand (D50 = 1.3 mm) and one of gravel (D50 = 8.4 mm). Masselink and Li (2001) showed that a swash asymmetry higher

than 2% is sufficient to cause measurable morphological change, which would correspond to a critical threshold D50 = 1.5 mm (i.e., below this value, the infiltration processes can be considered negligible regarding morphodynamics).

The variable level of the groundwater table also plays an important role in gravel beach dynamics by controlling the volume required to reach saturation, and by modulating the magnitude of the exfiltration process which plays a role in swash asymmetry (Austin and Masselink, 2005, 2006a; Horn and Li, 2006; Masselink and Turner, 2012).

3.4. Sediment transport

The relatively limited extension of the surf zone concentrates a maximum of the wave energy in the swash zone, instead of dissipating it over a larger area as bars typically do on a sandy beach. One consequence of this spatial concentration is that despite their large size and mass, the sediment entrainment threshold is almost always exceeded in the swash zone, even under calm conditions (Buscombe and Masselink, 2006; McCall, 2015). Surface coarse sediments thus remain mobilized to continuously reshape the beach face morphology. This transport occurs through bedload flow, sheetload flow, and saltation mechanisms, with suspended transport in the water column considered negligible due to the high fall velocity of such coarse sediments (Carter and Orford, 1993; Isla and Bujalesky, 1993; McCall, 2015). However, swash asymmetry leads to a reduction in backwash velocity and an increase in backwash duration, which generates a predominantly onshore sediment transport and leads to a steep reflective topographic gradient formed by one or more berms (Masselink and Li, 2001).

The forces generated by infiltration and exfiltration processes also affect the variation in effective weight and shear force applied to surface particles (Elfrink and Baldock, 2002; Pintado-Patiño et al., 2015). Infiltration will tend to increase effective clast weight and bed shear stress, thereby reducing sediment mobility, and exfiltration will have the opposite effect.

4. Research interests

Among the different types of coastal systems, gravel beaches have probably received the least scientific attention, hence knowledge and understanding of the dynamics of such a type of environment remains critically limited (Buscombe and Masselink, 2006; Orford and Anthony, 2022). The difficulty of deploying expensive and sensitive measurement equipment in such dynamic conditions with heavy and mobile gravels likely accounts for much of this shortcoming, despite significant scientific interest (Almeida et al., 2015; Mason and Coates, 2001; Orford and Anthony, 2022; Orford, 2020).

Current state-of-the-art studies view gravel beach dynamics as a complex set of feedback loops and relationships between morphological, hydraulic, and sedimentary variabilities (Buscombe

and Masselink, 2006; McCall, 2015; Orford and Anthony, 2022). This idea is the basis of the concept of hydro-morpho-sedimentary dynamics, which assumes that sediment heterogeneity is a fundamental controlling factor of gravel beach morphodynamics, the latter being itself in a dynamic equilibrium with the varying marine forcings.

The response of coastal systems to environmental changes occurs on spatiotemporal scales proportional to the size of their constituents: the larger the clasts, the broader and longer the morphological changes (Orford and Anthony, 2022). Thus, gravel beach dynamics are expected to operate on wide spatial and long temporal scales (hectometers to kilometers cross- and long-shore and months to years). Paradoxically, one of the primary forcings of these dynamics is the impact of extreme events, especially storms (McCall, 2015), which operate on relatively short temporal scales (from hours to days). Nevertheless, the state-of-the-art studies are limited by the measurement difficulties mentioned above. It is possible to survey long-term system dynamics but at the cost of low temporal and/or spatial resolutions (e.g., Pollard et al. (2020)), or conversely, to monitor high-frequency dynamics but in the shorter term (e.g., Guest and Hay (2021)).

The use of VMS for high-frequency (daily) monitoring of coastal morphology is a proven approach for sandy systems (Aarninkhof et al., 2003; Holman et al., 1991; Kingston, 2003; Osorio et al., 2012; Plant et al., 2007; Turner et al., 2004; Valentini et al., 2017). VMS are particularly well suited to the unique constraints and challenges of gravel systems as they can be deployed at a safe distance from the active shoreline and operated remotely at a high frequency (minutes to hours) for long periods of time (years). Surface From Motion (SFM) techniques, including UAV image photogrammetry, are also becoming more and more popular for coastal science applications, as they allow for measuring beach morphology accurately and inexpensively (Burdziakowski et al., 2020; Gonçalves and Henriques, 2015; Laporte-Fauret et al., 2019; Medjkane et al., 2018). In the case of gravel beaches, the orthophotographs generated by SFM processing contain surface grain size information (when the image resolution is pixel size is several times smaller than the gravel size), which could thus potentially be mapped and monitored.

In this context, this thesis work proposes to address the question of the hydro-morpho-sedimentary dynamics of gravel beaches in the short-medium term (days to years), at a high frequency (daily), especially during storm periods. This task will be achieved by coupling information extracted using remote sensing techniques applied to coastal imagery data acquired from multiple platforms (VMS and UAV). More specifically, this research will be focused on answering the five following scientific questions by achieving the associated tasks:

1. How can we reliably quantify the spatiotemporal variability of the gravel morphometry?
    - Development of an approach to map the size, shape and orientation of gravels on the surface of beaches.
    - Demonstration of effectiveness on the beaches of Normandy.

2. How can we reliably monitor the morphodynamics of gravel beaches?
    - Development of a method to automatically monitor the daily shoreline morphology.
    - Validation of performances for the beaches of Normandy.
3. How do beach morphodynamics respond to hydrodynamics?
    - Identification of the main mechanisms of shoreline mobility from daily up to the yearly timescale.
    - Identification of the main periods of shoreline variability.
    - Identification of the physical forcings responsible for gravel planform shoreline changes.
4. What is the spatiotemporal variability the beach surficial gravel size?
    - Identification of spatial dispersion patterns on gravel beaches.
    - Identification of their temporal changes and their potential cause in relation to the beach hydro-morphodynamics.
5. What is the effect of storm events on the beach permeability and its morphology?
    - Modelling of the impact of storms on a gravel beach profile and estimation of changes in the daily average permeability.

5. Chapter conclusion

In summary, gravel beaches provide significant protection to the coasts on which they rest, and are therefore an important issue, especially in the context of climate change. Their morphodynamics are singular in several aspects. This is especially due to the relatively short surfzone, which is unable to dissipate as a significant amount of energy as it is on sandy systems where it is wider, thus leading to a particularly energetic swash zone. Wave energy absorption is instead performed by infiltration into the higher permeability that is allowed by the larger grain size, making grain size derived permeability a key factor influencing the morphodynamics of gravel beaches. In addition, the position and intensity of this zone are modulated by tidal oscillations. The combination of all these factors makes measurements challenging, thus limiting our knowledge of the dynamics of these systems.

This thesis represents a research effort aiming to better understand gravel beach dynamics. To this end, it proposes to investigate on different scientific questions intended (1) to propose innovative measurement solutions that are adapted to the difficult measuring conditions of these environments, (2) to use these solutions to observe the morpho-sedimentary dynamics of gravel beaches at different time scales, and (3) to investigate on the relationships between the then observed hydraulic, morphological and sedimentary dynamics.

– CHAPTER 2 –

RESEARCH APPROACH

Following the description of hydro- and morphodynamics processes relevant to the study of gravel beaches in Chapter 1, this chapter firstly aims to describe the specific context of Normandy. The coastal geomorphology is presented along with the origin and transport of pebble particles, then insights are given about human settlements and coastal defense before presenting the climate, wave and tidal aspects of this coastal region. In a second section the three initially selected study sites are presented: Etretat, Hautot-sur-Mer and Villers-sur-Mer, along with a description of the installed VMS. Note that Villers-sur-Mer was abandoned for technical reasons and will not be considered in further analysis except for methodological development. Lastly, this chapter details the different methodologies used to process images (i.e., photogrammetry and image segmentation), to analyze the observed dynamics (Empirical Orthogonal Functions, correlation and wavelet analysis), and to model it using XBeach-G.

1. Regional setting of Normandy, France

1.1. Coastal geomorphology

The coasts of Normandy can be distinguished in 3 main categories: high cliffs, low coasts and accumulation areas (Figure 9). North of the Seine River, the Normandy coasts are exclusively composed of high cliffs. Further south, the composition of the coastline alternates between high and low rocky coasts, with some accumulation of softer sediment.

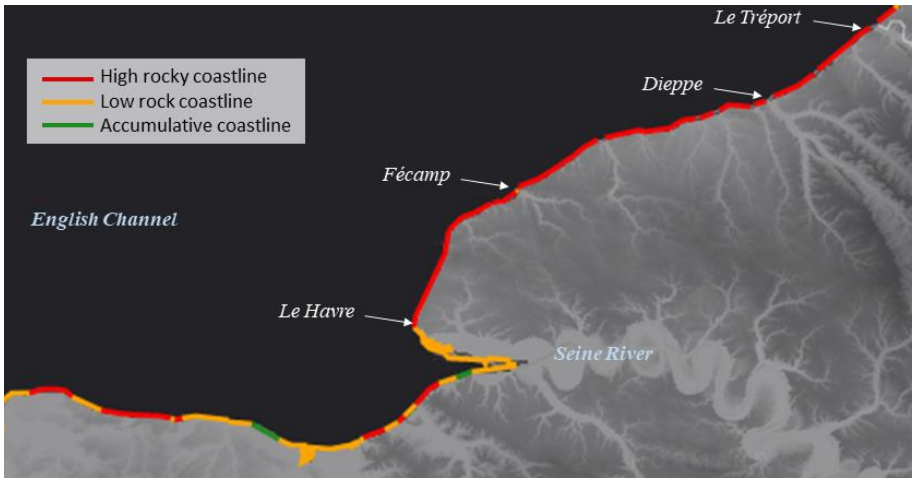

Figure 9 – Types of coastlines in Normandy, the background image shows the topography (ROL, 2019)

The cliffs of northern Normandy are the result of the erosion of a chalky substratum and constitute the visible edge of the sedimentary syncline basin of Paris. This basin was formed by the accumulation of skeletons of submarine organisms in the Upper Cretaceous, between Turonian (-93.9 Ma ± 0.3) and Campanian (-72.1 Ma ± 0.2), in a shallow sea under a tropical climate. The age of the sedimentary strata (Figure 10) has an influence on the coastal geomorphology: the older layers faced longer and harder diagenetic conditions, they are more compact than the younger ones and erode less easily. On the shoreline, this difference is generally reflected by the presence of a hardground platform at the foot of the cliff at an intertidal elevation, which can extend for several hundred meters from the cliff.

The sedimentary succession (Figure 10) is crossed by hollows of variable depth representing the river valleys. On the field, numerous faults in the cliffs can be observed. They are the result of ancient tectonic activity (Normandy is seismically stable today); the Fécamp fault, which extends across the entire Normandy region and shifts the sedimentary succession by a vertical offset of around 50m, is the main one.

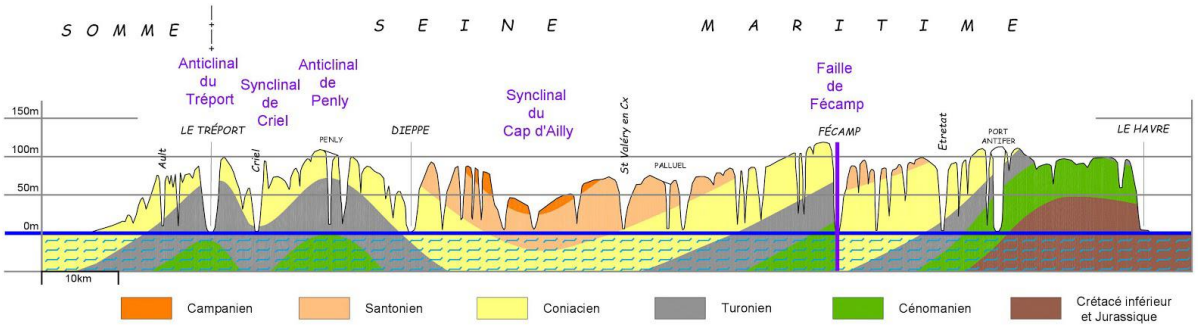

Figure 10 - Geological section of the cliffs of the Alabaster Coast (ratio length/height = 100) (Hoyez et al., 2020)

1.2. Origin and transport of pebbles

In northern Normandy, pebbles constitute an important part of the coastal sedimentary stock. They result from the erosion of limestone cliffs by meteorological and marine forces. Indeed, the sedimentary substratum of the Parisian basin includes numerous layers of flint (Figure 11), a hard silica sedimentary material whose formation process is, to the authors' knowledge, not known yet.

a

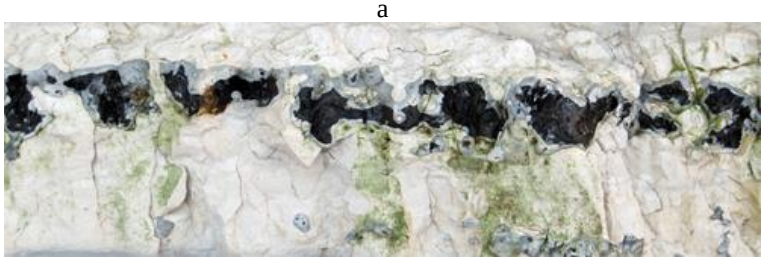

b

Figure 11 – a: Chalk cliff in Etretat with darker flint stratification layers (credit: N. Lecoq, 2018); b: Close-up view of a flint layer in a chalk cliff (B. Hoyez, nd, https://craies.crihan.fr/?page_id=36)

Along time, the cliff top chalk is altered by weathering into clays, which are much less consolidated than chalk. Meanwhile, the cliff bottom material is eroded by the action of waves. If the balance between material resistance and gravity gets disrupted, part of the cliff will collapse, and thus spread broken material at the foot of the cliff. While chalk will be dissolved in the sea, the fragments of flints will be rolled and rounded under the waves' action into pebbles.

The pebbles thus formed are then transported in a long-shore drift whose direction depends on swells. Between Etretat and Le Hourdel (Figure 12), the main direction of transport is northeastward. In calm conditions, the pebbles settle and accumulate near estuary mouths, in the hollows of bays and at the foot of obstacles to the longshore drift such as cross-shore defensive structures. The pebbles then form sedimentary bodies including pebble bars, barriers, and ridges.

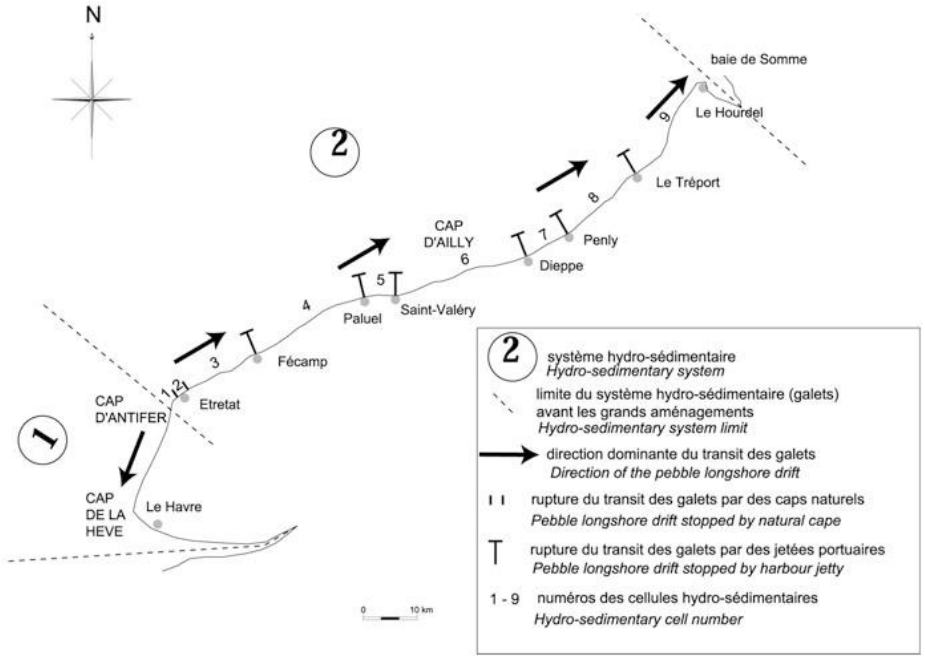

Figure 12 – Longshore drift along the coast of northern Normandy (Costa, 1997)

During a storm, much of the wave energy is dissipated by the pebble's movements and thus the erosion of the ridge, which has the advantage of protecting coastal structures and activities. As for any non-cohesive sedimentary body, the erosion and accumulation characteristics of the pebble ridge depends on the intrinsic parameters of its constituent elements. Thus, pebble size is expected to play a major role in the morphological dynamics of pebble beaches.

1.3. Human settlements and coastal defense

Historically, humans have settled preferentially along river and estuaries. As a result, current human settlements remain concentrated in these types of environments. This observation is particularly noticeable in Figure 13, which presents the coastal artificialization of Normandy and Hauts-de-France. The northern part of Normandy, consisting of high cliffs, is globally little anthropized (green), although some points located at the mouth of rivers show the presence of punctual human structures (blue).

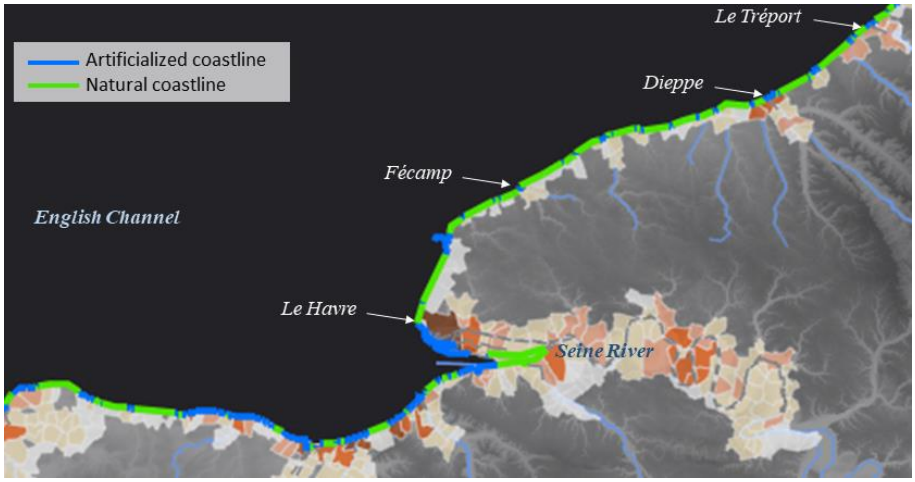

Figure 13 - Artificialization of the coastline in Normandy (ROL, 2019). *Brown polygons represent the relative density of buildings built under the centennial water level (clearer colors indicate a lower exposure to the risk of submersion)*

These structures correspond to the coastal structures used for channelizing and draining of river estuaries. They aim to protect human facilities against the impact of extreme events (storms, floods, etc.), while maximizing the space available for them. Generally, the estuary is closed by a seawall parallel to the coastline, which can be purposely breached to allow the river to flow through. Perpendicular groins are a common addition to limit longshore sediment transport and to accumulate material on the seawall, which improves its protection capability (Figure 14). Other types of coastal defense structures exist (i.e., dikes, jetties, riprap, wave brakers, etc.) and fulfill various tasks but are irrelevant to be described in the framework of this thesis.

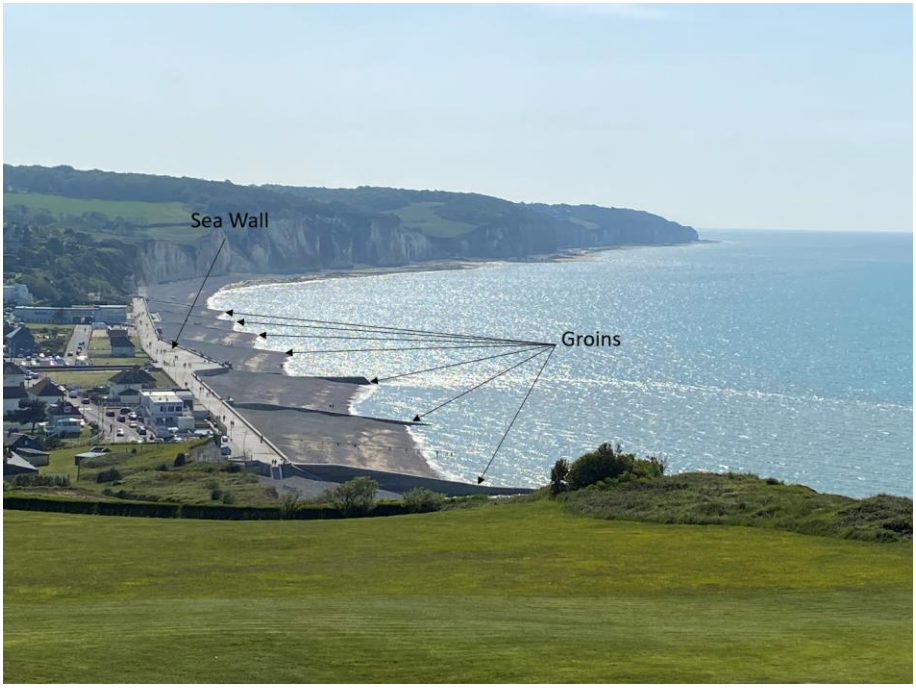

Figure 14 - Typical coastal defense structures encountered on the beaches of Normandy. Photography taken at mid- to high tide in Hautot-sur-Mer (credit: J. Steele, 2021).

1.4. Climate

Normandy is located in a temperate oceanic climate region. The temperature evolves seasonally, with averages between 2 and 7°C in winter (Figure 15a), and between 15 and 18°C in summer (Figure 15b). However, these temperatures are not completely spatially homogeneous, in summer a negative temperature gradient is established from the sea to the inland, which favors the land winds, and conversely in winter, which favors the sea winds. Topography also plays a role: valley bottoms and low-lying plateaus benefit from higher temperatures. This is particularly the case for the Cotentin Peninsula in winter that faces different wind conditions than the rest of the region, which explains the apparent anomaly observed. Low temperatures, and in particular sub-zero temperatures in winter, play an active role in coastal dynamics by breaking down cliff materials through a cryoclastic process.

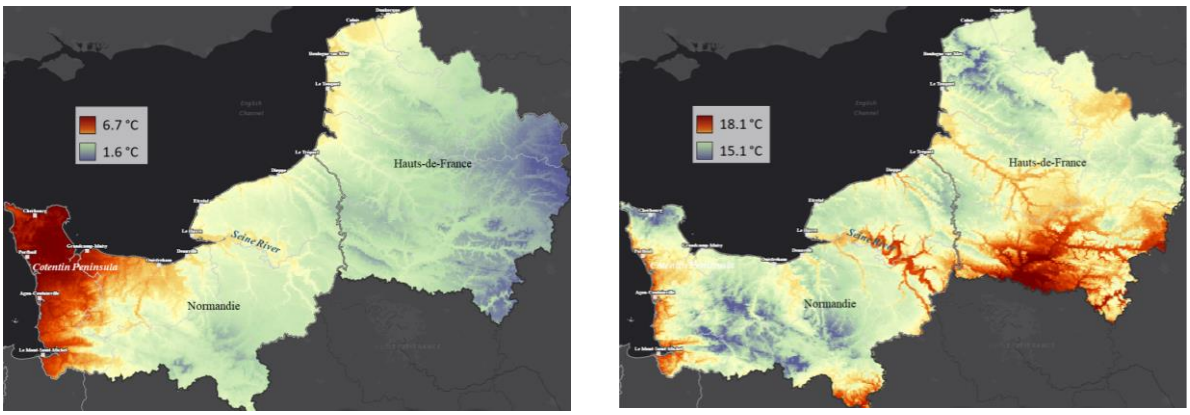

a b

Figure 15 – Average winter (a) and summer (b) temperatures in Normandy and Hauts-de-France (ROL, 2019)

The average winds (Figure 16a and b) come from the west and their speed varies between 0 and 5 m/s depending on the location: the speed increases as one moves away from the coast. One would expect to observe weaker winds in the enclosed English Channel than in the open Atlantic Ocean, but no significant difference is observed. On the contrary, the strongest mean winds are observed off Ireland, in the St. George's Channel, despite its landlocked morphology. However, on a smaller scale, the topography protects certain areas from the wind, particularly bays such as Mont Saint Michel or the Bay of Seine.

Maximum wind speeds (Figure 16c) reach between 10 and 25 m/s and are slower in the part of the English Channel located east of the Contentin Peninsula, and in the North Sea. During storm events, the funnel morphology of the channel tends to limit the wind speed in the eastern part. It is the Cotentin Peninsula that acts as a protective shield during climatic extremes by dissipating the energy of surface winds, which is probably associated with a heat transfer partly responsible for the anomaly in this area visible in Figure 15a.

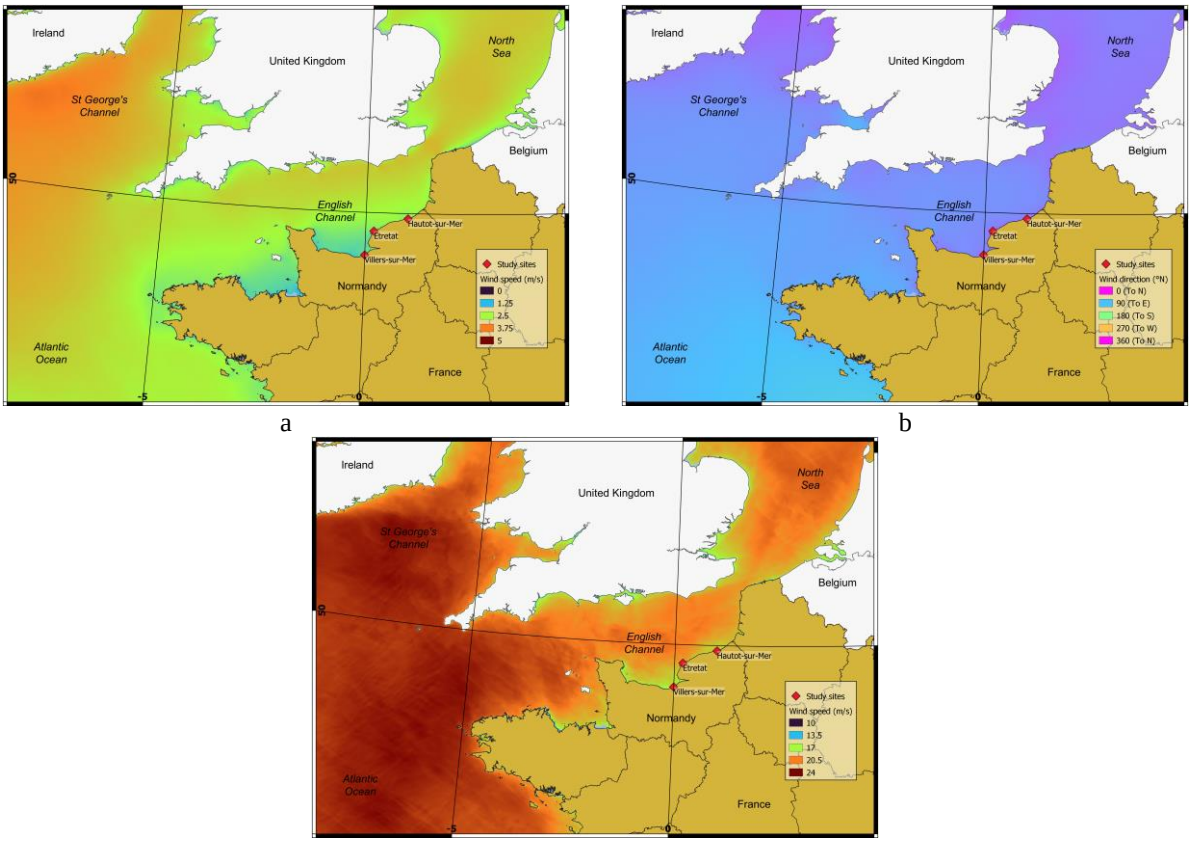

Figure 16 – Yearly average windspeed (a), wind direction (b) and maximum wind speed (c) at elevation 10 m in 2019 around the northern French coasts. These maps were built using data from the Arome model provided by SHOM.

1.5. Waves

The average wave height (Figure 17a) resembles that of the wind speed, which is expected. However, there is more spatial variability in both wave heights, for example the mean wave heights reach 2 to 3 m in the Atlantic Ocean, and only 1 to 2 m in the English Channel. This is the result of the channeling of waves by the funnel morphology of the English Channel: the fetch is limited by the edges of the channel.

The particular morphology of the English Channel also influences the wave direction (and thus the impact of storms) by directing winds and swells towards preferential directions, therefore constraining the associated wind fetches to only a few directions: W-E (infinite wind fetch), NE-SW (550 km wind fetch), NW-SE (200 km wind fetch), N-S (100 km wind fetch) (Figure 17b, Letortu (2013). Wave direction is also more heterogeneous than wind direction. One can see the effect of wave refraction by the coastal bathymetry, for example the western waves from the Atlantic reoriented towards the south when approaching the Normandy coast.

In storm conditions, wave heights tend to increase in proportion to the wind. They can reach up to 10 m in the Atlantic Ocean, and 5 to 7 m in the English Channel (Figure 17c). As they approach bays and estuaries, storm waves are significantly amplified (Figure 17d), especially in areas where the mean wave height is less than 1m, such as the Normandy coast where storm waves reach up to 5 m.

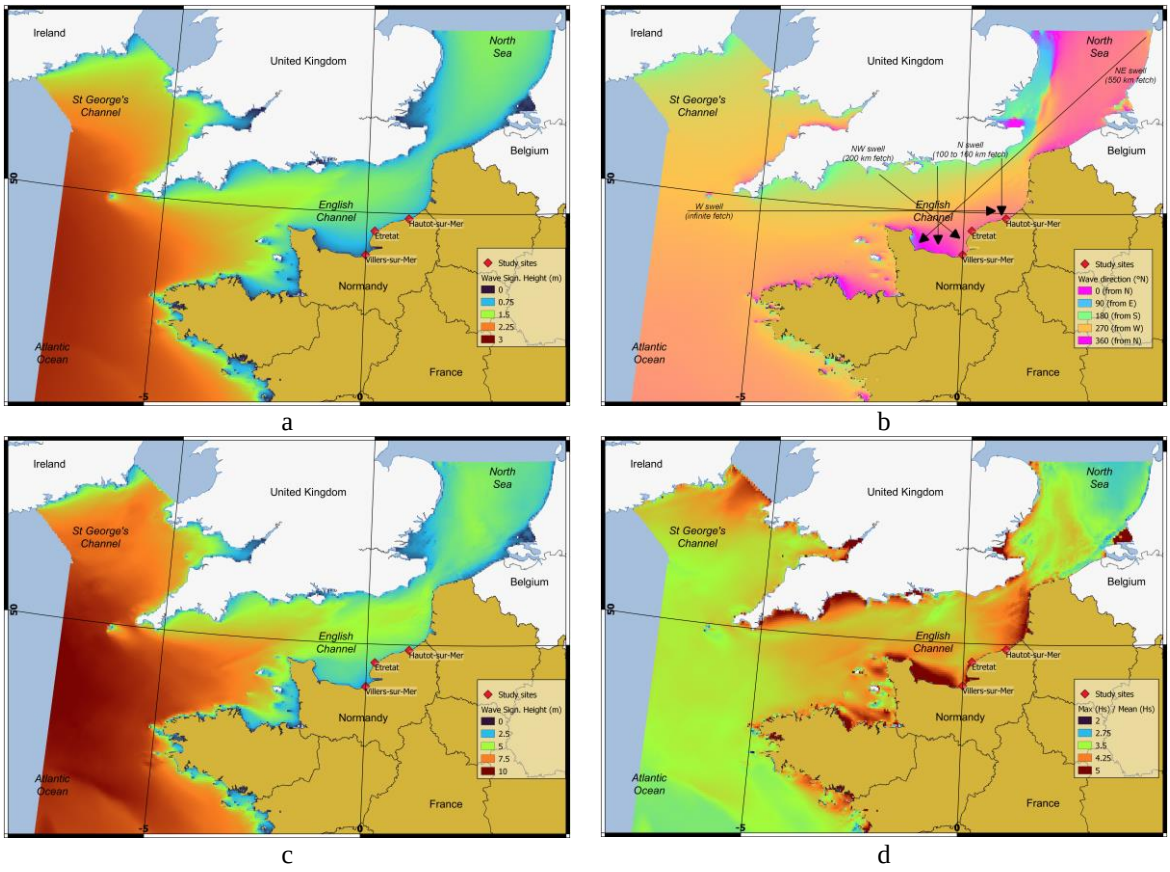

Figure 17 – Yearly average wave significant heigh (a), wave direction (b) maximum wave hight (c) and ratio between maximum and mean wave height (d) in 2019 around the northern French coasts. Fetch distances are indicated on b after Letortu (2013)*. Maps were built using data from the WaveWatch 3 model provided by Ifremer.*

1.6. Tide and currents

The funnel morphology of the channel is also responsible for the considerable amplification of tidal ranges (Figure 18) and their associated current speeds in the Channel and its surroundings. Indeed, the Normandy coasts in particular are characterized by amplitudes between macro- and megatidal, with values above 10 m in the Bay of Mont Saint Michel, located to the west of the Cotentin Peninsula, and between 8 and 10 m further east. Nevertheless, it is important to remember that these amplitudes correspond to the maximums reached during spring tides.

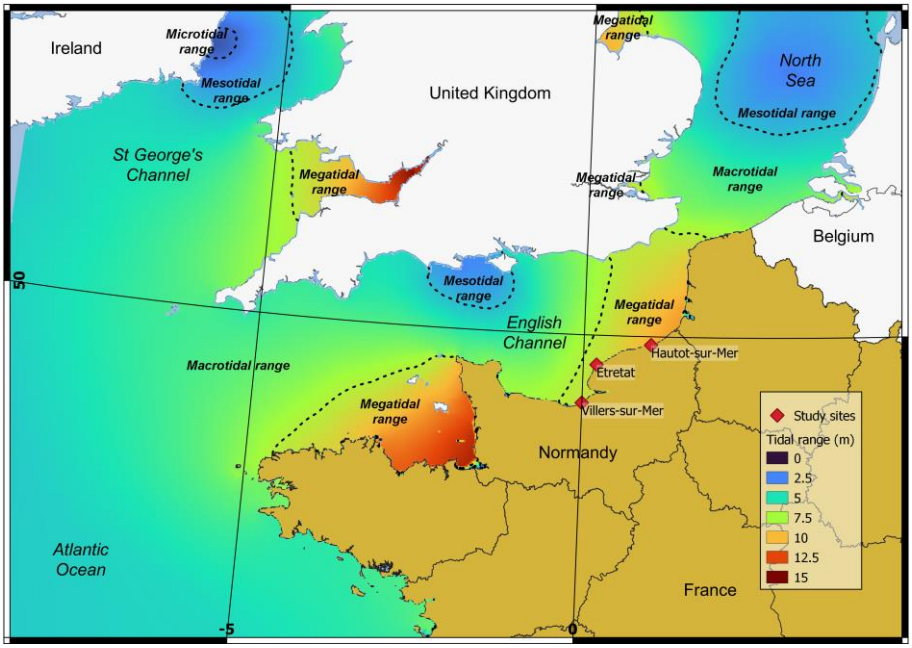

Figure 18 – Spring tidal ranges and classification according to Davies (1980) *and* Levoy et al. (2000) *around the northern French coasts. This map was built using data from the Hycom2D model provided by SHOM.*

Marine storms sometimes hit the coast concurrently with high spring tide and/or other environmental extremes such as river floods. Such events can lead to severe damages on the coastal structures, and urban facilities, and even human causalities. Indeed, not only to the overtopping and overwashing waves can breach coastal defense and cause floods (Figure 19), but they are also able to transport pebbles on ballistic trajectories (Figure 20). Hence, such events and associated risks are particularly surveilled.

a b c d

Figure 19 – The beaches of Etretat (a, b and c) and Saint-Malo (d) under energetic conditions during concurrent storm events (Storms Eleanor (a, b) and Gabriel (c, d)) and spring tide ranges of winter 2018-2019 (Credits: Marie-Agnès Godin, 2018 (a); Isabelle Simon/SIPA, 2018 (b); Morgan L.L., 2019 (c) and Mathieu Rivrin, 2019 (d))

a b

Figure 20 - Washover sediment found on top of the seawall of Hautot-sur-Mer after Storm Ciara on 2020/02/14 (Credit: A. Soloy, 2020)

In Normandy, currents are mainly generated by the tide and reach average speeds of 5 to 30 cm/s, with a strong spatial disparity (Figure 21a). In the Channel, the highest speeds are reached off the Bay of Mont Saint Michel, in the strait between Dover and Calais, and more generally at the tip of the capes and peninsulas. On the contrary, Atlantic current speeds come close to zero in the southwest of the area, which corresponds to the continental shelf slope. At this location the depth and basin openness increase significantly, allowing tidal waves to move without interacting with the bathymetric bottom, and therefore without initiating significant current.

In terms of current directions (Figure 21b), there is a particularly marked distinction inside the English Channel between the west and east of the Cotentin Peninsula, with W-E and NE-SW directions, respectively, and a very clear delineation. Importantly, current speed and direction vary with the tide phase and amplitude. They are maximum during flow and ebb of spring tides, and minimum during high and low tide, which happen at different time for different locations.

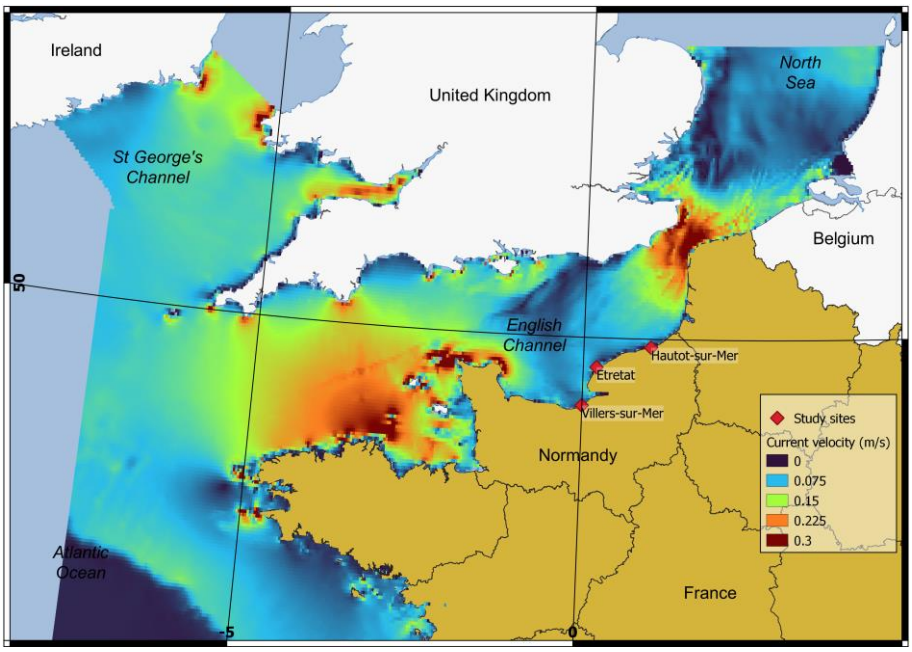

a

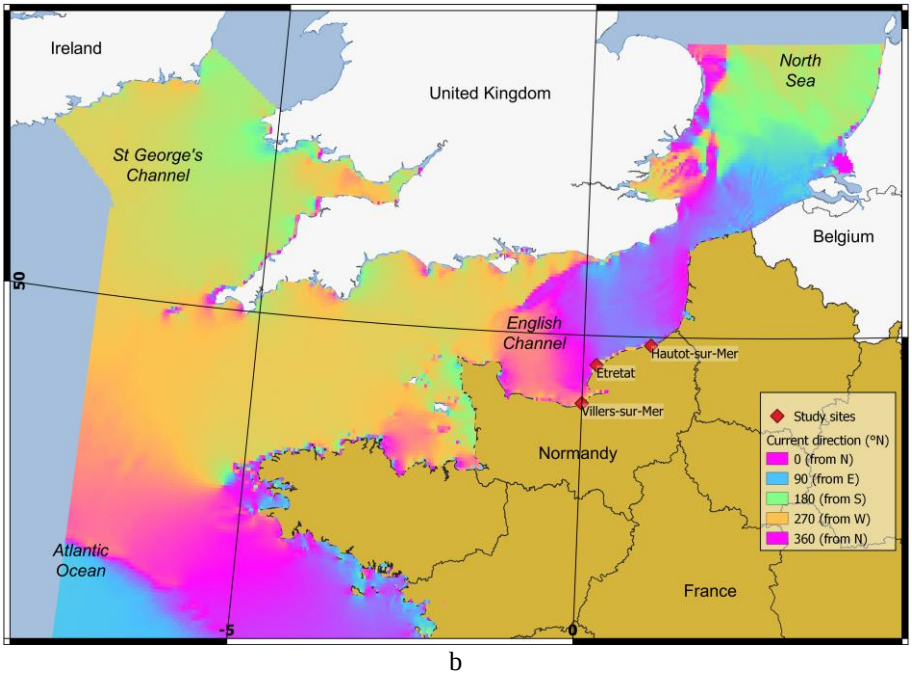

b

Figure 21 – Yearly average current velocity (a) and direction (b) in 2019 around the northern French coasts. These maps were built using data from the Hycom2D model provided by SHOM.

2. Study sites and video monitoring systems

During this work, three study sites were monitored: Etretat, Hautot-sur-Mer and Villers-sur-Mer (Figure 22). The three study sites were chosen to represent the wide variability of coastal systems

present in Normandy. Unfortunately, the site of Villers-sur-Mer had to be abandoned due to malfunctions that remained until the end of this thesis' timeframe. Nevertheless, all three sites will be described in this section. Tidal dimensions of each site are given in Table 1.

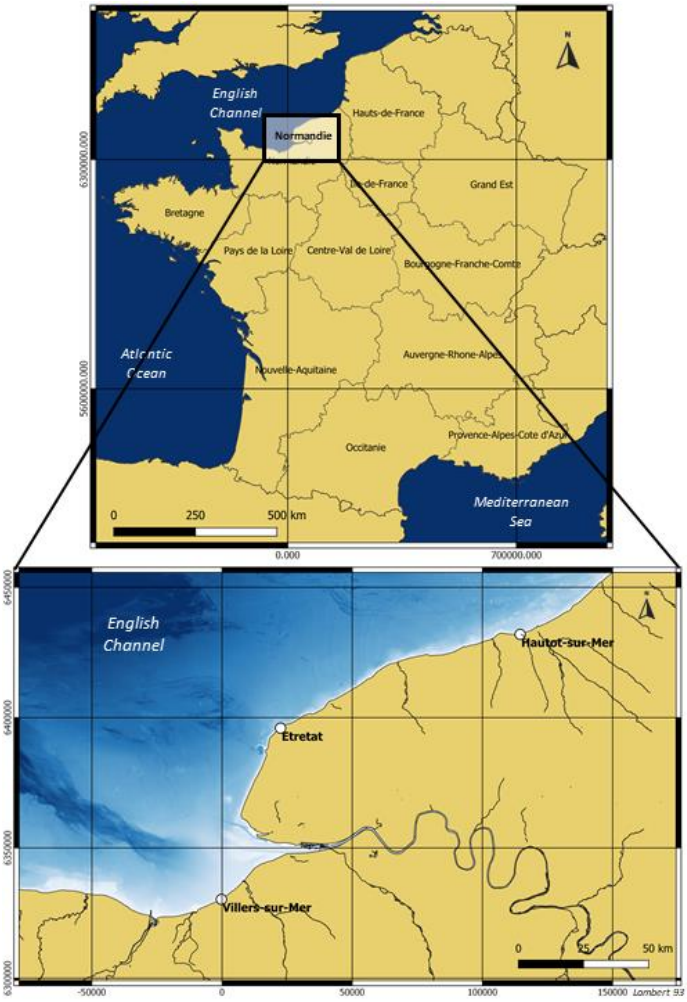

Figure 22 - Location map of Villers-sur-Mer, Etretat and Hautot-sur-Mer, in Normandy, France

Table 1 - Tidal and intertidal dimensions of the Normandy beaches of Villers-sur-Mer, Etretat and Hautot-sur-Mer

Sites	Etretat	Hautot-sur-Mer	Villers-sur-Mer
Average tidal range	6.08 m	6.79 m	5.11 m
Max tidal range	9.13 m	9.86 m	9.60 m
Min tidal range	3.20 m	2.96 m	0.16 m
Lowest Water Level (LWL) (datum: IGN69)	-4.80 m	-4.45 m	-3.81 m
Beach Length	1000 m	1100 m	4250 m
Beach width at LWL	150 m	210 m	310 m
Pebble ridge slope	> 12 %	> 10 %	
Pebbles D50	60 mm	75 mm	
Sand D50	0.80 mm	0.18 mm	0.19 mm

2.1. Hautot-sur-Mer

Hautot-sur-Mer is an approximately 1000 m long semi-open system located at the mouth of the Scie Valley (Figure 23). The 20 to 50 m high chalk cliffs that surround it show an average retreat of 20 to 50 cm per year (Costa et al., 2019), regularly replenishing the stock of pebbles. The ridge at the front of the seawall is formed by pebbles (D50 = 7.1 cm), which are trapped in the middle of seven cross-shore groins installed perpendicularly to a seawall oriented at 71°N. According to the classification of Jennings and Shulmeister (2002), the site corresponds to the definition of a composite beach: the ridge (slope > 10%) lies on a sandy low tide terrace (D50 = 0.18 mm, slope 1.3%) which can emerge over more than 210 m at low tide (Figure 27). Four kilometers to the east is the town of Dieppe, whose harbor is protected from the transit of pebbles at its entrance by a 500 m long pier. This structure accumulates a large part of the regional stock of pebbles.

a

b

Figure 23 – a: Satellite photography of Hautot-sur-Mer, the white rectangle indicates the area monitored with VMS; b: aerial cross-shore view of the beach including the pebble ridge and coastal defense structures (left), and the sandy low tide terrace (center). The image was taken at low tide using a drone (credit: P. Rouxin, 2019).

2.2. Etretat

The Bay of Etretat is an approximately 1000 m long enclosed system, framed by high cliffs made of more indurated limestone (average retreat of between 14 and 17 cm/year (Costa et al., 2019)), forming capes that block the longshore drift (Figure 24). The pebble stock is old, elements are smaller in size (D50 = 5.2 cm) and few are mobilized by coastal transit because they are trapped in the bay. This stock accumulates in the form of a pure pebble ridge (Figure 27) (Jennings and Shulmeister, 2002) with 10% slope, installed against the seawall (orientation 47°N) with four groins, over a cross-shore extension that reaches up to 150 m at lowest tides. A subtidal sandy substrate (measured D50 = 0.8 mm) appears on rare occasions when the beach becomes mainly sandy after long repetitive heavy storm conditions. The beach is crossed by 4 groins installed against the seawall, which has a mean orientation of 47°N. In the intertidal zone, bedrock emerges at low tide on the sides of the bay.

a

b

Figure 24 - a: Satellite photography of Etretat, the white rectangle indicates the area monitored with VMS; b: aerial cross-shore view of the beach including the pebble ridge and coastal defense structures. The image was taken at mid- to high tide from the top of the western cliff (credit: J. Braukmann, 2019, https://commons.wikimedia.org/wiki/File:Vue_d%27%C3%89tretat.jpg)

2.3. Villers-sur-Mer

The beach of Villers-sur-Mer is a 4250 m long open sandy system located southwest of the Seine River estuary (Figure 25). The beach lays at the foot of a small seawall (Figure 27) aligned towards the direction 62°N and is crossed by 15 large groins. Its gentle slope (< 1%) allow the intertidal area to uncover over 310 m in the cross-shore direction at the lowest low tides, while developing small pools and runnels. Due to the high touristic activity, the sediment is mechanically filtered on a daily basis in summer to keep the beach attractive.

a

b

Figure 25 - a: Satellite photography of Villers-sur-Mer, the white rectangle indicates the area monitored with VMS; b: elevated view of the beach including. The image was taken at low tide (credit: A. Soloy, 2019).

While the beach material is mainly sand (D50 = 0.19 mm), accumulations of pebbles were occasionally observed, although not measured (Figure 26). The origin of this coarse material is probably the Vaches Noires cliffs, a chalky and highly erodible site that borders the western limit of Villers-sur-Mer's beach.

Figure 26 - Accumulation of pebbles on the beach of Villers-sur-Mer. The photography was taken on 2020/06/28 at low tide, within the VMS monitoring area (credit. A. Soloy, 2020).

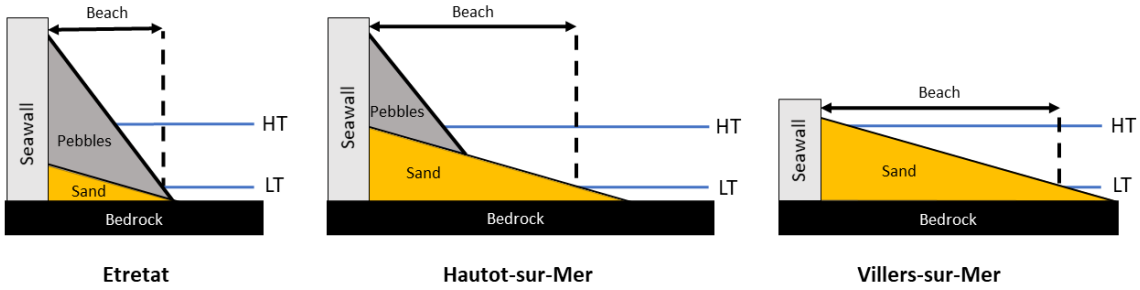

Figure 27 - Conceptual model of the cross-shore composition profile of Etretat, Hautot-sur-Mer and Villers-sur-Mer beaches (angles and proportions are not to scale). HT = High Tides, LT = Low Tides

2.4. Video Monitoring Systems

All three VMS are composed of three cameras (Figure 28) with different fields of view, each of which records 6 images per hour at daylight. This produces a total of 18 images per hour per study site, covering the entire beach (Figure 29). These so-called "timex" images are recorded with an exposure time of 10 minutes. Without considering possible losses likely due to malfunctions and bad imaging conditions (dirty lenses, foggy weather, rain drops, etc.), the expected data set for one year includes about 78000 images per VMS, with a resolution of 1936x1216 px in Hautot-sur-Mer, 3264x1856 px at Villers-sur-Mer and 3840x2160 px in Etretat.

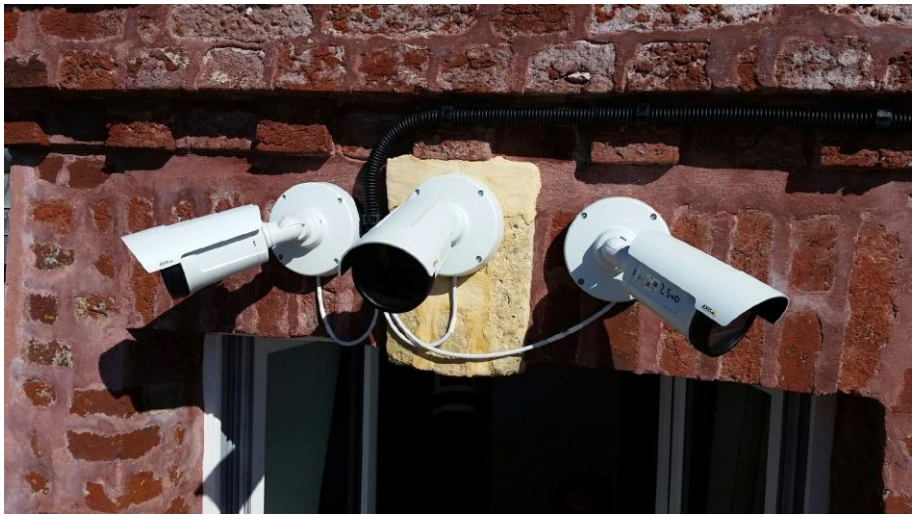

Figure 28 - Example of VMS cameras installed in Etretat (credit: Y. Soufflet, 2018)

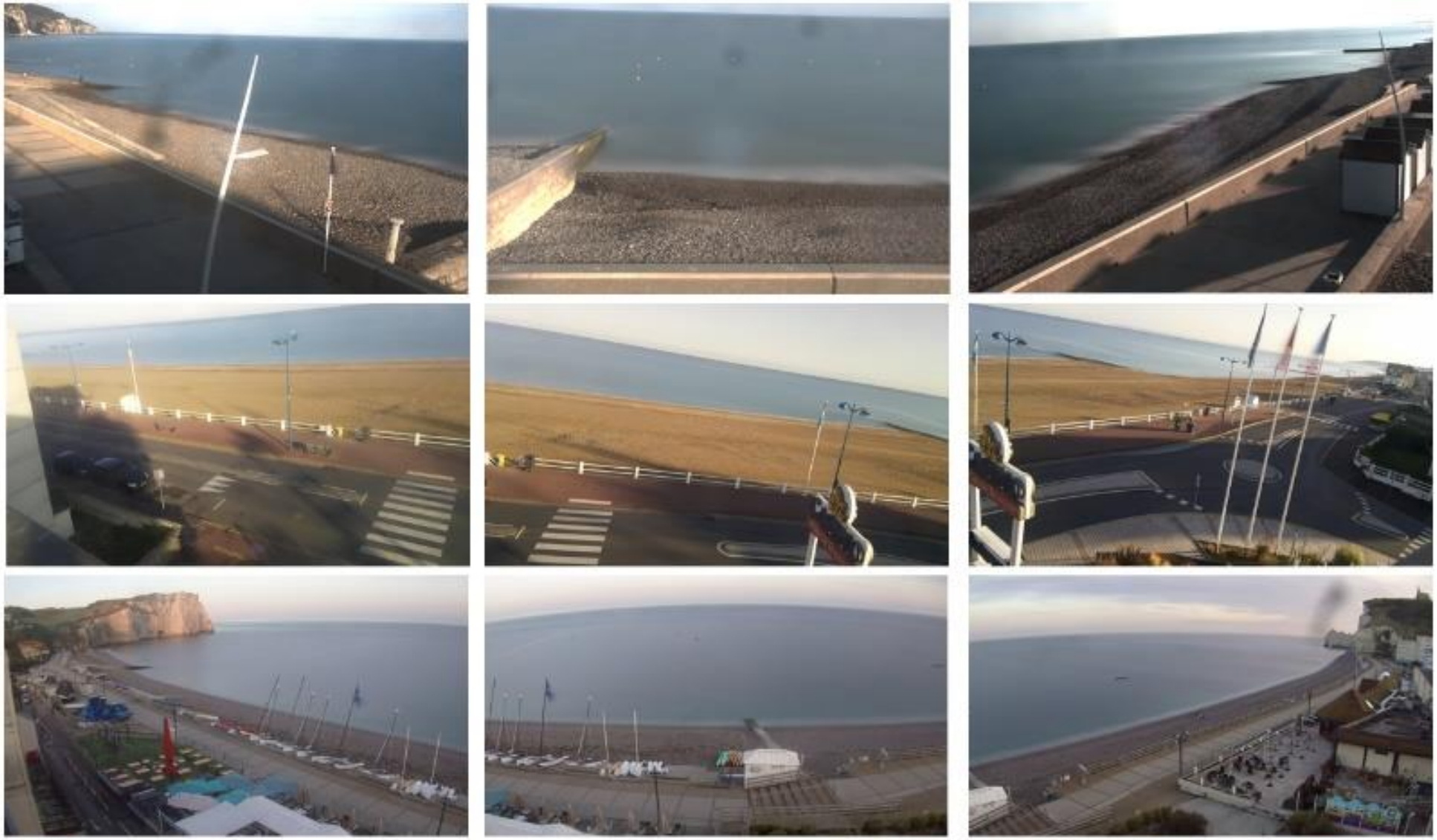

Figure 29 - Example of timex panoramas in Hautot-sur-Mer (top), Villers-sur-Mer (center) and Etretat (bottom)

3. Research methods

This section presents on the one hand the techniques used for image processing and measurement of terrain features by remote sensing (photogrammetry and image segmentation), and on the other hand the data processing tools used for statistical analysis (Empirical Orthogonal Functions, correlations and wavelet analysis). Lastly, the numerical model XBeach-G is described in a dedicated part.

3.1. Photogrammetry

Structure from Motion (SfM) photogrammetry is a technique used to estimate the 3D structure of terrains and objects from a series of images. The method takes advantage of the parallax effect visible on images of a scene taken from different perspectives. A correlation analysis is performed in order to find matching points between sets of images and the result is used to triangulate both the positions of the points and of the cameras. Additional information including camera georeferencing, optical parameters, and measured Ground Control Points (GCP) can be used to refine these estimations. The point cloud thus formed can be used to generate a 3D model of a scene of interest.

This method is increasingly employed for earth and coastal science topography applications using Unmanned Aerial Vehicles (UAV) (Gonçalves and Henriques, 2015; Westoby et al., 2012). In this case, a UAV is often flown following a gridded flight plan which not only ensures a consistent image quality and overlapping but also allows for automatic flight control. The method offers a good compromise between resolution (centimeters to decimeters per pixel) and monitorable area size (from meters to kilometers), while remaining relatively easy and inexpensive to perform (Gonçalves and Henriques, 2015; Nex and Remondino, 2014).

In the present study, photogrammetry methods were used to produce ortho-rectified mosaics of single images (orthoimages) of our study sites using UAV surveys. Orthoimages are images where the perspective effect was corrected in such way that the scale of each pixel is uniform. The Ground Sampling Size (GSD, i.e., metric size of one pixel) of an orthoimage can be calculated using the following equations:

$$GSD_w = \frac{Z \times S_w}{F \times I_w} \qquad GSD_h = \frac{Z \times S_h}{F \times I_h}$$

Where Z is the flight altitude (in m), F is the focal length (in m), S is the camera sensor size (in m), and I is the image size (in px). Moreover, w stands for width and h means height. Hence, the GSD is highly sensitive to the flight altitude, which is the only parameter one can easily play with once on the field, considering hardware and software with fixed settings.

The study sites of Normandy are surveyed using a Quadrirotor DJI Inspire 1 UAV (Figure 30), on which was mounted a Zenmuse X5 camera (F = 15 mm, Sw = 17.3 mm, Sh = 13 mm,

Iw = 4608 px, Ih = 3456 px). As our research interest is the size of gravel, GSD must be low enough to accurately see as small gravel particles as possible. We thus chose to fly at the lowest altitude allowed of 10 m above the top of the beach, which corresponds to a GSD of 2.5 mm/px. In practice, the relative flight altitude varies despite the horizontal flight plan due to the topography. On the pebble beaches, the GSD tends to be higher on the final orthoimage, up to 5 mm, as the previously mentioned scale uniformization is performed using the highest flight altitude (i.e., at the bottom of the beach). This value is still considered low enough as it allows most gravel particles to be seen. All surveys were performed using an overlapping rate target of 70%, and between 10 and 15 GCP measured using DGNSS.

Figure 30 - UAV used for mapping the pebble beaches of Normandy

3.2. Image segmentation / Mask R-CNN

Current capabilities for numerical imaging make it easy and relatively inexpensive to take high quality photographs. Progress made in the field of image recognition during the last decades now allow the automatic recognition of objects on such images, which is naturally interesting for research purpose. Convolutional Neural Networks (CNN) algorithms currently present the best performances in this regard, and not only are able to perform object detection but also segmentation (i.e., pixel-wise classification). Indeed, although it seems easy for a human operator to identify and delineate objects on an image, numerical segmentation is a challenging task, and parametric solutions remain very limited in both in performance and applications. For this matter, the development of efficient CNN models was a significant breakthrough.

Along the present study, images from VMS and drone surveys were available in great quantities. This data includes interesting information such as the position of the waterline and the size/shape of surficial gravel particles, respectively. However, the amount of data makes it unrealistic for a human operator to manually perform a relevant identification within a reasonable time. Although parametric solutions do exist, they remain objective specific (i.e., one algorithm detects one type of object), computationally costly, limited in performance due to the high variability in imaging conditions (luminosity, colors, weather, and other sources of noise) and often require supervision. Therefore, it was decided to investigate on the use of recently made openly available CNN technologies with the aim to complete both goals with one algorithm, with equivalent or better performance (detection time and rate), and little to no supervision/expertise required to operate.

The algorithm was chosen to perform the identification of shorelines and clasts is called Mask Regional Convolutional Neural Network (Mask R-CNN). This meta-algorithm was developed by He et al. (2017) and combines the proven object detection algorithms Faster R-CNN (Ren et al., 2016), which allows the identification of the nature (e.g., person, boat, car, etc.) and position of objects within bounding boxes (i.e., frame inside an image), and the Fully Convolutional Network (FCN) (Shelhamer et al., 2017), which allows semantic segmentation, a pixel-scale classification (Figure 31).

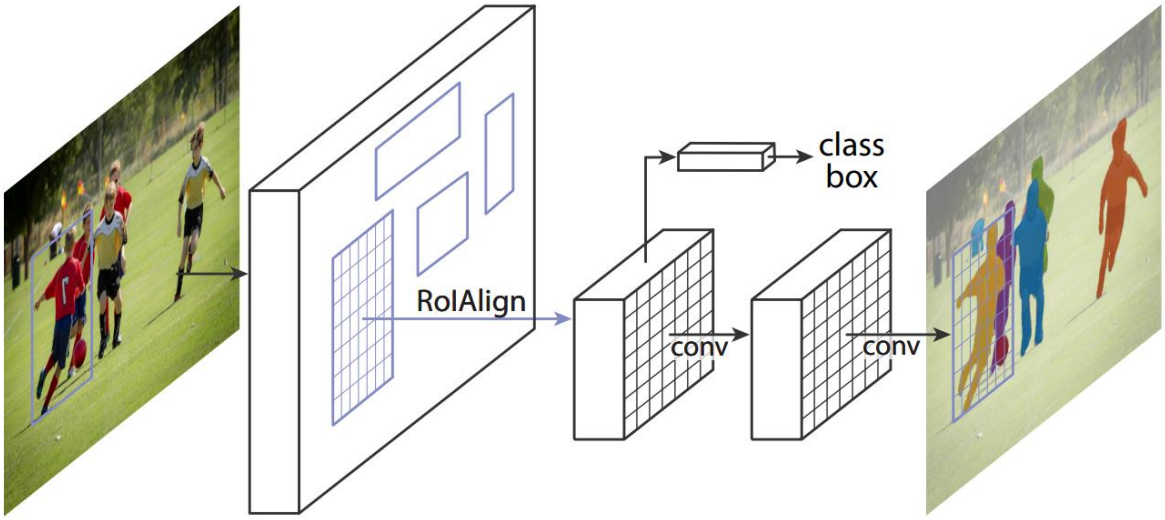

Figure 31 - The Mask Regional Convolutional Neural Network (R-CNN) framework for instance segmentation (He et al., 2017).

The choice for this specific algorithm was encouraged by the fact it was made freely accessible on various online platforms and easy to use without the need of a deep expertise of its complex working process. In addition, the algorithm is supported by a wide community of users and is densely documented through numerous technical notes and tutorials.

The working process of the Mask R-CNN can be described as a two-stages process. The goal of the first stage consists of scanning the image in order to find areas likely to contain an object, called “anchors”. These anchors will then feed the second stage, whose objective is to perform both an object

detection, and the classification of each pixel within the detected object's boundary box. As a result, the model produces a series of binary masks, each of them representing the pixels that belong to a certain object. It is important to understand that in one image, every object of the same nature will have its own dedicated mask, thus making it possible to distinguish each individual instance.

As described by He et al. (2017) in their article dedicated to Mask R-CNN, the first stage generates anchors using a backbone composed of a ResNet101 and a Feature Pyramid Network (FPN) that extracts the spatial information, then a Region Proposal Network (RPN) is responsible for generating random regions of interest (ROI), and then ranks their relevance according to the results of the backbone.

The second stage classifies the proposals from the first stage and generates bounding boxes and bounding masks in parallel. This is made possible by an ROI classifier which performs object detection (nature and bounding boxes) on the anchors, in order to extract the ROI. ROIs are then scaled to the fixed size of 28 pixels x 28 pixels which corresponds to the dimensions of the convolutional neural network, in order to perform a semantic segmentation on each of them and obtain a mask. Finally, the mask is resized to the initial object scale, and repositioned on the image.

More information regarding training data, and process as well as post-processing methods are provided in Chapter 3 - Section 1.2.2 and Chapter 4 – Section 1.2.1.2.

3.3. Empirical Orthogonal Functions

The analysis of the evolution of the beaches' morphology was performed using Empirical Orthogonal Functions (EOF). This statistical method was proven relevant to extract spatiotemporal variability patterns in time series of shoreline position (Aubrey, 1979; Medina et al., 1994, 1993; Turki et al., 2013; Winant et al., 1975).

The objective of this approach is to extract components driving the multi-scale changes in the shoreline position along both spatial and temporal dimensions, and to quantify their dependance from the original time series of 2D shoreline positions $Y(t,x)$. To do so, a map of linear regressions and correlations is calculated, the axis of maximum amplitudes determines the first spatial and temporal eigenfunctions, $E_1(x)$ and $C_1(t)$, respectively. The first functions' variability is then subtracted from the time series, and the same procedure is applied again to define the second eigenfunctions along an orthogonal axis. The methodology is iteratively repeated from $k = 1$ to $k = n$, where n is reached when the cumulative variance explained by all eigenfunctions reaches a previously defined threshold. Therefore $Y(t,x)$ can be described as a series of linear combinations of both spatial and temporal eigenfunctions.

$$Y(t,x) = \sum_{k=1}^{n} C_k(t) \cdot E_k(x)$$

3.4. Correlation

Along with the EOF, the correlation factor r was often used in this thesis to evaluate the linear links between different parameters.

$$r = \frac{Cov(X,Y)}{\sigma_X \times \sigma_Y}$$

Where $Cov(X,Y)$ is the covariance between two vectors X and Y, as calculated by $Cov(X,Y) = E[(X - \bar{X}) \times (Y - \bar{Y})]$.

r values can range from -1 to 1. However, as there was no need to discriminate negative from positive correlations along this study, r here refers as the absolute correlation value, therefore varying from 0 to 1. Correlation values r superior to 0.5 were considered significant.

3.5. Wavelet analysis

The temporal evolution of signals was also investigated using a wavelet analysis. The wavelet transform is a high-resolution frequency analysis technique that consists of decomposing a signal in both time and frequency in order to describe both periodic and non-periodic changes.

A wavelet transform is used to decompose the signal based on children wavelet, which correspond to scaled and translated versions of a reference parent wavelet. Each wavelet has a finite length (a scale) and is localized in time. The parent wavelet (i.e., morlet wavelet in this study) includes two parameters for time-frequency exploration: a scale parameter a and a temporal localization parameter b.

$$\Psi_{a,b}(t) = \frac{1}{\sqrt{a}} \Psi_0 \left(\frac{t-b}{a} \right)$$

The parameterization in scales and the translation of the children wavelet allows the detection of the different frequencies composing the signal. The continuous wavelet transform of a signal S(t) produces a local wavelet spectrum, as defined by $C(a,b) = \int_{-\infty}^{+\infty} x(t).\Psi_{a,b}(t).dt$. The local wavelet spectrum allows a description and visualization of the power distribution (color axis) along the different frequencies/periods (y axis) over time (x axis).

The wavelet power can then be averaged at each period to obtain the global wavelet spectrum (GWS), which highlights the periods (modes) of variability present in the signal.

3.6. XBeach-G

XBeach-G is an open-source numerical model developed by McCall et al. (2015, 2014) in order to simulate the hydro- and morphodynamics of gravel barriers, especially during storm events. It

is an evolution of the XBeach model, developed by Roelvink et al. (2010), which computes the propagation of offshore waves through the notoriously complex, dynamic and difficult to model nearshore zone, and the morphological response of sandy beaches. The development of XBeach-G was incentivized by the diverging results of XBeach when applied to gravel sediment suggesting that physical forcings needed to be considered differently in such context, and by the absence of alternative numerical model and more generally the lack of knowledge and understanding of gravelly coastlines' behavior compared to sandy ones (Masselink et al., 2014b).

In this study, XBeach-G was applied to a cross-shore profile of Etretat's beach, during four different storms of various intensity, with the aim of simulating the morphological dynamics observed with our coastal VMS. The model solves the nonlinear shallow water equations (NLSWE) to calculate the depth averaged flow due to waves and currents, taking groundwater exchange into account:

$$\frac{\delta\zeta}{\delta t} + \frac{\delta hu}{\delta x} + S = 0$$

$$\frac{\delta u}{\delta t} + u\frac{\delta u}{\delta x} - \frac{\delta}{\delta x}\left(\nu_h \frac{\delta u}{\delta x}\right) = -\frac{1}{\rho}\frac{(\rho\bar{q} + \rho g\zeta)}{\delta x} - \frac{\tau_b}{\rho h}$$

Where t and x represent the temporal and spatial (horizontal) coordinates respectively, ζ is the elevation of the free surface, h is the water depth, u is the depth-averaged cross-shore velocity, S is the exchange flux between surface water and groundwater (proportional to the hydraulic conductivity K), ν_h is the water viscosity (horizontal), ρ is the water density, $\bar{q}$ is the depth-average dynamic pressure (normalized by the water density), g is the acceleration due to gravity, and τ_b is the bed shear stress.

The bed level change in response to hydrodynamics conditions is calculated using the spatial gradient in the bed load transport, as:

$$\frac{\delta\zeta}{\delta t} + \frac{1}{(1-n_p)}\frac{\delta q_b}{\delta x} = 0$$

Where n_p is the sediment porosity, and q_b is the volumetric bed load transport rate as calculated using the Van Rijn's (2007) equation:

$$q_b = \Upsilon D_{50} D_*^{-0.3}\sqrt{\frac{\tau_b}{\rho}}\frac{\theta' - \theta_{cr}}{\theta_{cr}}\frac{\tau_b}{|\tau_b|}$$

Where Υ is a calibration coefficient set to 0.5 by Van Rijn (2007), D_{50} is the median grain size, $D_*^{-0.3}$ is the non-dimensional grain size, θ' is the Shields parameter modified by Fredsoe and Deigaard (1992) in order to take the beach slope into account, and θ_{cr} is the critical Shields parameter, threshold for initiation of movement. More details regarding both hydro- and morphodynamics equation solving are given by McCall (2015).

The model performance on simulating Etretat's morphological response to storms was estimated using the Brier Skill Score (BSS), which includes the initial observed, and both final observed and modeled profiles. The main advantage of this index is that it only takes into account the active part of the profile(Sutherland et al., 2004), thus limiting bias such as the presence of a non-erodible profile section. BSS values are generally considered good for values superior to 0.6, Table 2 provides an interpretation chart based on the work of Van Rijn et al. (2003).

$$BSS = 1 - \frac{\frac{1}{N}\sum_{i=1}^{N}\left(z_{final,i} - z'_{final,i}\right)^2}{\frac{1}{N}\sum_{i=1}^{N}\left(z_{initial,i} - z'_{final,i}\right)^2}$$

Where z is the observed elevation along the profile, and z' is the modeled one.

Table 2 - BSS interpretation table according to Van Rijn et al. (2003)

BSS Range	Interpretation
$BSS \leqslant 0$	Bad
$0 < BSS \leqslant 0.3$	Poor
$0.3 < BSS \leqslant 0.6$	Fair
$0.6 < BSS \leqslant 0.8$	Good
$0.8 \leqslant BSS$	Excellent

4. Chapter conclusion

Normandy is a coastal region located northwest of France, bordering the southeastern side of the English Channel. Its situation within the Parisian sedimentary basin engendered the remarkable chalky cliffs and flint pebble beaches that are so typical of this touristic seaside region. The funnel shape of the Channel is responsible for its extreme tidal ranges (5 to 10 m) and its eastward and southward preferred wave propagation direction observed near the coasts of Normandy. These characteristics lead to a mainly eastward sedimentary drift along the shore that is modulated by the presence of natural and human made obstacles arousing the formation of gravel barriers. Gravel beach dynamics remain relatively undocumented despite being an important component of the coastal resilience to storm events, particularly in the context of climate change. This is what incentivized the installation of video monitoring systems on two gravel beaches in Normandy, which record the hourly shoreline position and produce daily DEM of the shoreline.

Different methods are used to process the raw data from UAV and VMS platforms using image processing algorithms (photogrammetry and instance segmentation), to analyze observations using statistical tools (EOF, correlation and wavelet analysis), and numerically model the beach response to storm events using XBeach-G.

– CHAPTER 3 –

MEASURING THE VARIABILITY OF BEACH SURFACE GRAVEL MORPHOMETRY

Coastal sediments tend to accumulate under different forms (e.g., bars, barriers, etc.) whose morphology varies in response to external forcings (e.g., waves, tides, etc.), and in relation with intrinsic parameters (e.g., antecedent morphology, presence of obstacles, particles characteristics, etc.). As was seen in Chapters 1 and 2, in the case of gravel beaches, permeability, and hydraulic conductivity, were shown to be key factors, controlling morphodynamics. Hence knowledge about grain size, shape and spatial sorting are important information to understand and eventually predict the morphological evolution of beaches. However, measuring these parameters on gravel is often an expensive and time-consuming task, which tends to limit observational and forecasting investigations. Indeed, on one hand, physical seizing methods require heavy and numerous samples (in the order of ton(s)) to reach statistical significance while being destructive. On the other hand, alternative photography-based methods are often complicated and difficult to automatize. There is a need for gravel characteristics mapping automatic solutions, and the first part of this chapter presents a method using Mask R-CNN that was developed to fulfill it. The method was also successfully applied over different study sites in Europe and the USA, in the framework of an international research collaboration that was initiated by this work and that is presented in a second dedicated section.

1. Gravel size measurements and mapping

The present subsection describes a method we developed to measure and map the size of gravel particles on the surface of beaches, in order to record their spatiotemporal variability. This work was the subject of a research article published in Remote Sensing (MDPI): ***Soloy, A., Turki, I., Fournier, M., Costa, S., Peuziat, B., Lecoq, N., 2020. A deep learning-based method for quantifying and mapping the grain size on pebble beaches. Remote Sens. 12, 1–23. https://doi.org/10.3390/rs12213659***

1.1. Introduction

The size of the clasts that make up a sedimentary body is a fundamental geomorphic parameter that influences erosion, transport and deposition of particles, and by extension the morphology of the body (Buscombe and Masselink, 2006; Finkl, 2004; Gomez, 1983; Klingeman and Emmett, 1982; Mason and Coates, 2001). Knowing the spatial dispersion of particle size is therefore an issue for many applications such as calibration of numerical models (Bergillos et al., 2016; Masselink et al., 2014b), estimation of current directions (Dal Cin, 1968), calculation of sediment transport (Butt et al., 2001), and habitat classification (Kondolf and Wolman, 1993).

However, measuring the size of elements larger than a centimeter is a relatively costly and complicated task. Adams (1979) and Kellerhals and Bray (1971) calculated that between 10 and 100 kg per sample should be collected for size sieving purposes in order to obtain satisfactory statistical representativeness, depending on the size of the elements. Despite their cost, size sieving measurement methods are still used, particularly to calibrate and validate the more recent remote sensing methods (Barnard et al., 2007; Graham et al., 2005b). Other techniques based on in situ counting (i.e., counting the number of elements fitting into of different ranges of sizes) do exist (Fehr, 1987; Leopold, 1970; Wolman, 1954), but they also remain limited and cumbersome to implement as well.

In response to these constraints, photographic-based measurement methods have been developed (Adams, 1979; Kellerhals and Bray, 1971). Initially, these methods required the intervention of an operator to manually digitize the clasts; this procedure could take more than one hour per image (Ibbeken and Schleyer, 1986), which is approximately the time required to analyze a physical sample. These methods have been improved and automated through numerous studies, and now there can be distinguished two categorical approaches (Buscombe and Masselink, 2009): analysis of image texture properties (Buscombe, 2020, 2013; Carbonneau et al., 2004; Rubin, 2004; Verdú et al., 2005), and characterization of individual clasts (Butler et al., 2001; Graham et al., 2005b, 2005a; Purinton and Bookhagen, 2019; Sime and Ferguson, 2003).

Methods in the first family generally rely on brightness, including analysis of local semi-variance and autocorrelation, in order to determine an empirical relationship between image texture

and particle size. The second type of analysis seeks to carry out the segmentation of the elements visible on the image, by using a suite of image segmentation algorithms.

These techniques, when compared to physical samples, have proven to be effective but are limited by image resolution, the presence of buried, tilted or overlapping features, and the need to fine-tune light conditions (Graham et al., 2005b). If the texture-based methods are able to overcome this difficulty by using a parametrical correction, they strongly rely on local parameters to be calibrated, which makes them less able to be generalized. On the contrary, segmentation-based measurements only rely on the image resolution to be correctly calibrated and are therefore meant to be more resilient. However, most of the segmentation methods depend on the use of edge-detection algorithms which alone are not able to differentiate the actual grain edges from overlapping caused edges. To overcome this issue, Detert and Weibrecht (2013) proposed the use of an additional watershed segmentation step whose purpose is to identify the relevant particles. However, the algorithm still suffers from misidentifications and its complexity requires a high expertise while remaining limited to areas smaller than 10 m² for computational reasons. More recently, Purinton and Bookhagen (2019) have developed a semi-automatic method based on the use of a k-mean clustering. Although they greatly improve data processing time, these methods are still dependent on user expertise to determine image processing parameters (Detert and Weibrecht, 2013; Purinton and Bookhagen, 2019), and the processing time required ranges from one to several tens of minutes per image.

Given these constraints, segmentation methods based on Deep Learning can be very useful. Indeed, the abstraction and generalization capabilities of convolutional neural networks allow the recognition of non-trivial concepts (Le, 2013). It is therefore possible to perform automatic and unsupervised segmentation of coarse clasts, and even classification of non-overlapping ones, to reduce the processing time and expertise required to process an image.

This section will present an example of the application of the Mask Regional Convolutional Neural Network (R-CNN) Deep Learning algorithm (He et al., 2017) to measure and map the characteristics of the pebbles present on two pebble beaches with different element size properties: Etretat (D50 = 5.99 cm) and Hautot-sur-Mer (D50 = 7.44 cm) (Normandy, France).

1.2. Data and Methodology

1.2.1.Data

The developed methodology uses photographs taken at human height, which include a quadra structure of known shape and dimensions (0.84 x 0.84 m²) placed on the ground. The dataset thus created includes images taken from a bird's eye perspective, between 1.5 and 2 m high without a tripod (Figure 32a), and using two different cameras (Nikon D3200 and Apple iPhone 11). These images are corrected for lens distortion effects using a camera calibration model (Heikkila and Silven, 1997) and then ortho-rectified by planar transformation within the quadra, with a resolution fixed at

0.5 mm / pixel (Figure 32b). This fixed value was set for consistency purposes as the unprocessed images' resolution can vary from about 0.25 mm / pixel for a Nikon D3200 camera to about 0.5 mm / pixel for an Apple iPhone 11 camera. Each quadra is associated with the geographical coordinates of at least one of its corners, measured in situ using differential GNSS.

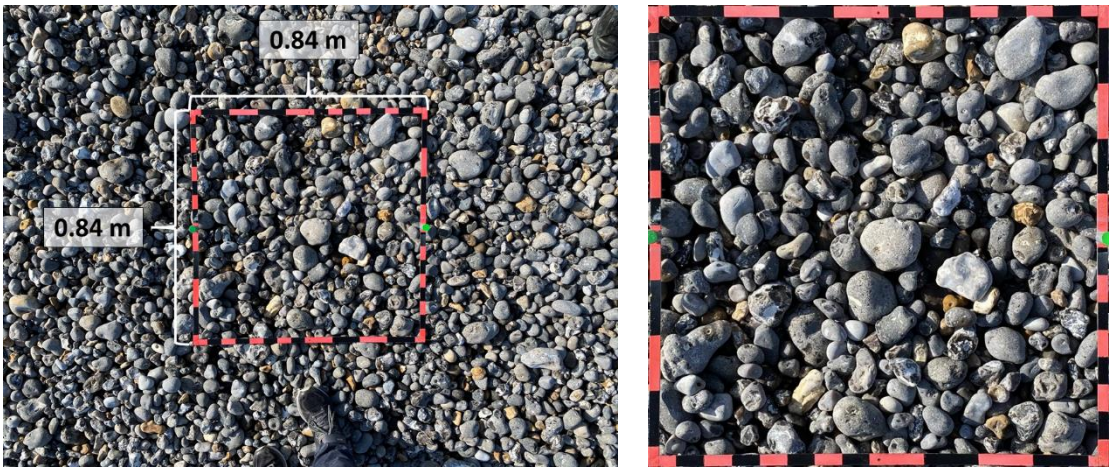

a b

Figure 32 - Example of a close-range top view image of a pebble ridge including a scaling quadra structure (a) before and (b) after orthorectification.

1.2.2.Mask R-CNN Segmentation

The model was trained with a dataset of 46 images and a total of 3598 manually digitized non-overlapping clasts. This dataset covers as wide a range of environmental conditions as possible with elements of all sizes (from gravels to cobbles), shapes and colors, low to high light, humidity and silting conditions, presence or absence of quadra, ground and Unmanned Aerial Vehicle (UAV) shots, raw or ortho-rectified. This dataset was artificially augmented in order to improve learning performance (Perez and Wang, 2017) which means that some images randomly selected in the dataset were copied and transformed (addition of blur/noise, crops, rotations/translations, etc.) using random parameters, in order to artificially increase the dataset's size. As the training step of a deep learning model works by iterations called epochs subdivided into steps, it is relevant to mention that a total of 100 epochs, each including 100 steps, was required to achieve a satisfactory segmentation capability.

After processing an image of clasts, the output of the model is recorded as a series of masks, one per detected element, each of them being associated with a probability value reflecting the certainty of the model to have correctly detected and segmented the object.

In general, the segmentation of a quadra image by the Mask R-CNN model takes 3 seconds on a mid-range computer (Intel® Core™ i7-8850H CPU 2.6GHz, 32GB RAM, NVIDIA Quadro P600 GPU). From one image to another, this duration can vary between 1 and 10 seconds depending on the number of clasts, the initial resolution, and the computer capabilities.

1.2.3.Clast Size Measurement and Validation

The clasts are measured on images with known resolution (0.5 mm/pixel). After detection of non-overlapping features by Mask R-CNN, each particle is measured along the major and minor axes of the ellipse on which they lie (Figure 33). It is important to mention that the actual particle shape is flattened by the photographing process, and therefore only two of the three dimensional axes of the sediment particle remain available, often referred as “long” and “intermediate” axes. This loss of a dimension by projection is also likely to be a source of slight errors, especially as the ellipse’s major and minor axis may not exactly equal the particle’s long and intermediate axes, although they will remain close. It is also possible to record the unprocessed mask characteristics, such as the probability value attributed by the algorithm, the area size or the full contour shape detected by Mask R-CNN for further morphological analysis.

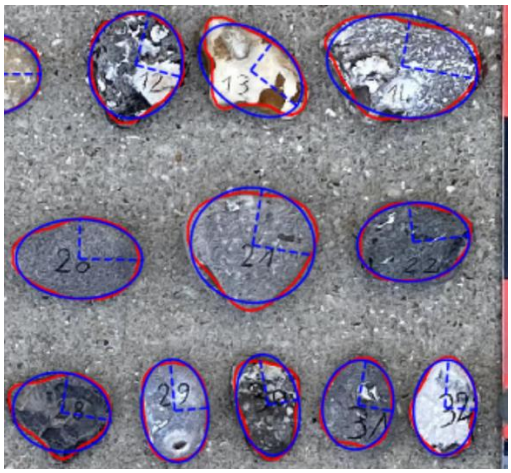

Figure 33 - Comparison between sediment particles’ shape as detected with Mask R-CNN (red) and the ellipse fitted around this shape (blue). The ellipses’ major and minor axes are displayed as dashed blue lines.

To validate this method, the three dimensions of a set of 105 clasts were measured using the methodology developed in this section (Figure 34a). The same clasts were then measured manually using a caliper with a millimetric precision, along the same axes as the ones positioned by the ellipse fitting step. These pebbles were originally sampled on the beach of Hautot-sur-Mer, they were naturally water-worked by the sea, and were chosen in order to show as a wide variability of sizes, shapes and colors as possible while remaining small enough in to fit in the quadra’s frame. The colors displayed in Figure 34a and b are numerical masks highlighting the algorithm’s detection results.

a b

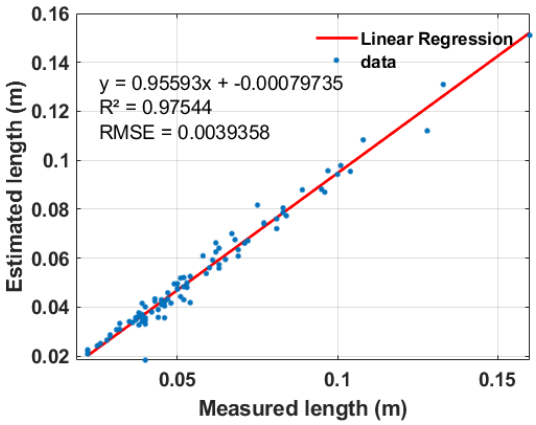

c

Figure 34 - Application of Mask R-CNN to manually measured validation data with (a) a non-overlapping disposition of the clasts (colors show the detected pebble instances), (b) an image including overlapping objects, (c) the overlapping scenario tested with the highest number of misidentifications (instances n°4 and n°25) and (d), a comparative distribution of the pebble major axis measured after Mask R-CNN detection vs. the data measured manually using a caliper.

The results show an average detection rate of 80 to 90% of the non-overlapping individuals, regardless of their arrangement (Figure 34 4a to c), with a R^2 of 98% and an RMSE of 3.9 mm, i.e. 8 px (Figure 34c). Most undetected objects have a long axis of less than 2 mm, i.e., 4 px, and are among the smallest sediment particles that were measured. Other methods relying on the segmentation of photographs of quadra structures show a minimal detection threshold ranging between 8 and 23 mm (Butler et al., 2001; Detert et al., 2018; Graham et al., 2005a; Ibbeken and Schleyer, 1986; Purinton and Bookhagen, 2019). On rare occasions, Mask R-CNN misclassifies partial clasts as complete ones. Among the 269 sediment particles detected through the 11 overlapping scenarios tested, only 10 individuals (the same ones in most cases) were misidentified as non-overlapped sediment particles while being overlapped, resulting in a misidentification score of 3.7%. Figure 34c shows the validation scenario presenting the highest number of misidentified features: elements n°4 and n°25.

This validation methodology was applied under different light (with and without shadows) and background conditions (asphalt, concrete, wood, dry/wet surfaces…), with numbers written either directly on the surface of the clasts or on glued pieces of papers, with similar results. It is important to note that the model can perform a satisfying classification of these images despite the fact that it was not trained using such data, thus enforcing the model's applicability.

1.3. Example of Applications

To show the potential and capabilities of the methodology developed here, this subsection presents two examples of analysis: The evolution of Etretat's pebble size under different wave conditions measured using a quadra on cross-shore profiles, and the pebble size spatial variability at the scale of a large area of the beach, measured on ortho-images of Etretat and Hautot-sur-Mer.

1.3.1.Influence of the Hydrodynamics on Etretat Pebbles' Size

Two campaigns of pebble size measurements by quadra were carried out in Etretat one week apart in March 2020. Three profiles (Figure 35a) were recorded during each campaign: A, D and F on March 5 and B, C and E on March 13, including one common profile: C and D.

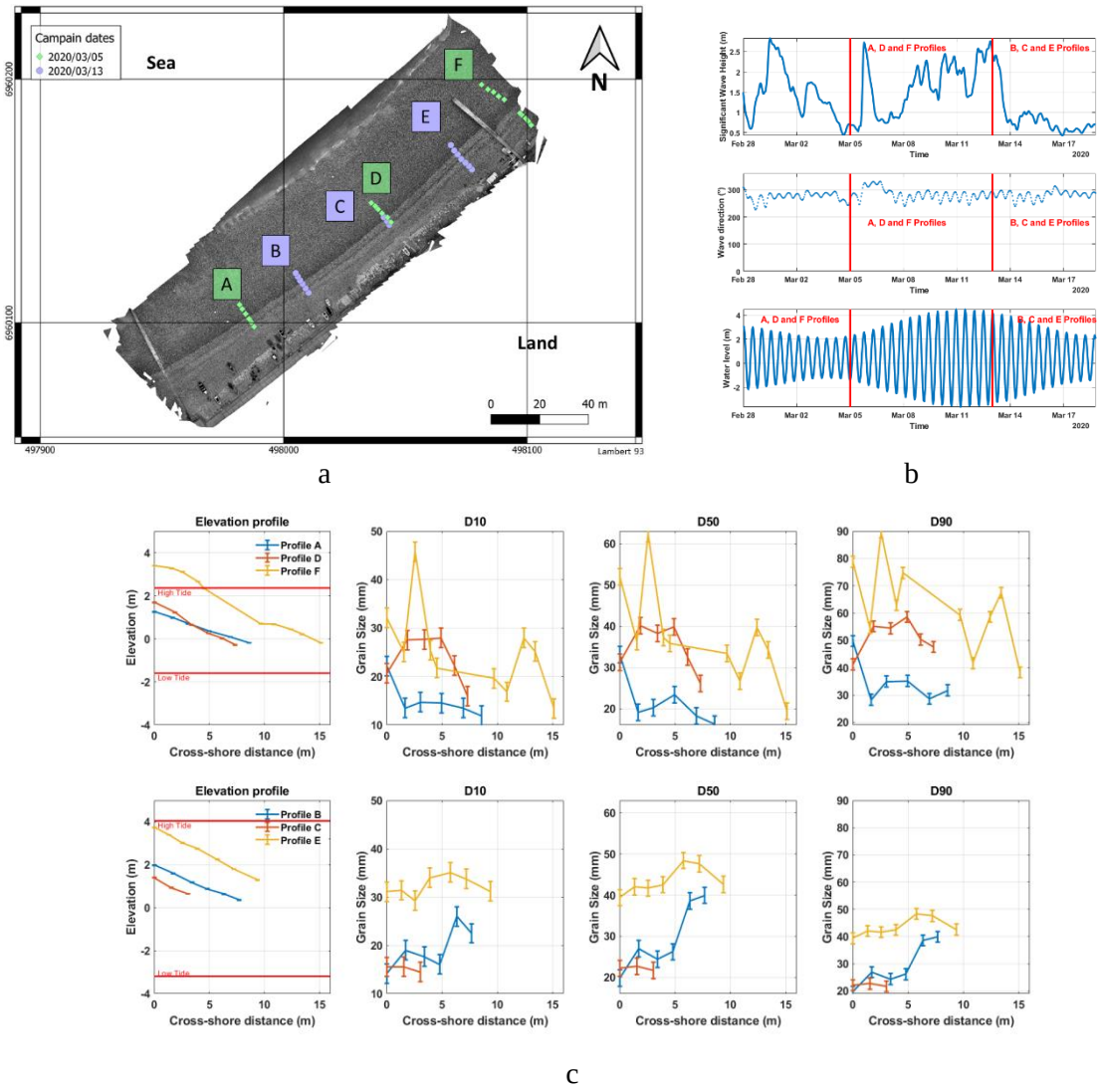

Figure 35 - (a) Location of the cross-shore quadra measurement profiles in Etretat on 5 March and 13 March 2020. (b) Hydrodynamic conditions during the measurements: significant wave height (top), wave direction (center) and water level (bottom). (c) Elevation and pebble size profiles of D10, D50 and D90 on 5 March, 2020 (top) and 13 March, 2020 (bottom). Vertical bars show the measurement uncertainty, and horizontal red lines show the intertidal extension of the last tide.

Figure 35b shows the evolution of the significant wave height and origin direction as well as the water level estimated by the WaveWatch 3 model off Etretat during the studied period. The March 5 measurements were carried out in a rather calm hydrodynamic context with western waves of less than one meter in height during the five days preceding the measurement, during spring tide. On March 13, more agitated conditions were observed, with waves reaching more than 2.5 m in height coming from the west during the four days preceding the campaign at neap tide.

The sediment size used for this analysis was the length of the ellipse's major axis that provided the best fit to each object. Figure 35c shows the pebble size results from previously mentioned measurement campaigns. The topographic profiles are presented on the left, along with the vertical extension of the latest tide. The origin of the x-axis is taken at the most upstream point of each profile. The smaller extension of the profiles on 13 March is explained by a larger tidal range that constrained the measurement area.

In general, values of D10, D50 and D90 observed in Etretat vary between 1 cm and 5 cm, between 2 cm and 6 cm, and between 3 cm and 6.5 cm respectively, all dates combined. Among all measurements, only the five first ones located on the top the F profile are at a higher elevation than the latest high tide and were therefore not affected by the tidal dynamic during the few days to weeks before 5 March, 2020.

There is a greater elevation in the east than in the west, with, for example, profile A being lower than profile F, and with a similar relationship between profiles B and E (Figure 35c). This elevation reflects a greater sediment accumulation in the east due to the long-shore sediment transport phenomenon. The grain size evolution follows the same trend, with larger sizes also in the east for higher elevations (Figure 35c), which suggests the presence of a relationship between elevation and pebble size.

However, while a negative upstream to downstream gradient is observed on all profiles on 5 March, the gradient becomes positive on 13 February. The significance of the slopes was tested using a Mann–Kendall test (Table 3). All pebble size profiles from 5 March, 2020 show an upward trend, while all those from March 13 are downward, although only 6 of the 18 size class profiles (6 × D10 + 6 × D50 + 6 × D90) show a significant trend (p-value < 0.1) due to the low number of measurement points.

Table 3 - Mann–Kendall statistical test applied to the pebble size profiles measured in Etretat on 5 March and 13 March, 2020, p-Values in bold are inferior to the 0.1 significance threshold.

Date	Profile	Quantile	P-value	Tau	Slope
2020/03/05	A n = 6	D10	0.06	-0.73	-0.55
		D50	0.13	-0.60	-1.26
		D90	0.71	-0.20	-0.95
	D n = 6	D10	0.85	-0.07	-0.64
		D50	0.45	-0.33	-1.21
		D90	0.85	-0.07	-0.47
	F n = 10	D10	0.07	-0.47	-1.01
		D50	0.03	-0.56	-1.54
		D90	0.11	-0.42	-1.63
2020/03/13	B n = 6	D10	0.26	0.47	1.08
		D50	0.06	0.73	2.53
		D90	0.06	0.73	4.76
	C n = 3	D10	0.60	-0.33	-0.35
		D50	0.60	-0.33	-0.15
		D90	0.60	0.33	1.01
	E n = 7	D10	0.55	0.24	0.29
		D50	0.07	0.62	0.80
		D90	0.23	0.43	1.24

On the other hand, the D90 decreases significantly between 5 February and 13 February, from an average of 5 cm to 3 cm. In particular, the comparison of profiles C and D shows a decrease in all three indices.

Previous studies carried out by the Laboratoire Central d'Hydraulique de France (LCHF) (1972) show that for 15 pebble ridges along the Normandy coastline, there is a tendency for the pebble size to decrease from upstream to downstream, with a D50 in particular evolving from 4 cm to 5.5 cm in Etretat. These values correspond to the range of lengths measured during this study: between 2 and 6 cm.

Other authors such as Bujan et al. (2018) found a similar positive correlation between beach elevation and coarse clast size to the one found for profiles A, D and F (Figure 35c), while surveying a pebble beach in Taiwan's region using an analogous methodology. However, the works of Costa et al. and Letortu (Costa et al., 2006; Letortu, 2013) show that pebble size can have significant spatial variability at the tidal cycle scale, depending on the marine conditions preceding the observation. Other comparable studies do not seem to find any evident linear relationship between elevation and grain size (Bertoni et al., 2020). The results presented here support this observation and show that particle size sorting can be positively or negatively correlated with elevation depending on the previous wave conditions.

These observations are in good alignment with previous studies' findings about clast transport in the swash zone under different energetic conditions. Under calm wave conditions, the asymmetrical balance between the uprush and the backwash energy tends to carry more material upslope than downslope, which eventually leads to an accumulation of sediment on the surface of the beach (Masselink et al., 2006). When the wave height the reaches a certain threshold in the swash zone, the processes of infiltration and percolation are not able to completely dissipate the wave energy anymore, and the swash becomes saturated (Aagaard, 1990; Guza and Thornton, 1982; Holman, 2018). For such energetic wave conditions and higher ones, more sediments are carried downslope and eventually dispersed until the occurrence of calmer conditions that will allow the beach to grow again. The coarser sediments are then expected to be transported at a slower pace than the finer ones, as their transport will require more energy. This difference in transport speed is expected to sort the surface sediment by size. This hypothesis is supported by previous studies that highlighted the existence of such seaward shift, the direction of which has been found to rely on a wave height threshold (Bertoni et al., 2020; Ciavola and Castiglione, 2009; Sarti and Bertoni, 2007). When associated with the alternance between spring and neap tide, one can understand that the previously mentioned accumulating conditions associated with spring high tides are likely to store and preserve the sediment on the backshore, at elevations that are only reached by the sea during spring tides and/or storms.

If the previous accumulating conditions lasted long enough, a significant amount of the largest clasts, previously found downstream, could have been transported on the backshore and been preserved from the neap tide storm of February 29 (five first measurements of profile F, Figure 35c), resulting in the upstream to downstream negative grain size gradients observed on March 5. Although the saturation wave height threshold is unknown for Etretat, it is fair to assume that such conditions

were reached shortly before the measurement campaign of March 13. Therefore, the clasts located at higher elevations were dispersed, which lowered the grain size quantiles and reversed the gradients.

1.3.2.Clast Size Mapping in Etretat and Hautot-Sur-Mer

Two UAV campaigns were carried out in Hautot-sur-Mer and Etretat on June 9 and June 10, 2020. These campaigns made it possible to create ortho-images at the scale of the beach, with a resolution of 5 mm/pixel covering 9000 m2 in Etretat (Figure 36a) and 12,000 m2 in Hautot-sur-Mer (Figure 36b) using Surface From Motion (SFM) techniques. On both sites, the flight was carried out using a DJI Inspire 1 with a Zenmuse X5 camera (image size = 4608 pixels × 4608 pixels; sensor size = 17.3 mm × 13 mm; Focal length = 15 mm). Flights were attended at a fixed altitude of 20 m above the top of the beach, with an increase due to the beach slope up to 30 m in Hautot-sur-Mer and 35 m in Etretat. Therefore, the expected Ground Sampling Distance (GSD) values range from 5 to 7.5 mm/pixel in Hautot-sur-Mer, and from 5 to 8.8 mm in Etretat, and are correctly oversampled by the image resolution of 5 mm/pixel.

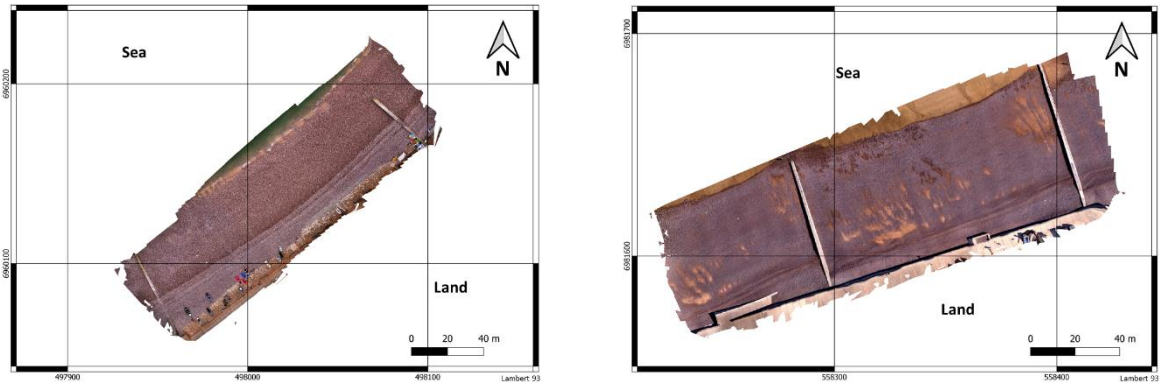

a b

Figure 36 - Unmanned Aerial Vehicle (UAV) derived Ortho-images of the pebble ridges at (a) Etretat and (b) Hautot-sur-Mer.

1.3.2.1. Validation

As the size of the image that can be input into the Mask R-CNN algorithm is limited for computational reasons, the ortho-images were cut out into tiles of 1 × 1 m² in size (Figure 37), to be analyzed one by one. Although convenient, the fixed size of 1 × 1 m² constrains the size of the detectable objects to smaller dimensions. Once detected, the pebble coordinates and dimensions are stored in an output table file containing all the previously detected pebbles of the entire ortho-image. The overall process takes around one day per ortho-image.

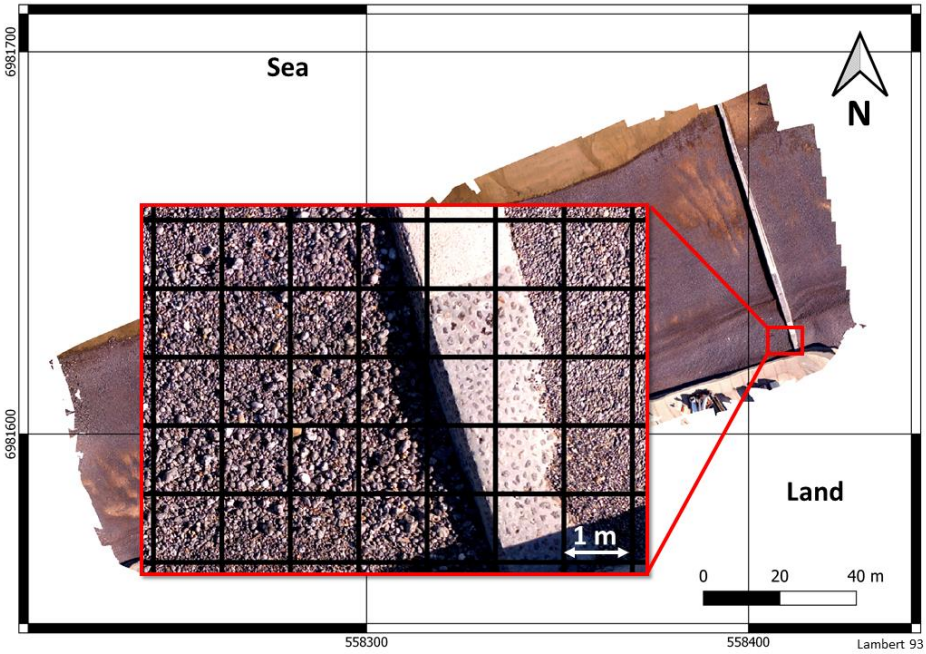

Figure 37 - Relative scale of the 1 m tiles in comparison to the whole ortho-image in Hautot-sur-Mer.

Since the validation results presented in Section 1.2.3 showed that measurements by quadra were accurate and reliable, here they were considered as ground truth data for validation purposes. Therefore, some were carried out in parallel with the flight of the UAV to allow cross-validation of the results. A total of 46 and 28 quadra measurements were realized in Etretat and Hautot-sur-Mer, respectively, covering the whole surveyed area on both sites.

Validation is performed by comparing each quadra distribution (here called “terrestrial samples”) to the one being extracted at the same location from the ortho-image, on areas covering 1 × 1 m² so called “UAV samples”, considering the terrestrial samples as ground truth. It is important to understand that this validation process only compares distribution indices (quantiles, means, etc.), as the automatic cross-identification of individuals on both datasets remains a challenging task.

On the ortho-image segmentation, smaller objects are expected to be under-represented, due to the lower resolution in comparison to the quadra data (0.5 mm/pixel) (Figure 38a and b).

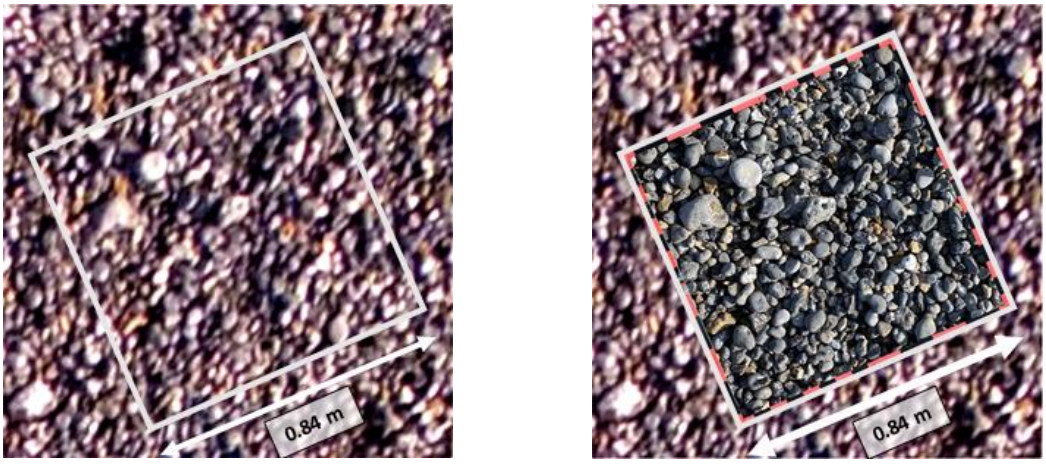

a b

Figure 38 - Comparison between the image quality of (a) an ortho-image (resolution 5 mm/pixel), and (b) a quadra image (resolution 0.5 mm/pixel). The white square shows the quadra position.

Therefore, the distribution measured on the ortho-images reflects the tail of the distribution measured with quadra (Figure 39a). In order to compare both types of datasets as relevantly as possible, the clasts detected in the terrestrial samples were filtered. The filtering operation consists of eliminating the pebbles that are smaller than a defined threshold in each terrestrial sample. This threshold is set to be the size of the smallest object detected in the UAV samples of the same location. When filtered out, the respective ranges of the results and the number of detected pebbles per area unit of the two datasets correspond to what is expected: more small elements are found in the filtered terrestrial samples, and similar amounts are detected for the bigger ones (Figure 39b).

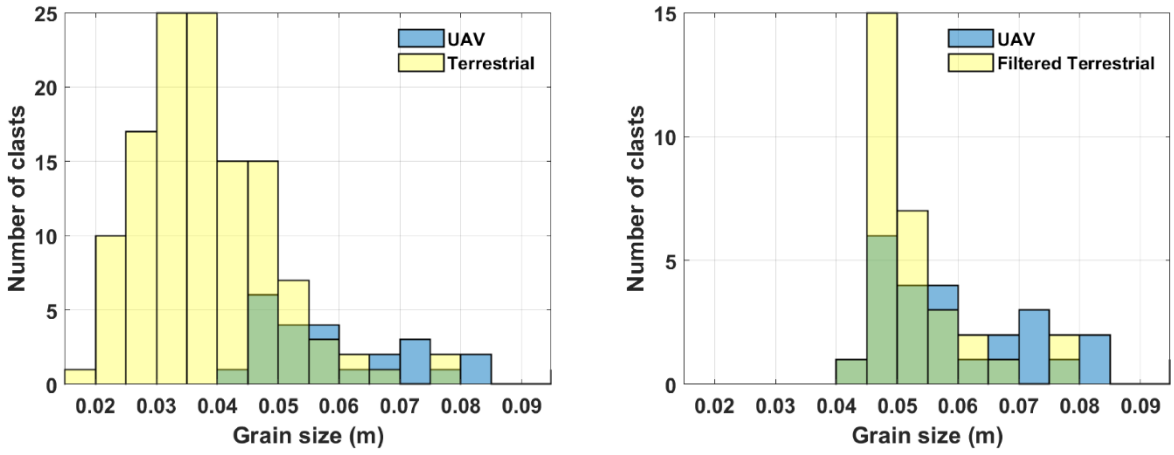

a b

Figure 39 - Comparison between the clast size distribution of a terrestrial sample (yellow) with a UAV sample (blue) at the same location, (a) before and (b) after applying the filtering processing.

Figure 40a and b show the distributions (before and after filtering) of the clasts from the terrestrial samples as well as the distributions from the UAV samples, in Etretat and Hautot-sur-Mer, respectively. For the vast majority of samples, the filtering operation brings the terrestrial means significantly closer to the UAV sample ones, regardless of the site, which shows the relevance of this operation.

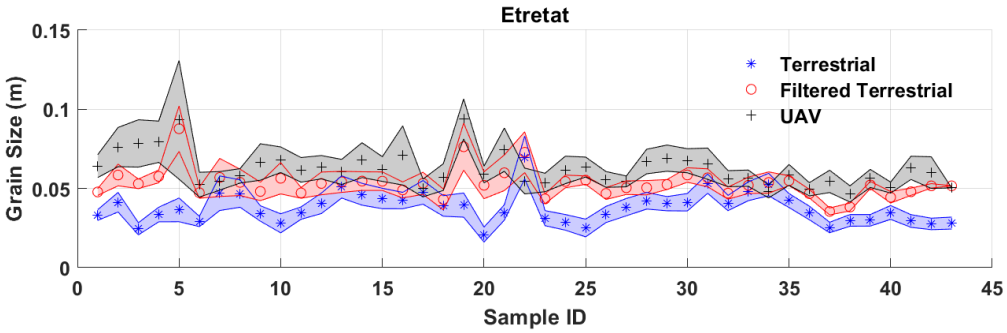
Etretat
Terrestrial
Filtered Terrestrial
UAV
Grain Size (m)
Sample ID

a

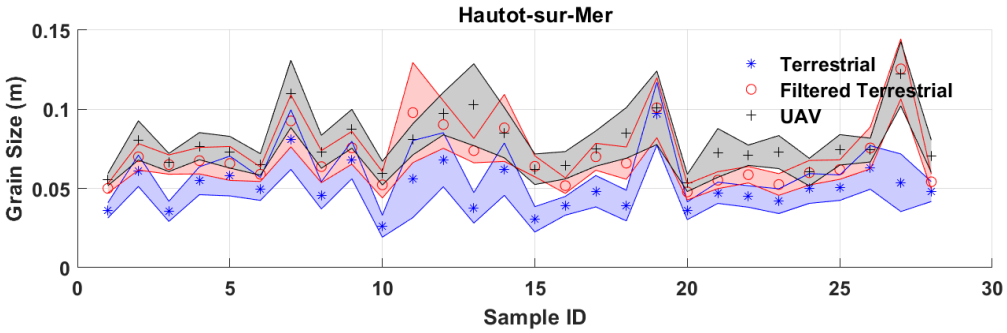
Hautot-sur-Mer
Terrestrial
Filtered Terrestrial
UAV
Grain Size (m)
Sample ID

b

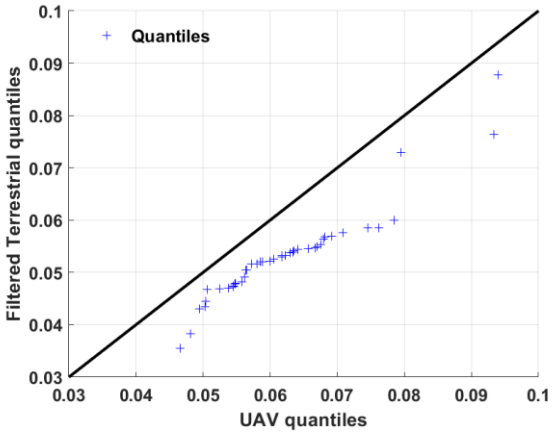
Quantiles
Filtered Terrestrial quantiles
UAV quantiles

c

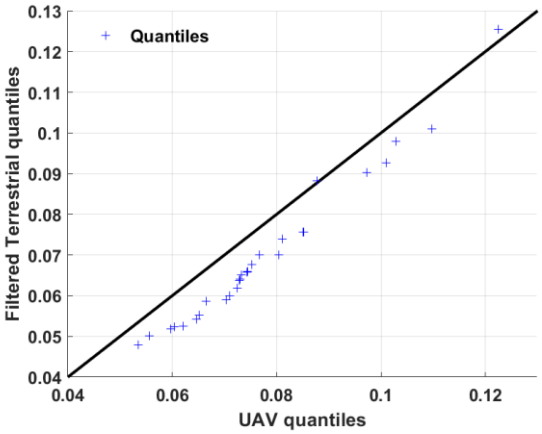
Quantiles
Filtered Terrestrial quantiles
UAV quantiles

d

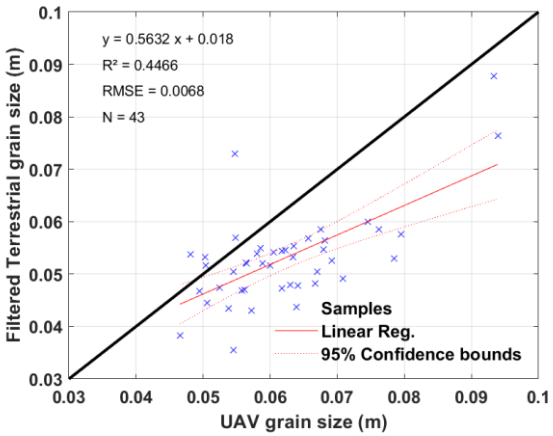
y = 0.5632 x + 0.018
R² = 0.4466
RMSE = 0.0068
N = 43
Samples
Linear Reg.
95% Confidence bounds
Filtered Terrestrial grain size (m)
UAV grain size (m)

e

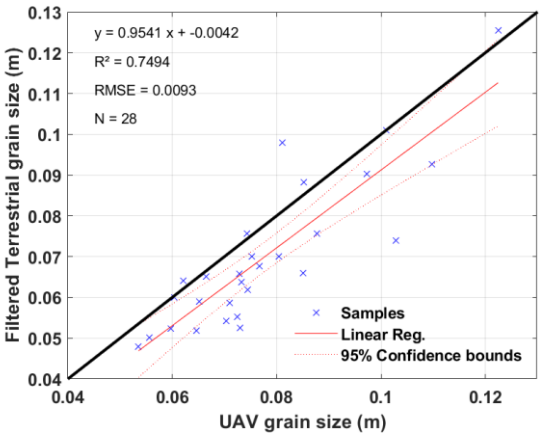
y = 0.9541 x + -0.0042
R² = 0.7494
RMSE = 0.0093
N = 28
Samples
Linear Reg.
95% Confidence bounds
Filtered Terrestrial grain size (m)
UAV grain size (m)

f

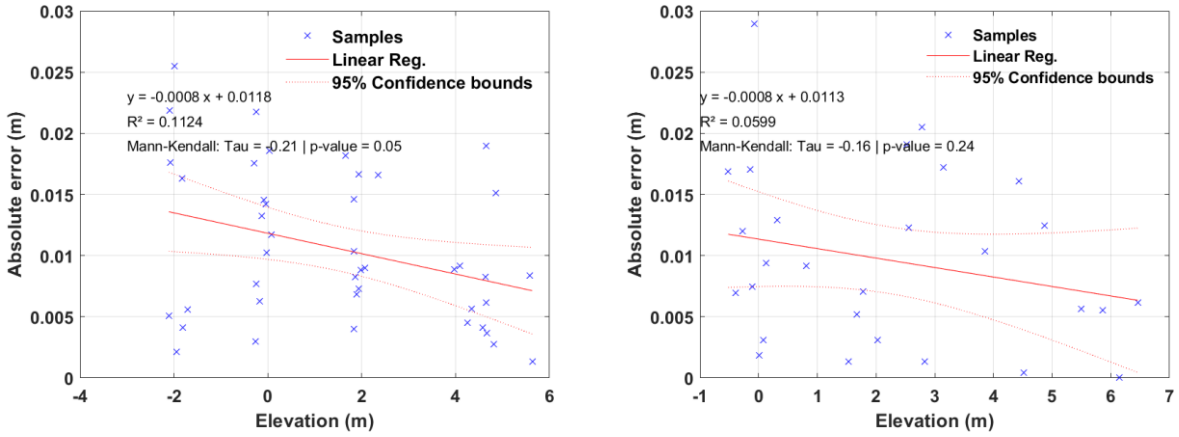

Figure 40 - Clast size mapping validation results. (a,b): Comparison of the average grain size as measured on the terrestrial samples (blue "" symbols), the filtered terrestrial samples (red "o" symbols) and by the UAV samples (black "+"symbols at (a) Etretat and (b) Hautot-sur-Mer. Colored envelops present the standard deviation intervals. Compared mean values of the UAV and filtered terrestrial distributions at (c) Etretat and (d) Hautot-sur-Mer. Quantile–Quantile diagrams comparing the UAV and filtered terrestrial distributions at (e) Etretat and (f) Hautot-sur-Mer. Absolute error on the pebble size measurements as a function of the elevation at (g) Etretat and (h) Hautot-sur-Mer.*

The variability of the mean values from one sample to another is similar between filtered terrestrial and UAV samples. This shows the ability of the method to produce relevant distributions above a certain threshold. According to the minimum size limit of four pixels found in Section 1.2.3., this threshold should be 2 cm with 5 mm/pixel resolution. However, elements under 4 to 5 cm in size remain difficult if not impossible to identify on ortho-images. This tends to show that the overall GSD is closer to 10 mm/pixel or higher. This seems to be aligned with the calculated values ranging between 5 and 8.8 mm/pixel considering the eventual potential additional loss of resolution due to the SFM processing.

The quantiles–quantiles diagrams (Figure 40c and d) highlight a quasi-linear relationship between the filtered terrestrial and UAV sample quantile classes, although the UAV samples slightly overestimate these values.

Figure 40e and f show the comparative distributions of mean sizes between filtered terrestrial and UAV samples. The R2 values of 0.45 and 0.75 and RMSE values of 6.8 mm and 9.3 mm in Etretat and Hautot-sur-Mer, respectively, confirm the ability of the present methodology to determine the size of pebbles on ortho-images. The lower R2 in Etretat (Figure 40e) and the regression line's slope of 0.56 seem to be associated with the small range of sizes, the majority of samples measuring between 43 and 59 mm. Although the precision is expected to be ± eight pixels, (i.e., ± 4 cm for 5 mm/pixel resolution), the calculated RMSE values suggest an uncertainty of only one to two pixels. This tends to show that the relationship between the Mask R-CNN detection uncertainty and the image resolution is not linear. Indeed, assuming that the model was sufficiently trained, Mask R-CNN will only delineate the elements that are likely to be actual clasts. Therefore, for a given image, a decrease in the resolution will result in a lower number of detected elements and a higher smallest element size, with a similar size measurement accuracy only increased up to the pixel size.

It is expected that the measurement error on the ortho-images is higher downstream than upstream as the UAV evolves on a horizontal plane above the inclined plane of the pebble ridge. The greater observation distance above the beach's downstream area implies a higher GSD value. An increase in absolute error is indeed observed with the increase in observation distance of about 0.8 mm per meter of elevation at the two study sites (Figure 40g and h). The statistical significance of these trends was tested by a Mann–Kendall test and shows p-values of 0.05 and 0.24 in Etretat and Hautot-sur-Mer, respectively. However, the R2 values of 0.11 and 0.05 remain low and highlight the variability of the absolute error, which is on average less than 1 cm, but can reach almost 3 cm at times.

These observations confirm the good capability of this methodology to map the spatial variability of pebble size in a relevant way.

1.3.2.2. Results and Discussion

A total of 182,218 clasts were detected on Etretat beach (Figure 41a) with a D10 of 4.59 cm, a D50 of 5.99 cm and a D90 of 8.6 cm. In Hautot-sur-Mer, 153,824 clasts were detected (Figure 41b) with a D10 of 5.18 cm, a D50 of 7.44 cm and a D90 of 11.55 cm (Figure 41c and d). These clast size values are similar to those measured by Laboratoire Central d'Hydraulique de France (LCHF) (1972), although the D10s measured here are slightly higher by about 1 cm. The minimum dimensions are similar on both sites with around 2 cm and 3 cm for the minor and the major axis, respectively (Figure 41c and d). On the contrary, maximum values differ with about 10 cm and 15 cm for the minor axis, in Etretat and Hautot-sur-Mer respectively, and about 13 cm and more than 20 cm for the major axis. However, these values are not to be considered as the actual observed maxima due to the 1×1 m² cropping window used for the detection that is likely to have cut the boulders of similar or larger dimensions, which are therefore not detected.

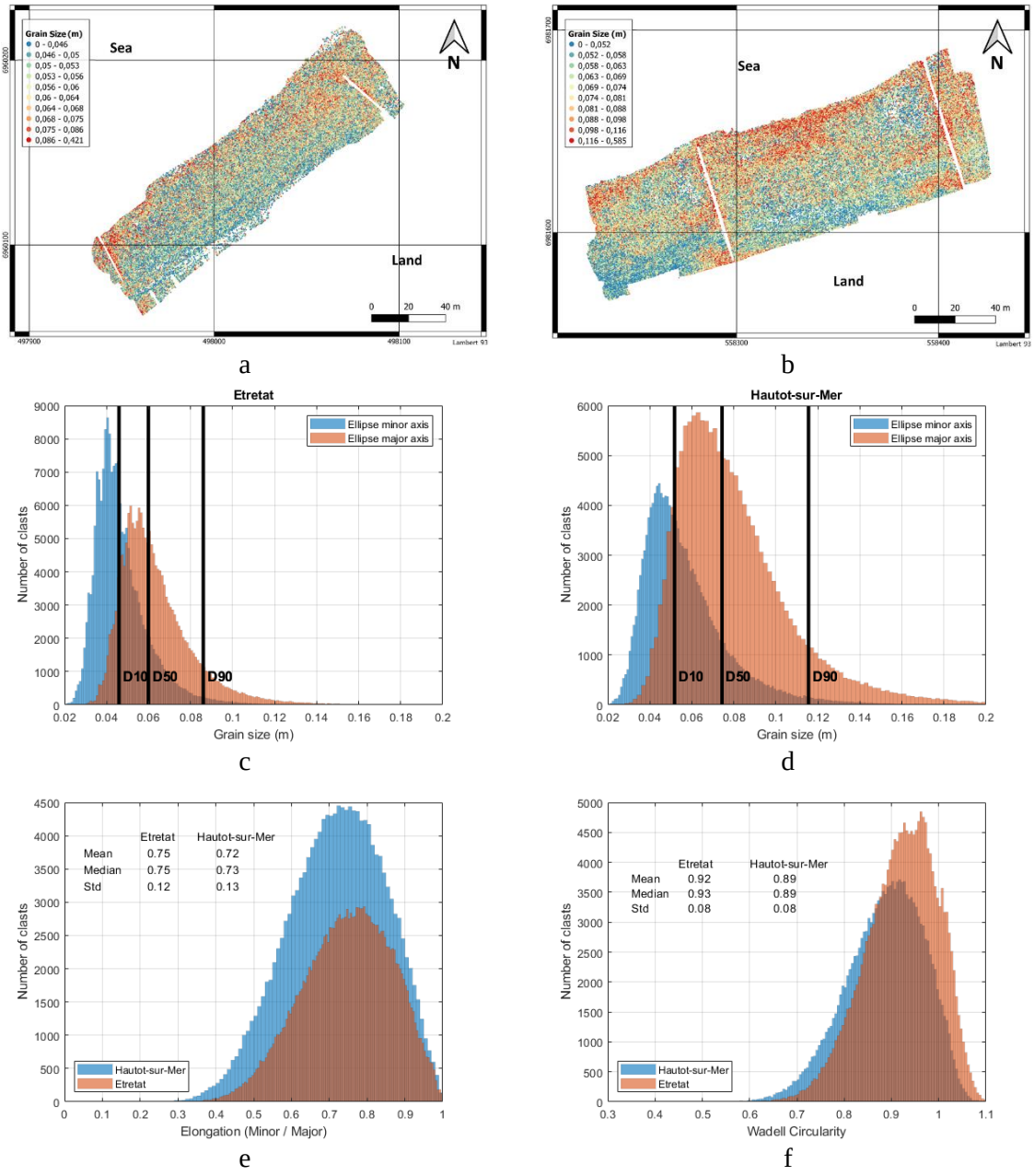

Figure 41 - Distribution of individual pebbles on the surface of the beaches of (a) Etretat and (b) Hautot-sur-Mer. Histograms of the grain size distribution at (c) Etretat and (d) Hautot-sur-Mer, orange bars show the ellipse major axis dimensions, blue bars refer to the minor axis, and black vertical lines locate the major axis distribution's D10, D50 and D90 values. Histogram of the grain elongation values (e) and of the grain circularity values (f) Etretat (orange) and Hautot-sur-Mer (blue).

A quick analysis of the elongation and circularity was made possible by the availability of a major and a minor axis dimension for each sediment particle. The elongation was calculated by the ratio ellipse minor axis over major axis (Zingg, 1935), and provides results ranging from zero (infinitely long particle) to one (the major axis equals the minor axis). For circularity, Wadell's (1932) definition was considered and calculated by the ratio between the particle's equivalent diameter (i.e., diameter of the circle that equals the surface of the detected sediment particle mask) and the ellipse major axis. Circularity values are expected to range from zero to one (i.e., ellipse like shapes to circle like shapes).

Figure 41e presents the histogram of elongation values found in Etretat and Hautot-sur-Mer. Results show similar elongations on both sites with a lower average value of 0.72 in Hautot-sur-Mer as compared to 0.75 in Etretat. Figure 41f shows the histogram of circularity values. As expected for wave-worked sediment material, values stay close to one for both sites with 0.92 in Etretat and 0.89 in Hautot-sur-Mer on average. This also tends to show that Etretat's pebbles are typically rounder than Hautot-sur-Mer ones. Values superior to one are likely to show the limits of the ellipse fitting process which could produce ellipse axis dimensions being slightly smaller than the actual sediment particle dimensions.

At both sites, the measurement campaign took place during a mildly agitated hydrodynamic period (hs < 1 m for several days) in the presence of a N–NW swell at the end of the spring tide (Figure 42a and b). A week before, these campaigns were preceded by a more energetic event with waves up to 2 m in height on both sites, during the spring tide peak.

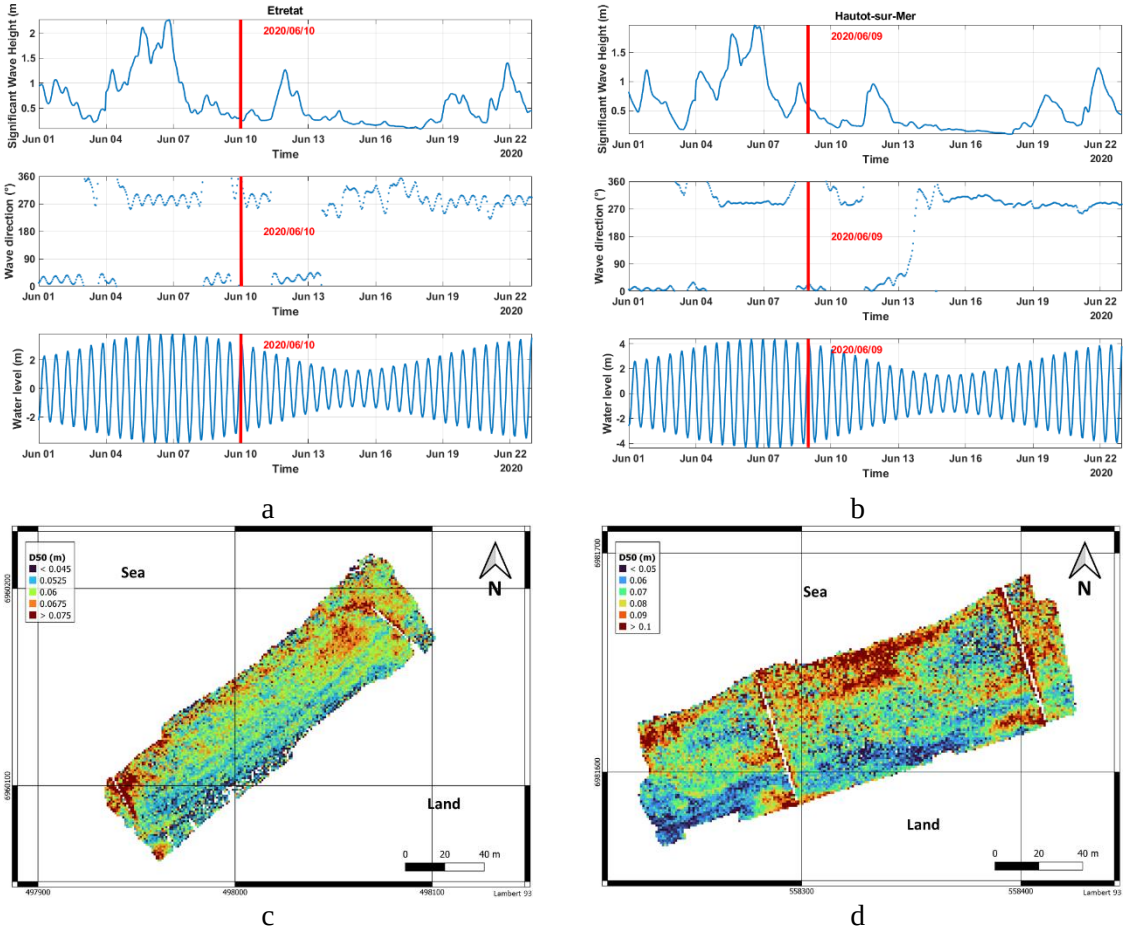

Figure 42 - Hydrodynamic conditions at (a) Etretat and (b) Hautot-sur-Mer preceding the UAV campaigns. Significant wave height (top), wave direction (center) and water level (bottom). Distribution of individual pebbles on the surface of the beaches of (c) Etretat and (d) Hautot-sur-Mer. Spatial variability of D50 at (e) Etretat and (f) Hautot-sur-Mer.

After the Mask R-CNN detection processing, detected sediment particles sizes were rasterized in order to be analyzed in an easier way (Figure 42c and d). The present rasters were produced by finding the quantile 50 of each cell of a grid of 1 × 1 m² in size covering the beaches.

In general, the results show a positive upstream to downstream particle size gradient over both ridges (Figure 42c and d). This observation contradicts the systematic negative gradient measured by Laboratoire Central d'Hydraulique de France (LCHF) (1972) but both types of observation can be explained with the mechanism described in the Section 1.3.1.

However, this gradient is very heterogeneous, with preferential areas of coarser or finer sediment accumulation. On Figure 42c, Etretat's beach shows a specific accumulation spot with sediment larger than 6.7 cm on the northeast part of the beach face. Other spots can be identified along the groins, especially around their tip, with even higher sizes. On the contrary, the back of the beach is characterized by finer grains of 4.5 cm in size and less. Longshore oriented patterns can be identified along the different berm slopes.

On Figure 42d, the beach of Hautot-sur-Mer presents a more contrasted picture, with similar observations. Interestingly, the same observations can be made in the two visible areas of beach that are embayed by the groins, although the western one is only partial: the presence of two distinguishable patches of high values (D50 $\geqslant$ 9 cm) on the west side of the groins, one on the beach's top, the second one more towards the center; another wider area of high values (D50 $\geqslant$ 9 cm) is located along the front of the beach; the eastern side of the beach front is showing significantly lower values (D50 $\leqslant$ 6 cm) with some a high local variability (punctual D50 $\geqslant$ 10 cm); the top of the beach is also an homogeneous area of low values (D50 $\leqslant$ 6 cm); the eastern side of each groin seems to accumulate a mix between moderate (6 cm $\leqslant$ D50 $\leqslant$ 9 cm) and high values (D50 $\geqslant$ 9 cm); the rest of the beach face presents homogeneous moderate values (6 cm $\leqslant$ D50 $\leqslant$ 9 cm).

Other more specific observations tend to show effects of the slope on sediment size sorting, and the interactions between the sediment and the defense structures, such as the groin's ability to capture the larger elements.

Based on the occurrence of an energetic event during the spring tide peak, a week before the measurement campaign, the observed negative upstream to downstream gradient of D50 can be explained by the same mechanism as the one mentioned in Section 1.3.1. When the spring tide amplitude is able to completely flood the beach, highly energetic conditions are likely to disperse pebbles of all sizes if the wave height is superior to a saturation threshold (Aagaard, 1990; Holman, 2018). While this value remains unknown for the beaches of this study to this day, it seems reasonable to assume that it was reached on June 6 for both sites. Therefore, under fairer weather conditions, the beach is expected to grow back thanks to the one-way swash transport associated with the high tidal amplitude. During this mechanism, larger clasts are likely to be transported at a slower pace than the finer ones, resulting in a temporary negative gradient. If such calm conditions remain, one can expect to see the upstream D50 increase back, and even reach a positive upstream to downstream gradient.

1.4. Discussion

Mask R-CNN allows the satisfactory segmentation of uncovered clasts on an image. On close range images with a quadra structure for scale, the clasts are correctly segmented when their dimensions are greater than 2 mm, with an uncertainty of ± 4 mm (for a resolution of 0.5 mm/pixel). On orthoimages, it was possible to obtain a satisfactory detection of the sediment particles greater than 4 cm with an uncertainty of ± 6.8 mm in Etretat and 9.3 mm in Hautot-sur-Mer. The minimal size threshold value was shown to strongly depend on the GSD (tested values of 0.5 mm/pixel for the terrestrial images, and 5 to 8.8 mm/pixel for UAV images) while the uncertainty ranges between 4 and 9.3 mm. The processing time of a few seconds per square meter of image (numerical resolution between 0.5 and 5 mm/pixel), along with the ability of the model to function without human supervision are valuable assets.

Although more precise, the terrestrial technique remains more punctual and therefore provides less spatially representative results than the UAV method. Moreover, in time constrained environments such as semi-diurnal intertidal areas, the efficiency of the UAV methodology potentially allows the investigation of larger domains. Nevertheless, it has been proven possible to combine both methods' strengths in order to provide reliably validated results.

The methodology described in the present section has shown the tool's strong performance when monitoring the spatial and temporal evolution of the pebbles' size on two pebble ridges.

The results obtained show the evolution of the beach's D50 upstream to downstream gradient as a function of the hydrodynamic conditions. They support the hypothesis of a multi-factor process at the origin of the seaward sorting gradient as it was observed to be negative at neap tide before a storm in Etretat, then positive at spring tide after a storm. Furthermore, positive gradients were observed in Etretat and Hautot-sur-Mer after a spring tide storm.

The acting mechanism relies on the supposition that the swash saturation threshold (Aagaard, 1990; Holman, 2018) was reached during the spring tide energetic events preceding the measurements, thus eroding and dispersing the beach's top sediment. Under calmer conditions, this sediment accumulates again, each element moving at a speed that is proportional to its size, which results in the appearance of surface sediment sorting patterns. These observations and explanations are supported by several comparable other studies conducted on different coarse clastic beaches, with similar conclusions about a seaward grain size shift whose direction depends on a wave height threshold (Bertoni et al., 2020; Ciavola and Castiglione, 2009; Sarti and Bertoni, 2007).

In a more specific perspective, the results highlight the effect of the beach slope and of the groins on the particle size sorting, with an accumulation of the coarsest elements at the around the structures. The presence of similar patterns in side-by-side groin embayed beach areas once again

confirms the relevance of the method by showing its ability to produce consistent measurements for consistent sorting conditions.

These results therefore provide a better understanding of the coastal pebble system dynamics. In Normandy, these results will be used to feed a model of the morpho-sedimentary evolution of beach pebble barrier beaches, and thus provide a better understanding of the sedimentary dynamics at work in the extreme tidal conditions of the region.

1.5. Conclusions

The Mask R-CNN model is a versatile instance segmentation method that has proven its performance in many areas and is particularly suitable for clast size measurement applications for several reasons. First, convolutional neural networks are useful for the classification of non-trivial concepts, such as non-overlapping pebbles. This capability allows the minimization of sampling bias by disqualifying partially visible objects. In addition, the processing speed associated with the tool's ability to operate without human supervision after image scaling makes it a remarkably efficient asset.

The methodology developed for this study is validated with an uncertainty of ±8 pixels (±4 mm for a resolution of 0.5 mm/pixel) against a manually measured dataset. Part of this uncertainty can be attributed to the loss of a dimension, a photograph being the projection of a 3D scene on a 2D plane, as well as to the simplification of the morphology of the pebbles into ellipses. However, the measurement uncertainty does not seem to increase much with the decrease in the image resolution (RMSE of 6.8 to 9.3 mm for images with 5 mm/pixel of resolution), as the algorithm will not detect unclear features.

This methodology was applied as an example to Normandy beaches made up of pebbles on two different types of data: terrestrial photographs in top view at a height of about 2 m without a tripod using a quadra structure for scale, and ortho-images produced at the end of a UAV flight.

The results obtained are consistent with previous observations, and allow analysis of the spatial and temporal evolution of the pebble size variability in Etretat and Hautot-sur-Mer. These observations highlight the particle size sorting, and its spatial and temporal heterogeneity. The occurrence of size changes concomitant to the presence of specific hydrodynamic conditions suggests that the responsibility for sorting the coarse clasts is shared by a combination of several factors such as significant wave height and tidal amplitude. This paves the way for a better understanding of the dynamics of pebbles on the beaches of Normandy and will form the basis of further research.

Although these results have demonstrated that the method is suitable for monitoring the size of pebbles on the beaches of Normandy, the spectrum of applications remains a lot wider. Indeed, the model can be trained to classify other types of elements and records their complete shapes and not only their size. Therefore, it is now possible to map and study the morphological characteristics of

clasts and their evolution through time and space with good accuracy, low cost, and low expertise, in a relatively short time.

2. Application to different study sites

After demonstrating effectiveness on two pebble beaches in Normandy, an international collaboration including 13 scientific experts in various domains belonging to 5 different laboratories was initiated in order to challenge the clast size mapping method on different sites. We applied the model to five sites abroad (Iceland, Ireland, Switzerland, and USA) exhibiting a wide variety of conditions in terms of clast sizes, shapes and colors. In this section, we present the preliminary results of this analysis, which show that the model can detect clasts on these sites with the same efficiency as in Normandy. The model has been made available from a public repository on https://github.com/soloyant/clast-size-mapping.

Part of these results were presented at the American Geophysical Union Fall Meeting of December 2021, in New Orleans, USA:

Soloy, A., Grottoli, E., Lorang, M.S., De Graffenried, B., Pascal, I., Bertoni, D., Turki, I., Lecoq, N., Jackson, D.W., Guisado-Pintado, E., Ancey, C., Trembanis, A.C., Laignel, B., 2021. Mapping the size and shape of coarse clasts using Mask R-CNN: spatial and temporal variability over six different study sites including sea shores, and lake and river banks, in: EP34A - Grains to Satellites: Sediment and Hydrological Processes Across Scales II Oral. New Orleans, USA. https://agu.confex.com/agu/fm21/meetingapp.cgi/Paper/861821

2.1. Natural mixed sand and gravel seashore: Ireland

The beach of Five Finger Strand is a 500+ m long convex with a 50 to 100 m wide intertidal area mostly composed of mixed sand and gravel located at the mouth of a river. Gravel particles tend to accumulate on the back shore in the form of a 30 to 40 m wide ridge, although sand remains significant on the ridge. The site's orthophotography was kindly provided by Dr. Edoardo Grottoli (University of Ulster), Dr. Emilia Guisado Pintado (University of Seville) and Dr. Dereck Jackson (University of Ulster) after a flight performed on 2021/07/20. The clast detection was performed using a window of 1x1 m and took approximately 6h to cover the ridge area. Results include approximately 270,000 clasts with an average size of 7.8 cm (min size = 1.4 cm, max size = 63.0 cm, STD = 2.8 cm).

The dispersion of mean clast sizes (Figure 43) is not random. To the south, there is a negative cross-shore gradient from the top to the bottom of the beach, which has only been observed once in Normandy (Figure 35c) although it has not been mapped. To the north, the gradient appears to be the opposite, with coarser particles at the bottom of the slope, and finer particles at the top. Between these two zones is a transition area with rapid longshore gradient. The validation results were produced with the same method as presented in part 1 of this chapter and show a good overlap between the

distributions obtained on the images taken from the ground and those taken from the drone, and an average RMSE of 5 mm.

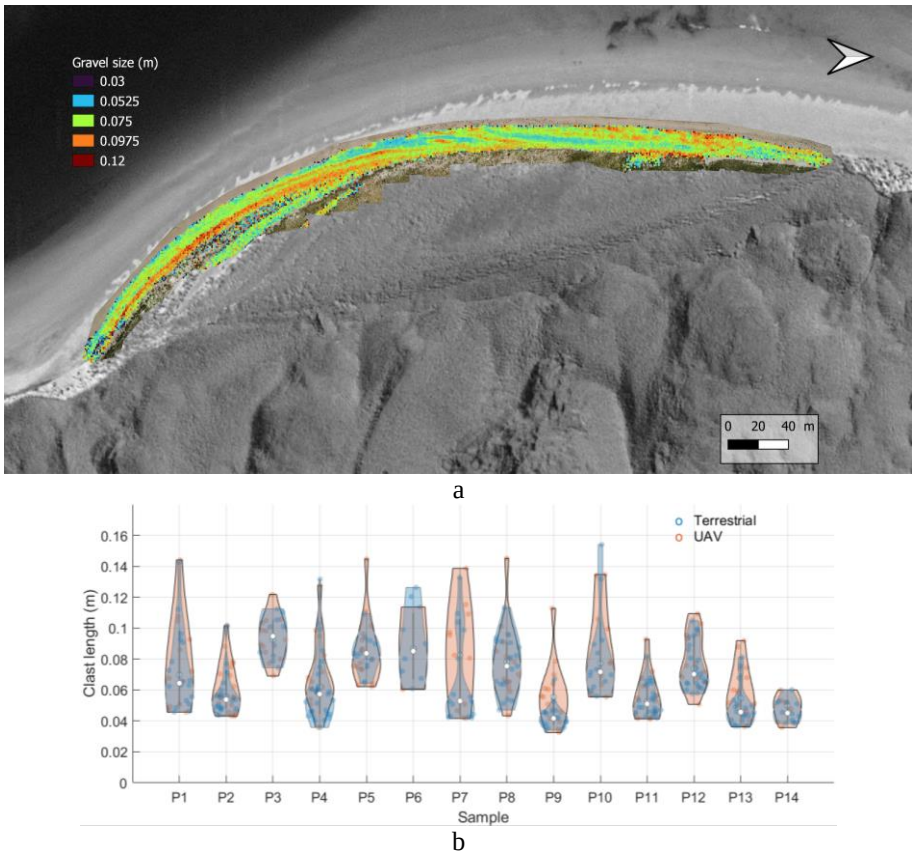

Figure 43 - Results of the clast size mapping on Five Finger Strand beach, in Ireland. a: map of the mean gravel size; b: cross validation results between measurements on terrestrial imagery and UAV orthophotography.

2.2. Riverbanks: Switzerland

The Navisence is an Alpine river flowing in Switzerland. Bob de Graffenried, Ivan Pascal and Dr Christophe Ancey (École Polytechnique Fédérale de Lausanne) provided orthophotography data on a section of about 25x150 m centered on the narrow active channel (5 to 10 m) that was recorded on 2020/09/08. This type of environment is challenging for the clast detection methodology because the particles are often angular and their sizes generally range much more widely (from centimeters to meters). In addition, the river banks are littered with woody debris, and the shading conditions are variable due to the strong sunlight and the presence of tall trees nearby.

The detection with a 1x1 m window took about 1 hour. It allowed the detection of around 30000 clasts, but led to errors on the coarsest ones and to the detection of many false positives. False positives were found especially in the channel (misclassification of turbulent water patterns), and on the surface of the largest clasts that were partially cut because they were too large for the selected window size. A second detection was therefore carried out with a window size of 2.5x2.5 m, better adapted to the size of the largest elements. This detection found only about 10000 clasts with a relatively small number of false positives, probably because the larger image provides enough information to the neural network to significantly improve its classification. However, the difference

between the two window sizes is not only due to false positives, the 2.5x2.5 m window causes an under sampling of the finest clasts, which was not the case with the 1x1 m size. The two datasets were therefore combined by filtering double detections and false positives by union and intersection, this fusion contains about 30000 clasts, about the same as the 1x1 m window size detection list.

Two images, one with a grazing sun and one with a sun at zenith were analyzed. They provided substantially similar results, indicating that the angle of the sun had little influence on the detection, except for the density of detected objects (more objects in the shade than in the sun). The results presented in Figure 44a show the 1x1 m and 2.5x2.5 m combination. The particle size distribution shows an area of on average coarser clasts to the north of the meander, and finer ones in the center and south of the area. The broad dark blue patterns are sandy areas with a few small gravels. The average particle size is 15.9 cm, and the STD is 10.7 cm (max size = 112.3 cm and min size = 1.8 cm). The validation was performed by comparing detection results to field caliper measurements in 5 different areas, and is presented in Figure 44b. The compared distributions show a satisfactory overlap, with an average RMSE of 4 cm.

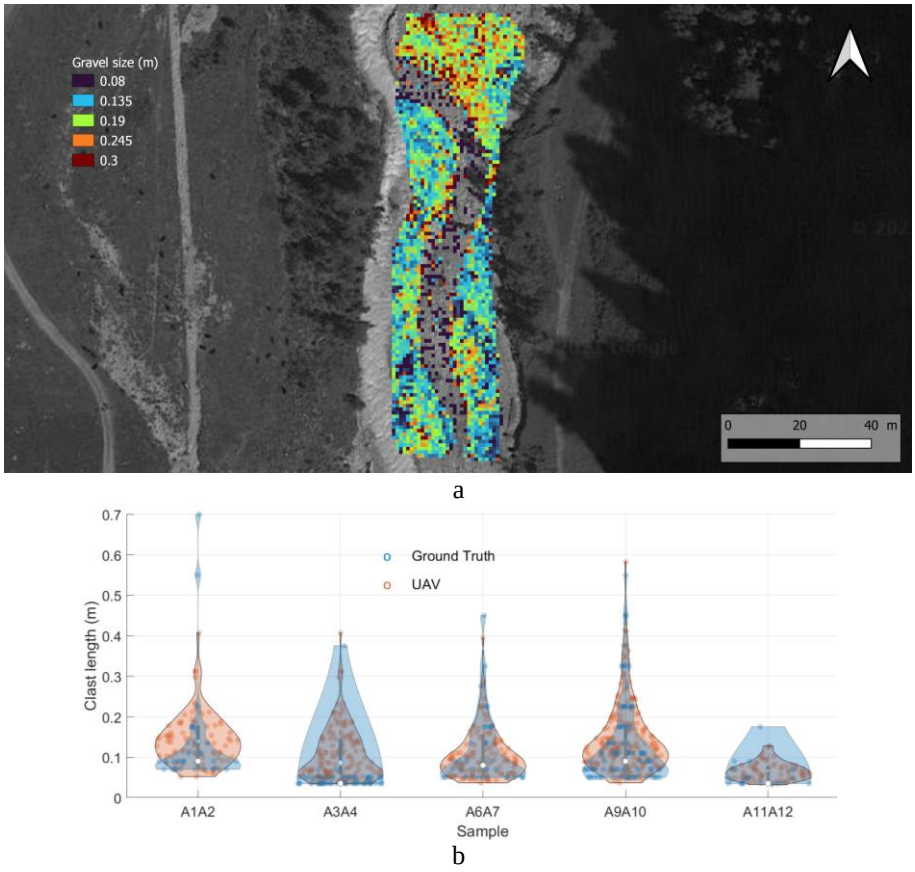

Figure 44 - Results of the clast size mapping on the banks of the Navisence River, in Switzerland. a: map of the mean gravel size; b: cross validation results between measurements on ground samples and UAV orthophotography.

2.3. Lake artificial gravel beaches: Montana, USA

2.3.1.Bio-station beach

Bio-station beach is a 135x15 m artificial beach located on the eastern shore of Flathead Lake, Montana, USA. The data was collected by Dr. Mark Lorang and Diane Whited (University of

Montana) during a drone flight on 2020/07/09. The detection was performed using a 1x1 m window, it took about 1h to run and produced a list of around 35000 detected clasts. The mapping shown in Figure 45a essentially presents a cross-shore gradient with coarser sediment at the bottom of the slope, and finer at the top, consistent with field observations. Grain sizes range between 1.6 cm and 50.6 cm, with an average size of 7.5 cm and an STD of 3.3 cm. Validation was performed by the method proposed in Part 1 of this chapter, and shows a satisfactory overlap of grain sizes distributions, with an average RMSE of 7 mm. Four samples (P4, P5, P6 and P7) were removed from the analysis because they were located outside the image area, thus not images by the drone.

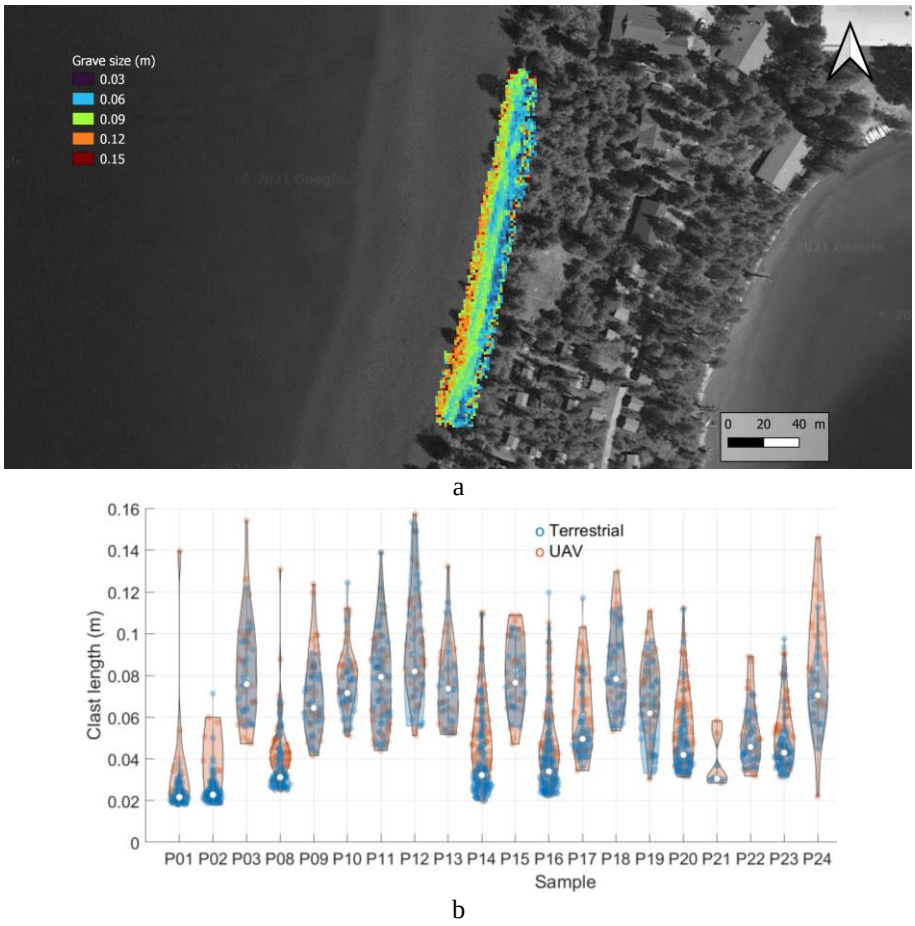

Figure 45 - Results of the clast size mapping on the Bio-station artificial beach on the Flathead Lake, in Montana, USA. a: map of the mean gravel size; b: cross validation results between measurements on terrestrial imagery and UAV orthophotography.

2.3.2.Salish Point beach

Salish Point is another artificial beach bordering Flathead Lake that is also monitored by Dr. Mark Lorang and Diane Whited. The site measures 200x10 m, it is enclosed with two groins and has a small jetty at its center. The image was processed using the same setting as the Bio-station. The detector produced around 48000 clasts in 1h30, with sizes ranging from 1.9 cm to 35.8 cm, with a mean size of 6.2 cm and an STD of 2.6 cm, thus presenting slightly smaller sizes than at the Bio-station site. Mapping (Figure 46a) shows a strong alongshore gradient with coarser clasts to the east and finer ones to the west. As the beach was built several years before the survey with no spatial sediment sorting, this gradient is likely related to an westward current as the lake outlet channel is

located immediately behind the west groin, although this hypothesis remains to be confirmed with measurements. Validation results show a good agreement between UAV and terrestrial data, with an average RMSE of 7 mm, although one point (P4) was removed as being outside of the monitored area.

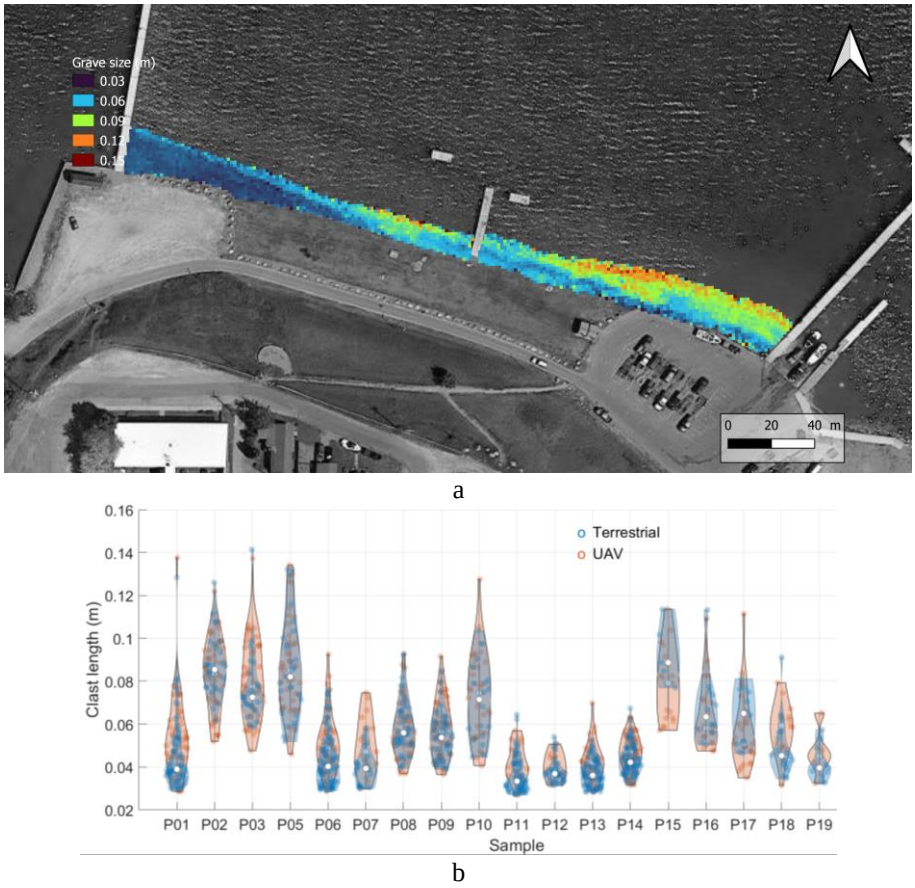

Figure 46 - Results of the clast size mapping on the Salish point artificial beach on the Flathead Lake, in Montana, USA. a: map of the mean gravel size; b: cross validation results between measurements on terrestrial imagery and UAV orthophotography.

2.4. Natural boulder beach: Iceland

Valahnukur is a boulder beach located in Iceland. The site has been monitored annually during surveys conducted in May since 2015 (except in 2020 due to covid). Dr Pierre Stéphan (University of Western Britanny) provided the orthoimages from these campaigns to test the performance of the tool on a very coarse sediment with volcanic colors. Unfortunately, no field data were measured by any other means, so it is impossible to validate the results as was done for the other sites.

The processing took about 2h for each year and combines 2 different window sizes (2.5x2.5 m and 5x5 m), similarly to the method used for the Navisence river data in Switzerland. Each campaign results cumulates on average about 57000 clasts, with sizes ranging from 4.5 cm to 2.2 m, for an average size of 49.5 cm and an average STD of 22.2 cm.

The mapping shows a strong cross-shore gradient with the largest boulders at the bottom of the beach, and the smallest ones at the top. A zone of intermediate clast sizes is found to the North. Interestingly, the coarse assemblage at the bottom of the beach slope is continuous along the entire

length of the beach in 2015 (Figure 47a), then a gap opens the sediment pattern from its center in 2016 (Figure 47b) and continues to be present in subsequent years (Figure 47c, d, e and f). In parallel, the average size of the lower slope clasts to the south of the area increases. The area where intermediate clast sizes are concentrated is also changing, with a gradual decrease from year to year. An overall shift from NW to SW could explain the observed changes but needs to be confirmed by field measurements. Although no validation data is not available, these maps appear to be consistent with field observations (P. Stéphan, personal communication, 2021), and demonstrate some degree of measurement reproducibility.

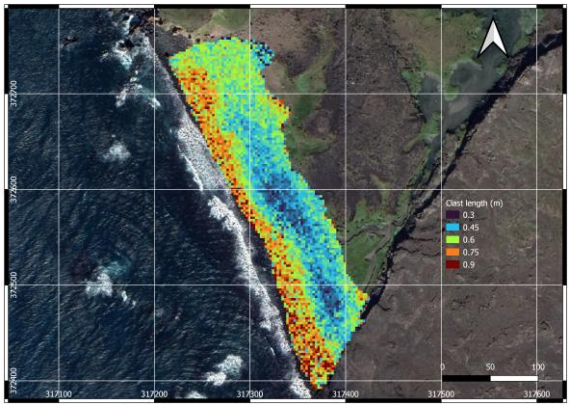

December 2015

a

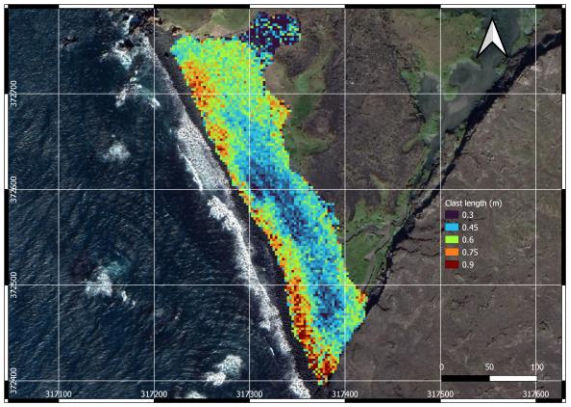

December 2016

b

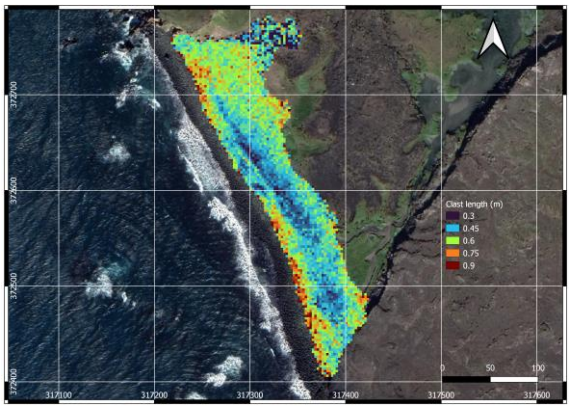

December 2017

c

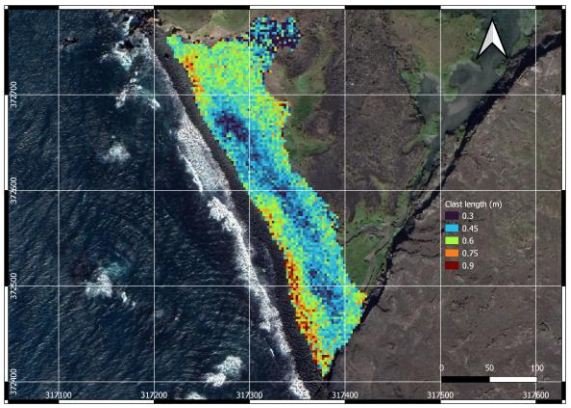

December 2018

d

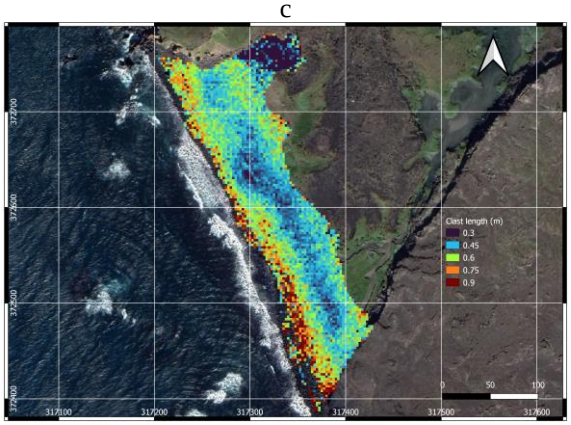

December 2019

e

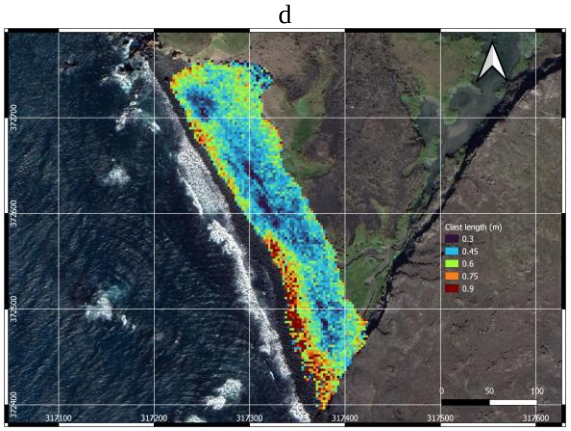

December 2021

f

Figure 47 - 7 years of boulder size mapping at Valahnukur beach, Iceland (2020 is missing due to the covid at this period). The colormap is consistent between maps and goes from 30 cm (blue) to 90 cm.

3. Chapter conclusion

In Chapter 2 - Section 4, we stated the first question this thesis aims to answer: *how can we reliably quantify the spatiotemporal variability of the gravel morphometry?*

In order to answer this question, a Mask R-CNN model was trained to recognize clasts present on terrestrial and UAV images, with rounded shapes and no overlapping. This approach was shown to be very effective in quantifying and mapping the spatial variability of cobble morphometry (size, shape and orientation), and was the subject of a scientific publication (Soloy et al 2020). The method was then challenged on data from different sites with specific characteristics (a mixed sand-gravel beach, an artificial beach on a lake, an alpine river banks and a volcanic boulder beach) in the framework of an international collaboration initiated for this purpose. The method proved to be relatively efficient in quantifying the spatiotemporal variability of clast morphometry on sites not included in its initial training set.

– CHAPTER 4 –

BEACH MORPHODYNAMICS IN RESPONSE TO HYDRODYNAMICS

Observing, understanding, and predicting the morphological evolution of shorelines is crucial to protect coastal environments, inhabitants, and economical activities, especially considering the context of global change. The morphology of shorelines can be monitored at a local scale using Coastal Video Monitoring Systems (VMS), by delineating the visible waterline on coastal images. Waterlines within a tidal cycle are used as contour lines of the intertidal morphology and provide digital elevation models (DEM). VMS usually record coastal images every ten minutes, but the resulting dataset weight and varying imaging conditions make it difficult to automatize shoreline detection. This chapter introduces a method based on Mask R-CNN to automatically detect the shoreline and provide daily DEMs of the beaches in Normandy. The method was applied in Etretat and Hautot-sur-Mer to identify the main mechanisms of morphological variability and their temporal periods. The grain size variability was also measured using the method presented and discussed in Chapter 3. DEM and grain size measurements were then used to feed XBeach-G model, the results of which were discussed in light of previous findings, with a focus on permeability.

1. Intertidal topography monitoring

This first subsection introduces a methodology developed in this PhD thesis to automatically monitor the intertidal beach topography. This method is based on the use of a deep learning algorithm called Mask R-CNNN to produce coastline delineation on coastal VMS images. It is the same algorithm as used to identify gravels in images, presented in Chapter 3 - Section 1, although trained on a different dataset.

This work was published in the journal Coastal Engineering (Elsevier): ***Soloy, A., Turki, I., Lecoq, N., Gutiérrez Barceló, Á.D., Costa, S., Laignel, B., Bazin, B., Soufflet, Y., Le Louargant, L., Maquaire, O., 2021. A fully automated method for monitoring the intertidal topography using Video Monitoring Systems. Coast. Eng. 103894.*** ***https://doi.org/10.1016/j.coastaleng.2021.103894***

1.1. Introduction

Coastal environments are continuously subjected to the natural processes of weathering, marine erosion and flooding (Nicholls et al., 2007). The impacts of these processes and events vary depending on the geometric structure of the coastlines, their characteristics, and their relative exposure to the impacts of waves and tides.

In the context of climate change and the growing environmental strain caused by human activity, coastal communities are increasingly vulnerable to environmental hazards. Additionally, these communities are facing an intensification of natural hazards including shoreline change induced by coastal erosion, and changes in nearshore topography (Jongejan et al., 2016; Le Cozannet et al., 2019; Ranasinghe et al., 2012; Wainwright et al., 2015).

In this frame of reference, beaches provide protection against wave action by dissipating their energy when their sediment is mobilized, especially during storm event. These systems are subject to multiple maritime forcing whose relative influence determines the morphological response of the beach. Although the dynamics of these systems are complex, they are not impossible to predict (Davidson et al., 2017; Esmail et al., 2019; Hanson, 1989; Jara et al., 2015; Montaño et al., 2020; Yates et al., 2009). It is therefore important to monitor the geomorphology of coastal systems in order to acquire capabilities of prediction.

Among the different methods used for monitoring the coastal morphology, Video Monitoring Systems (VMS) allow the morphology of a site to be measured thanks to both variations of the water level and the position of the waterline, with a spatial resolution of a few centimeters, and a temporal resolution of one day or less.

However, extracting the position of the coastline from VMS images remains a long and often tedious task. Historically, it was first necessary to manually delineate the waterline (Holman et al., 1991), then it was made easier with the development of several detection methods (Plant et al., 2007).

A large part of these methods is inherited from the SLIM (ShoreLine Intensity Maximum) model of Plant and Holman (1997), based on the presence of a wave breaking zone with a visible high light intensity near the waterline. Examples include the PIC (Pixel Intensity Clustering) or the method of Aarninkhof et al., (2003) also known as IBM (Intertidal Beach Mapper), the ANN (Artificial Neural Network) model of (Kingston, 2003), and the CCD (Color Channel Divergence) model of (Turner et al., 2001).

Although these methods have greatly improved data processing time, their application is limited by variability in data quality and requires extensive expertise (Osorio et al., 2012). More recently, new approaches have been developed in order to address these constraints and move closer to a fully automatic detection. For instance, Osorio et al. (2012) developed the Physical and Statistical Detection Model (PSDM) based on edge detection algorithms. Another example is the SDM (Shoreline Detection Model) of Valentini et al. (2017) which proposes to perform the semantic segmentation of the image pixels in order to determine the land/water interface by processing the histogram of RGB channels. Nevertheless, most of these algorithms remain strongly constrained by the multiple environmental variabilities (luminosity, contrast, rain, fog, presence of users, boats, dirty lenses, etc.) and therefore require the action of a human operator to fine-tune the parameters before being applied to a new site.

To overcome such limitations, the present research proposes the use of deep learning techniques to be applied to a large dataset of remote sensing images from coastal VMS for mapping nearshore intertidal topography. Many advances have been made in the field of image classification, notably with the rise of the use of convolutional neural networks (CNN) as reported in various academic articles (Chen et al., 2020, 2019; He et al., 2017; Huang et al., 2019; Kirillov et al., 2020; Wang et al., 2020).

More specifically, if trained using enough data, the algorithm called Mask R-CNN (He et al., 2017) can detect and delineate concepts as abstract as coastline delimited bodies of water on images under various conditions, unaffected by the presence of objects and people. During this study, Mask R-CNN was used for mapping the nearshore topography in three megatidal coastal areas characterized by different morphological properties with the aim to propose a fully automated method for monitoring coastal morphology using VMS.

1.2. Datasets and Methodological Approach

1.2.1.Methodological approach

The methodology for building intertidal topography from VMS is a multi-step process that was described by Aarninkhof et al. (2003). It was applied to the newly installed coastal VMS in Normandy, which is original in that it implements the use of the Mask R-CNN as the waterline classification model. As presented in Figure 48, the method includes two branches.

The first branch represents the series of steps that are necessary to implement a model able to detect bodies of water, in the event that there is no existing model already trained leading to satisfying results. Training the neural network requires manually labeled image data, as explained in Section 1.2.1.2 in more detail. This series of steps can be repeated to increase the detection performances of a previously trained neural network, using new labeled data.

The second branch is the operational stage. Once the model is trained and shows satisfying results, the neural network can delineate waterlines without further human labeling, allowing the methodology to efficiently produce intertidal Digital Elevation Models (DEMs).

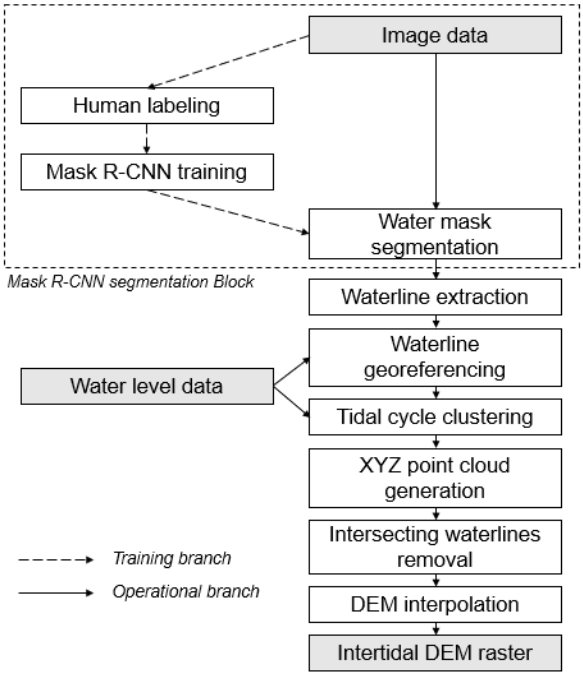

Figure 48 - Algorithm for the intertidal topography reconstruction process: First an image is analyzed by the Mask R-CNN model to be segmented, either for training or operational purpose. Then the shoreline is extracted and stacked with other shorelines belonging to the same tidal cycle. Intersecting waterlines are removed before interpolating the point cloud.

1.2.1.1. Shoreline definition and manual delineation

Besides Dolan's et al. (1980) definition stating that the shoreline represents the interface between land and sea, there is currently no real consensus on a more accurate definition for a shoreline. However, Mask R-CNN's output fully relies on the way that the human operator providing the model's training data will understand this definition and eventually delineate the shoreline accordingly by hand. Clearly defining the object of our interest is therefore an important step in this methodology.

In previous video-based monitoring studies, the shoreline has often been defined as a visible component of the wave breaking zone that can be identified thanks to the SLIM (ShoreLine Intensity Maximum) introduced by Plant and Holman (1997). As the objective is to measure the intertidal topography using the waterline as an indicator associated with a previously known water level, these

indicators remain reliable. Nevertheless, they strongly depend on the presence of a foamy wave breaking zone, which is likely to constrain the shoreline detection capabilities to wavy conditions, while calmer and waveless ones wouldn't be processable despite their likely better accuracy.

In this study, it was decided to define the shoreline as the line that a human operator is able to detect as the separation between land and water on timex images, regardless to the presence of wave breaking conditions. This definition is closer to the approaches adopted by Aarninkhof et al. (2003), Kingston (2003), Osorio et al. (2012) and Turner et al. (2001), considering the shoreline as the interface between a wet and a dry domains, but remains more open to interpretation as it allows the operator to include or exclude elements to either domains depending on the context (e.g. a floating boat can be considered wet, an object occulting the shoreline can be ignored). With this in mind, an operator could manually delineate the body of water that represents the sea on a timex image. The polygon thus digitized will be limited by the sides of the image, the horizon and the defined shoreline (Figure 49). In order to avoid the ambiguity implied by the multiple meanings of the word "shoreline", the detected lines will be called "waterlines" in the rest of this section.

1.2.1.2. Mask-RCNN parametrization, and training

The neural network was trained on a total of 1062 manually labelled images from the study sites' VMS. The images cover as wide a set of situations as possible, including sunny weather, storms, rain, fog, backlight sun, sunrise and sunset, presence of people and objects on the beach (tourists, boats), in the water and in front of the waterline, presence of insects on the camera lens, and so on. A total of 95 epochs each including 1000 steps with various augmentation operations (rotations, crop, addition of noise) were necessary to obtain a satisfactory detection quality.

The algorithm learning performance is evaluated during learning steps by comparing the detected masks to the manually digitized ones. This is done using a set of metrics including class loss, mask loss and boundary box loss, each of which is calculated separately for both the training and the validation datasets. The evolution of these metrics helps to prevent the model from overfitting. The detection is considered satisfactory when the algorithm plateaus at a minimum value of loss.

The influence of the human labeling bias on the algorithm's results is considered negligible as the mask output provided by Mask R-CNN will mandatorily be 28 x 28 pixels in size, as constrained by the neural network's architecture, before being upscaled to the image original size. Therefore, an aliasing effect can sometimes be visible (Figure 49). As a consequence, the maximal resolution of detectable morphological structures on a specific object is equal to 1/28 of the total size of the object. On shoreline images for instance, some structures called cusps sometimes appear as a series of oscillations of the waterline along the beach. In this case, only cusps with a wavelength appearing larger than 3/28 of the body of water's width in pixels (often equivalent to the width of the image) will be detectable. For the same reasons, the pixel uncertainty range of the detected mask edge will be

relative to the object itself, equaling 1/28 of the detected object's bounding box dimensions. Thus, the metric accuracy is not consistent as it is always relative to the detected object size, which changes from one image to another, and is expected to decrease with the distance to the camera, as pixels cover wider surfaces. In addition, it is interesting to note that as the body of water's apparent size may depend on the state of the tide – especially in images from cameras pointing towards the alongshore direction - the detection accuracy is expected to increase at low tide as the body of water becomes smaller, as compared to high tide.

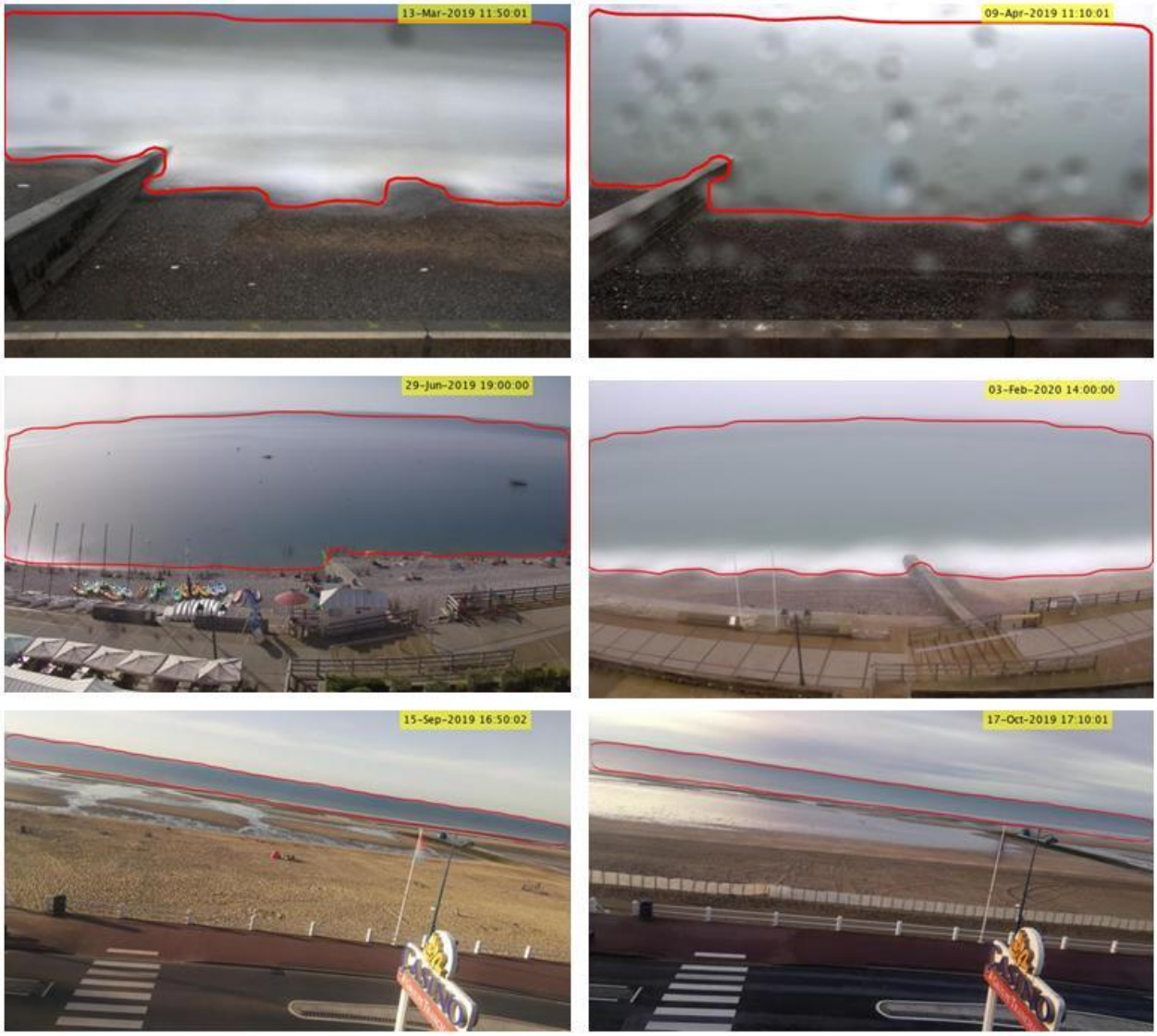

Figure 49 - Example of body of water detection using Mask R-CNN in Hautot-sur-Mer (top), Etretat (center) and Villers-sur-Mer (bottom), during various filming conditions

As shown on Figure 49, the algorithm performs well in most cases even when conditions are not optimal such as during rain, storms, presence of users, presence of channels and ponds at low tide, etc. However, these conditions are also likely to confuse the model (Figure 52) and therefore can represent a limit to detection. The strongest advantage of the Mask R-CNN lies in the generalization and abstraction capabilities inherent in convolutional neural networks, which makes it possible to train a model only once, and then use it on various types of sites, orientations and conditions. Moreover, it

is always possible to improve it by completing or even complexifying the training dataset in order to reduce the number of errors and open the detection capabilities to new object classes.

1.2.1.3. Intertidal topography reconstruction

The first step of the operational branch is the Mask R-CNN segmentation. Each timex image is subjected to detection by the trained neural network, which will delineate the edges of the visible body of water.

Then, the waterline is extracted by a ROI mask that also excludes the groins from the detected polygon (Figure 50). and is associated to its respective water level. This water level allows georeferencing, i.e. the transformation of image coordinates into geographical XYZ coordinates by projecting the waterline on the plane of the water surface.

Figure 50 - Example detected waterlines on the 3 cameras of the Hautot-sur-Mer's VMS

Once georeferenced, waterlines belonging to the same half semi-diurnal tidal cycle (i.e over about 6h12) are clustered together, thus creating XYZ intertidal point clouds (Figure 51a). This allows the identification of the potentially miss delineated waterlines which are likely to cross one other waterline or more. To do so, the number of intersections is calculated for each waterline, and the waterline that crosses the highest number of different other ones is removed. This operation is iteratively performed until the total number of intersections goes down to zero.

Finally, the point cloud is converted into a raster with normalized coordinates (Figure 51b) using a 2D linear interpolation. The raster is then cropped to the surface covered by the waterlines in order to remove the irrelevant extrapolated information, thus allowing the tide-to-tide comparison of the beach intertidal morphology.

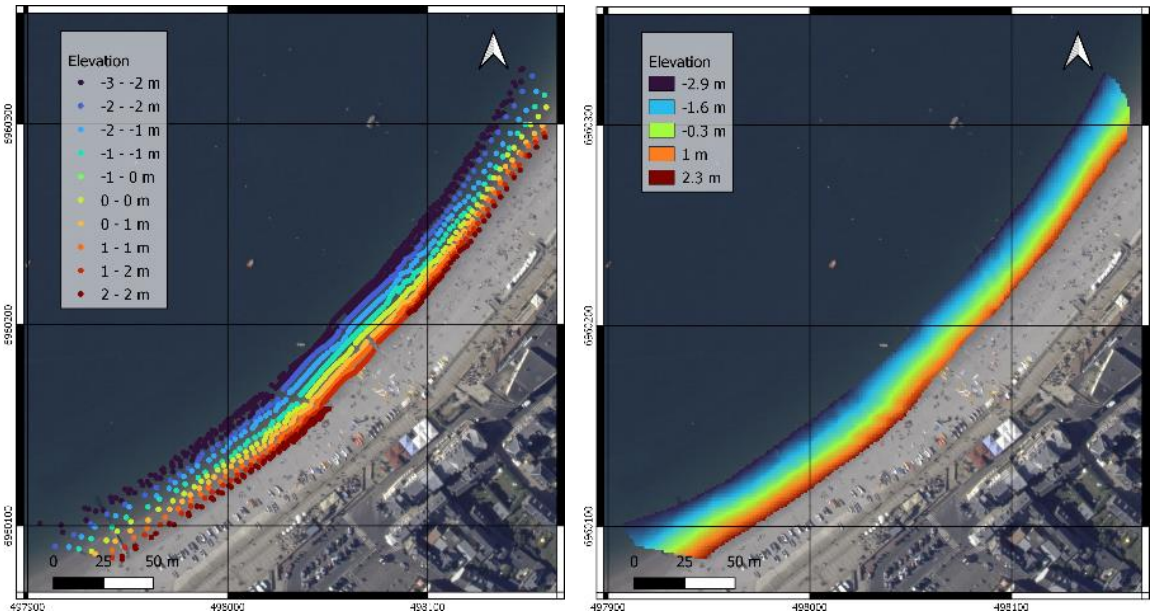

a b

Figure 51 - XYZ point cloud (a) formed by the georeferenced waterlines detected using Mask R-CNN during a complete tidal cycle in Etretat and (b) interpolated DEM. Dotted lines show the surface covered by each camera of the VMS.

Although the Mask R-CNN algorithm works in the vast majority of cases (Table 4) it sometimes misidentifies the waterline, usually due to factors of confusion such as low light, presence of fog, presence of obstructions on the camera lens (water droplets or insects), or unclear waterline (too smooth transition from dry to wet sand) (Figure 52). In order to limit detection errors, it is possible to filter out ambiguous data prior to detection. The filtering applied in this study uses an established threshold for both brightness and blur metrics to separate the good quality images from the darker and blurrier ones. For each camera, these metrics are calculated over an appropriate section of the image, in this case the sea, and objects with visible and contrasted edges respectively. Brightness is measured by adding the averaged red, green and blue channels of the image, and the blurriness index has been outlined by Crété-Roffet et al. (2007). After calculating both metrics on the whole dataset, thresholds are empirically selected from their respective histogram for each camera in order to determine the combination that allows the best filtering possible.

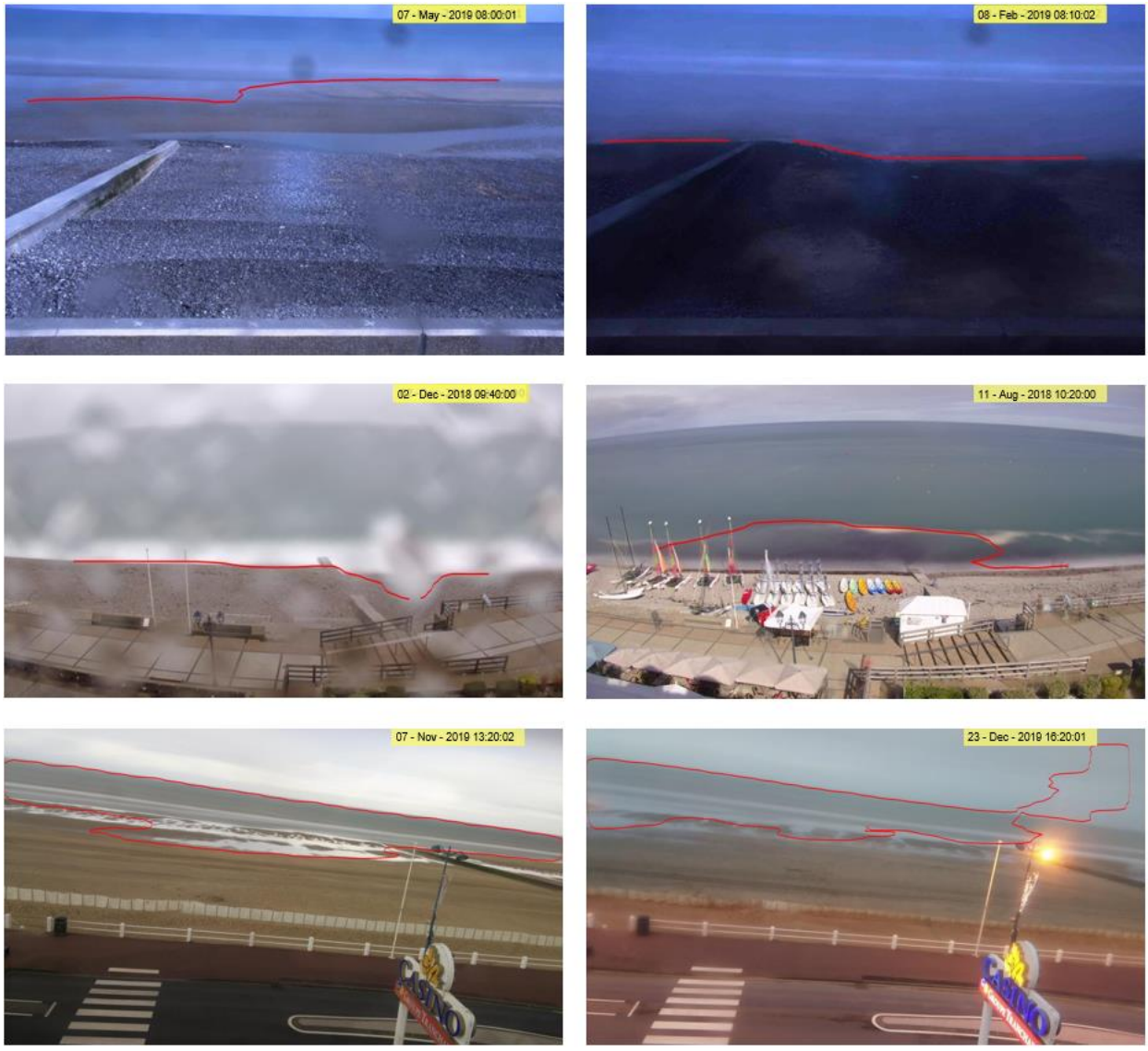

Figure 52 - Example of unsatisfactory detections using Mask R-CNN in Hautot-sur-Mer (top), Etretat (center) and Villers-sur-Mer (bottom)

In addition, it is important to mention that on images showing alongshore perspectives, the water mask resolution remains 28 x 28 pixels although the mask is then being scaled up to the body of water's actual size. Therefore, because of both the limited accuracy of 1/28 of the body of water's size and the smoothing effect due to the mask resizing process, closed angles may appear rounder, and impose a horizontal offset that can become significant for long distances to the camera (e.g. the extremity of the beach on Figure 53). Consequently, care should be given to the selection of the ROI's size being used for extracting the waterline to a reasonable extent.

Figure 53 - Example of body of water detected by Mask R-CNN on a lateral perspective

1.3. Results and Discussions

1.3.1.Ground truth validation

1.3.1.1. Detection validation

For the purpose of estimating Mask R-CNN's capabilities to delineate the waterline, the methodology was applied to the data acquired by the central camera of each site, covering periods of 9, 20 and 11 months, between 2018 and 2020 at Villers-sur-Mer, Etretat and Hautot-sur-Mer respectively (Table 4).

After stacking the extracted waterlines on their respective images, each detection was individually and manually analyzed by a human operator in order to empirically classify the detected waterlines' quality as satisfactory or unsatisfactory. It was then possible to calculate a satisfactory detection performance value by comparing the number of images classified as satisfactory to the number of images leftover after the parametric filtering.

In Etretat, the detection by Mask R-CNN followed by parametric filtering is successful in 97.33% of the data, i.e. the manual operation will have classified only 2.67% of the detections as unsatisfactory. With 69.87% and 67.11% success respectively, Villers-sur-Mer and Hautot-sur-Mer also show very satisfactory performances, although slightly lower. This difference between Etretat, Villers-sur-Mer and Hautot-sur-Mer beaches can be explained by the texture contrasts, the slope, and the morphological complexity of the beach. At Villers-sur-Mer, the association between the gentle slope and the megatidal ranges makes the interface between the dry and the wet sand move very fast which tends to blur the intertidal area whose sand already smooths the texture of, and thus makes the identification of a clear shoreline particularly difficult on timex images, even for a human eye. In addition, the complex topography sandy dissipative beaches (bars, ponds, channel networks…) is hard

to catch for the mask resolution that can't store more complex structures than 1/28 of its own size. The issue is even stronger in Hautot-sur-Mer and seem to be making the waterlines over the site's sandy area even more difficult to detect for unidentified reasons. However, the steep slope and contrasted texture of the pebble ridges makes the waterline clearly identifiable in almost all cases in Etretat and Hautot-sur-Mer, which compensates the poorer sampling capabilities over the sandy area for the last site in the presented detection performance value.

It is important to mention that these misdetections are in the vast majority of the cases possible to automatically identify and remove during the intersecting waterline removal part of this methodology (Figure 48).

Table 4 - Mask R-CNN detection validation results

Sites	Villers-sur-Mer	Etretat	Hautot-sur-Mer
Image dataset start	11/03/2019	28/06/2018	11/12/2019
Image dataset end	31/12/2019	13/02/2020	04/01/2020
Total number of images	23579	11720	27532
Images after parametric filtering	17373	10000	18490
Images manually classified as satisfactory	12138	9733	12409
Detection performance	69.87%	97.33%	67.11%

1.3.1.2. DEM Validation

For each study site, a validation geodesy campaign was carried out using a differential Global Navigation Satellite System (dGNSS) in order to measure the ground truth topography. Measurements have been carried out with a non-gridded uniform spread of the sampling points over the video recorded area, covering the beach from the highest point of its top part to the low tide waterline, with number of points ranging from 100 to 150 per site in total, measured on both slope breaks and centers.

The intertidal topography was reconstructed at the geodesy campaign dates using the methodology described 2.2.4 and then compared to the dGNSS data for validation. Comparisons are evaluated using the Root Mean Squared Error (RMSE) calculated between the dGNSS points' elevation and the DEM's elevation at the same XY locations, thus corresponding to an average vertical offset. As some of the dGNSS points were out of the DEM coverage, these points were excluded from the calculation, resulting in the counts visible in Table 5.

Table 5 shows the vertical RMSE values calculated for all sites, with 22 cm in Etretat, 29 cm in Hautot-sur-Mer and 33 cm at Villers-sur-Mer, which correspond to ranges found by previous studies (Uunk et al., 2010). R^2 are also provided with values ranging from 0.93 to 0.99, which confirms method's ability to provide reliable beach morphology estimations on all sites.

Table 5 - DEM validation results

	Villers-sur-Mer	Etretat	Hautot-sur-Mer
DEM date	31/12/2019	10/01/2020	14/02/2020
GNSS campaign date	08/01/2020	10/01/2020	14/02/2020
GNSS points count	59	48	54
Vertical RMSE (m)	**0.33**	**0.22**	**0.29**
R^2	0.95	0.99	0.93

In addition, the evolution of the vertical offset with the omnidirectional distance to the camera was analyzed using a Mann Kendall statistical test. Results presented in Table 6 show that although the error tends to increase with the distance in all cases, the only found significant p-value at the 0.05 threshold is seen in Hautot-sur-Mer. For this site, the trend remains under 2.4 vertical mm / per horizontal meters. However, on this site the low tide shoreline can go as far as 210 m in the cross-shore direction (Table 1), therefore the vertical error can be increased by an order of 50 cm at this distance and is thus important to consider. Similar calculations would show an increase of about 20 cm and 4 cm at Villers-sur-Mer and Etretat respectively, for low tide vertical uncertainties. This error increasement is due to a combination between the lower resolution for longer distance to the camera and the Mask R-CNN intrinsic uncertainty. Nevertheless, these values should be considered as orders of magnitude as the vertical error doesn't properly fit to a linear trend, as showed by the low R^2 values in Table 6.

Table 6 - Sensitivity analysis results of the vertical error to the distance from the camera

	Villers-sur-Mer	Etretat	Hautot-sur-Mer
RSE/Dist R^2	0.04	0.01	0.06
RSE/Dist Mann Kendall Tau	0.05	0.02	0.20
RSE/Dist Mann Kendall p-value	0.58	0.82	0.04
RSE/Dist Slope (m/m)	6.35E-04	3.21E-04	2.39E-03

1.4. Discussions

The task of extracting the shoreline position from camera images to reproduce the intertidal bathymetry has been realized with an increasing efficiency over the last decades. In most cases, authors' methodology implied the classification of pixels based on their individual intensities in order to to identify either the swash zone (Plant and Holman, 1997) or the wet and dry pixels (Aarninkhof et al., 2003; Kingston, 2003; Turner et al., 2001; Valentini et al., 2017).

The SLIM model (ShoreLine Intensity Maximum) of Plant and Holman (1997) locates the waterline along pre-defined cross-shore transects by thresholding pixel intensities in order to parametrically extract the pixels that are considered belonging to the swash zone. The edge of swash zone is a good proxy of the shoreline, but its inconsistent presence makes the technique unreliable in a

lot of cases, such as dissipative beaches, intertidal zones with complex morphologies (bars, channels…), and waveless weathers.

The CCD (Color Channel Divergence) model of Turner et al. (2001) and the PIC model (Pixel Intensity Clustering) developed by Aarninkhof et al. (2003) were both created to overcome some of the issues of the SLIM model. CCD uses the expected difference between sand and water colors to find their interface point along pre-defined cross-shore transects. PIC identifies wet and dry pixels within a pre-defined ROI on images. This classification is possible using two discriminator functions that consider the hue, saturation, and grayscale values applied on each pixel. The classification of each individual pixel is then performed by thresholding the function's results. Contrary to SLIM, these two models don't rely on the presence of a swash zone, although they require a fine calibration to the site to which it is applied, as well as a significant contrast between the two domains of interest.

Both the ANN (Artificial Neural Network) and SDM (Shoreline Detection Model) models from Kingston (2003) and Valentini et al. (2017) respectively are a semantic segmentation algorithms that produce a classification of each pixel in an image as water and sand, the interface of which is the waterline. Models require to be trained on manually labeled images and the misclassified pixels need to be manually filtered.

While these methods remain efficient, they require case-specific calibration processes, rely on the concomitance of a wide range of conditions (presence of a single swash zone, absence of users/obstructions, specific difference in color between wet and dry pixels) and require a significant amount of manual work in order to be successfully deployed.

The present study overcame some of these difficulties thanks to the use of instance segmentation, in particular Mask R-CNN, with the aim of building an automatically working algorithm. Mask R-CNN is a deep learning algorithm that performs instance segmentation on RGB images, which has been used for a wide variety of applications such as measuring snow depth (Kopp et al., 2019), counting the number of cows present in a farm corridor (Qiao et al., 2019), mapping the grain size of pebbles (Soloy et al., 2020), and determining the shape of molds present on the walls of a tunnel (Zhao et al., 2020).

Mask R-CNN allowed more characteristics to be additively taken into account when identifying a body of water than parametric solutions would (textures, shapes, presence/absence of a swash zone, variabilities in brightness, colors, weather, human activity, sediment types…) thus increasing the range of satisfactory identifications while significantly lightening the need for calibration and thresholding steps. In addition, using a modular algorithm that is not specific to the coastal field such as Mask R-CNN and training the model including multiple sources data tends to optimize the generalization capabilities of this methodology, thus allowing it to be applied on new sites with limited parametrization work.

This method has proven to be reliable when detecting contours of bodies of water on shoreline images at Villers-sur-Mer, Etretat and Hautot-sur-Mer, with a detection performance rate of 69.87%, 97.33% and 67.11% respectively, and considering an accuracy of 1/28 of the detected body of water's bounding box size in pixels. For comparison, Plant et al. (2007) recorded detection performance rates ranging from 15% to 50% for SLIM, from 0 to 91% for CCD, from 24 to 78% for PIC and from 32 to 92% for ANN while comparing different methods applied to four different study sites. Rates obtained with Mask R-CNN therefore surpasses the other detection models with higher average detection rates and less difference from site to site. The exceptional rates are made possible thanks to the adaptability of Mask R-CNN and its ability to detect abstract concepts, such as a body of water, unaffected by the many sources of image variability (e.g. weather conditions, waterline obstruction, etc.), which are difficult to take into account using a parametric detection model.

Extracting and georeferencing multiple waterlines along tidal cycles allows the reconstruction of good intertidal topographies at Villers-sur-Mer, Hautot-sur-Mer and Etretat, with RMSE values of 33 cm, 29 cm and 22 cm respectively. It is important to mention that at Villers-sur-Mer the RMSE value was calculated using a DEM from a week before the geodesy campaign due to a malfunction of the VMS during this period. The value is therefore likely to be overestimated. With on average 10 cm for SLIM, 20 for CCD, and 20 to 34 cm for PIC (Plant et al., 2007; Uunk et al., 2010), vertical biased calculated for this methodology remain of the same order of magnitude as other intertidal DEM building strategies from video monitoring techniques.

However, the methodology remains sensitive to the distance of the waterline and faces difficulties to correctly identify the proper waterline in the context of a megatidal and gently sloped beach. Additionally, the neural network has troubles classifying large, complex geometries, including the presence of ponds and channels due to sand bars, which therefore represent a limit to its use. Nevertheless, misidentified waterlines can be parametrically detected and cleared out. It is therefore possible to use this new methodology for monitoring the daily intertidal topography in a fully automated way.

More generally, the model's resilience and abstraction abilities could make Mask R-CNN a powerful asset to the coastal science field, as it already is for other remote sensing applications (Maxwell et al., 2020; Nie et al., 2018; Soloy et al., 2020; Yang et al., 2020; Zhao et al., 2018). Moreover, coastal VMS are relatively efficient, high resolution and low priced in comparison to aerial and satellite technologies, especially when associated with Mask R-CNN for measuring multi-scale variables.

The Mask R-CNN method has been successfully used for other scientific and societal applications (Kopp et al., 2019; Qiao et al., 2019; Soloy et al., 2020; Zhao et al., 2020), and is now proven to be useful for coastal science applications despite its current limitations. Recently, major progress have been made in the instance segmentation field and new tools are now available with

better capabilities such as BlendMask (Chen et al., 2020), TensorMask (Chen et al., 2019), Mask Scoring R-CNN (Huang et al., 2019), PointRend (Kirillov et al., 2020), SOLOv2 (Wang et al., 2020), and even more. One can expect that these tools, freely accessible for the most part, will become a standard in further coastal applications.

1.5. Conclusion

Monitoring the evolution of coastline morphology is a key challenge in the context of global change. Using coastal VMS addresses this problem with a high frequency, high resolution and low price that enables the surveillance of the waterline's position. The multiscale changes of the waterline's position are very important and depend on the physical characteristics of sediment, the topography and the local hydrodynamic conditions of waves and tides. The large variability of these influential factors complexifies the assessment of the shoreline and the study of its evolution at different timescales, from storm events to seasonal and interannual variations, with the aim of quantifying the long-term coastal erosion due to climate change. In this frame of reference, coastal VMS have been installed to survey the morphodynamics of 3 megatidal coastal systems of Normandy (France) including a sandy beach at Villers-sur-Mer, a pebble beach in Etretat, and a composite beach in Hautot-sur-Mer.

Extracting the waterline from the images provided by coastal VMS can be a complicated and time-consuming task because of the many sources of noise specific to this type of data (e.g. weather, sun angle, brightness, sea state variabilities, presence of obstructing objects, people etc.). In recent years, the development of convolutional neural network methods, including Mask R-CNN to process instance segmentations, made it possible to automatically extract detailed information from images and identify complex and abstract concepts in a wide variety of contexts.

The methodology presented in this research proposes the use of Mask R-CNN as a tool to classify bodies of water, with the aim of extracting the waterline from a large dataset of VMS images. This approach provides a robust technique to automatically identify the waterline of the Normandy beaches on RGB images provided by VMS, as Mask R-CNN is able to perform segmentation over 67% to 97% of the provided datasets. The waterlines can then be georeferenced with low uncertainty estimates, with vertical RMSEs of 33 cm, 29 cm and 22 cm at Villers-sur-Mer, Hautot-sur-Mer and Etretat respectively. Some limitations remain on sandy and gently sloped areas such as Villers-sur-Mer and Hautot-sur-Mer due to the very specific conditions of the Normandy sandy beaches (complex morphology, low slope, very wide intertidal zone, and unclear water-land delimitation). These conditions tend to increase the cumulative uncertainty of both segmentation and georeferencing as they make it a complicated task to identify the waterline, even for the human eye. Despite these limitations, this methodology was successfully and satisfactory deployed at the three monitored study sites of this research: Etretat, Villers-sur-Mer and Hautot-sur-Mer.

In addition to being freely available, Mask R-CNN applications can be extended to a wide spectrum of scientific questions due to its adaptability and its abstraction abilities and can therefore be a very interesting tool for coastal science. The recent major advances made in the field of instance segmentation could extensively open the possibilities for the coastal science studies.

2. Spatiotemporal variability of the morpho-sedimentary dynamics in response to hydrodynamic forcing

Chapter 4 - Section 1 presented the development of an efficient method to monitor the intertidal beach topography based on the processing of coastal VMS images. This approach was applied to a 2+ year long data set daily of daily topography in order to evaluate the morphological dynamics of the beaches of Etretat and Hautot-sur-Mer in response to marine forcing. Surface sedimentary aspects were also investigated using measurements performed following the protocol detailed in Chapter 3 - Section 1.

The present subsection introduces the results of this study which were the subject of a research paper published in the journal Marine Geology (Elsevier): ***Soloy, A., Turki, I., Lecoq, N., Solano, C.L., Laignel, B., 2022. Spatiotemporal variability of the morpho-sedimentary dynamics observed on two gravel beaches in response to hydrodynamic forcing. Mar. Geol. 106796. https://doi.org/10.1016/j.margeo.2022.106796***

2.1. Introduction

Monitoring, understanding and predicting coastal dynamics are key issues in coastal engineering in order to cope with coastal risks, especially in the context of climate change and sea level rise. It is a challenging task, as coastal morphodynamics are the complex result of non-linear interactions between hydrodynamic forcing (currents, waves, tides) and local characteristics (sediment size, embayment, intertidal zone structuration, etc.). Over the past few decades, great progress has been made in this regard thanks to improved monitoring technologies, which now allow the study of coasts at different scales, from the global and regional ones through satellite imagery, to the local scale through ground surveys and Video Monitoring Systems (VMS).

Satellite techniques rely on data provided by optical or radar sensors to identify coastal features at a regional or larger scale, at a daily to weekly measuring frequency constrained by orbital parameters (Salameh et al., 2019; Vos et al., 2020). “Ground surveys” gather all the methods for in situ measurement of a site’s topography at a defined moment, including lidar, total stations, differential GNSS (dGNSS) and photogrammetry (Andriolo et al., 2018; Lee et al., 2013; Mason et al., 2000; Morton et al., 1993). Among them, the profiling methods (dGNSS and total stations) are particularly used for long term repeated measurements as the method is relatively versatile and can provide morphological monitoring records down to the hourly scale. Nevertheless, measurements are

most often carried out on a weekly to monthly frequency and sometimes even shorter, depending on research-specific needs (Lacey and Peck, 1998; Larson and Kraus, 1994; Turner et al., 2016).

The use of VMS is a popular methodology that made it possible to monitor the shoreline of specific study sites on the long term, during daylight, with high resolution (from centimeters to meters), applying a commonly used sampling time step of 10 min (Davidson et al., 2007; Holman and Stanley, 2007; Silva et al., 2009; Turner et al., 2004). The idea is to georeference the moving shoreline visible on images, using its pixel coordinates associated with the local water level, assuming a good knowledge of the cameras' position and orientation relative to the environment in their field of view (Aarninkhof et al., 2003). Using this technique makes it possible to monitor the intertidal morphology with a repeatability up to the tidal cycle, although consistently delineating the shoreline over long periods can be challenging due to the high variability of image-taking conditions (light, weather, sea states, boats, users, camera lens cleanness, etc.). Authors report vertical biases ranging from 10 to 34 cm on reconstructed intertidal digital elevation models, depending on the site, hardware, dataset and delineation method used (Plant et al., 2007; Soloy et al., 2021b; Uunk et al., 2010).

VMS data are often processed with an Empirical Orthogonal Function (EOF) statistical analysis in order to decompose the complex movements of the shoreline through time into simpler components of variability, each of which summarizes a certain part of the total variability. By doing this, authors were able to identify mechanisms such as cross-shore translation, beach rotation (Blossier et al., 2017; Harley et al., 2015; Robinet et al., 2020; Turki et al., 2013), breathing (Blossier et al., 2017; Ratliff and Murray, 2014; Robinet et al., 2020), boundary effect of cross-shore structures (Miller and Dean, 2007), nourishment effects (Lemke and Miller, 2017) and even geological variations (Hapke et al., 2016). However, this improvement in monitoring techniques has mostly benefited the understanding of sandy coastal systems, and our knowledge of gravel ones remains relatively modest in comparison, despite the fact that they represent a significant - although unknown - part of the world's coastline (Buscombe and Masselink, 2006; Jennings and Shulmeister, 2002; Mason and Coates, 2001; Van Wellen et al., 2000). The main reason for this discrepancy is probably the cost and difficulty of measuring the spatial variability of gravel particle size, as well as its temporal variability, although this information is thought to be essential to understand and model the dynamics of gravel beaches (Buscombe and Masselink, 2006). Indeed, the spatial variability of gravel sizes and shapes as well as their temporal variabilities play a significant role in the reciprocal relationship between sediment transport, hydrodynamic processes, and morphological changes (Bluck, 1967; Buscombe and Masselink, 2006; Flemming, 1964; Isla, 1993; Orford, 1975; Williams and Caldwell, 1988).

To address this disparity and take the variability of sediment characteristics into account, the present study aims to investigate the geomorphodynamics and gravel size variability of two coastal systems, Etretat and Hautot-sur-Mer, a purely gravel beach and a composite one, respectively, both located in Normandy, France. Using the methodology developed by Soloy et al. (2021) and applied to nearly two years of VMS image data, it was possible to automatically monitor the shoreline position

on both beaches on various elevations within the tidal range. Combined with the other recently developed algorithm from Soloy et al. (2020), with the aim of mapping the distribution of surface gravel particle size at different times, this study intends to propose a first analysis of the morpho-sedimentary relationship of two pebble beaches of Normandy.

The extracted information will help us answer different questions regarding morphodynamics and sedimentary variability of gravel beaches in Normandy, including: (1) How does the shoreline shape change through time? (2) Are changes homogeneous at all elevations? (3) Are there specific mechanisms of shoreline change and what are their typical temporal period of variability? (4) What physical phenomena are responsible for morphological changes? (5) What is the shoreline's fabric made of? (6) How do the fabric's properties vary over time? (7) Can we link the morphological variability to the sedimentary one?

To bring relevant solutions to this questioning, an Empirical Orthogonal Function (EOF) analysis was performed using VMS-derived intertidal bathymetry datasets in order to identify the different mechanisms describing the shoreline variability at various elevations. Then, a wavelet analysis was used to identify and compare the main periods of variability of morphological parameters (beach width, beach orientation angle and beach slope) with hydrodynamic ones (wave energy, current velocity, and tidal range), and determine the main acting physical forcing processes. Finally, the spatial and temporal variability of gravel size were analyzed in light of the results brought by previous analysis.

2.2. Material and Methods

2.2.1.Nearshore Hydrodynamics

The hydrodynamic parameters of this study were used to serve two different purposes: (1) estimating the beaches' 3D morphology using VMS-derived waterlines of known elevation (water level), and (2) comparing morphodynamics with hydrodynamics (wave energy, tidal currents, tidal ranges).

For measuring the morphology (georeferencing the waterlines) in Hautot-sur-Mer, water level data was provided by the tide gauge ran by the French Naval Hydrographic and Oceanographic Service (Service Hydrographique et Oceanographique de la Marine, SHOM) and located in the harbor of Dieppe (49° 55' 45.0114"N, 1° 5' 4.1634"E), 4.2 km North East from the VMS (https://doi.org/10.17183/REFMAR#24). Unfortunately, there exist no other hydrodynamic observation stations near the study sites. Hence, other hydrodynamic parameters were extracted from hindcast model outputs.

As there is no tidal gauge anywhere near Etretat, water levels (tide and surge) used for estimating the morphology of the beach were provided by the Hycom2D model (Chassignet et al., 2007). The model's output is given on a curvilinear grid with a resolution ranging from 2 km far from the coast to 500 m close to the coasts. The time series was extracted from the point of coordinates

49° 42' 45.7194"N, 0° 11' 34.4394"E. The maximum error on the water elevation is expected to happen during high surge with an underestimation of 10 cm, while the tidal phase difference uncertainty is 12 min (Pasquet et al., 2014). A comparison between Hycom2D and the water level gauge in Dieppe shows a Root Mean Square Error (RMSE) of 0.26 m and a coefficient of determination (R^2) of 0.98 (0.13 m and 0.53 for surge alone). Figure 54a presents the time series of water elevations in Etretat used in this study. Elevations are centered around zero and vary from ± 2 m to ±5 m during the tidal cycle, with a maximum amplitude of 9.13 m. It is worth mentioning that setup elevations are not considered by Hycom2D. Consequently, morphological data are projected with a bias that tends to reduce their elevation by an order of magnitude of a few centimeters.

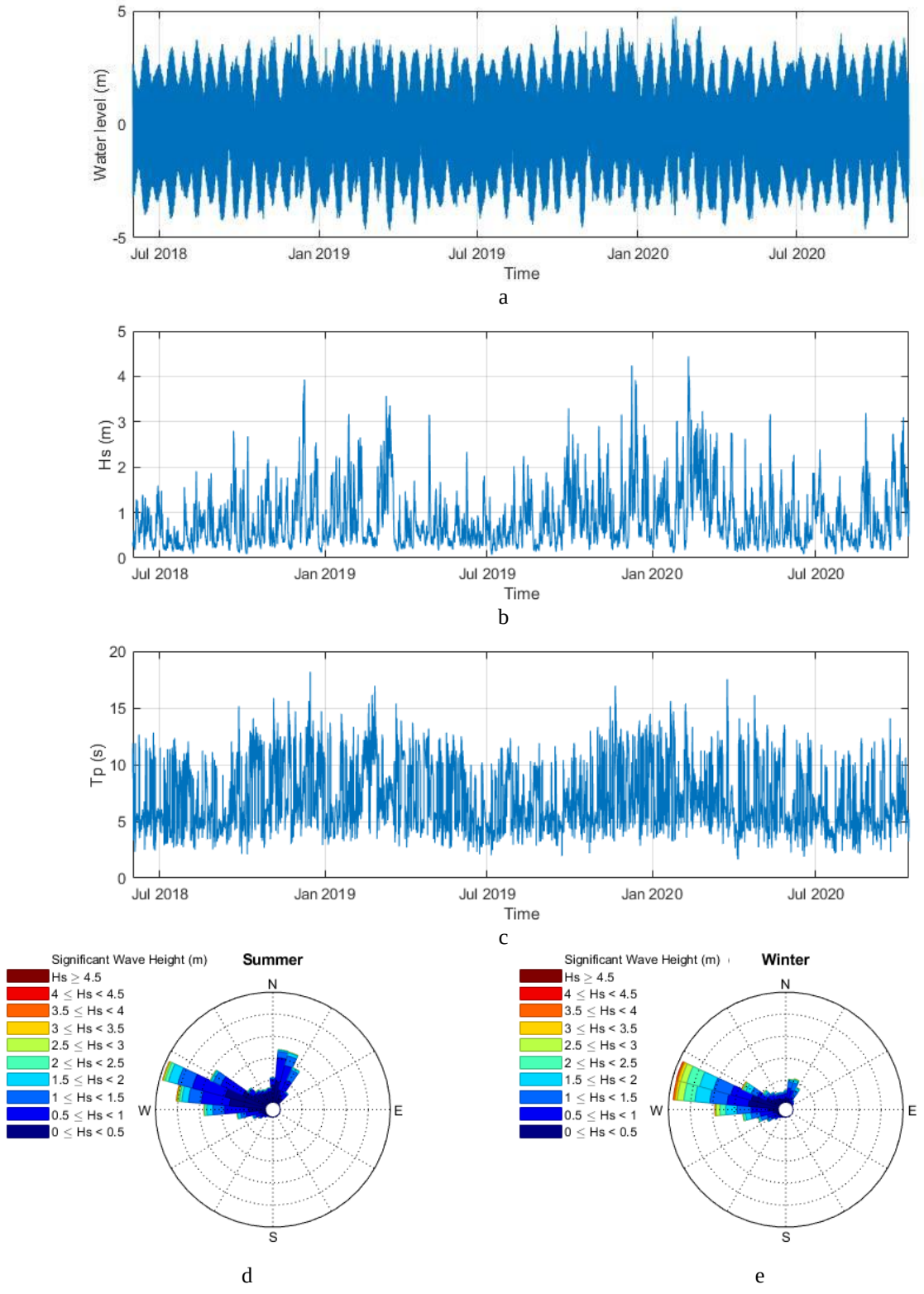

Figure 54 - Hydrodynamical parameters in Etretat from July 2018 to December 2020: Water level (datum: mean water level) (a) ; Wave Significant Height (b) ; Wave Peak Period (c) ; Roses of Wave Significant Height during Summer (April – October) (d) and Winter (October – April) (e) periods.

Wave data were provided by the implementation of the WaveWatch 3 model (Tolman, 2009) by Ifremer (French Research Institute for Exploitation of the Sea) over the English channel called PREVIMER_WW3-NORGAS-UG (Dumas et al., 2014). The output is given on an unstructured grid with a resolution varying from 2 min of arc off the shore to 200 m near the coast. Data were extracted at the point 49° 42' 53.7114"N, 0° 10' 58.35"E for Etretat (depth h = 21 m), and at the point

49° 56' 55.5936"N, 1° 1' 2.7042" for Hautot-sur-Mer (depth h = 17.5 m). This model has been extensively validated with data from buoys and satellite altimeters (Michaud et al., 2015) showing an RMSE of 25 cm and an R^2 of 0.94 on the sea surface wave significant height parameter (Hs) (Castelle et al., 2020). Output parameters used in this study include Hs and wave direction, from July 2018 to November 2020.

Figure 54b and c present the wave significant height and period respectively in Etretat, as used in the present study. During the period 2018 – 2020, the average Hs was 0.88 m with a maximum of 4.44 m, and the average peak period was 7.0 s with a maximum of 18.2 s. Both parameters show a seasonality with higher values during winter (October to April) and lower values during summer (April to October). Energetic events take place mainly during winter seasons including Storm Ciara recorded on 10th of February 2020, when waves reached 4.44 m in height.

Wave roses presented in Figure 54e and f show that there are two main incoming wave directions: West and North. During winter, 71.6 % of waves are coming from the Western sector (250°N - 310°N), and especially 50.0 % come from directions ranging between 270°N and 290°N, with a maximum height of 4.44 m. The Northern sector (0°N - 30°N) hosts 14.0 % of the waves with a maximum wave height of 2.76 m. On the other hand, summer waves are coming from the Western sector 59.6 % of the time, 49.3% of the waves being concentrated between directions 270°N to 290°N, with a maximum wave height of 3.30 m. The Northern sector hosts 26.1 % of the waves with a maximum height of 3.16 m.

For each site, wave characteristics were used to calculate the energy flux EF.

$$EF = E \times C_g$$

Where EF is the total wave energy determined using $E = \frac{1}{8} \times \rho \times g \times {H_S}^2$, and C_g is the wave group velocity given by $C_g = \frac{c}{2}\left(1 + \frac{2kh}{\sin(2kh)}\right)$, h is the water depth, k is the wave number $k = \frac{2\pi}{L}$, L is the wavelength, and c is the wave celerity in transitional water $c = \frac{gT}{2\pi}\tanh(kh)$, g is the acceleration of gravity of 9.81 m/s, and T is the wave period.

This allows us to project EF along the cross-shore and longshore local axis of the beach:

$$EF_C = EF \times \cos(\alpha)$$

$$EF_L = EF \times \sin(\alpha)$$

Where EF_C and EF_L represent the cross-shore and the longshore projections respectively, and α is the angle between the incoming waves and the beach orientation.

2.2.2.Shoreline Variability

On both sites, the morphological variability of the beach was evaluated through the analysis of three morphological indices: the beach width (BW), the beach slope (BS) and the beach orientation angle (BOA). These indices were extracted from our VMS-derived point clouds datasets.

BW is obtained by measuring the cross-shore distance separating waterlines to a predefined baseline along cross-shore transects (Figure 55). In total, the beaches are segmented into 211 and 114 transects for Etretat and Hautot-sur-Mer, respectively. Each transect starts from a perpendicular baseline located along the beach's seawall where it is separated by 2 m from its neighbors. Transects are all 100 m long while heading towards the sea and do not cross each other. BW is the horizontal distance separating the baseline to a point of fixed elevation along each transect. Target elevations range from -2 m to +3 m in Etretat (0 m being the local mean water level), and from +1 m to +3 m in Hautot-sur-Mer, and are vertically separated by 1 m. When no waterline was recorded at the exact target elevation, an interpolated value between the neighbor waterlines was used. Elevation limits indicated below were constrained by data availability throughout the tidal cycle. The lower number of elevations in Hautot-sur-Mer is due to the difficulty of identifying a clearly contrasted shoreline on the lower part of the composite system ($z < +1$ m).

BS was computed as the slope $\frac{\Delta z}{\Delta x}$ along each transect, and between neighboring target elevation.

BOA is calculated by approximating the shoreline to a parabola. The orientation angle is then calculated as the angle between the seawall and the parabola's tangent of a selected transect. On both sites, the transects located at the center between two groins were chosen to compute the BOA: P050 in Etretat and P075 in Hautot-sur-Mer.

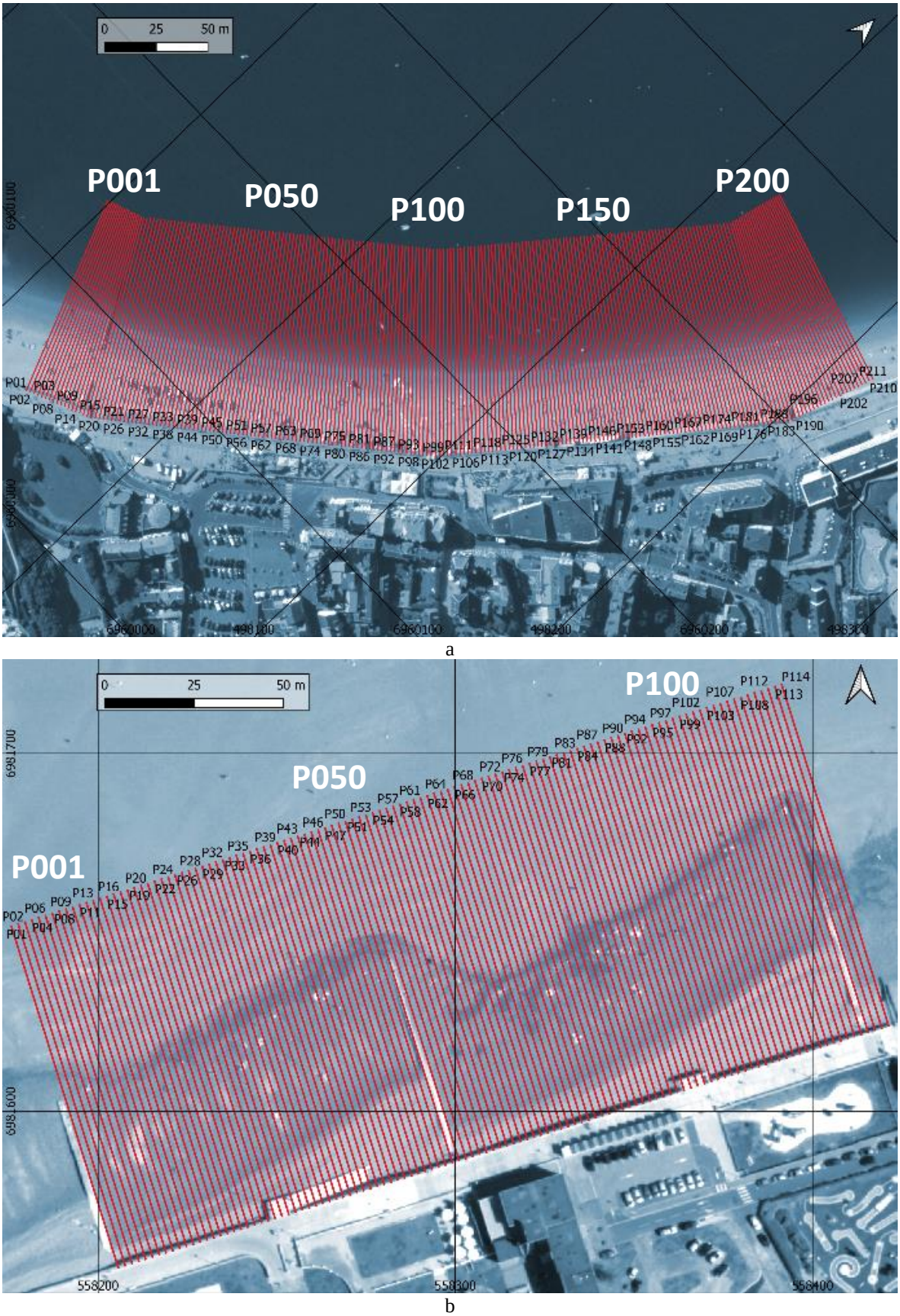

Figure 55 - Cross-shore transects used for discretizing the shoreline position along the beach of Etretat (a) and Hautot-sur-Mer (b).

For all parameters, values were averaged at a daily time scale, and gaps were filled with linearly interpolated ones. On both sites a malfunction disabled the right-side camera in November

2019 in Etretat and in June 2020 in Hautot-sur-Mer. Consequently, the lateral extension of the beach being monitored changed through time. Thus, our analysis will focus only on the profiles that remained in the left and center camera frames in Etretat, i.e., transects from P20 to P114 (from July 2018 to June 2020), and only take into account the dates at which the right camera was still working in Hautot-sur-Mer, i.e., from December 2018 to June 2020 (with transects from P20 to P99), in order to maximize both the duration and beach lateral extension being analyzed.

This approach allows the study of one beach cell bounded with two groins on the sides and the sea wall at the back for the two sites, which is here considered a local morphological unit whose evolution remains a good approximate to the one of the larger scale coastal system. In Hautot-sur-Mer, the available data covers the halves of two different boxes siding the groin located at P50 instead of a full one. Assuming that morphodynamics can be considered consistent from one box to its direct neighbors as long as they remain similar in size, shape, composition and orientation, it is assumed that results are representative of a full unit. The studied beach cell length is 188 m long in Etretat and are 100 and 140 m long in Hautot-sur-Mer for both the West and the East cells, respectively.

2.2.3.Grain size mapping

The spatial variability of the sediment size was measured using the methodology developed by Soloy et al. (2020). Ortho-images were produced using Structure from Motion (SfM) techniques applied on UAV data (Westoby et al., 2012). The UAV measurement campaigns took place on 2020/06/10 in Etretat, and on 2019/04/09, 2019/06/04 and 2020/06/09 in Hautot-sur-Mer. The maps used for this study were produced by averaging the sediment long axis size using a grid of resolution 1 m x 1 m.

2.3. Results and discussions

2.3.1.Morphological Changes in shoreline position

The spatial and temporal variability of the shoreline position of Etretat and Hautot-sur-Mer beaches was investigated using 2 years of daily observations. The shoreline position at elevations ranging -2 m to +3 m (1 m step) from mid-2018 to late 2020 in Etretat, and at elevations +1 m to +3 m from early 2019 to mid-2020 in Hautot-sur-Mer, are presented in Figure 56a and b, respectively. Time series of the average BW at each elevation are shown in Figure 56c and d, as well as the average planform shape of the shoreline in Figure 56e and f.

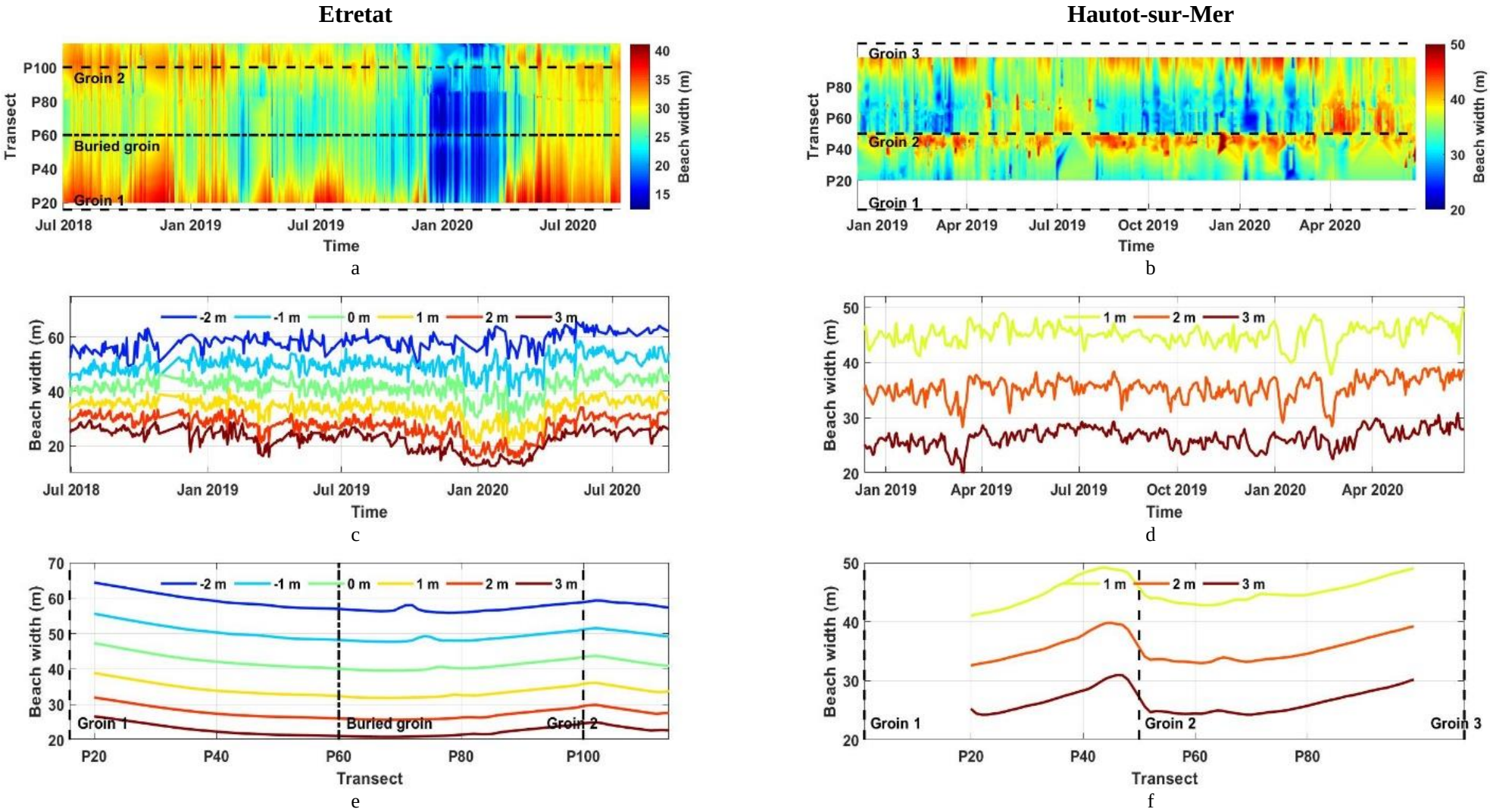

Figure 56 - Planform evolution of the +2 m elevation shoreline position in Etretat (a) and Hautot-sur-Mer (b), from July 2018 to November 2020. Time series of average beach width between elevations -2 m and +3 m in Etretat (c), and from +1 and +3 m in Hautot-sur-Mer (d), with 1 m of span. Average planform shape of the shoreline at the same elevations in Etretat (e) and Hautot-sur-Mer (f). The position of groin structures is indicated with black dashed lines.

As a first observation, the shorelines' planform shapes visible on Figure 56a, b, e, and f differ from one site to the other. In Etretat, the shoreline adopts the shape of a parabola with a center part being closer to the seawall than both of its ends near Groins 1 and 2. The shape is more linear in Hautot-sur-Mer where the right side of a cell (left side of groins) is on average farther from the seawall than the left one (right side of groins). Regarding cross-shore slopes, Figure 56e shows the increasing slope with elevation, from around 0.14 between -2 m and -1 m, to 0.25 between +2 and +3 m. The small bump visible at each elevation on a diagonal from P70 at -2 m to P80 at +3 m corresponds to a small discrepancy in camera alignments that is also visible on Figure 56a. In Hautot-sur-Mer (Figure 56f), the average slope is 0.10 between +1 m and +2 m, and 0.12 between +2 m and +3 m. Although the smaller number of elevations does not allow for the lower profile to be evaluated here, a slope of 0.013 was measured on the sandy substrate by Soloy et al. (2020).

On Figure 56a and b, the succession of reddish and blueish colors corresponds to a series of advance and retreat movements. Changes are differently manifested along the beach, especially in Hautot-sur-Mer where the wide side changes from west to east through time. This variation is likely associated with a beach planform rotation around a pivotal point generated by the wave diffraction near the groins and its obliquity responsible for a longshore transport. Figure 56b suggests a seasonality in the rotation mechanism with an alternance between two main beach orientations: (1) a wider side to the left of the beach cell (beach facing NE) from April to August, and (2) a wider side to the right (beach facing NW) throughout the rest of the year.

In Etretat, the time series of average BW Figure 56c do not show any clear seasonal pattern. The +3 m beach width consistently retreats from 30 m in July 2018 to 20 m in December 2019. It then suddenly reaches its low around 12 m where it remains from December to April 2020 before advancing to 30 m again by April – May, where it remained until the end of the time series. The period of retreated shoreline observed from December to April 2020 corresponds to a cluster of severe winter storms. During this cluster of storms, an old groin that is usually covered by sediment emerged around P60 in Etretat (Figure 56 and Figure 56Figure 57), thanks to erosion, and the top of the beach even became sandy for a few weeks. At the bottom of the beach, the -2 m beach width consistently remained around 60 m, with no significant change during winter 2020, but advancing towards 63 m on average at the end of the storm period.

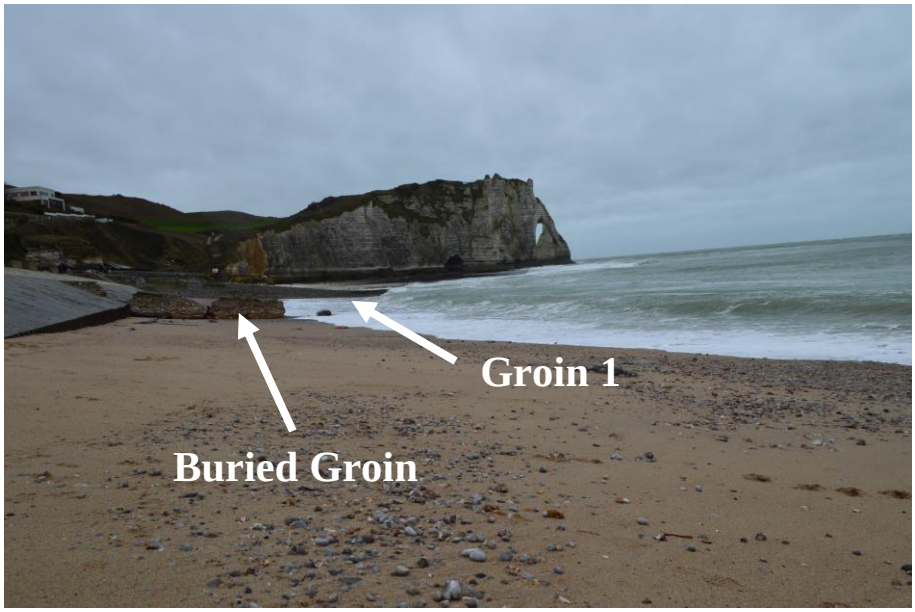

a

b

Figure 57 – Sand covering the beach in Etretat, normally covered with gravel (2020/02/16). An old rocky and usually buried groin is visible on a, as well as old wooden groin poles on b.

In Hautot-sur-Mer, a subtle seasonality pattern is visible in the time series of beach width with values evolving from 25 m in December to 30 m in July, at +3 m of elevation and from 33 to 38 m at 0 m at the same dates. The amplitude of daily changes also evolves with 2 to 3 m on average during summer seasons up to 7 to 8 m during winter ones. However, the early 2020 cluster of storm events in Hautot-sur-Mer did not provoke a period of minimum beach width as was observed in Etretat, although large variations are visible during this period.

Despite their proximity, both sites present significant morphodynamical differences. The difference in shoreline planform shapes is first explained by the difference in openness between both coastlines: embayed/enclosed beaches like Etretat naturally adopt a concave shape while open beaches are more linear at a large scale. At the scale of the beach cell, groin structures also play a role in the shoreline shape by accumulating the alongshore-drifted sediment on one side while creating a deficit

on the other side. The effect of groins on the shoreline planform shape was modeled by Leont'yev (2018, 2007), who showed that the planform shape consecutive to the presence of groins can be summarized as a linear function describing the accumulative side of the groin, and as a sinusoid for the erosive one. The extent of the groin's influence zone depends on both groin characteristics (size, elevation, spacing, etc.) and the longshore sediment flux characteristics (i.e., sediment "discharge", flux "channel size", etc.). The author explains that if the distance between groins is lower than the extent of the groin's influence on one of its sides given a certain sediment flux, the erosive side of a groin will interact with the accumulative side of its neighbor. This interaction limits the development of a sinusoid pattern, resulting on a more linear shoreline such as what can be observed in Hautot-sur-Mer. The average left-facing planform shoreline orientation also suggests an asymmetric longshore drift in a West to East direction, which is confirmed by the observations of Costa et al. (2015). The location of Etretat near the Cape of Antifer - where the sediment alongshore drift asymmetry is lower (Costa et al., 2015) - allows the average planform shoreline between groins to be more parabolic, thanks to the more even permutations between accumulative and erosive sides of groins (Leont'yev, 2018).

Etretat seems to be more sensitive to the impact of storms than Hautot-sur-Mer, and especially clustered ones. The influence of storm clustering on the eroded sediment volume was shown by Karunarathna et al. (2014) to be largely higher than the influence of the sum of each individual storms on sandy beaches. Assuming that the same phenomenon happens with coarser sediment, it could explain the observed retreat in Etretat. The reason why Hautot-sur-Mer does not experience the same retreat is probably due to the protection offered by the dissipative low tide terrace. Indeed, Almeida et al. (2014) were able to compare the offshore significant wave height to the onshore one on different types of beaches and showed that storm wave height was reduced by a factor of 2 to 2.5 on composite beaches due to the low tide terrace dissipative effect, while wave height was not reduced and even be slightly increased on purely gravel beaches.

The transition from gravel to sand by erosion in Etretat during the storm period changed the properties of the fabric exposed to the waves, likely lowering its permeability (Krumbein and Monk, 1943) while still offering a reflective profile to incoming waves, although more gently slopped. Hay et al. (2014) reported similar observations on a mixed sand gravel beach of Canada, with a decrease in surficial sediment median diameter when the wave energy was increasing. The consecutive relative stability of the +2 m and +3 m beach width at this period while lower elevations present a higher variability is a phenomenon observed by Karunarathna et al. (2012), who explained that composite beaches may become unstable during storms due to the cutback of the upper beach during a previous storm. Although Etretat's beach is considered purely gravel, this transition from gravel to sand makes it somewhat comparable to a composite one. Our hypothesis is that the gravel sediment eroded from the top of the beach was deposited at the subtidal bottom, unmonitored, thus building the beach step

and providing a focus point to stabilize the runup extent and the swash to lower elevations, thus protecting the upper beach, as already evidenced on a gravel beach by Poate et al. (2013).

2.3.2.Principal components of variability

EOF were calculated using time series of average beach width at the various selected elevations with the aim of extracting principal components (PC) of morphological variability to characterize the beaches' spatiotemporal morphodynamics. Each PC describes a percentage of the shoreline's total variability in space and time between -2 m and +3 m in Etretat (Figure 58), and from +1 m to +3 m in Hautot-sur-Mer (Figure 59). Linear correlation coefficients were then calculated between different components and morphological parameters (BW, BS, BOA and PCs), and with hydrodynamical ones (wave energy, current velocity, and tidal range). The result correlation matrices are presented in Figure 60. In all cases, the significance threshold is set to 0.5 which was selected as the conventional value for rejection of the null hypothesis (absence of correlation). Figure 61 presents a conceptual model, which describes how each PC is related to one or several mechanisms, and to which spatial extent.

Table 7 presents the percentage of the total variability explained by each PC. Results show that up to six PCs are necessary to explain at least 90% of the total variability of Etretat's shoreline position. In Hautot-Mer, the number of PCs required to reach the same threshold is 14, thus showing higher complexity. Therefore, the threshold of cumulated explained variability was lowered to 80% for this site, although it still includes up to 7 PCs. However, PC6 in Etretat and PC5 to 7 in Hautot-sur-Mer are considered residual in further discussion as their behavior is erratic and their relative variability remains low. For both sites, the first PC explains around half of the total variability, with 62.4% in Etretat and 46.1% in Hautot-sur-Mer. Further PCs account for significantly lower amounts, although similar from site to site.

Table 7 - Percentage of the total variability explained by the EOF components in Etretat and Hautot-sur-Mer.

Site	Principal Components							Total
	1	2	3	4	5	6	7	
Etretat	62.4	14.1	5.8	3.9	2.3	2.0		90.5
Hautot-sur-Mer	46.1	14.8	7.0	4.3	3.4	3.2	2.4	81.2

Figure 58 presents the results of the EOF in Etretat. Both spatial ($E_k(x) \times E_k(y)$) and temporal ($C_k(t)$) eigenfunctions are presented at the top and at the bottom of each PC's subfigure, respectively. Elevations are displayed on an inversed axis to make the figure's top correspond to the sea side, while the bottom is the land side. Dashed black lines locate the position of groin structures, and the black line represents the stability line (i.e., line of zero variability). The red line on figures of $C_k(t)$ is the equivalent stability through time.

2.3.2.1. Etretat

2.3.2.1.1. PC 1 – Cross-shore translation

On Figure 58a, $E_1(x) \times E_1(y)$ shows consistent positive values with no crossing of the stability line, which indicates that the entire region moves all together in the same direction, either seaward or landward. The magnitude of variability is larger towards the high elevation left side than the low right side. Therefore, PC1 depicts a cross-shore translation mechanism, with an alternation between advances and retreats. McCarroll et al. (2019) observed that cross-shore mechanisms tend to become significant on embayed beaches longer than 1 km, which agrees with our observation. However, the subtle longshore gradient indicating slightly larger magnitudes on the left side than the right one suggests that the observed translation could be a related to a rotation mechanism at the scale of the entire beach. A small drop is visible around the buried groin at the highest elevations, which tends to show the structure's influence on the cross-shore variability.

Although $C_1(t)$ does not show a specific seasonal variability, it resembles the time series of BW (Figure 56c), including a period of significantly lower values between December 2019 and April 2020, which corresponds to the storm period mentioned in Section 2.3.1. Positive values correspond to advanced shoreline positions while negative ones reflect a retreated state.

PC1 is primarily correlated to BW with values ranging from 0.72 to 0.96 (Figure 58a), and to a lower extent is also correlated to BOA with values from 0.52 to 0.56 (except for elevation -2 m with r = 0.38 and 0.36, respectively). The link observed between PC1 and BOA remains difficult to explain with our data alone, although it could be the manifestation of an alongshore gradient in the cross-shore wave energy such as the one observed by Harley et al. (2015) on a sandy beach.

Regarding hydrodynamics (Figure 58c), none of Etretat's PCs is significantly correlated to any of the considered parameters at the 0.5 threshold. It is generally accepted that hydrodynamics alone are not enough information to the shoreline position change of gravel systems, and that the spatial dispersion of gravel sizes and shapes and their temporal variability are necessary to be considered (Buscombe and Masselink, 2006), therefore low correlation values between hydro- and morphodynamical parameters is not surprising.

2.3.2.1.2. PC 2 – Rollover

Figure 58b presents PC2, which describes an alternation between states of advanced shorelines at low elevations while high elevations shorelines are retreated, and the opposite. This would correspond to a mechanism of beach rollover (Buscombe and Masselink, 2006) affecting the beach slope, whose axis of rotation would be located around elevations 0 m and +1 m, according to the alongshore-extended stability line's location on the $E_2(x) \times E_2(y)$ subfigure. To the authors' knowledge, it is the first time that a rollover mechanism is identified using an EOF analysis applied on a shoreline position dataset, although this process is important especially for gravel beaches (Austin

and Masselink, 2006a; Buscombe and Masselink, 2006), and was often described in the literature (e.g. Isla and Bujalesky (2000); Odezulu et al. (2018); Talavera et al. (2018)).

$C_2(t)$ shows a negative trend that could be interpreted as a decreasing tendency of the beach slope throughout the two years of monitoring. Positive values translate a steep slope and negative values correspond to a gentle slope. Buscombe and Masselink (2006) described the rollover process as a response to storms, which seems to be the case on $C_2(t)$, for instance with the storm of January 2020 that significantly lowered the slope. But $C_2(t)$ variability appears to be more complex, especially considering the negative trend, and it is likely that other factors might be responsible for a significant part of it such as climate parameters (e.g. Sea Level Pressure, see Montaño et al., 2020), intrinsic characteristics (e.g. granulometry, permeability, etc.), or larger scale mechanisms (e.g. global rotation).

Regarding correlations to morphological parameters, PC2 is expectedly well correlated to BS (r = 0.82). However, it also shows significant correlations with BW at -1 m and -2 m (r = 0.6 and 0.83, respectively), while these elevations were the ones presenting the lowest correlations between BW and PC1. This observation shows that the lower the elevation, the lesser the response of the shoreline to cross-shore translation processes, and the larger its link with rollover processes.

2.3.2.1.3. PC 3 – Breathing

Figure 58c presents PC3, a breathing mechanism, first described by Ratliff and Murray (2014), and defined as "changes in shoreline curvature as [sediment] move from the middle of the [beach cell] to the edges, and back". Indeed, $E_3(x) \times E_3(y)$ draws two stability lines developed in the alongshore direction and separating the site into 3 alongshore extended regions: high (z > +1 m), intermediate (-1 < z < +1 m), and low elevations (z < -1 m). When both high and low elevations' shorelines are retreated, intermediate ones are advanced, and vice versa. The "eye" shape of this pattern tends to show that the lowest stability line could be extended further to the left towards elevations lower than -2 m, although not monitored here.

Interestingly, PC3 shows a cross-shore curvature simultaneous to the longshore one, but with an even higher magnitude of variability. To the authors' knowledge, this type of cross-shore component in a breathing mechanism was not yet described in the literature. This shows that sediment mostly moves along the cross-shore direction, from low and high elevations towards intermediate ones (i.e., around the mean sea level) and back.

Regarding $C_3(t)$, positive values of correspond to a "deflated" state (i.e., concave cross-shore profile), negative values represent an "inflated" state. The time series presents a seasonal dynamic with on average deflated states during winter and inflated ones during summer. The daily variability is also higher during the winter season. Similar variability was observed in breathing mechanisms by Ratliff and Murray (2014) and Robinet et al. (2020) on embayed beaches, and by Blossier et al. (2017)

on a barline. Concerning correlations, $C_3(t)$ presents no significant correlation with any of the tested parameters.

2.3.2.1.4. PC 4 – Large scale rotation

PC4 shown in Figure 58d is the first mainly longshore mechanism. It is evidenced by the presence of a cross-shore oriented stability line separating two compartments on $E_4(x) \times E_4(y)$, the left one of which is retreated when the right one is advanced, and vice versa. This can be understood as a mechanism of rotation, which generally takes place around a pivotal point and defines retreat movements at one end and advance ones at the other end. The pivotal point was defined by Short et al. (2000) as the point of minimal variability along the beach which here corresponds to the stability line. On present results, the stability line is formed by the succession of pivotal points forms at different elevations.

The stability line starts from P90 at the top of the beach (+3 m) and goes towards the left to P50 at 0 m, and then goes back towards the right to P80 at -2 m, although one would expect it to be vertical. The change in direction of the stability line at elevation 0 m highlights the existence of a symmetrical process centered on 0 m, with a wider variability at the lowest elevations. These observations indicate that this specific rotation mechanism is likely related to the effect of tides. Indeed, Masselink and Short (1993) showed that tides shift horizontally and vertically the position where processes such as shoaling, surf and swash happen and dissipate the wave energy. Moreover, authors explain that the relative amount of time that the profile is impacted by each process also depends on the tidal range and phasis: Swash has two maximums at both turns of tides. Hence the lowest and highest regions being more variable than the center one. In addition, the oblique stability line could be the result of a change in relative the relative influence of the longshore projection of the swash, due to the same effect. The position of groins does not seem related to any pattern on $E_4(x) \times E_4(y)$, the rotation mechanism described by PC4 thus probably describes a mechanism of larger spatial scale than one of the beach cell.

Regarding $C_4(t)$, positive values along $C_4(t)$ correspond to a clockwise orientation, negative ones reflect a counterclockwise orientation. The variability is higher during the winter season although there is no clear seasonal pattern: the beach was on average oriented towards opposite directions between January and July of 2019 than between the same period of 2020. In terms of correlations, PC4 is only corelated to BOA at -2 m and -1 m (r = 0.54 and 0.52, respectively), correlation values then decrease with the elevation, under the significance threshold of 0.5, which confirms our previous observations.

2.3.2.1.5. PC 5 – Beach cell rotation

PC5, Figure 58e, represents another longshore mechanism of rotation, this time influenced by the presence of groin structures. Indeed, the left beach cell - bounded by Groins 1 and 2 - is divided

into mainly two lateral compartments, the left one of which follows the dynamics of the area located on the right side of Groin 2 (i.e., the left side of the unmonitored beach cell at the right extremity).

The stability line adopts the same shape as the one of PC4, except that instead of connecting both cross-shore sides, it connects between the two beach cells and forms a thin string of warmer colors at elevation -1 m. This string translates the presence of a local change in the slope at the lowest elevations provoked by a difference of cross-shore translation rates between elevations -1 m and -2 m. This phenomenon is thought to be the result of sediment by passing Groin 2, which is rarely exposed to water under 0 m, contrary to Groin 1. In addition, the stability line follows the direction of Groin 2, which once more highlights the influence of groins on the sediment dynamics. Similar observations on a beach of North Carolina, USA were made by Miller and Dean (2007).

Considering the temporal evolution, $C_5(t)$ present a periodic variability with cycles from a few weeks up to 3 months, that do not correspond to the ones of the larger scale rotation $C_4(t)$. Positive values correspond to a clockwise orientation, while negative ones are relative to a counterclockwise orientation. $C_5(t)$ is correlated with BOA at +1 m, +2 m and +3 m which is the opposite of PC4 and confirms that rotation is affected by the presence of groin structures, hence the need for 2 modes to describe this mechanism while including or excluding groins.

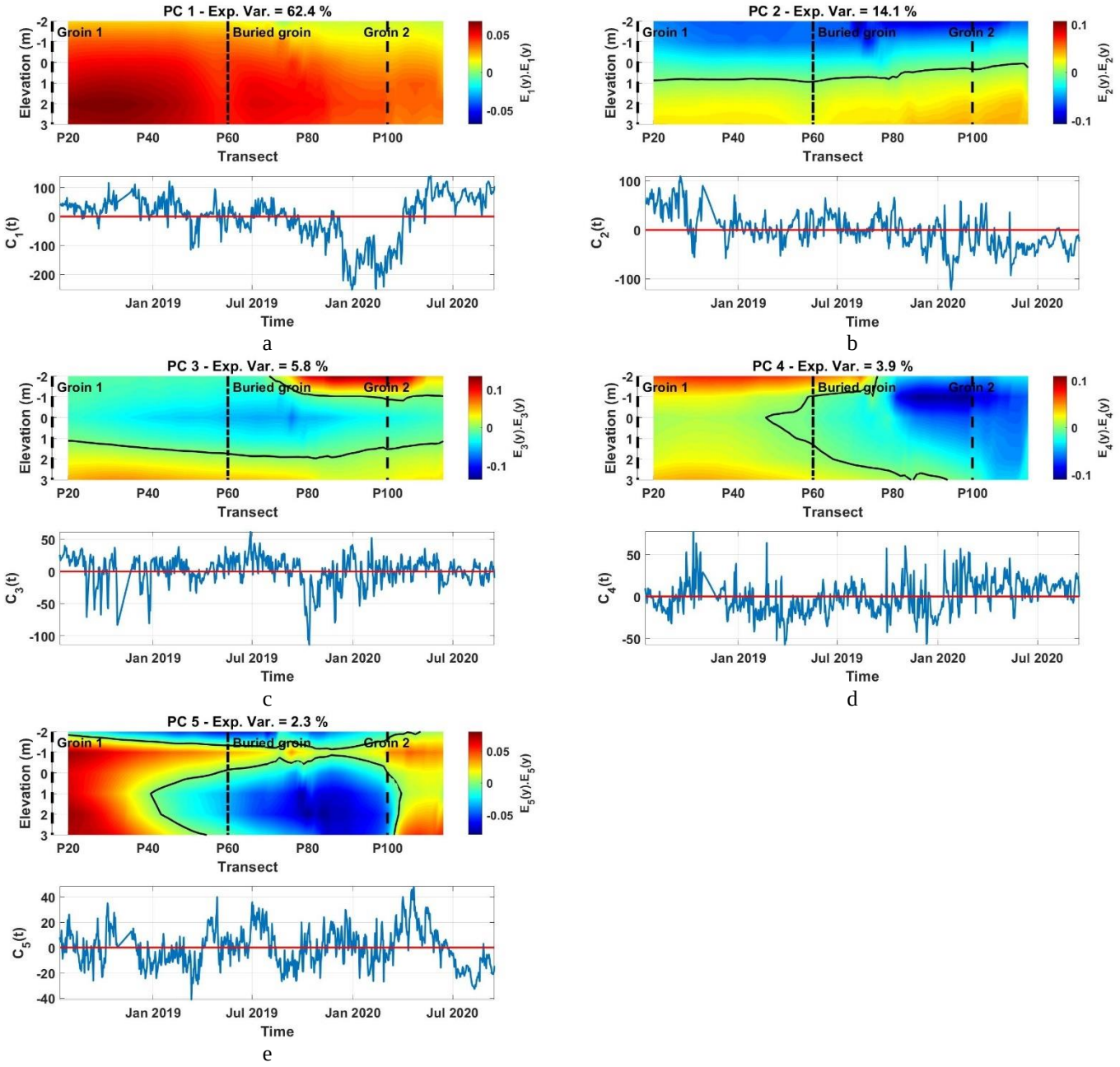

Figure 58 - Results of the EOF analysis applied to Etretat's shoreline position from elevations -2 m to +3 m. Principal Components 1 to 5 are presented in frames a to e, respectively. Top surface plots are presenting the spatial eigenfunction $E_k(x) \times E_k(y)$, the Y axis was inversed so the sea side is towards the figure's top and the land side is towards the bottom. Groin structures were marked with black dashed lines, and the contour of zero variability (i.e. stability line) was drawn as a solid black line. Bottom time series show the temporal eigenfunction $C_k(t)$ associated with each component, the red line highlights the minimum of variability.

2.3.2.2. Hautot-sur-Mer

2.3.2.2.1. PC 1 – Right-centered beach cell rotation

Figure 59 presents the results of the previous methodology applied to Hautot-sur-Mer. $E_1(x) \times E_1(y)$, displayed in Figure 59a, opposes both left and right sides of the beach cells with a quasi-vertical stability line located towards the right and a maximum of variability to the left. PC1 is therefore characterizing a longshore rotation mechanism with a stability/pivot line located around transects P90 and P30 for the right and left beach cells, respectively. Another cross-shore oriented

stability line can be seen at the position of Groin 2, which shows that this rotation mechanism is limited to the beach cell spatial scale.

$C_1(t)$ shows a very clear seasonality pattern with negative values from April to September, and positive ones from September to April, following a near binary evolution with values averaging either +50 or -50, and rarely others. This situation translates the presence of two main stable shoreline orientations: counterclockwise when $C_1(t)$ values are negative, and clockwise when they are positive, while most states in between seem to be transitory.

Regarding correlations (Figure 60), PC1 shows high correlations with both BW and BOA, the first of which increases with elevation (r = 0.72, 0.83 and 0.87 for +1 m, +2 m, and +3 m, respectively) when the second decreases (r = 0.88, 0.86 and 0.84 for +1 m, +2 m, and +3 m, respectively). The reason for such high correlation values with BW being related to a beach rotation mode is the unbalance in size and relative variability between both sides of the cell. With a higher magnitude of variability to the left and a wider region where this variability applies, losses in the left side are not fully compensated by right side's gains, resulting in a rotation-induced cross-shore translation: an overall advance/retreat that will be simultaneous to the rotation event (Figure 61).

When compared with morphodynamics, BW is the only parameter to show any significant correlation, with r = 0.53 and 0.5 for elevations +3 m and +2 m, respectively. Regarding hydrodynamics, correlation with the longshore wave energy (r = 0.45) and both the cross-shore and total wave energy (r = 0.39) remain relatively high compared with other parameters despite being bellow the significance threshold of 0.5. This tends to indicate that PC1 and more specifically its cross-shore translation aspect is likely linked to wave dissipation processes.

2.3.2.2.2. PC 2 – Left-centered beach cell rotation

$E_2(x) \times E_2(y)$ in Figure 59b exhibit a very similar spatial variability as PC1 although this time, the stability line present at +3 m and +2 m does not go all the way down to +1 m and stops when reaching the groin and is located towards the left of the beach cells with a maximum of variability to the right. We interpret PC2 as the expression of a second mode of beach cell rotation mechanism, less influential than PC1, especially acting at high elevations, and with a stability/pivotal line to the left around P70 and P20 for the right and left beach cells, respectively. At +1 m, the shoreline essentially migrates a cross-shore movement with higher magnitudes of variability towards the left of the beach cells.

In $C_2(t)$, positive values correspond to a clockwise orientation, and negative values represent a counterclockwise one. The time series does not present any remarkable pattern such as seasonality or opposed binary states similar to the ones observed with PC1. When calculating correlation values (Figure 60), PC2 does not show any significant relationship with the tested parameters.

2.3.2.2.3. PC 3 – Large scale rotation

$E_3(x) \times E_3(y)$ (Figure 59c) presents an opposition between the left and right sides of the monitored region, with a large near zero variability area around Groin 2, which is shown by the apparent chaotic behavior of the stability line, although it overall separates both left and right compartments. It therefore translates a third mode of rotation mechanism, at a larger spatial scale than the previous ones.

$C_3(t)$ does not seem to show any significant seasonality or opposed binary states either. Positive values refer to a counterclockwise orientation while negative ones are relative to a clockwise one. In terms of correlation, no significant link was found between PC3 and any of the tested parameters.

2.3.2.2.4. PC 4 – Rollover

PC4 presented in Figure 59d highlights a mainly cross-shore gradient of variability although the stability line shown on $E_4(x) \times E_4(y)$ is not straight. This means that PC4 encapsulates information about the slope and thus translates a mechanism of rollover, whose variability varies in the longshore direction, in this case within a center of rotation located at lower elevation near the groins and at higher elevation around the middle of the beach cell.

$C_4(t)$ shows a slight seasonal alternation of negative values (gentle/dissipative slope) between May and October (i.e., summer), and positive (steep/reflective slope) the rest of the time. However, the minimum (most gentle slope) is reached in January 2020, i.e., during the storm period. Regarding correlations, PC4 is significantly correlated with BS, which confirms our interpretation of this mode being a characterization of a rollover mechanism.

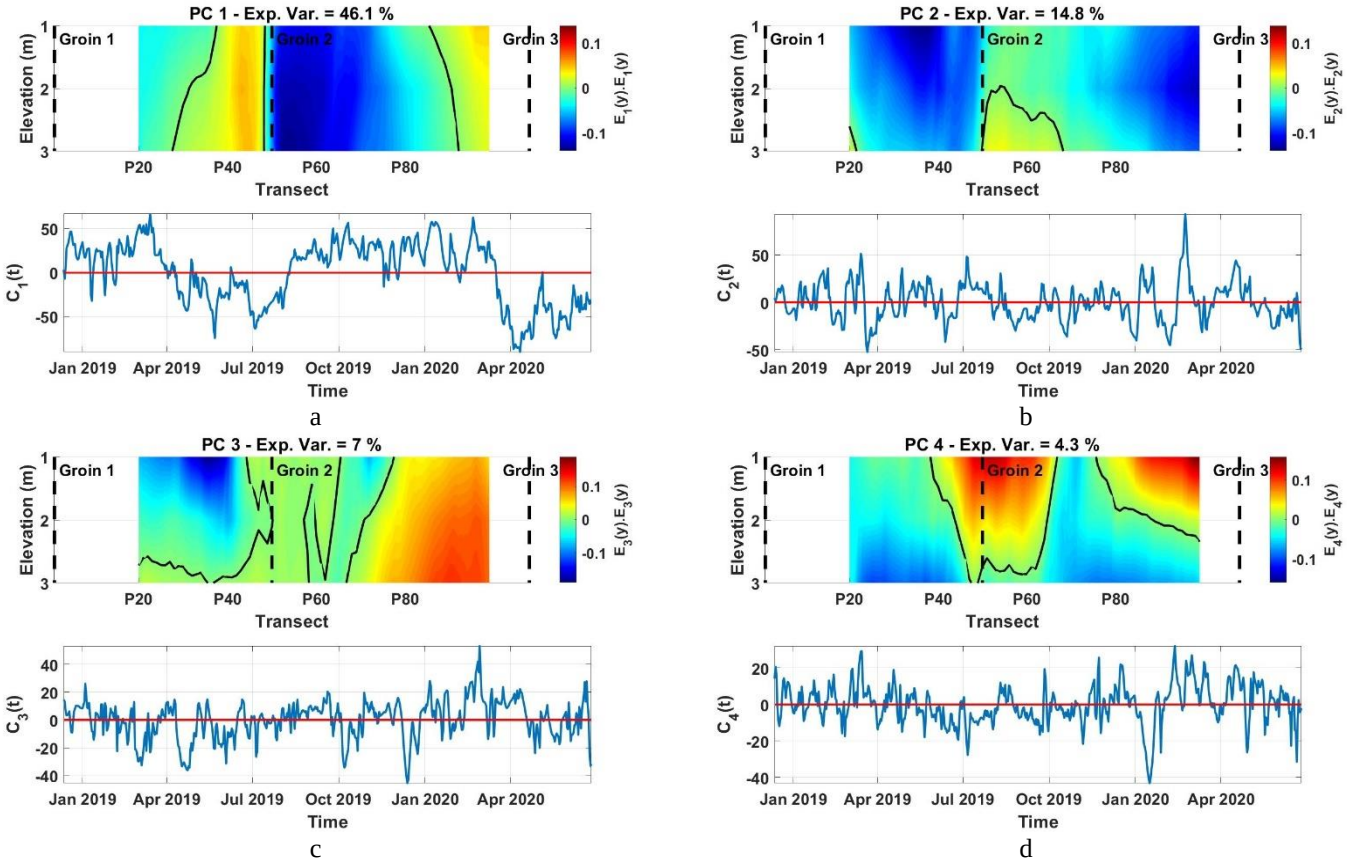

Figure 59 - Results of the EOF analysis applied to Hautot-sur-Mer's shoreline position from elevations +1 m to +3 m. Principal Components 1 to 4 are presented in frames a to d, respectively. Top surface plots are presenting the spatial eigenfunction $E_k(x) \times E_k(y)$, the Y axis was inversed so the sea side is towards the figure's top and the land side is towards the bottom. Groin structures were marked with black dashed lines, and the contour of zero variability (i.e. stability line) was drawn as a solid black line. Bottom time series show the temporal eigenfunction $C_k(t)$ associated with each component, the red line highlights the minimum of variability.

Etretat | Hautot-sur-Mer

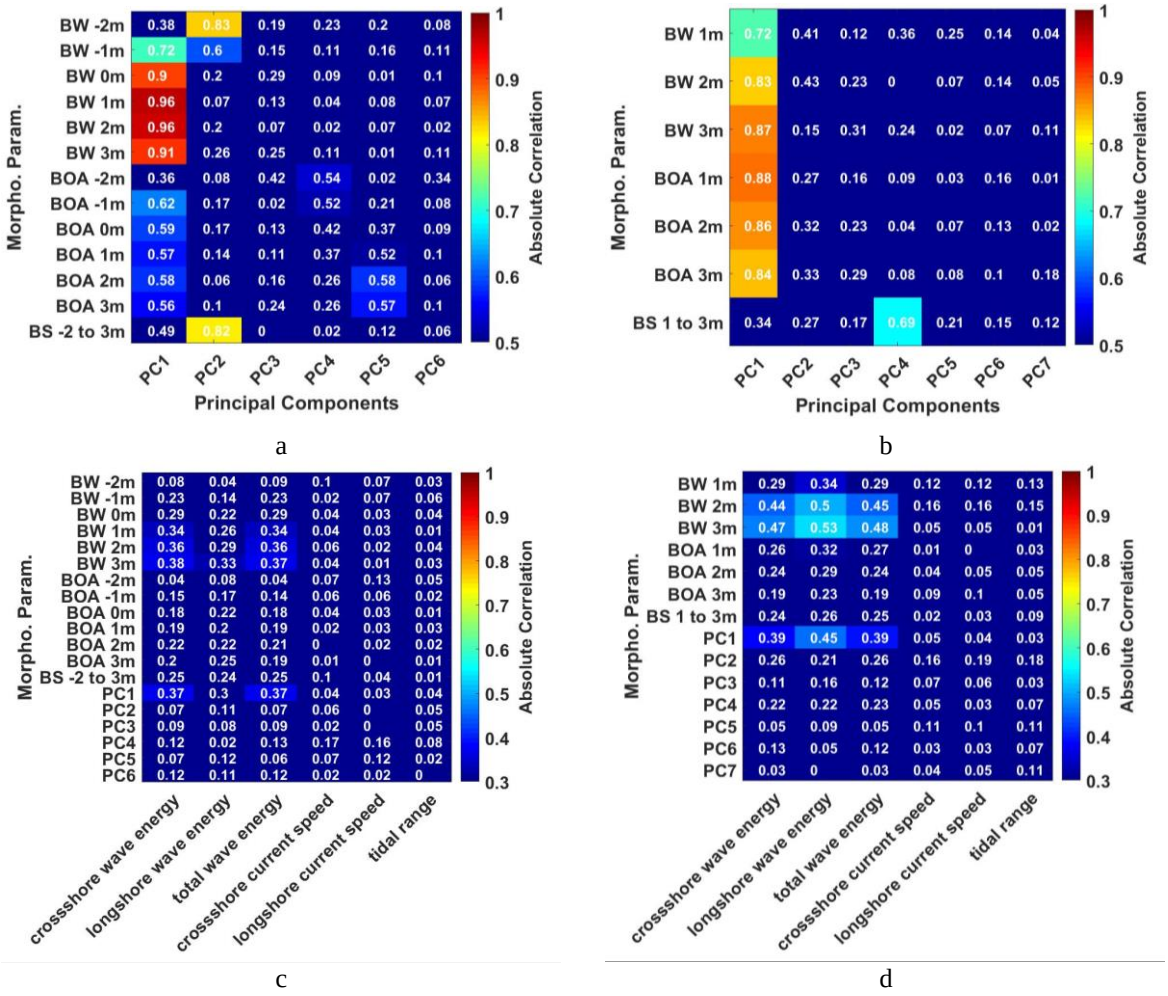

Figure 60 - Correlation matrix between morphodynamical parameters including beach width (BW), beach orientation angle (BOA) and beach slope (BS) and the temporal eigenfunction of the principal components (PC) resulting from the EOF analysis applied to Etretat's shoreline position from elevations -2 m to +3 m (a), and to Hautot-sur-Mer from elevations +1 m to +3 m (b). c and d present the same operation calculated with hydrodynamic parameters including wave energy, current velocity and tidal range.

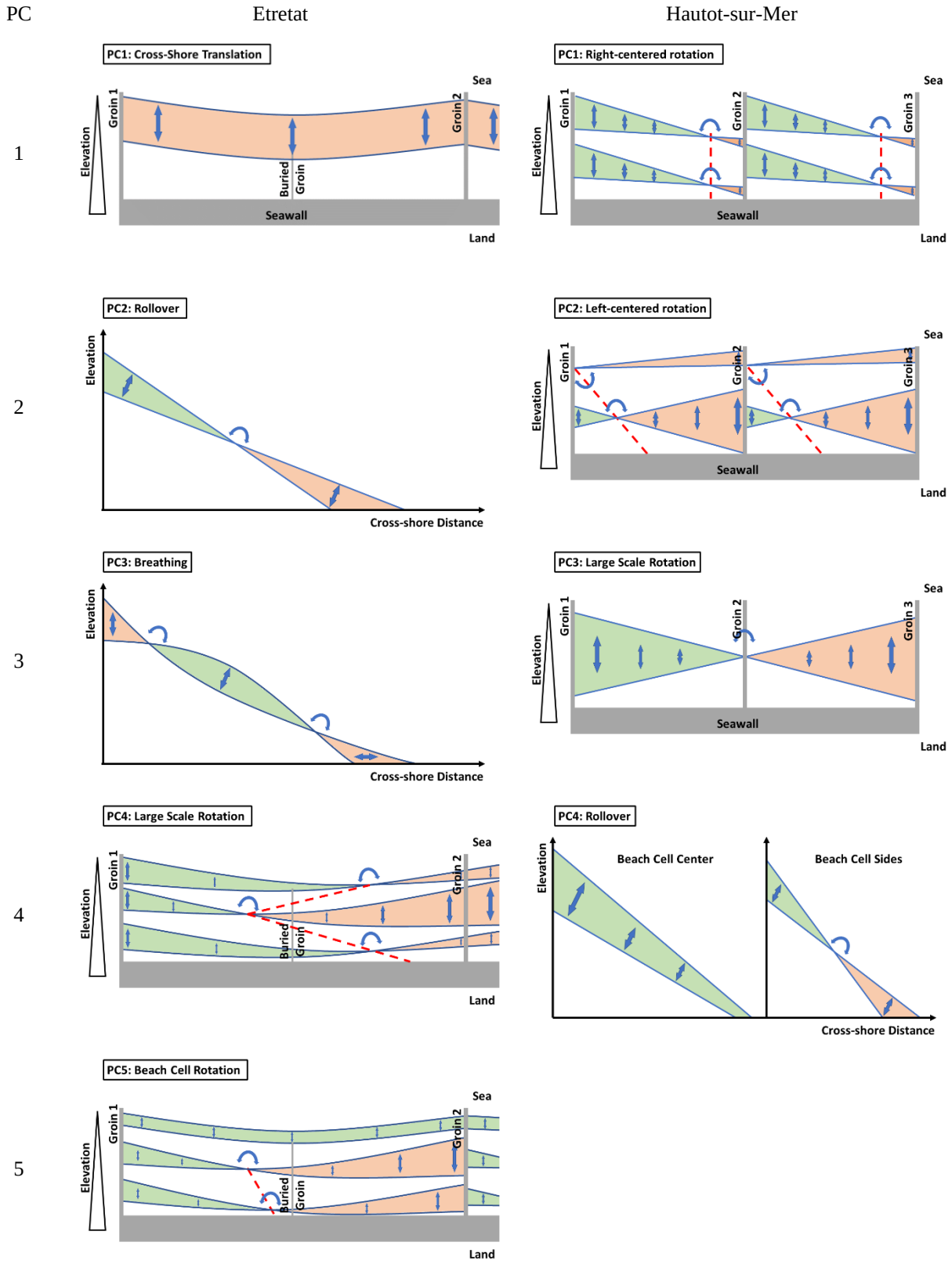

Figure 61 - Conceptual model of the isolated mechanisms of beach morphological variability in Etretat (left) and Hautot-sur-Mer (right), associated with their corresponding principal component (PC).

2.3.3.Periods of variability and morphological response to hydrodynamic conditions

The temporal variability of the different shoreline's morphological parameters (BW, BOA and BS) was assessed using a wavelet analysis. For each elevation, the wavelet power was temporally

averaged (GWS), thus highlighting the period(s) carrying the most variability (full spectrums are provided in the Appendices section, from Figure 72 to Figure 76). Due to the limited length of the time series, only shorter periods than approximately 6 months in Hautot-sur-Mer and 8 months in Etretat fell within the wavelet's cone of influence, which are therefore the longest periods to be analyzed. Results are presented in Figure 62a to f. For comparison, the same analysis was performed using time series of different hydrodynamic parameters including wave energy, current velocities, and tidal range (Figure 62e to j). Table 8 summarizes the main periods of variability identified on Figure 62.

For both sites, most of the variability is located towards the longest periods (6 to 8 months), regardless of the parameter or the elevation. Morphological variability is also depending on the elevation, especially for longer periods than 5 months (Figure 62). This corresponds to the observations made by multiple authors (Lemos et al., 2018; Reeve et al., 2007) although investigations are usually carried out over longer timeframes (typically decades using monthly measurements). Interestingly, the magnitude of BOA's variability in Etretat is not proportional to the absolute elevation but rather to the relative elevation compared to the mean sea level. This observation suggests that the amplitude of beach rotation is minimal towards z = 0 m and increases at both higher and lower elevations, which was not reported in the literature, to the authors' knowledge.

In Etretat, identified periods of morphological variability include 2, 3, 5 and 8+ months, all parameters and elevations considered (Figure 62, Table 8). In Hautot-sur-Mer, periods were identified at 2 and 6 months for all parameters, with an additional period at 3 months for BS alone. The observed periods correspond to medium-scales components of variability, which are usually related to seasonal or near-seasonal hydrodynamic processes (Loureiro and Ferreira, 2020). More specifically, the wave exposure and the occurrence of storms are often documented as the main process responsible for medium-term morphological changes (McCarroll et al., 2019; Ruiz de Alegria-Arzaburu and Masselink, 2010; Turki et al., 2013). Hydrodynamics' spectral patterns remain very similar from one site to the other. The wave energy spectrum presents two main periods at 2 and 8+ months in Etretat, and at 2 and 6 months in Hautot-sur-Mer. The tidal range spectrum shows two main periods at 1 month and 2 weeks, the latter also being the only period identified on the current velocity spectrum. These periods respectively correspond to the monthly lunar (Mm, T = 27.5 d) and the fortnightly lunar (Mf, T = 13.6 d) tidal components. Although tidal ranges play an essential role in distributing the wave energy along beach profiles (Masselink and Short, 1993), and tidal energy converted into currents is proportional to the tidal amplitude squared (Hammons, 1993), investigated tidal processes do not modulate a significant part of the beaches' morphodynamical variability for shorter periods than 6 to 8 months. Thus, the wave energy is the only parameter to show common periods of variability with morphodynamics, meaning that wave processes are in good part responsible for temporal changes of BW, BOA and BS signals. These results tend to agree with findings from Stark and Hay (2016), who showed that the bottom stress of tidal currents in a mega-tidal context was too low to significantly move single gravel.

These results provide insights into the possible processes responsible for the beach changes; These insights remain limited by availability in time and quality of data. Indeed, wave breaking and swash were specifically shown to be linked with morphological processes especially for gravel beaches (Guest and Hay, 2021) although their variability is expected to be more significant at longer time scales (Almeida et al., 2014; Buscombe and Masselink, 2006; Karunarathna et al., 2012; Poate et al., 2013; Ratliff and Murray, 2014).

Table 8 - Summary of the identified temporal periods of variability in morphological (yellow) and hydrodynamical (blue) signals in Etretat and Hautot-sur-Mer. Parameters include beach width (BW), beach orientation angle (BOA), beach slope (BS), wave energy (WE), current velocity (CS), and tidal range (TR).

Periods (months)	≤1	2	3	4	5	6	7	≥8	
BW		X	X		X			X	Etretat
BOA		X	X		X			X	
BS		X	X		X			X	
WE		X						X	
CV	X								
TR	X								
BW		x				X			Hautot-sur-Mer
BOA		X				X			
BS		X	X			X			
WE		X				X			
CV	X								
TR	X								

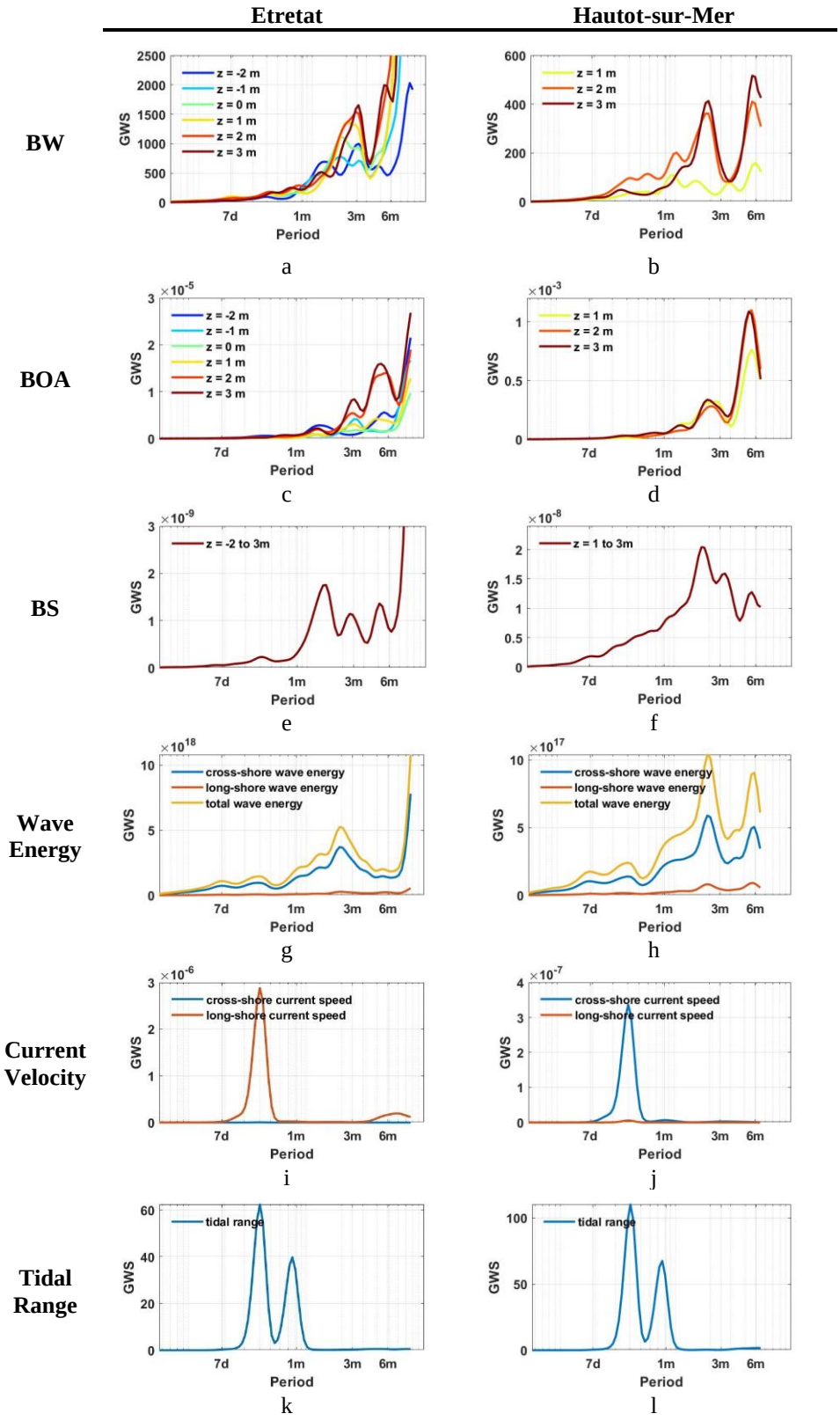

Figure 62 - Global Wavelet Spectrum (GWS) calculated from beach width (a, b), beach orientation angle (c, d), beach slope (e, f), wave energy (g, h), current velocity (i, j) and tidal range (k, l) time series in Etretat (left) and Hautot-sur-Mer (right).

2.3.4.Spatiotemporal variability of the surficial gravel size

Gravel beaches' ability to dissipate wave energy through infiltration was shown to be a function of the permeability associated with the local size distribution of the gravel fabric (McCall et al., 2012, 2015). Other studies reported results suggesting that the surface roughness is also and maybe

even more important than permeability as a controlling factor of the wave energy dissipation and reflection, and thus of the beaches' response to hydrodynamics (Jennings and Shulmeister, 2002; Mason et al., 1997; Powell, 1990). Moreover, at each instant the mobilizable gravels on a beach are expected to be the surficial ones, as they are the ones receiving most of the drag force due to waves while remaining relatively free to move, which can be summarized by the concept of entrainment threshold (Brayne et al., 2020; Lorang, 2000). Surficial gravels tend to get sorted by size and shape, thus forming a patchwork of so called clast assemblages, each of which corresponds to a "discrete population of gravel clasts which is characterized by textural unity" (Bluck, 1999). The presence of assemblages on the beach face highlights the spatial variability of surface roughness (Stark et al., 2014). Position, orientation, size, shape, and composition of assemblages are the result of antecedent conditions of sediment supply availability, and sediment sorting processes (Buscombe and Masselink, 2006). Their temporal variability could potentially be used as a proxy of surface sediment transport processes, as was demonstrated by Guest and Hay (2021) using remote sensing techniques applied on 14 days of high frequency video images, over a 2.7 m longshore span.

In this section, we aim to characterize some components of spatial and temporal variability of surficial grain size at the scale of the beach cell, and to associate them with morphodynamics given a relatively limited dataset composed of one map of mean grain size in Etretat (2020/06/10, Figure 63a) and three in Hautot-sur-Mer (2019/04/09, 2019/06/04 and 2020/06/09, Figure 63b, c and d, respectively). Importantly, although variability of gravel shapes is thought to play an important role in gravel system's dynamics (Buscombe and Masselink, 2006), shapes are not investigated in this study. In Table 9, the commonly used grain size values related to each campaign are presented (D16, D50, D84, mean size and std) along with other statistical factors.

2.3.4.1. Mean Grain Size

The mean grain size is lower in Etretat (5.6 cm ± 1.7) than Hautot-sur-Mer (7.2 cm ± 2.8 to 8.2 cm ± 2.9). Indeed, Etretat's pebbles are resupplied less often due to the lower erosion rate of its chalk cliffs (source of the flint supply), while being kept trapped on an embayed beach without the protection of dissipative low tide terrace like in Hautot-sur-Mer (Costa et al., 2015). Therefore, Etretat's pebble tend to shrink down through abrasion to a lower diameter that is more at the equilibrium with the local conditions of higher wave energy, lower longshore mobility and lower resupply fluxes (Bertoni et al., 2012).

In Hautot-sur-Mer, the mean sediment size varies between 8.2 cm ± 0.29 on 2019/04/09 and 7.2 cm ± 2.6, on 2019/06/04. This temporal variability corresponds to 32% change of volume in 2 months (considering spheres with a diameter equivalent to the averaged measured clast' surface). A temporal decrease in gravel size on beaches was documented by Bertoni et al. (2016), who measured an average weight loss of almost 20% after an 8- to 10-month period, and 60% after 13 months on 240 retrieved marked marble pebbles, at Pisa's beach, in Italy. Considering these results, 32% of volume

difference due to abrasion in only two spring months seems high, especially with flint material. Another explanation could be the occurrence of a local size sorting mechanism such as rotation (measured rotation of 5° clockwise between the two dates) and mixing. In addition, the occurrence of percolation through the oscillatory forcing of swash could have a segmentary effect by burying/uncovering selected size ranges of clasts ("Brazil Nut Effect" (BNE) and "Reverse BNE" (RBNE)(Nadler, 2012; Ulrich et al., 2007)).

2.3.4.2. Sedimentary patterns

On Figure 63, in general, the average clast length tends to increase from higher to lower elevations. Two main types of sedimentary patterns can be identified on the maps, namely clast assemblages and cusps, with spatial and temporal variabilities in the order of one to several centimeters. Assemblages are textural zonation that can be located anywhere on the beach face and extend in any direction, with a typical scale of several tens of meters. For example, a 50 m long assemblage (Average size > 10 cm, surrounding size < 8 cm) can be seen at the bottom of the beach face in Hautot-sur-Mer on 2020/06/09 (Figure 63d) and a similar one (Average size > 7 cm, surrounding size < 6 cm) at the northeast side of Etretat's beach cell (Figure 63a), one day later. Such patterns, located bellow the elevation of the last tide, were likely formed (at least partly) within hours to days, depending on the antecedent conditions of wave energy. Higher elevation patterns such as the accumulations at the top east corner of the beach cells of Hautot-sur-Mer are likely due to older events. Groin structures seem to attract larger thus clasts forming groin assemblages at various elevations, generally asymmetrically. Interestingly, assemblages in Hautot-sur-Mer are in general periodic from beach cell to beach cell, which suggests that their conditions of formation are influenced by the presence of groins, even at the beach cell's center. Enlarged versions of the maps presented in Figure 63 are available in the Appendices section from Figure 77 to Figure 80.

Gravel cusps are described by Buscombe and Masselink (2006) as quasi-periodic topographic oscillations of the shoreline provoked by swash flows, forming cross-shore extended horns with coarser clasts and bays with smaller ones. Although no cusp is observed in Etretat, they are present at every measured date in Hautot-sur-Mer with varying wavelengths and amplitude. Their presence and characteristics seem to be largely responsible for the quality of size sorting: the more developed the cusps, the poorer the sorting at the scale of the beach cell. However, despite being supposedly well correlated to the swash energy (Guest and Hay, 2019; Jennings and Shulmeister, 2002), our limited dataset doesn't allow to draw a strict relationship between the characteristics of cusps and simultaneous incoming waves.

The similarity in size sorting between both sites in June 2020 (hardly visible to no visible cusps, 50 m long assemblages at the bottom of the beach face) contrasts with the high temporal variability evidenced in Hautot-sur-Mer. It suggests that similar wave climate led to the appearance of similar spatial types of sorting patterns between groins, despite the differences in sediment supply

(available volume, gravel size), and general context (embayment, low tide terrace, vertical structure (e.g., porosity and permeability)).

Table 9 - Grain size results in meters for each UAV measurement campaign.

Site	Date	D16	D50	D84	Mean	Std
Etretat	2020/06/10	0.042	0.060	0.069	0.056	0.017
Hautot-sur-Mer	2019/04/09	0.056	0.074	0.108	0.082	0.029
	2019/06/04	0.048	0.067	0.096	0.072	0.026
	2020/06/09	0.051	0.069	0.098	0.075	0.028

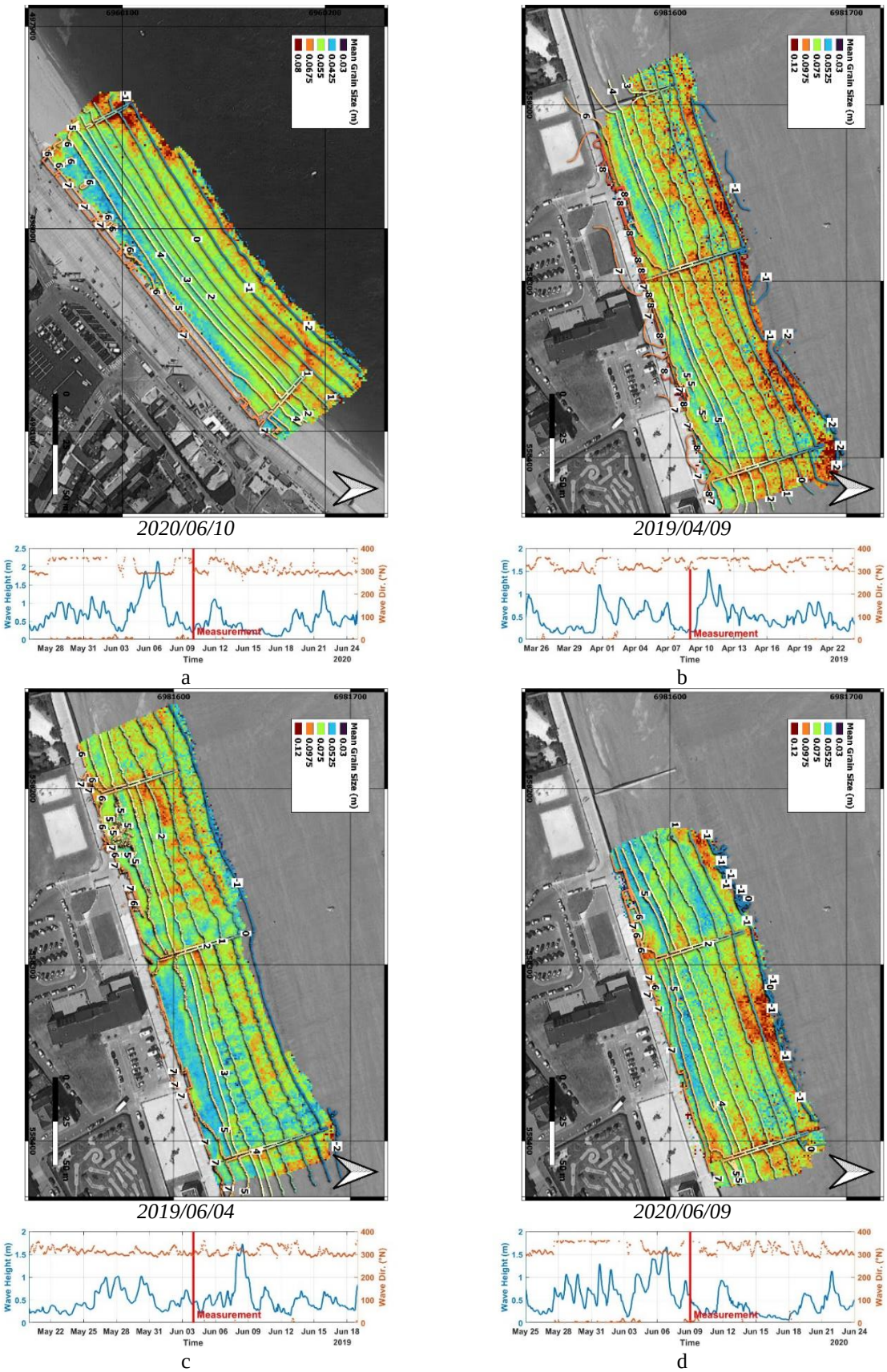

Figure 63 - Maps of mean clast length measured in Etretat on 2020/06/10 (a) and Hautot-sur-Mer on 2019/04/09 (b), 2019/06/04 (c) and 2020/06/09 (d). Contour lines of elevation are indicated for each round elevation with a vertical separation of 1 m. Hydrodynamic conditions are provided for a 30-day period centered on the UAV measurement campaign including the wave significant height (blue line, left y axis) and the wave direction (orange dots, right y axis).

2.4. Conclusion

The morphological evolution of two pebble beaches, including a purely gravel one in Etretat and a composite one in Hautot-sur-Mer, was investigated using an Empirical Orthogonal Function (EOF) analysis applied to a 2-year time series of shoreline positions at different elevations. The EOF's Principal Components (PC) highlighted the existence of at least four mechanisms of shoreline change including rotation, cross-shore translation, rollover and breathing. Despite their relative proximity, the two beaches present different sets of modes: 88.5% of Etretat's shoreline position variability is explained by cross-shore translation (PC1, 62.4%), rollover (PC2, 14.1%), breathing (PC3, 5.8%), large scale rotation (PC4, 3.9%) and beach cell rotation (2.3%). The first mode could be related to a rotation at the scale of the entire embayment, whose pivotal point would be located out of the monitored area. The variability of Hautot-sur-Mer's shoreline position is explained at 72.2% by right-centered rotation (PC1, 46.1%), left-centered rotation (PC2, 14.8%), large scale rotation (PC3, 7%) and rollover (PC4, 4.3%). The interpretation of most of the PCs was confirmed when calculating correlation coefficient between PCs and morphological parameters including beach width (BW), beach orientation angle (BOA) and beach slope (BS). Moreover, the analysis showed that elevation plays a significant role in all mechanisms of shoreline position change, and that the influence of groin structures is more important in Hautot-sur-Mer, where it plays a role in every single PC, than in Etretat, where it is only visible in PC5.

Comparison between time series of morphological and hydrodynamic parameters did not show any significant linear correlation. The hydrodynamic data used in this study consists of offshore waves provided by the WaveWatch 3 model, therefore non-linear nearshore transformations are not taken into account, which significantly limits the observed correlations. Nevertheless, a wavelet analysis highlighted common temporal periods of variability at a mid-term scale including 2, 3, 5, 6 and 8+ months. Periods of 2, 6 and 8+ months also identified in signals of wave energy, however tidal range and current velocity did not share any common period of variability with the considered morphodynamical parameters.

Analyzing the granulometric spatial dispersion of surface gravel particles was possible thanks to a segmentation methodology applied to UAV-derived ortho-imagery. Gravel size was measured once in Etretat, and at three different dates in Hautot-sur-Mer, allowing for some first order estimate of temporal variability to be investigated on the latter site as well, under summer conditions. In general, both sites present different gravel size with D50 values of 5.2 cm in Etretat 7.0 cm in Hautot-sur-Mer (time averaged). The spatial dispersion generally evidenced the presence of patterns such as a cross-shore gradient, cusps and clast assemblages whose periodicity from one beach cell to its neighbors demonstrates the impact of groin structures. The temporal analysis highlighted differences through time in both the average granulometry and the presence and position of patterns. For instance, an average difference of -1 cm in all recorded sizes (mean, D16, D50 and D84) was observed between April and June 2019, while the only significant morphological change of the beach was its orientation

(5°). Possible explanations include seasonal abrasion and the presence of physical processes leading to sorting, such as percolation and processes related to rotation. The influence of cusp variability on the sediment distribution variability was also highlighted. As the need for better knowledge and understanding in the granulometric spatiotemporal variability is widely acknowledged by the community of coastal scientists, this methodology shows promising results in regard to this matter. However, the length and sampling frequency of time series need to be improved in order to precisely characterize the reciprocal relationship existing between hydrodynamics, morphodynamics and sediment characteristics/transport.

3. Response to storm events in Etretat using XBeach-G

3.1. Introduction

The previous section highlighted the existence of specific mechanisms in the geomorphological evolution of beaches, such as cross-shore translation, rotation, rollover and breathing. Many authors have shown that these phenomena are the result of a dynamic equilibrium between the continuously changing marine forcings and the perpetually adapting response of the coast (Cambers, 1976; Dean, Robert G, 1991; Hack, 1960; Yates et al., 2009). This equilibrium is modulated by a set of environmental parameters such as grain size, porosity, permeability, slope, openness, and the presence of hard structures.

Although there is no clear significant linear correlation between the morphological dynamics of Normandy's beaches and wave characteristics (Figure 60), the seasonal periodicity of some of these mechanisms suggests a causal relationship between wave energy and response of the coast. Indeed, the English Channel's swell also evolves seasonally with a calm summer season and a more energetic winter season (Figure 54). However, this energy is not distributed evenly over time, it is mainly reflected in the occurrence of extreme events more frequent in winter than in summer: storms. Storms cause sudden and significant geomorphological changes on the coast and are therefore important events for the morphological dynamics of beaches. The processes that cause these changes are related to the transformation, dissipation, and reflection of wave energy. These processes in association with the tidal oscillation modulate the response of the beach through erosion, transport, and deposition of particles. In response to the extra energy provided during an event of storm, coastal morphology adapts according to local characteristics and wave conditions.

Figure 64 shows the evolution of the daily cumulative variance of the principal components extracted from the EOF analysis applied to beach morphology over time. The dates of occurrence and the characteristics of the storms are also represented by vertical bars whose height shows the storm energy. The direction of bar heads indicates the direction of wave propagation (most often eastward, occasionally southwestward), the method used for characterizing these events is described in section 3.2.4. From this figure, both storm intensity and clustering appear to be related to increasing geomorphic variance in Etretat, which is consistent with observations of Karunarathna et al., (2014) on

sandy beaches. For example, for summer 2019 (May to October), there is no record of storms while winters of 2019-2020 were impacted by 16 events (between October 2019 and March 2020), resulting in a stable summer (cumulative variance < 1) and a dynamic winter (cumulative variance between 2 and 8). In comparison, winter 2018-2019 had only 7 storms, resulting in a maximum daily cumulative variance of only 2. This variance is mainly reflected by cross-shore translation movements, and to a lesser extent rollover. In Hautot-sur-Mer, the relationship is less explicit. Although the impact of storms is concomitant with peaks in variance, some of these peaks do not see any storms occur, for example from June to September 2019 with 2 peaks in variance and no storm. More generally, the frequency of storms is lower in Hautot-sur-Mer due to the presence of a dissipative intertidal terrace, and rotational movements dominate with significant alongshore exchanges. Thus, while Etretat responds to the impact of storms by cross-shore movements, the response of Hautot-sur-Mer is essentially long-shore and remains more complex and difficult to characterize.

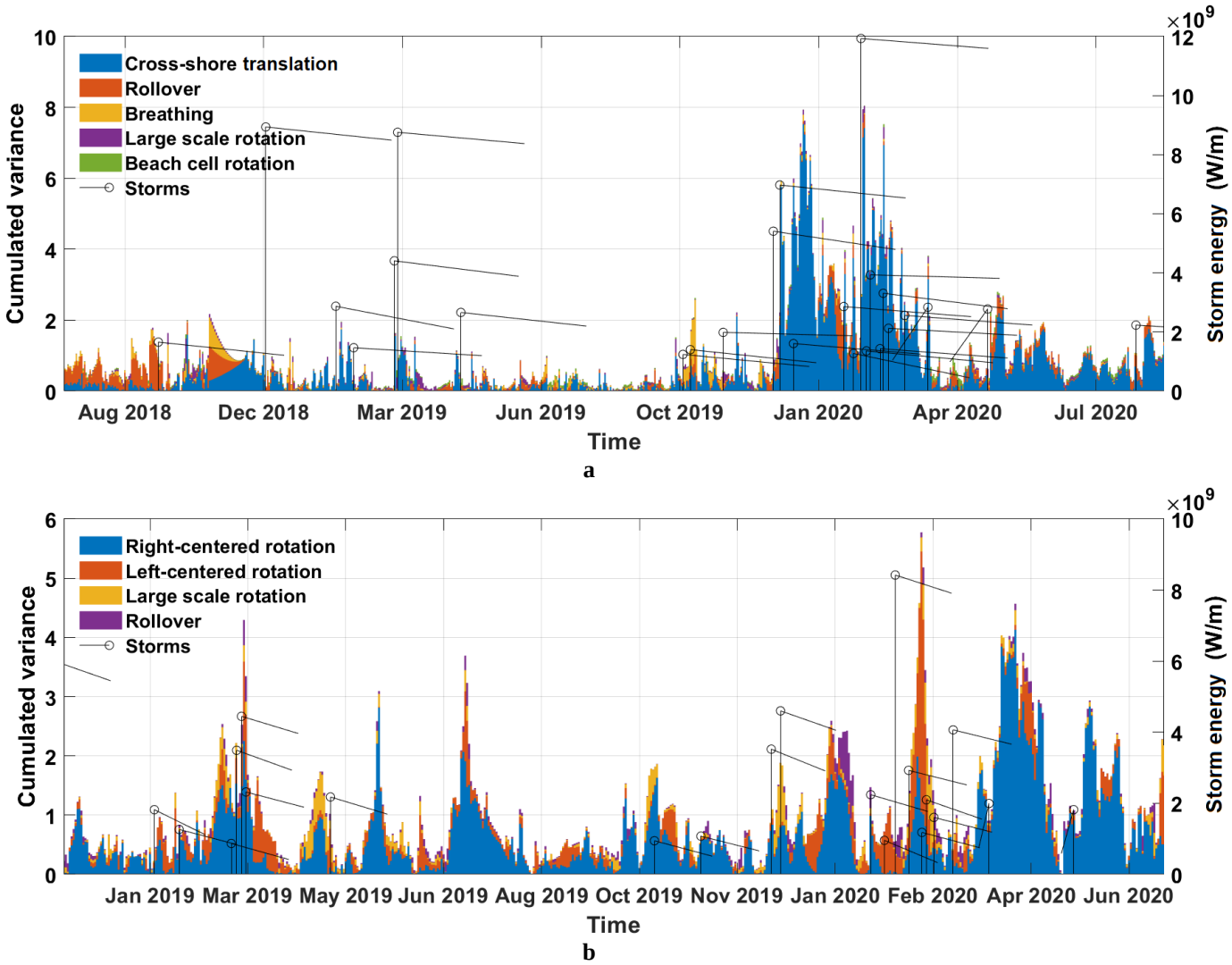

Figure 64 - Cumulated variance of the morphological variability in Etretat (a) and Hautot-sur-Mer (b) observed using coastal video monitoring systems. Each color is related to a specific type of movement, and storm events (Hs ⩾ μ+2σ and Δt ⩾ 48h between events) are represented as vertical bars, quantified by their wave energy flux integral. The offshore average wave direction relative to the North (upward) is indicated through the bar head arrows.

Storms pose a significant risk to coastal populations. The ability of the coast to dissipate/reflect wave energy depends on its potential to adapt to the new dynamic equilibrium caused by the occurrence of a storm. Thus, it is crucial to be able to observe and predict the response of the coast to the impact of storms, in order to define the most important influence parameters and to better protect exposed populations. In this perspective, the XBeach model was developed by (Roelvink et al., 2009) to predict the morphological dynamics of sandy beaches during extreme events (storms, tsunamis, etc.). More recently, the XBeach-G model, an evolution of XBeach that includes two additional modules, was developed by McCall et al. (2014) with the aim of simulating the dynamics of gravel barriers during similar conditions. The first module is a non-hydrostatic pressure correction module that propagates individual waves one by one to ensure an accurate resolution of wave transformation (shoaling, surf and breaking), setup, runup and overtopping processes (McCall et al., 2014). In addition, the module allows for the influence of infragravity waves (frequency ranging from 0.005 to 0.05 Hz) to be considered, as they are particularly important for coastal dynamics under storm conditions (Billson et al., 2019). The second module solves the groundwater flow, i.e., infiltration and exfiltration exchanges between open water and beach water table. Indeed, as Buscombe and Masselink (2006) and Wright and Short (1984) have shown, these exchanges are important to be considered for the dissipation and reflection of wave energy by gravelly shoreline.

XBeach-G is a powerful tool that has already proven useful for modeling the evolution of different barriers and some gravel beaches. However, the performance of the model remains limited by assumptions and simplifications made. For example, the model does not take into account longshore sediment exchange, so the modeling of sites where this component is most important, such as Hautot-sur-Mer, is likely to provide unrealistic results. In addition, permeability is assumed to be temporally constant in the model. However, rapid and important variations of the beach granulometry have been observed during storm events. For example, the beach in Etretat, normally characterized as a "pure gravel beach" (Jennings and Shulmeister, 2002), became sandy during a storm in February 2020 (Figure 57). Grain size and permeability are correlated (Buscombe and Masselink, 2006; Krumbein and Monk, 1943), although this relationship is probably not linear for coarse material (Horn, 2002). Thus, it seems reasonable to assume that permeability is not constant over time and may even change significantly during a single storm event, and from one storm to the next. As Austin and Masselink (2005) has shown, the response of gravel systems is very sensitive to this parameter. Indeed, authors explain that the more important infiltration happening through a coarser beach fabric tends to weaken the runup energy that can transport surficial sediment, and thus influences morphological changes. Hence the question of the temporal variability of permeability at the time scale of a storm event seems relevant.

To study this question, we propose to apply XBeach-G to a cross-shore profile of the beach of Etretat, as morphological changes are mostly cross-shore, contrary to Hautot-sur-Mer. The morphological response of the beach to different events of storm is simulated while varying the

permeability and the results are analyzed and compared with VMS observations to determine an optimal permeability value and its evolution over time. The methodology and data used are described in more detail in section 3.2. The results are presented in section 3.3, and discussed in section 3.4. Finally, the conclusions of this study are given in section 3.5.

3.2. Data and model setup

3.2.1.Bathymetry and granulometry

As of 2022, the currently available versions of XBeach-G only allow for 1D modeling along a cross-shore transect (i.e., results are only valid for purely cross-shore sediment mobility). Therefore, the model needs to be implemented using a 1D bathymetric profile, in addition to sea state time series (tide, surge, waves and wind), and sedimentary information (D15, D50, and D90), which are described in this section.

The model is established on the beach of Etretat. The cross-shore profile starts offshore at a depth of 24.6 m with a resolution of 3 m (Figure 65). It extends over 3490 m, up to the level of the seawall, at +9 m, where the resolution was gradually refined to 1 m to allow for good resolution of the wave processes. This transect corresponds to P48, on Figure 55. Selecting this specific transect was incentivized by the inability of XBeach-G to consider long-shore transport. As this transect is located around the beach cell rotation pivot, the amount of morphological change due to alongshore processes should be minimal. However, it is important to mention although the net alongshore transport balance is expected to be near zero on this profile, there still is a significant transport happening, as demonstrated by the existence of shoreline rotation mechanisms (Chapter 4 - Section 2.3.2.1).

The merging of three different data sources was necessary to establish a sufficiently long and detailed bathymetric cross-shore profile. Offshore data was provided by SHOM (2015) (Figure 65a), with a resolution of 0.001° (~111 m) on a regular grid. For our study, this data was refined up to 3 m using linear interpolation. Closer to the coast (Figure 65b), the nearshore bathymetry (sub- to supratidal) is derived from phase 2 of the aerial lidar surveys by ROL (2019) (Réseau d'Observation du Littoral de Normandie et des Hauts-de-France), with a resolution of 1 m and a vertical uncertainty of about 20 cm (S. Costa, personal communication, 2021). The transition between SHOM and ROL data is smoothened by the linear interpolation refinement. Finally, the intertidal area was measured daily by the VMS installed in Etretat (Figure 65c), with a vertical RMSE of 22 cm (Soloy et al., 2021b). This section of the profile was measured by both ROL and VMS; however, VMS observations are more up to date. Therefore VMS-derived elevations are used in the profile wherever available in the intertidal area, and ROL data fills up both sub- and supra-tidal parts of the profile. Importantly, the extent of the VMS-derived DEM varies daily following tidal range variations and changes in the number of delineated shorelines after the image quality filtering process. Hence, there are two transitions between VMS and ROL data, at the upper and lower limits of the daily tidal range, which

move from day to day. No smoothening was applied to these transitions, this can sometimes lead to the appearance of a jump in the profile.

The grain size was measured using the method developed by (Soloy et al., 2020). The values used in our XBeach-G models correspond to the D15, D50 and D90 measured on the 2020/06/09 ortho-image (Figure 42), i.e., 4.59 cm, 5.99 cm, and 8.60 cm, respectively. The embayment of Etretat tends to trap gravel inside the bay (Costa et al., 2015), therefore it seems fair to assume that the overall grain size (unmeasured at the storm dates of this study) will remain close to those previously mentioned. However, events of Etretat's beach becoming mainly sandy were witnessed in the past (Figure 57). Although there is no direct observation of the place where gravels were then stored, we assume that they remained trapped in the subtidal part of the bay. Such grain size variability could not be considered given the current limitations of data and model capabilities.

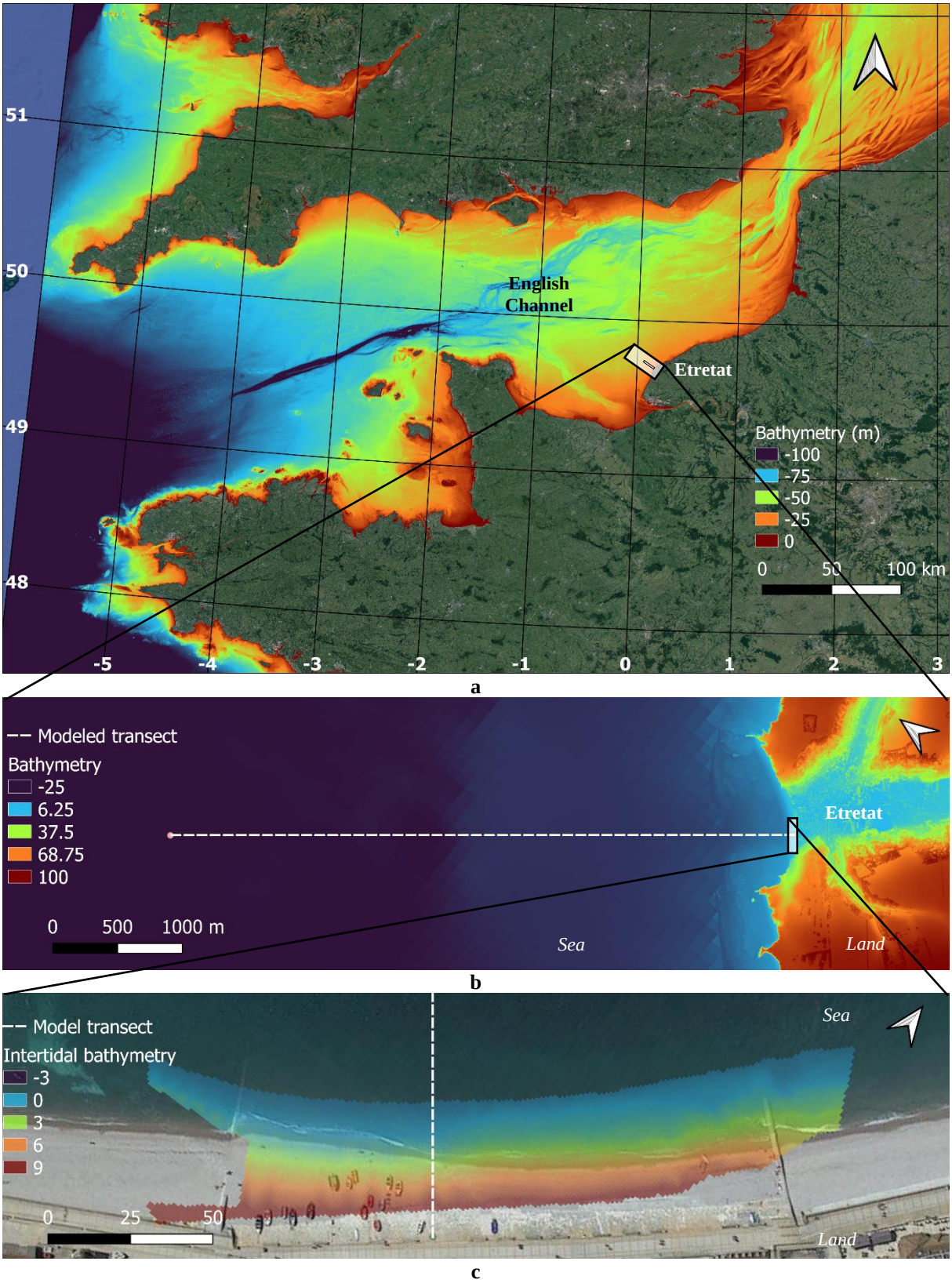

Figure 65 - Bathymetry dataset of the English Channel from SHOM (a), of the subtidal along the offshore to nearshore transect from SHOM and ROLNP (b), and of the intertidal area observed using coastal video monitoring systems (c). All datasets were merged, and elevations were extracted along the transect in order to provide profiles for each modeled day

3.2.2.Hydrodynamics

The wave data was initially extracted from a WaveWatch 3 (WW3) model (Tolman, 2009), as there is no active buoy in this region. Waves were then propagated to shore using the SWAN model

(Booij et al., 1999). Propagation was forced over a total of 26 months, between June 2018 and September 2020, on a regular rectangular grid of 20 m resolution. The model was validated against buoy data near Le Havre (~25 km South to Southwest from Etretat) with an RMSE of 0.235 m and a correlation coefficient of 0.927. The time series of wave characteristics used for our XBeach models was extracted from the cell where the offshore end of the cross-shore bathymetric transect is located. A more precise description of SWAN model setting is provided in Solano et al. (2022).

Astronomical tide, surge, and wind data were extracted from a Hycom2D model (Chassignet et al., 2007), built on a curvilinear grid with a resolution of 500 m near the coast. As for the SWAN data, the extraction point is located in the cell where the cross-shore transect ends. During storms, Pasquet et al. (2014) reported measuring a tidal phase shift of up to 12 min and an underestimation on the total water level of -10 cm when during the peak of surge in the models' outputs, although it is not clear where such errors were observed exactly. One possible consequence of this is a slight underestimation of the elevation on VMS-derived DEMs during storms, up to -10 cm. Nevertheless, this remains lower than the DEM's measured RMSE of 22 cm and corresponds to less than 2 times the median grain size.

3.2.3.Model setup and modeling strategy

The objective of this numerical investigation is to evaluate the evolution of the beach permeability by taking advantage of the daily coverage offered by VMS morphological observations. To achieve this, the implemented strategy is to model storms of different characteristics while varying the permeability k in a range between 0 and 0.6 m/s. Indeed, the optimal value of k is expected to be is in this interval, given the measured surficial grain size (Buscombe and Masselink, 2006; McCall et al., 2015; Poate et al., 2016). Each storm will be segmented and modeled in 24-hour intervals. This time seems to be appropriate considering the observation frequency of the intertidal bathymetry (up to 6h). For each model corresponding to a date t, the associated daily DEM will be used as both the input bathymetry, and the ground truth final state to evaluate the t-24h model results. This should allow us to monitor the model performance, and the permeability variation associated with the most optimal results every 24 h.

The almost 3500 m long bathymetric profile (Figure 66a) is distributed on a 1D mesh of 1232 nodes with a variable spacing ranging between 3 m offshore and 1 m close to the beach. A non-erodible layer was empirically defined to immobilize the section of the profile corresponding to the seawall and the section below elevation -6 m (Figure 66b). This threshold corresponds to a break in the profile slope, which is interpreted as the foot of Etretat's beach. Underneath lays a hardground called "platier", made of hard limestone and sometimes visible underwater. Thus, only the section of the profile between -6 and +9 m in elevation is composed of material mobilizable by waves, although sediment could theoretically be deposited and then remobilized outside these limits, depending on hydrodynamic conditions. Importantly, the precise morphology of the seawall below the sediment is

unknown. The non-erodible seawall profile is shown as a vertical wall extending from -6 m to +9 m (Figure 66b), although it is most likely an inclined plane.

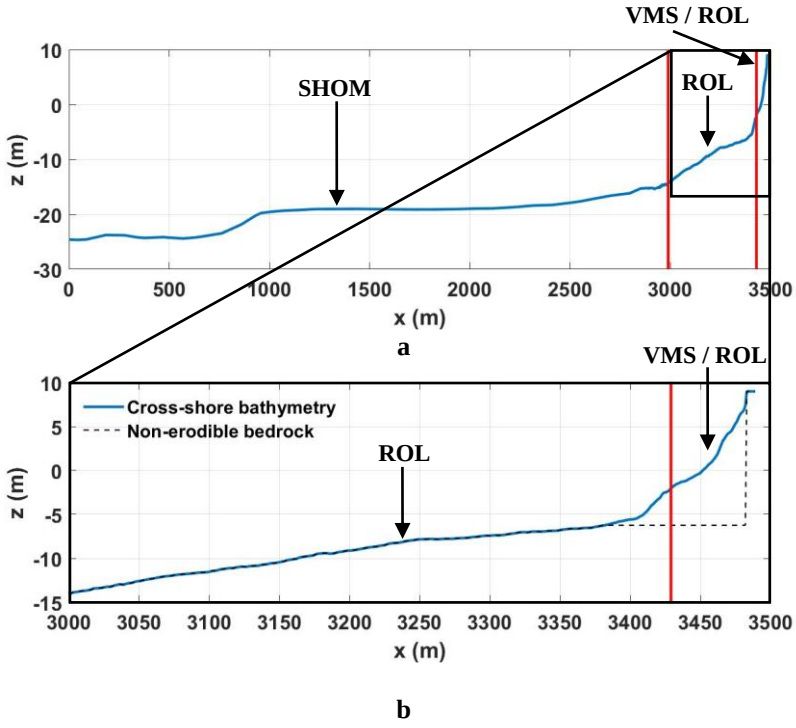

Figure 66 - Cross-shore bathymetric profile used as the input for our XBeach-G model of Etretat. Figure a shows the full 3.5 km long profile while figure b focuses on the intertidal beach and shows the non-erodible bedrock in black. Vertical red lines indicate the transition between different datasets: SHOM, ROL and VMS

The sensitivity analysis to the permeability k is performed by running 10 to 13 model scenarii (depending on the total number of days) varying k between 0 and 0.6 m/s for each modeled day while keeping other parameters constant. Once all the models of one day have been computed, three metrics are measured to estimate the performance of the model including the BSS, the RMSE computed between the elevation of both final measured and modeled profiles, and the R^2 computed on the relative change in elevation (final-initial profiles) between model and observation. The calculation of these indices only takes into account the part of the profile located within the intertidal zone, i.e., where elevation data is derived from VMS (i.e., contemporary observations).

3.2.4.Storm classification and selection

Storm events were identified using an excessive wave significant height method. Subsequently, identified storms were ranked according to their total energy (E_{storm}). This method is often used to procedurally establish a sorted list of marine storm events (Amarouche and Akpınar, 2021; Boccotti, 2000; Mendoza et al., 2013; Molina et al., 2019; Ojeda et al., 2017). For this study, a marine storm was defined an event during which the significant wave height exceeds $H_{s\,threshold}$ and lasts at least 12 hours. We introduce $H_{s\,threshold}$ as the mean value of H_s plus two standard deviations. In addition, consecutive events separated by an interval of less than 48h are merged and considered as one longer event.

$$H_{s\,threshold} = \mu_{H_s} + 2\sigma_{H_s}^2$$

The list of storm events identified in Etretat includes 30 storms distributed between June 2018 and September 2020. Their classification by order of magnitude is performed after calculating their cumulated energy E_{storm}, which corresponds to the integral of the Energy Flux (E_{flux}) over the duration of each event.

$$E_{flux}(t) = \frac{\varrho g^2}{64\pi} H_s^2 T$$

$$E_{storm} = \int_{t_{storm\ start}}^{t_{storm\ end}} E_{flux}(t)\, dt$$

Where ϱ is the sea water density (1025 kg/m^3), g is the acceleration of gravity (9.81 m/s^2), H_s is the wave significant height in meters, et T is the wave period in seconds.

After ranking the storms in descending order of cumulated energy (Figure 67), we selected three events representative of the highest intensities for which intertidal bathymetry data appeared sufficient to observe the change in intertidal bathymetry on a daily scale. Since each model lasts only 24 hours, not all storms could be modeled due to lack of intertidal bathymetry information. Indeed, storm weather conditions tend to decrease the quality of VMS images (water drops on the images, overtopping, depth of field reduced by rain and spray), which prevents the identification of an accurate coastline and the reconstruction of the bathymetry. Nevertheless, digital terrain models could be reconstructed over a total of 11 days, including periods before and during the three selected storms.

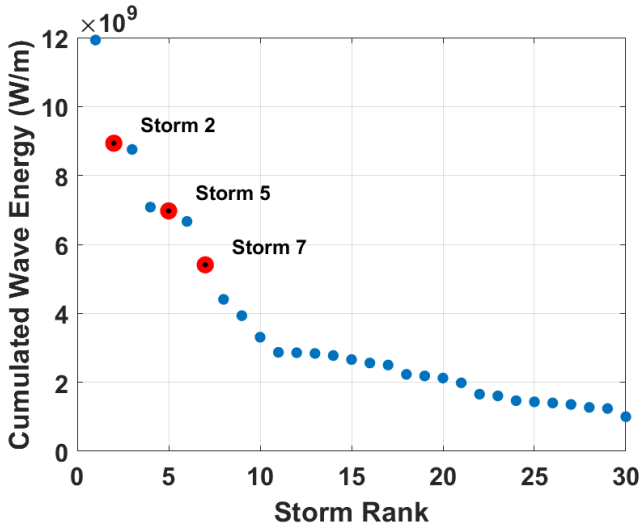

Figure 67 - Storm events ranking

The selected events correspond to storms number 2, 5, and 7, their characteristics are summarized in Table 10. A photograph taken in Etretat during storm 5 (Figure 68) illustrates the waves height of this event, with a strong overtopping leading to a flooding of the backshore. Fortunately, no damage or casualties were recorded during this event (ROL, 2019), although this is not always the case (Figure 68b).

Table 10 - Modeled storms' characteristics

Storm name	Storm start	Storm duration	Model start	Model duration	Wave direction	Maximum Energy Flux	Cumulated Energy Flux	Rank
Etienne	2018/12/07	58 hr	2018/12/06	2x24 hr	104 °N	7.1 e4 W/m/s	8.9 e9 W/m	2
N/A	2019/12/13	42 hr	2019/12/12	3x24 hr	104 °N	7.5 e4 W/m/s	7.0 e9 W/m	5
Atiyah	2019/12/08	35 hr	2019/12/04	5x24 hr	109 °N	8.3 e4 W/m/s	5.4 e9 W/m	7

a

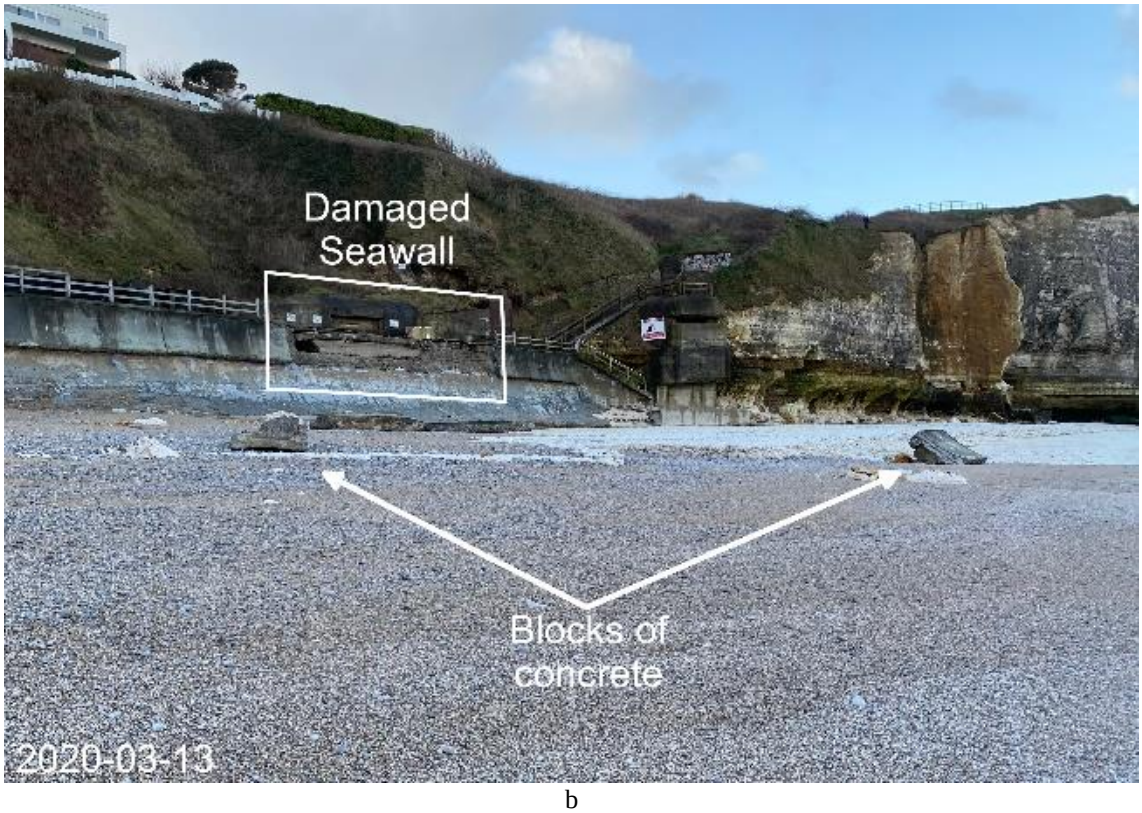

b

Figure 68 – a: Photograph taken on 2019/12/13 (Storm 5) in Etretat showing the overtopping of waves over the seawall (Département de Seine-Maritime, (ROL, 2019)*) ; b: Seawall damages observed in Etretat on 2020/03/12 after a storm event.*

Figure 69 shows the evolution of E_{flux} during the 3 selected storm events, as well as the dates on which the intertidal bathymetry data could be measured by the Etretat VMS (i.e., start, transition and end dates of the simulations). Only dates where VMS-derived DEMs were wider than 35 m (an empirically chosen threshold) were considered usable, to minimize the potential temporal decorrelation between our profile and the real bathymetry. Storm 2 (Figure 69a) consisted of a series of four peaks of E_{flux} increasing between 5.10^4 and 7.10^4 W/m/s, of which only the first (i.e., E_{flux} = 5.10^4 W/m/s) could be monitored and modeled. Since the calmer period preceding the storm was also covered by one VMS observation, three DEMs were used to model two days in XBeach-G, each model lasting 24 hours. Storm 5 (Figure 69b) consists of three peaks with E_{flux} varying between 5.10^4 and 8.10^4 W/m/s. It is covered from start to finish by four daily intertidal DEMs that allowed three consecutive days of XBeach-G models to run. Storm 7 (Figure 69c) consists of only a single peak where E_{flux} = 8.10^4 W/m/s. Unfortunately, only observations prior to the peak are available, although the last DEM was measured during the event, when E_{flux} reached 5.10^4 W/m/s and was intensifying. However, the period preceding this peak had another peak of lower intensity (E_{flux} = 2.10^4 W/m/s) with good temporal coverage. It was therefore decided to model this pre-storm period using the 6 DEMs available to model 5 days.

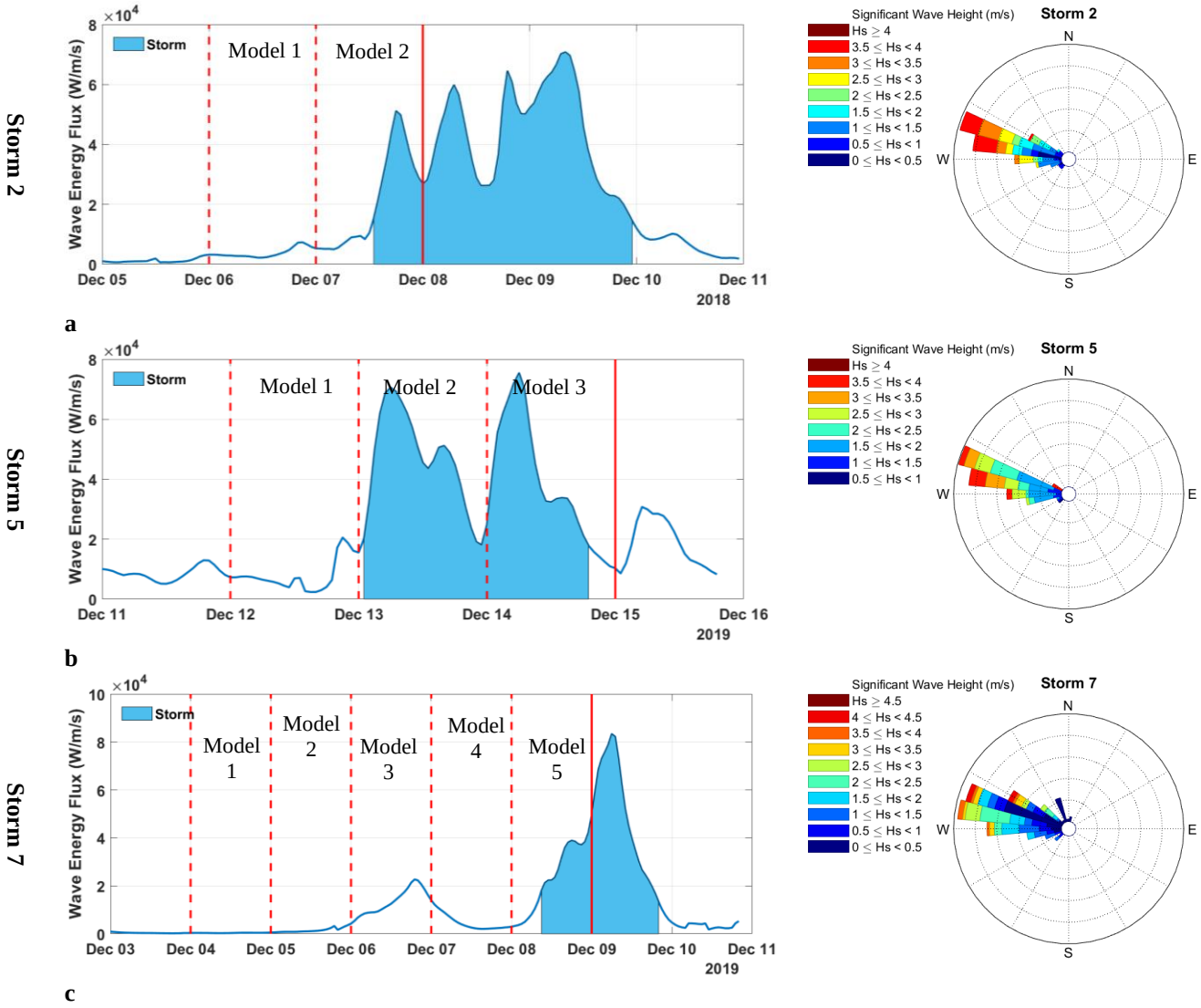

Figure 69 – Time series of wave energy flux during the three storms modeled using XBeach-G by intervals of 24h. Vertical red lines (both dashed and solid) indicate the dates at which VMS-derived intertidal DEMs were available, the dashed ones specifically correspond to model starting dates while the solid lines indicate the last date with data available for model performance assessment.

3.3. Results

The Table 11 summarizes the results of BSS, RMSE and R^2 for all tested scenarios. Among the modeled dates, only 4 have BSS values higher than 0.3 (threshold of the "fair" category, Van Rijn et al. (2003)), of which 2 are higher than 0.6 ("good" category, Van Rijn et al. (2003)). The highest BSS values are obtained during the most intense storm (Storm 2), especially during the maximum intensity peak between 2018/12/07 and 2018/12/08 (5e4 W/m/s). However, higher intensity peaks such as Storm 5 (8e4 W/m/s) did not yield BSS values greater than 0.3, hence there is no clear correlation between BSS and intensity of wave conditions. The lowest BSS values are associated with the permeability value k = 0, i.e., when the groundwater flow process is deactivated.

The BSS values vary with permeability. Assuming that the model setting is as close to reality as possible, the BSS variation should be continuous with a maximum corresponding to the optimal permeability value. We were thus able to identify 2 consecutive dates associated with different

permeability values whose BSS exceeds 0.6: On 2018/12/06, optimal k is between 0.2 and 0.35 m/s, and on 2018/12/07, optimal k is in a range between 0.01 and 0.15 m/s (maximum for k = 0.01 m/s). The first date corresponds to relatively calm conditions (EF_{max} = 5e3 W/m/s), and the second date to a storm peak (EF_{max} = 5e4 W/m/s). For these two dates, these values are associated with minimum RMSE of 0.26 m each, and maximum R^2 of 0.73 and 0.75, respectively.

The other two dates with BSS classified as "fair" (2019/12/13, BSS = 0.33 and 2019/12/05, BSS = 0.32) remain in the lower limit (0.3) of the associated range. They correspond to EF_{max} of 7e4 W/m/s (storm conditions) and 1e2 W/m/s (calm conditions), respectively, and are associated with RMSE values of 0.49 m and 0.11 m, and R^2 of 0.07 and 0.57, respectively. In the presence of such combinations of low BSS and R^2 values, it is more prudent to consider these two models as unsuccessful. Thus, only the results of storm 2 will be analyzed in the following, however the results of all models will be presented in Appendix A.

Table 11 - Validation results of the XBeach-G simulations applied on P48 in Etretat during 4 periods of storms. Metrics include the Brier Skill Score (BSS), the Root Mean Square Error (RMSE) and the Coefficient of determination (R^2). Red values highlight scenarios with BSS > 0.6, RMSE < 0.25 m, or R^2 > 0.9. Yellow values indicate BSS > 0.3, RMSE < 0.5 or R^2 > 0.5.

Parameter	Storm	Dates	k (m/s) 0	0.01	0.05	0.1	0.15	0.2	0.25	0.3	0.35	0.4	0.45	0.5	0.6
BSS	2	2018/12/06	-36.19	0.43	0.50	0.56	0.60	0.63	0.63	0.63	0.63	0.60	0.57	0.54	0.49
		2018/12/07	-27.65	0.68	0.69	0.68	0.63	0.58	0.52	0.46	0.38	0.31	0.25	0.16	0.02
	5	2019/12/12	-12.54	-0.53	-0.48	-0.48	-0.50	-0.48	-0.50	-0.49	-0.50	-0.48	-0.48	-0.47	-0.44
		2019/12/13	-76.51	-0.68	-0.53	-0.41	-0.31	-0.20	-0.13	-0.04	0.05	0.12	0.21	0.22	0.33
		2019/12/14	-12.68	-3.03	-2.75	-2.55	-2.42	-2.29	-2.20	-2.13	-2.04	-1.93	-1.87	-1.78	-1.55
	7	2019/12/04	-	-0.05	-0.19	-0.33	-0.41	-0.49	-0.52	-0.52	-0.52	-0.51	-	-	-0.37
		2019/12/05	-	0.32	0.14	-0.07	-0.23	-0.37	-0.51	-0.59	-0.66	-0.64	-	-	-0.51
		2019/12/06	-	-1.69	-2.12	-2.52	-2.85	-3.17	-3.45	-3.74	-3.95	-4.10	-	-	-4.11
		2019/12/07	-	-0.30	-0.41	-0.49	-0.55	-0.58	-0.59	-0.60	-0.56	-0.55	-	-	-0.41
		2019/12/08	-	0.29	0.08	-0.14	-0.40	-0.67	-0.94	-1.21	-1.47	-1.72	-	-	-2.56
RMSE (m)	2	2018/12/06	2.86	0.34	0.32	0.30	0.28	0.27	0.26	0.26	0.27	0.28	0.28	0.29	0.31
		2018/12/07	2.43	0.28	0.26	0.26	0.30	0.32	0.34	0.37	0.39	0.42	0.44	0.47	0.51
	5	2019/12/12	2.74	0.90	0.87	0.87	0.88	0.89	0.90	0.90	0.91	0.90	0.91	0.90	0.90
		2019/12/13	5.65	0.78	0.75	0.73	0.70	0.68	0.65	0.62	0.59	0.56	0.53	0.53	0.49
		2019/12/14	1.40	0.81	0.80	0.78	0.77	0.76	0.75	0.74	0.72	0.71	0.70	0.68	0.64
	7	2019/12/04	-	0.22	0.23	0.24	0.24	0.25	0.25	0.25	0.24	0.24	-	-	0.23
		2019/12/05	-	0.11	0.13	0.14	0.15	0.15	0.16	0.17	0.17	0.17	-	-	0.16
		2019/12/06	-	0.40	0.43	0.46	0.48	0.49	0.51	0.52	0.53	0.53	-	-	0.52
		2019/12/07	-	0.35	0.37	0.38	0.39	0.40	0.39	0.39	0.38	0.38	-	-	0.34
		2019/12/08	-	0.44	0.48	0.53	0.59	0.65	0.70	0.75	0.79	0.83	-	-	0.97
R^2	2	2018/12/06	0.21	0.56	0.63	0.69	0.71	0.73	0.72	0.71	0.70	0.66	0.62	0.59	0.53
		2018/12/07	0.72	0.75	0.73	0.74	0.73	0.72	0.70	0.69	0.64	0.56	0.47	0.32	0.12
	5	2019/12/12	0.68	0.24	0.18	0.14	0.10	0.07	0.05	0.03	0.02	0.00	0.00	0.00	0.00
		2019/12/13	0.24	0.02	0.02	0.01	0.01	0.01	0.00	0.00	0.00	0.01	0.03	0.03	0.07
		2019/12/14	0.01	0.09	0.07	0.06	0.05	0.04	0.04	0.03	0.03	0.02	0.01	0.01	0.01
	7	2019/12/04	-	0.02	0.13	0.19	0.19	0.20	0.20	0.19	0.18	0.17	-	-	0.11
		2019/12/05	-	0.57	0.59	0.59	0.59	0.59	0.57	0.55	0.53	0.52	-	-	0.42
		2019/12/06	-	0.11	0.13	0.13	0.14	0.14	0.15	0.17	0.19	0.19	-	-	0.17
		2019/12/07	-	0.47	0.55	0.60	0.64	0.62	0.58	0.53	0.48	0.45	-	-	0.19
		2019/12/08	-	0.56	0.45	0.35	0.25	0.18	0.11	0.07	0.04	0.02	-	-	0.00

3.3.1.Storm 2 – Etienne

The intertidal profile of 2019/12/06 (calm conditions) forms a straight slope whose section observed by the cameras extends from -2 m to +3 m in elevation. It is interrupted at +2 m by 10 m long flat berm. On 2019/12/07, profile changes remain small, only the berm has risen from +2 m to +3 m. These changes correspond to an erosion of the bottom of the beach ($x < 3450$), and an accretion of the top (Figure 70). The model reproduces the accretion quite accurately, especially for $k = 0.25$ m/s, however the simulated movements in the lower part of the beach are largely underestimated, especially with the lowest permeability values excluding $k = 0$ m/s. For this value, on the contrary, the model results show a very exaggerated erosion, everywhere except at $x = 3450$ m. Modeled movements outside the area monitored by VMS are relatively small.

Between 2019/12/07 and 2019/12/08, the hydrodynamic conditions are stronger, and the opposite phenomenon is observed with an accretion of the lower beach (+0.5 m), and an erosion of the upper beach (-1 m). We note the erasure of the berm observed the day before, leading to a smoothening of the profile. Overall, the accretion at the bottom of the slope is very well reproduced by the model, whatever the permeability value. Judging by the small variations resulting from different k values, it seems that the accretion phenomenon at the bottom of the slope is not very sensitive to permeability. On the other hand, the erosion of the upper slope is only reproduced for low k values, with an amplitude similar to observations for k values around 0.05 m/s. Moreover, for $k > 0.3$ m/s, the model predicts accretion of the upper beach instead of erosion. On this part of the profile, the wider range of predicted elevations for different permeability settings shows a greater sensitivity to this parameter. Also, for this day, the scenario of $k = 0$ m/s greatly overestimates both the lower beach accretion and upper beach erosion, although the values are correct around $x = 3450$ m. The modeled subtidal dynamics ($x < 3430$, $z < -2$) is much larger than the previous day (between -0.5 and +0.5 m in places) and suggests exchanges with the intertidal zone. Notably, models showing accretion at the top of the beach ($k > 0.3$ m/s) present subtidal erosion, and conversely for models showing erosion at the top of the beach.

Storm 2

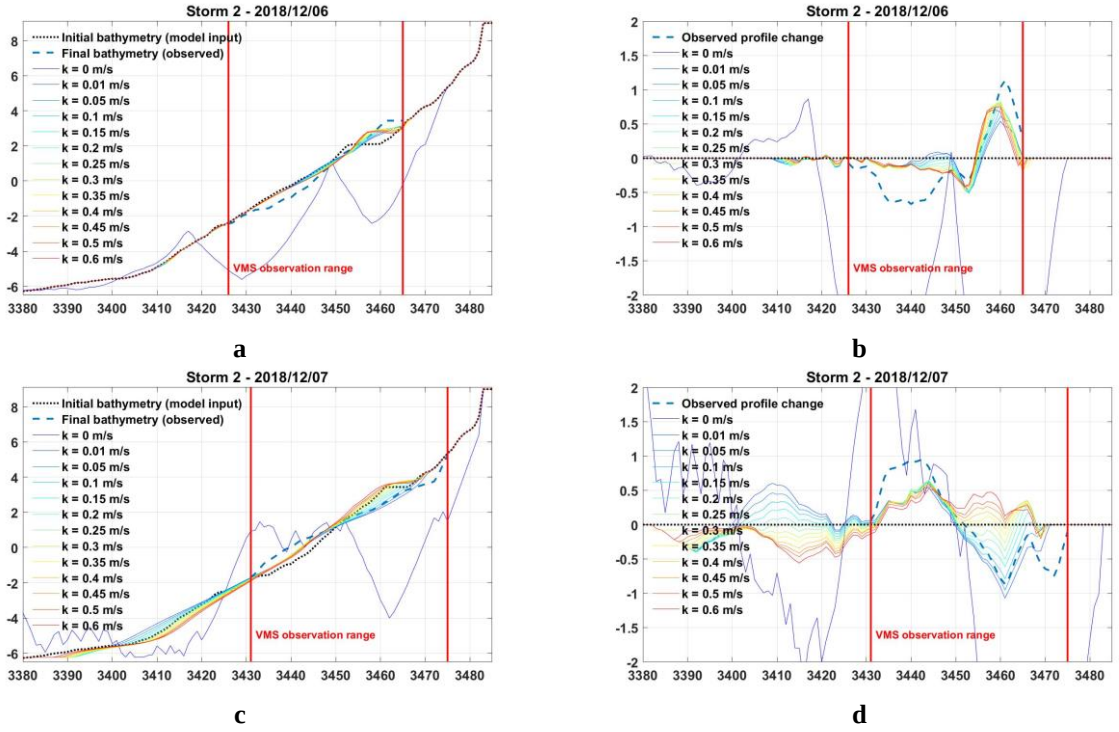

Figure 70 – Comparison between observed (black dotted and blue dashed lines) and modeled cross-shore profiles of Etretat using Xbeach-G (colored solid lines, one color per value of permeability k). Each row presents results after one day of observation/modeling during storm 2 (2018/12/07 to 2018/12/09). Figures on the left side present the initial and final profiles, figures on the right show the associated elevation change. The red vertical lines present the extent of the area monitored daily through video monitoring system (i.e., the section of the profile that was observed at the model's beginning and ending dates).

3.4. Discussions

The low number of models satisfying the BSS $\geqslant 0.6$ condition shows the limitations of our approach. Indeed, the quality of the VMS images decreases with winter conditions, especially during storms, which limits the number, the extension and potentially the quality of the digital terrain models that can be reconstructed (although this last point has not been evaluated). On the other hand, only the intertidal section of the profile visible to the cameras is updated in the model from one storm to the next. Thus, no subtidal modification will be taken into account although elements such as the beach step have proven their importance in the dynamics of gravel beaches (Austin and Buscombe, 2008; Buscombe and Masselink, 2006; Masselink et al., 2010). Similarly, the supratidal morphology that constitutes a sedimentary stock accessible to storm overtopping waves is not updated either. Nevertheless, the model results obtained during storm 2 show a good match with the observed morphological changes. We can therefore legitimately believe that the model setup for this date is relatively close to reality, despite the limitations mentioned above.

Similar studies at different sites obtain comparable results. For example, Pollard (2020) modeled the storm response of a gravel barrier in the UK where the D50 varies between 1 and 2 cm. Forty-five calibration runs, including permeability variations, yielded a maximum BSS of 0.71 for k = 0.2 m/s. The model was then applied to 7 different profiles, among which 2 resulted in BSS values greater than 0.6. Bergillos et al. (2016) applied XBeach-G to a mixed sand and gravel deltaic coastline

with a D50 of 2 cm. Permeability was not reported by the authors, but their results show BSS values greater than 0.89. Brown et al. (2019) tested the model on a mixed sand and gravel beach in New Zealand, with a D50 of 1.36 cm, and a permeability k=0.01 m/s. Only 7 of the 30 scenarios obtained a BSS greater than 0.6, with a maximum of 0.79.

The results observed during storm 2 show that the morphodynamics of the pebble beach is very sensitive to the permeability value. Indeed, the absence of groundwater flow (k = 0 m/s) leads to a significant exaggeration of the sediment erosion and accumulation phenomena, which shows the indispensable character of considering the groundwater flow to estimate these dynamics. This was already by Buscombe and Masselink (2006), Jennings and Shulmeister (2002), and Mason and Coates (2001), and was one of the main incentives to adapt XBeach for gravel environments (McCall, 2015). For non-zero values, the permeability controls the amplitude and type of response of the profile to wave impact. In general, the results show that k influences the amplitude of the profile changes, while the position along the profile of the maximum and minimum changes depends on the antecedent topography and hydrodynamic conditions (tidal amplitude, wave characteristics). In calm conditions a low k value tends to smoothen the profile, while a high k value favors berm build up in the upper part of the intertidal zone. In all cases, most of the changes are observed in the intertidal zone, and almost no change happens in the subtidal area. Under energetic conditions, a low permeability favors profile erosion and accumulation at the beach step, whereas a high value would tend to build a berm by eroding the beach step. Thus, under such conditions the subtidal section (especially the beach step) of the profile participates significantly in the intertidal response. This is consistent with results obtained by She et al. (2007) who observed an increased offshore sediment transport and a reduced onshore one when decreasing permeability in a mixed sand and gravel beach physical model.

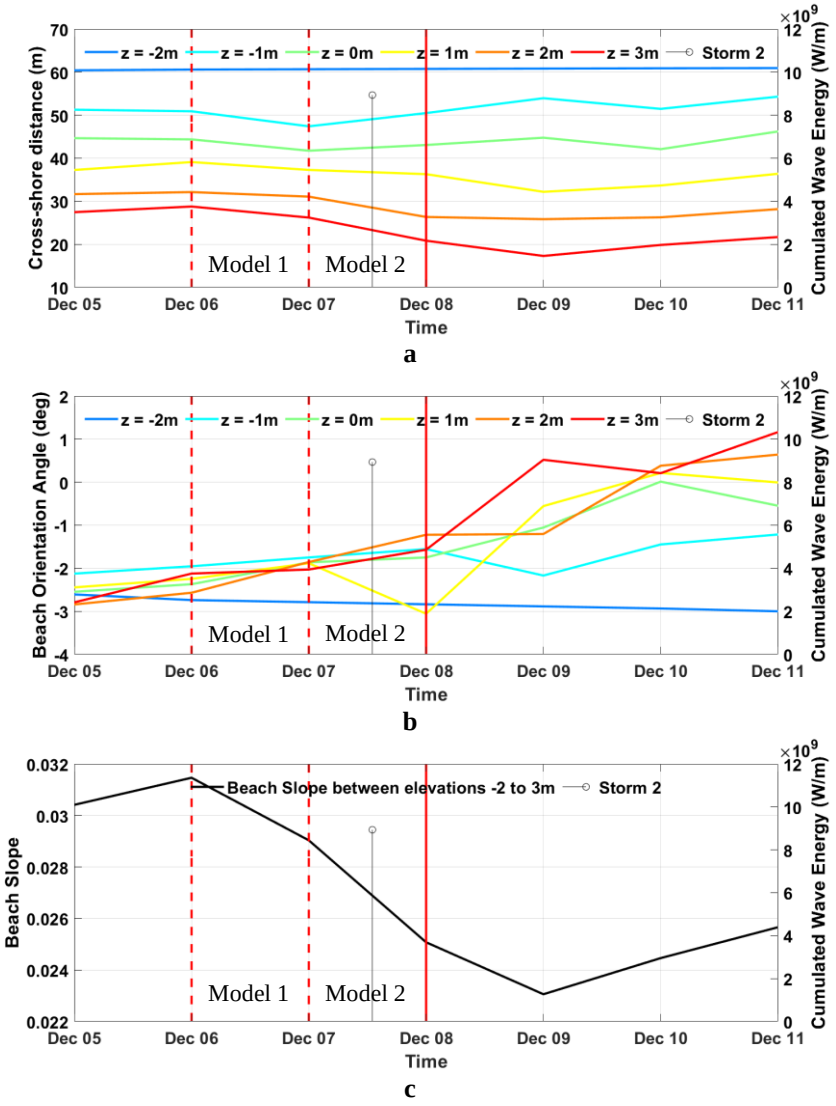

Figure 71 – Beach Width (BW, a), Beach Orientation Angle (BOA, b) and Beach Slope (BS, c) observed using VMS during storm 2, at various elevations from -2 m to +3 m. The storm starting date is presented as a vertical bar, its height relates to the cumulated wave energy. Vertical red lines (both dashed and solid) indicate the dates at which VMS-derived intertidal DEMs were available, the dashed ones specifically correspond to model starting dates while the solid lines indicate the last date with data available for model performance assessment.

The morphological change observed during the calm period corresponds to the construction of a horizontal berm, while the first storm peak results in berm erosion and profile smoothening. Both behaviors are similar to those observed by de McCall et al. (2015) and correspond to the mechanism identified by the PC2 component of the EOF analysis, rollover (Chapter 4 - Section 2.3.2.1.2). McCall et al. (2015) define rollover as the cross-shore landward displacement of the entire profile of a barrier without change in height, width, or slope. However, the beach of Etretat is not exactly a barrier since it is held against a fixed seawall, which limits its ability to translate landward. The rollover therefore results in an oscillation of the slope around a pivot axis (Figure 61), here located at the x = 3450 m coordinate and between 0 and +1 m in elevation (Figure 70 and Figure 71a and c), which correspond to the elevation found in our EOF analysis results. Moreover, the position along the profile and the width of the horizontal berms vary from one date to another, and seem to be correlated to the

permeability value as well as to the intensity of the hydrodynamic conditions. Indeed, for any given date, a larger k value will generally shape the berm while a lower k will likely erase it and smoothen the profile shape (Appendices A). The study of the morphological characteristics of the berms as a proxy of the permeability during a storm seems to be a relevant research axis for future investigations.

Indeed, insofar as there is a significant granulometric sorting on gravel beaches with a strong spatial and temporal variability (Buscombe and Masselink, 2006; Soloy et al., 2020), and that storm events mobilize a significant amount of sedimentary material in a short period (Coco and Ciavola, 2017), it seems reasonable to postulate that the permeability of a beach varies at the daily scale. Specifically, in the case of a gravel beach, one would expect to see greater permeability during sustained calm conditions over a long period of time, as the finer sediments have had time to migrate through the porosity. Under more energetic conditions, the sudden mobilization of a large quantity of sediment may mix the grain sizes and thus decrease permeability. Indeed, studies of mixed gravel and sand beaches (Jennings and Shulmeister, 2002) show that the presence of sand greatly influences the response of the beach profile to wave impact, permeability being controlled by the finest 10% (Holmes et al., 1997; Horn and Walton, 2007). In addition, Mason et al. (1997) showed that when the surface sedimentary layer (depth < 1 m) contains more than 25% of its weight in sand, the beach morphodynamics becomes closer to that of sandy beaches than mixed ones. Although Etretat is considered a purely gravel beach, there exists a significant amount of underlying sand in the system that can occasionally become the main substrate of the beach after storms. Thus, even if this remains a rare event, it shows that finer material could fill up the gravels' porosity and reduce the permeability of the beach. Under this hypothesis, successive storms of moderate intensity in a cluster could potentially have a greater impact than stronger but isolated storms. This is because these storms would occur on a beach with low permeability and thus less ability to absorb wave energy. Storm 2 was preceded by a month of calm conditions, the previous storm having occurred on November 8. Before the first peak of storm 2, model results show that the permeability optimum was between 0.20 and 0.35 m/s in calm conditions, later reduced to around 0.05 m/s under more energetic conditions. These values approximately correspond to coarse and fine well sorted gravel sizes respectively (Buscombe and Masselink, 2006; Wentworth, 1922). These results suggest a strong and rapid temporal variability of the permeability of gravel beaches, with a decrease by a factor of 4 within a day. However, this questions the relevance of the strict "purely gravel" characterization of Etretat's beach, as it seems to occasionally become a "mixed sand and gravel" type of system. Indeed, considering that storms are seasonal events, the transition from pure gravel to mixed sand and gravel behavior (i.e., not necessarily resulting in surface sand) could be seasonal too. An analogous seasonal transition between beach types was documented by Casamayor et al. (2022) on a composite beach. Authors found that their composite site is behaving as a pure gravel system at winter, and as a composite system during summer due to wave climate variability and associated morphological changes. They proposed to add a seasonal component to the composite beach type of Jennings and Shulmeister (2002), and our results tend to show that it could a relevant addition for the pure gravel type as well. Moreover, the

low BSS results obtained with models of storms 5 and 7 could be partly due to the beach behaving like more like a sandy one, in which case the sediment transport equations used by XBeach-G could be obsolete.

In summary, it was possible to successfully model a portion of Storm 2 in Etretat, despite the inherent limitations of the dataset discussed earlier in this discussion section. However, the modeling capabilities remain limited by the previously mentioned data accuracy limitations, and by the conceptual simplifications of XBeach-G. Indeed, only 1D model computation is possible, which leads to ignore potentially important long-shore exchanges as demonstrated in Chapter 4 - Section 2.3.2.1, especially in the case of an oblique storm swell such as in Etretat. On this matter, storm 2 is the only modeled event during which the beach orientation was the same at all elevation (i.e., the beach face was not “twisted”, all elevations ranging from -2 to -3 degrees), with only 1 degree of clockwise rotation during the modeled period. Other storms (Appendices A) show wider spread of shoreline orientations (e.g., during storm 5, the 0 m elevation shoreline was oriented at -0.5 degrees while the +1 m one was around 2 degrees), with various magnitude of changes depending on the elevation. Hence, the alongshore processes leading to rotation can be localized and create a significant complexity, that is not considered by XBeach-G. Moreover, the results tend to show a strong daily variability of permeability, which is supported by recent observations on the spatiotemporal variability of the surface grain size of shingle beaches. However, k is imposed as spatially and temporally uniform constant, due to the difficulty in measuring this important parameter, which may limit model convergence and by extension the ability to model gravel coasts. In addition, although gravel size is strongly linked to permeability and was shown to vary in time and space as well (Horn and Walton, 2007), it is described in XBeach as spatially and temporally uniform, using one value of D50 and D90. With improved coastal monitoring and grain size mapping techniques such as those proposed by Soloy et al. (2021, 2020), it seems feasible to build observational data sets with high spatial and temporal resolution. These data could allow for a better consideration of spatiotemporal variability of permeability during storms in future enhanced models.

3.5. Conclusion

The impact of three of the most intense storms of the 2018 - 2020 period was simulated using XBeach-G, on the beach of Etretat, Normandy, France. The modeling scenarios were developed to calibrate the permeability value k in order to characterize its evolution from one day to another during a specific storm event, as well as from one storm to another. Among the modeled events, only storm 2 obtained satisfactory results with maximum BSS values of 0.63 on the first modeled day, and 0.69 on the second. These results indicate a permeability k = 0.20 m/s to 0.35 m/s and k = 0.05 m/s, respectively. These values are within the order of magnitude expected for a coarse to fine cobble beach (assuming the sediment is well sorted), which is appropriate to the expectations for this type of site.

The unsatisfactory results obtained for storms 5 and 7 are probably related to the limitations of the approach used, in particular the imprecision of the subtidal and supratidal topography, and its non-updating, and the non-consideration of the long-shore sediment transport. Indeed, times series of Beach Orientation Angle seem to indicate a significant longshore transport, uneven at different elevations and variable over time, which cannot be translated into the model.

In general, the beach profile is relatively sensitive to the permeability value k. A high value tends to build a berm at the top of the profile, while a low value results in its erosion, and the intensity of wave conditions modulates the horizontal and vertical amplitude of topographic changes. This sensitivity is well documented in the literature and is explained by the importance of water seepage in the rapid loss of wave energy during beach uprush. Thus, a value of k close to zero limits infiltration, which favors surface transport and topographic heterogeneities.

The results obtained for storm 2 show that the permeability is likely to be divided by up to 4 within 24 h during the uprush of a storm. This decrease is expected for a pebble beach with a sandy component: the mixing caused by the sudden and simultaneous movement of all sedimentary fractions during a storm will reduce the surface porosity and decrease the permeability. Porosity can be expected to increase again under calmer conditions, as the interstitial sand in the surface layers will flow down with the seepage water to the deeper layers of the beach. These results question the strict "purely gravel" characterization of Etretat's beach as it seems to occasionally become a "mixed sand and gravel" type of system, which could be a seasonal phenomenon. Thus, the spatial and temporal uniformity of k, as well as other related factors such as grain size and porosity are also limitations to modeling beach response to storm impact. However, in the absence of reliable measurements of these parameters, such simplifications are still necessary to allow modeling of gravelly systems. For this matter, a promising line of development could be to consider the granulometric observations obtained during by the methods proposed in this thesis in a modified version of XBeach-G, along with the longshore sediment transport processes.

4. Chapter conclusion

This chapter was aiming to answer the 4 last scientific questions asked in Chapter 1 - Section 4:

(1) How can we reliably monitor the morphodynamics of gravel beaches?

For this question, the Mask R-CNN algorithm was once again put to use and trained to detect the contours of water bodies on timex images. Once the model is trained, the rate of satisfactory detections is particularly high, which is a valuable feature that allows the automatic constitution of very complete data sets. The detected shoreline positions were then clustered in tidal cycle pointclouds in order to be gridded into DEMs of the intertidal zone when the light and weather conditions allow

sufficient visibility. Using this approach, it was possible to collect 2+ years of planform shoreline position in Etretat and Hautot-sur-Mer.

(2) How do beach morphodynamics respond to hydrodynamics?

The shoreline position dynamics were investigated using an EOF analysis, which allowed the identification of different types of beach movement mechanisms. In Etretat, these mechanisms are the following (sorted by decreasing importance): cross-shore translation, rollover, breathing and rotation. In Hautot-sur-Mer, identified mechanisms are different: rotation and rollover. Wavelet analysis of the variability of beach width, beach slope and beach orientation angle all indicate a link to the wave energy forcing, which varies with similar time periods, although no significant linear correlation was found.

(3) What is the spatio-temporal variability the beach surficial gravel size?

The UAV campaigns allowed us to produced maps of the distribution of pebble size on one date in Etretat, and on three different dates in Hautot-sur-Mer. These maps were used to identify patterns common to the sites, as well as others more singular. First, a systematic cross-shore gradient with coarse sediments at the bottom of the beach, and finer sediments at the top is observed at the mapped dates. The results presented in Chapter 3 Section 1.3.2.2 and Section 2 show that it is possible to observe a reverse gradient, but this was not the case here. Second, we observe assemblages of clasts sorted by size, whose number and position change from one date to another. In Hautot-sur-Mer, they are often periodic from one beach cell to another, which implies that they are influenced by groin structures. Also in Hautot-sur-Mer, we observe cusps with a coarse horn and a finer bay and with a time-varying wavelength. Finally, a reduction in mean size of up to 1 cm in 2 months was measured on the same site. Hypotheses are proposed to explain this last observation, but more data are needed to clearly identify the processes at work.

(4) What is the effect of storm events on the beach permeability and its morphology?

The XBeach-G model was used to answer this question. The model was implemented using the beach morphology estimated from VMS images in Etretat, and mean gravel size measured during a UAV campaign. Subtidal bathymetry and hydrodynamics data from different sources were used in addition to feed the model. Three storms were simulated with a daily update of the bathymetry input, and a strategy of permeability calibration using a set of selected values. The results are mixed: only one of the three storms was successfully modeled. Results of the successful scenario show that permeability is reduced by a factor of 4 within 24 hours at the beginning of the storm. Since permeability is considered a constant and homogeneous parameter over time in XBeach-G, such a large and rapid variation shows the limits of the simplifications imposed by the model. The morphological changes associated with the impact of a storm on the profile vary from one event to

another but are always sensitive to the permeability value: a higher value favors the construction of the berm, and a lower value leads to its erosion.

CONCLUSIONS AND PERSPECTIVES

1. Thesis conclusion

The main research interest of this thesis work was the hydro-morpho-sedimentary dynamics of pebble beaches, considering two pebble beaches in Normandy as study sites. Both sites are located along the French coasts of the English Channel, and are separated by a distance of 64 km. Therefore, they are considered similar in terms of tidal conditions (megatidal amplitudes) and offshore (i.e. out of the nearshore zone) wave energy (bimodal W-E and NE-SW directions, maximum wave significant height ~ 4 m), though they differ in their intrinsic characteristics. Etretat is a pure gravel and Hautot-sur-Mer is composite sand and gravel system with a low tide terrace. Each site is backed with a ~1000 m long seawall and crossed by multiple groin structures (nine and seven, respectively).

Although the dynamics of sandy beaches are well understood, those of gravel beaches are still misunderstood, and the accuracy of simulations thus remains limited. These dynamics are complex due to a large number of influential parameters such as sediment permeability, groundwater table level, gravel supply volume, sediment turnover and abrasion rates, coastal structure impact, particle entrainment threshold and many more. For many of them, very few studies have been conducted and hence scientific understanding about them remains limited. Nevertheless, permeability has long been known to play a major role in the absorption of wave energy and, by extension, in morphodynamics. During the runup, the swash lens infiltrates the sediment porosity at a rate depending on the permeability. On a sandy beach, the low permeability does not allow for a significant amount of water to infiltrate during a swash cycle (average period 5 to 20 sec). However, on a gravel beach, the infiltration is relatively increased, creating an imbalance between runup and rundown water volumes. This physical mechanism is responsible for an onshore residual current on gravel beaches, acting as a driver for transporting gravel particles and thus shaping the beach face. Therefore, gravel beach dynamics are currently understood as a set of feedback loops between morphological, hydrodynamic and sedimentary conditions. It is therefore important to consider the spatial and temporal variability of these three aspects all together to properly understand gravel beach dynamics.

To address such complexity and improve our understanding of gravel beaches hydro-morpho-sedimentary dynamics, we used a coupling between different approaches including numerical and multi-captors. Therefore, one of the first objectives of this thesis work was to quantify the spatiotemporal variability of pebble beach grain size which is the main factor controlling porosity and thus permeability. One of the current challenges is that in order to reach statistical significance, large quantities of sediment must be collected: the larger the clast, the heavier the mass to be sampled. Since the 1970s, image-based methods have been developed to reduce the cost of sampling, but they require significant expertise and processing time. To overcome these constraints, I developed a new method based on machine learning (specifically, the Mask R-CNN instance segmentation algorithm). After training on manually labeled data, the model is able to perform automatic detection, classification and contouring of non-overlapping clasts visible in the images, and in turn quantify their size, shape, position and orientation. With rapid and accurate detection, the model works well with both small

terrestrial images and large high-resolution ortho-mosaic images from drone imagery, allowing for efficient and low-cost assessment of how the morphometric characteristics of the surficial coarser clasts vary in space and time. The development of this tool has been published (Soloy et al., 2020).

After demonstrating its effectiveness on two pebble beaches in Normandy, we applied the model to five new sites located in Iceland, Ireland, Switzerland and Montana, USA, including a wide variety of conditions in terms of clast sizes and shapes. The results show that the model is able to detect clasts at these sites with the same efficiency as in Normandy. The comparison shows the ability of the model to determine the spatial heterogeneity of the sediment and its temporal changes. The model has been made available in a public repository. This work initiated an international collaboration including 13 scientific experts in various fields related to gravel sediments dynamics from 5 different laboratories and continues to grow. The results of this collaboration were presented at the AGU Fall Meeting 2021 international conference (Soloy et al., 2021a).

The next objective was to quantify the spatial and temporal variability of beaches' morphology in order to understand their dynamics. To do this, both sites were equipped with Video Monitoring Systems (VMS) installed between late 2018 and early 2019, each consisting of 3 cameras. The large amount of data incentivized the development of an automatic waterline delineation method. The Mask R-CNN algorithm was trained again to perform this task, and results show that the tool successfully detects the coastline on between 67 and 97% of the dataset, depending on the study site. These rates are significantly higher than other methods and allowed the construction of a valuable time series of continuous shoreline position measurements. Digital Elevation Models (DEM) could then be computed using this data, with vertical RMSE ranging from 22 to 33 cm, which is the same range of uncertainty as using alternative methods. The development of this approach has been described and published in a dedicated scientific paper (Soloy et al., 2021b). This application further highlights the high versatility and resilience of Mask R-CNN, which can be useful for very complex and varied types of image segmentation tasks.

The method was applied to VMS data recorded at Etretat and Hautot-sur-Mer between 2018 and 2020. The spatiotemporal variability of the coastal morphology could be studied by extracting the shoreline planform at different elevations, then identifying the main mechanisms of shoreline movement. This analysis has been published in a scientific paper (Soloy et al., 2022). An Empirical Orthogonal Function (EOF) analysis identified the principal components (PC) of pebble shoreline motion, the sum of which expresses a high degree of complexity. Despite their relative proximity, the two beaches are distinguished by different morphodynamic mechanisms including cross-shore translation, local and larger scale rotation, rollover and breathing.

Wavelet analysis of the morphological signals (beach width, slope and orientation angle) revealed that the coastline variability is expressed at similar main periods for all parameters: 2, 3, 5 and 8+ months in Etretat, 2 and 6 months in Hautot-sur-Mer. Similar periods were found when

applying the wavelet analysis to wave energy signals. Although no significant linear correlation was found between the evolution of hydro- and morphological parameters, these results tend to show that the hydrodynamic factor with the most influence on morphological dynamics is the energy of waves.

Furthermore, the spatial dispersion of surficial pebble grain sizes was mapped at both sites. The dataset remains temporally limited and consists of only one date in Etretat (2020/06/10) and three dates in Hautot-sur-Mer (2019/04/09, 2019/06/04 and 2020/06/09). Nevertheless, these data allowed us to formulate a first estimate of the temporal variability at the latter site, under summer conditions. In general, the two sites show different gravel sizes with D50 values of 5.2 cm in Etretat and 7.0 cm in Hautot-sur-Mer (temporal average). Spatial dispersion generally revealed patterns such as a cross-shore gradient, cusps and clast assemblages whose periodicity from one beach cell to its neighbors demonstrates the influence of groins on sediment dynamics. Temporal analysis revealed differences in both the mean grain size (down to -1 cm between April and June 2019 in Hautot-sur-Mer) and in the presence and position of clast assemblages. Explanations are proposed about the observed temporal variability (e.g., abrasion, percolation, rotation-related processes), but the amount of data limits the analysis to speculations. However, the need for a better knowledge and understanding of granulometric spatiotemporal variability is widely recognized by the coastal science community, and these results show promise in this regard.

Finally, the data collected was used to model the response of the beach of Etretat to the impact of three of the most intense storms that occurred during the monitoring period. The model used to perform this task is XBeach-G, a 1D non-hydrostatic model that takes into account groundwater flows (considering a global and time fixed value of permeability). Of the three events modeled, only one storm (Storm 2) showed satisfactory model performance. The results indicate a sharp decrease in permeability over 24 hours, from values corresponding to coarse gravel, to values related to fine gravel. Such a decrease tends to indicate changes in porosity, with potentially a mixing of sand and gravel happening under energetic conditions. The assumption of spatial and temporal uniformity of permeability, as well as other related factors such as grain size and porosity, are therefore important limitations to modeling the response of gravel beaches to storm impact. In the absence of reliable measurements of these parameters, however, these simplifications remain necessary for modeling purpose.

2. Research perspectives

The results of this thesis work are limited by two main factors: (1) the lack of hydrodynamic measurements close to the beach for model validation, especially during storms, and (2) the poor temporal coverage of grain-size variability measurements. Addressing such issues seems to be a key step in order to obtain a more accurate understanding of the complex dynamics of pebble systems.

The first point requires the deployment of hydrodynamic sensors in the nearshore zone. This information seems to be crucial in Hautot-sur-Mer where the association between the low tide terrace and the large tidal range influences and modulates the incident wave transformation processes. An Acoustic Doppler Current Profiler (ADCP) and a pressure gauge were recently deployed for this purpose, the results of which are being analyzed. In Etretat, these transformations are expected to be less important, but still significant, especially because of the bay morphology of this system, which tends to induce wave refraction. Discussions are underway to equip the site with an instrumented buoy. For both sites, such data will be useful to calibrate the hydrodynamic model outputs and thus improve the accuracy of the intertidal DEMs produced from VMS data, which depend on water level information. Using these results, some parameters of the surf and swash zones (breaking height and position, runup distance, etc.) could also be measured from the VMS images, which would potentially bring substantial understanding.

The second point requires the organization of regular in situ UAV measurements, at a frequency chosen depending on the scientific interest. A first campaign of daily measurements was carried out over two weeks in Hautot-sur-Mer, during the deployment of the ADCP and pressure gauge equipment. The data are being processed at the time of writing. The objective of these measurements is to estimate changes in the spatial distribution of pebbles and subsequent assemblages. They could be complemented by a strategy of deposition/detection of pebbles equipped with Passive Integrated Transponder (PIT) tags in order to track and measure the movements of individual pebbles identified. This method was tested during energetic conditions in Hautot-sur-Mer, but recovery rates remained low. Furthermore, permeability plays a crucial role in the dynamics of gravel beaches, and the position, size, shape and orientation of sedimentary patterns such as cusps or assemblages is most likely related to local spatial variations in permeability. Thus, mapping clast size on pebble beaches could be a very useful proxy for estimating permeability dispersion during deposition and its variations over time.

More generally, there are many issues and development areas concerning the future of research on gravel beach dynamics. To begin with, the consequences of climate change such as the sea level rise and the increase in intensity and frequency of extreme events call for a better understanding of these systems. Although no data exists on their global distribution, gravel beaches are not rare and their dynamics are therefore linked to those of a large number of natural environments, human installations and economic activities which are important to protect. In fact, the protective aspects of gravel beaches against wave attack are well

established. Moreover, the installation of human structures (seawalls, groins, jetties, etc.) is not without effect on coastal dynamics on a large scale and can, for example, stop longshore drift and accelerate coastal erosion in some places. In this respect, the impact on hydraulic and sediment dynamics of offshore wind farm construction projects, which are becoming increasingly popular, must be assessed. It is therefore important to conserve coastal sites where the natural presence of pebbles is in dynamic equilibrium with the environmental conditions, as in Etretat and Hautot-sur-Mer. In addition, beach nourishment and the creation of artificial beaches with pebbles are increasingly used for coastal protection projects. These solutions are effective and often considered more "natural" than the alternatives (i.e., riprap, concrete, etc.), while allowing the development of tourism activities. However, the physical properties of gravel particles (e.g., entrainment threshold, sorting mechanisms, abrasion rates, seasonal dynamics, etc.) still seem relatively unknown and understanding them is necessary to predict the long-term dynamics of these systems. In this regard, several studies following a physical experimentation approach in wave channels have already produced very useful information, and more should be carried out. For all these reasons, it is important to continue and increase the continuous monitoring of pebble beaches in Normandy, and elsewhere in the world.

Regarding the continuation of collaborations engaged during this thesis, Dr. Duccio Bertoni (University of Pisa) is preparing the monthly monitoring of an artificial pebble beach in Pisa, Italy, with the aim to highlight possible seasonal and mid- to long-term trends. In the USA, Dr. Mark Lorang (University of Montana) is evaluating the distribution of pebbles on a large remediation beach that is under construction in order to estimate the properties, quality and potential evolution of the beach. Dr. Arthur Trembanis (University of Delaware) is planning on surveilling the gravel size of mixed sand and gravel beaches his team uses as study sites. In Canada, a collaboration including Dr. Ronan Autret and Dr. David Didier (Université du Québec à Rimouski) is working to adapt the pebble measurement methodology to other types of geological artifacts. In France, the collaboration started with Dr. Pierre Stéphan (University of Western Brittany) on the Valahnukur orthoimaging data set (Iceland), which extends over 7 years, continues for the next years of data to come. Finally, in Spain, a collaboration with Dr. Erica Pellón was engaged on the processing of a historical 10-year dataset of VMS imagery in Barcelona using the methodology developed during this thesis. Results on the evolution of the shoreline position are being analyzed.

REFERENCES

Aagaard, T., 1990. Swash oscillations on dissipative beaches-Implications for beach erosion. J. Coast. Res. 738–752.

Aarninkhof, S.G.J., Turner, I.L., Dronkers, T.D.T., Caljouw, M., Nipius, L., 2003. A video-based technique for mapping intertidal beach bathymetry. Coast. Eng. 49, 275–289. https://doi.org/10.1016/S0378-3839(03)00064-4

Adams, J., 1979. Gravel Size Analysis from Photographs. J. Hydraul. Div. 105, 1247–1255.

Almeida, L.P., Masselink, G., Russell, P., Davidson, M., McCall, R., Poate, T., 2014. Swash Zone Morphodynamics of Coarse-Grained Beaches During Energetic Wave Conditions. Coast. Eng. Proc. 1, 35. https://doi.org/10.9753/icce.v34.currents.35

Almeida, L.P., Masselink, G., Russell, P.E., Davidson, M.A., 2015. Observations of gravel beach dynamics during high energy wave conditions using a laser scanner. Geomorphology 228, 15–27. https://doi.org/10.1016/j.geomorph.2014.08.019

Amarouche, K., Akpınar, A., 2021. Increasing Trend on Storm Wave Intensity in the Western Mediterranean. Climate 9, 17. https://doi.org/10.3390/cli9010011

Andriolo, U., 2018. Nearshore hydrodynamics and morphology derived from video imagery. Universidade de Lisboa (Portugal).

Andriolo, U., Almeida, L.P., Almar, R., 2018. Coupling terrestrial LiDAR and video imagery to perform 3D intertidal beach topography. Coast. Eng. 140, 232–239. https://doi.org/10.1016/j.coastaleng.2018.07.009

Atkinson, J., Esteves, L.S., 2018. Alongshore Variability in the Response of a Mixed Sand and Gravel Beach to Bimodal Wave Direction. Geosci. 2018, Vol. 8, Page 488 8, 488. https://doi.org/10.3390/GEOSCIENCES8120488

Aubrey, D.G., 1979. Seasonal patterns of onshore/offshore sediment movement. J. Geophys. Res. Ocean. 84, 6347–6354. https://doi.org/https://doi.org/10.1029/JC084iC10p06347

Austin, M., Masselink, G., 2005. Infiltration and exfiltration in the swash zone of a steep gravel beach. Implications for morphological change, in: Proceedings of the Coastal Dynamics. pp. 9–16.

Austin, M.J., Buscombe, D., 2008. Morphological change and sediment dynamics of the beach step on a macrotidal gravel beach. Mar. Geol. 249, 167–183. https://doi.org/10.1016/j.margeo.2007.11.008

Austin, M.J., Masselink, G., 2006a. Observations of morphological change and sediment transport on a steep gravel beach. Mar. Geol. 229, 59–77. https://doi.org/10.1016/j.margeo.2006.02.003

Austin, M.J., Masselink, G., 2006b. Observations of morphological change and sediment transport on a steep gravel beach. Mar. Geol. 229, 59–77. https://doi.org/10.1016/J.MARGEO.2006.02.003

Bagnold, R.A., 1940. Beach formation by waves; some model-experiments in a wave tank. J. Inst. Civ. Eng. 15, 27–52. https://doi.org/10.1680/ijoti.1940.14279

Barnard, P.L., Rubin, D.M., Harney, J., Mustain, N., 2007. Field test comparison of an autocorrelation technique for determining grain size using a digital “beachball” camera versus traditional methods. Sediment. Geol. 201, 180–195. https://doi.org/10.1016/j.sedgeo.2007.05.016

Bear, J., 1972. Dynamics of fluids in porous media. American Elsevier, New York, N.Y., and Amsterdam.

Bergillos, R.J., Masselink, G., McCall, R.T., Ortega-Sánchez, M., 2016. Modelling overwash vulnerability along mixed sand-gravel coasts with xbeach-g: Case study of playa granada, southern Spain. Proc. Coast. Eng. Conf. 35, 1–9.

Bertoni, D., Dean, S., Trembanis, A.C., Sarti, G., 2020. Multi-month sedimentological characterization of the backshore of an artificial coarse-clastic beach in Italy. Rend. Lincei 31, 65–77. https://doi.org/10.1007/s12210-019-00852-2

Bertoni, D., Sarti, G., Benelli, G., Pozzebon, A., 2012. In situ abrasion of marked pebbles on two coarse-clastic beaches (Marina di Pisa, Italy). Ital. J. Geosci. 131, 205–214. https://doi.org/10.3301/IJG.2012.04

Bertoni, D., Sarti, G., Grottoli, E., Ciavola, P., Pozzebon, A., Domokos, G., Novák-Szabó, T., 2016. Impressive abrasion rates of marked pebbles on a coarse-clastic beach within a 13-month timespan. Mar. Geol. 381, 175–180. https://doi.org/10.1016/j.margeo.2016.09.010

Billson, O., Russell, P., Davidson, M., 2019. Storm waves at the shoreline: When and where are infragravity waves important? J. Mar. Sci. Eng. 7. https://doi.org/10.3390/jmse7050139

Blossier, B., Bryan, K.R., Daly, C.J., Winter, C., 2017. Shore and bar cross-shore migration, rotation, and breathing processes at an embayed beach. J. Geophys. Res. Earth Surf. 122, 1745–1770. https://doi.org/10.1002/2017JF004227

Bluck, B.J., 1999. Clast assembling, bed-forms and structure in gravel beaches. Trans. R. Soc. Edinburgh, Earth Sci. 89, 291–323. https://doi.org/10.1017/s026359330000242x

Bluck, B.J., 1967. Sedimentation of Beach Gravels: Examples from South Wales. SEPM J. Sediment. Res. Vol. 37, 128–156. https://doi.org/10.1306/74d71672-2b21-11d7-8648000102c1865d

Boccotti, P., 2000. Wave mechanics for ocean engineering. Elsevier.

Booij, N., Ris, R.C., Holthuijsen, L.H., 1999. A third-generation wave model for coastal regions: 1. Model description and validation. J. Geophys. Res. Ocean. 104, 7649–7666.

Brayne, R.P., Lorang, M.S., Naylor, L.A., Reinhardt, L., 2020. Field-based observation of the entrainment threshold of cobbles with motion loggers. J. Coast. Res. 95, 392–397.

Brown, S.I., Dickson, M.E., Kench, P.S., Bergillos, R.J., 2019. Modelling gravel barrier response to storms and sudden relative sea-level change using XBeach-G. Mar. Geol. 410, 164–175. https://doi.org/10.1016/j.margeo.2019.01.009

Bujan, N., Cox, R., Lin, L.C., Ducrocq, C., Hwung, H.H., 2018. Semiautomatic Digital Clast Sizing of a Cobble Beach, Nantian, Taiwan. J. Coast. Res. 34, 1367–1381. https://doi.org/10.2112/JCOASTRES-D-17-00165.1

Bujan, N., Cox, R., Masselink, G., 2019. From fine sand to boulders: Examining the relationship between beach-face slope and sediment size. Mar. Geol. 417, 106012. https://doi.org/10.1016/j.margeo.2019.106012

Burdziakowski, P., Specht, C., Dabrowski, P.S., Specht, M., Lewicka, O., Makar, A., 2020. Using UAV Photogrammetry to Analyse Changes in the Coastal Zone Based on the Sopot Tombolo (Salient) Measurement Project. Sensors 2020, Vol. 20, Page 4000 20, 4000. https://doi.org/10.3390/S20144000

Burke, L.A., Kura, Y., Kassem, K., Revenga, C., Spalding, M., Mcallister, D., 2005. Coastal Ecosystems. Springer, Dordrecht, The Netherlands.

Buscombe, D., 2020. SediNet: a configurable deep learning model for mixed qualitative and quantitative optical granulometry. Earth Surf. Process. Landforms 45, 638–651. https://doi.org/10.1002/esp.4760

Buscombe, D., 2013. Transferable wavelet method for grain-size distribution from images of sediment surfaces and thin sections, and other natural granular patterns. Sedimentology 60, 1709–1732. https://doi.org/10.1111/sed.12049

Buscombe, D., Masselink, G., 2009. Grain-size information from the statistical properties of digital images of sediment. Sedimentology 56, 421–438. https://doi.org/10.1111/j.1365-

3091.2008.00977.x

Buscombe, D., Masselink, G., 2006. Concepts in gravel beach dynamics. Earth-Science Rev. 79, 33–52. https://doi.org/10.1016/j.earscirev.2006.06.003

Butler, J.B., Lane, S.N., Chandler, J.H., 2001. Automated extraction of grain-size data from gravel surfaces using digital image processing. J. Hydraul. Res. 39, 519–529. https://doi.org/10.1080/00221686.2001.9628276

Butt, T., Russell, P., Turner, I., 2001. The influence of swash infiltration–exfiltration on beach face sediment transport: onshore or offshore? Coast. Eng. 42, 35–52. https://doi.org/10.1016/S0378-3839(00)00046-6

Cambers, G., 1976. Temporal scales in coastal erosion systems. Trans. Inst. Br. Geogr. 246–256.

Carbonneau, P.E., Lane, S.N., Bergeron, N.E., 2004. Catchment-scale mapping of surface grain size in gravel bed rivers using airborne digital imagery. Water Resour. Res. 40, 1–11. https://doi.org/10.1029/2003WR002759

Carr, A.P., Blackley, M.W.L., 1974. Ideas on the origin and development of Chesil Beach, Dorset, in: Proceedings of the Dorset Natural History and Archaeological Society. pp. 9–17.

Carter, R.W.G., Orford, J.D., 1993. The Morphodynamics of Coarse Clastic Beaches and Barriers: A Short- and Long-term Perspective. Source J. Coast. Res. 158–179.

Casamayor, M., Alonso, I., Valiente, N.G., Sánchez-García, M.J., 2022. Seasonal response of a composite beach in relation to wave climate. Geomorphology 408, 108245. https://doi.org/10.1016/J.GEOMORPH.2022.108245

Castelle, B., Bujan, S., Marieu, V., Ferreira, S., 2020. 16 Years of Topographic Surveys of Rip-Channelled High-Energy Meso-Macrotidal Sandy Beach. Sci. Data 7. https://doi.org/10.1038/s41597-020-00750-5

Cazenave, A., Llovel, W., 2010. Contemporary sea level rise. Ann. Rev. Mar. Sci. 2, 145–173. https://doi.org/10.1146/ANNUREV-MARINE-120308-081105

Chassignet, E.P., Hurlburt, H.E., Smedstad, O.M., Halliwell, G.R., Hogan, P.J., Wallcraft, A.J., Baraille, R., Bleck, R., 2007. The HYCOM (HYbrid Coordinate Ocean Model) data assimilative system. J. Mar. Syst. 65, 60–83. https://doi.org/10.1016/j.jmarsys.2005.09.016

Chen, H., Sun, K., Tian, Z., Shen, C., Huang, Y., Yan, Y., 2020. BlendMask: Top-down meets bottom-up

for instance segmentation, in: Proceedings of the IEEE/CVF Conference on Computer Vision and Pattern Recognition. pp. 8573–8581.

Chen, X., Girshick, R., He, K., Dollár, P., 2019. Tensormask: A foundation for dense object segmentation, in: Proceedings of the IEEE International Conference on Computer Vision. pp. 2061–2069.

Ciavola, P., Castiglione, E., 2009. Sediment dynamics of mixed sand and gravel beaches at short timescales. J. Coast. Res. II, 1751–1755.

Coco, G., Ciavola, P., 2017. Coastal Storms.

Costa, S., 1997. Dynamique litorale et risques naturels: l'impact des aménagements, des variations du niveau marin et des modifications climatiques entre la baie de seine et la baie de somme. University of Paris I.

Costa, S., Lageat, Y., Hénaff, A., 2006. The gravel beaches of north-west France and their contribution to the dynamic of the coastal cliff-shore platform system. Ann. Geomorphol. 144, 199–214.

Costa, S., Letortu, P., Laignel, B., 2015. The Hydro-sedimentary System of the Upper-Normandy Coast: Synthesis BT - Sediment Fluxes in Coastal Areas, in: Maanan, M., Robin, M. (Eds.), . Springer Netherlands, Dordrecht, pp. 121–147. https://doi.org/10.1007/978-94-017-9260-8_6

Costa, S., Maquaire, O., Letortu, P., Thirard, G., Compain, V., Roulland, T., Medjkane, M., Davidson, R., Graff, K., Lissak, C., Delacourt, C., Duguet, T., Fauchard, C., Antoine, R., 2019. Sedimentary Coastal Cliffs of Normandy: Modalities and Quantification of Retreat. J. Coast. Res. 88, 46–60. https://doi.org/https://doi.org/10.2112/SI88-005.1

Crété-Roffet, F., Dolmiere, T., Ladret, P., Nicolas, M., 2007. The Blur Effect: Perception and Estimation with a New No-Reference Perceptual Blur Metric, in: SPIE Electronic Imaging Symposium Conf Human Vision and Electronic Imaging. San Jose, United States, p. EI 6492--16.

Dal Cin, R., 1968. "Pebble clusters": Their origin and utilization in the study of palaeocurrents. Sediment. Geol. 2, 233–241. https://doi.org/10.1016/0037-0738(68)90001-8

Davidson, M., Van Koningsveld, M., de Kruif, A., Rawson, J., Holman, R., Lamberti, A., Medina, R., Kroon, A., Aarninkhof, S., 2007. The CoastView project: Developing video-derived Coastal State Indicators in support of coastal zone management. Coast. Eng. 54, 463–475. https://doi.org/10.1016/j.coastaleng.2007.01.007

Davidson, M.A., Turner, I.L., Splinter, K.D., Harley, M.D., 2017. Annual prediction of shoreline erosion

and subsequent recovery. Coast. Eng. 130, 14–25. https://doi.org/10.1016/j.coastaleng.2017.09.008

Davidson, N.C., Dam, A.A. van, Finlayson, C.M., McInnes, R.J., Davidson, N.C., Dam, A.A. van, Finlayson, C.M., McInnes, R.J., 2019. Worth of wetlands: revised global monetary values of coastal and inland wetland ecosystem services. Mar. Freshw. Res. 70, 1189–1194. https://doi.org/10.1071/MF18391

Davies, J.L., 1980. Geographical Variation in Coastal Development (2nd edition), Longmans. ed. London.

Dean, Robert G, 1991. Equilibrium beach profiles: Characteristics and applications. J. Coast. Res. 7, 53–84.

Detert, M., Kadinski, L., Weitbrecht, V., 2018. On the way to airborne gravelometry based on 3D spatial data derived from images. Int. J. Sediment Res. 33, 84–92. https://doi.org/10.1016/j.ijsrc.2018.02.001

Detert, M., Weibrecht, V., 2013. User guide to gravelometric image analysis by basegrain, Advances in Science and Research. CRC Press, Boca Raton, FL, USA.

Dolan, R., Hayden, B.P., May, P., May, S., 1980. The reliability of shoreline change measurements from aerial photographs. Shore and beach, 48, 22–29.

Dumas, F., Pineau-Guillou, L., Lecornu, F., Le Roux, J.-F., Le Squère, B., 2014. General Introduction: PREVIMER, a French pre-operational coastal ocean forecasting capability. Mercat. Ocean.

Durnkerley, D., Foody, G., Goudie, A., Meadows, M., Montgomery, D., Nicholson, S., Spencer, T., 2016. The Dictionary of Physical Geography, 4th ed. Wiley, Hoboken, NJ, USA.

Elfrink, B., Baldock, T., 2002. Hydrodynamics and sediment transport in the swash zone: a review and perspectives. Coast. Eng. 45, 149–167. https://doi.org/10.1016/S0378-3839(02)00032-7

Esmail, M., Mahmod, W.E., Fath, H., 2019. Assessment and prediction of shoreline change using multi-temporal satellite images and statistics: Case study of Damietta coast, Egypt. Appl. Ocean Res. 82, 274–282. https://doi.org/10.1016/j.apor.2018.11.009

Fehr, R., 1987. Einfache Bestimmung der Korngrös¬senverteilung von Geschiebematerial mit Hilfe der Linienzahlanalyse (Simple detection of grain size distribution of sediment material using line-count analysis). Schweizer Ing. und Archit. 105, 1104–1109.

Finkl, C.W., 2004. Coastal classification: Systematic approaches to consider in the development of a comprehensive scheme. J. Coast. Res. 20, 166–213. https://doi.org/10.2112/1551-5036(2004)20[166:ccsatc]2.0.co;2

Flemming, N.C., 1964. Tank experiments on the sorting of beach material during cusp formation. Bull. Japan Inst. Met. 3, 249–258.

Fredsoe, J., Deigaard, R., 1992. Mechanics of coastal sediment transport. World scientific publishing company.

Gomez, B., 1983. Temporal variations in bedload transport rates: The effect of progressive bed armouring. Earth Surf. Process. Landforms 8, 41–54. https://doi.org/10.1002/esp.3290080105

Gonçalves, J.A., Henriques, R., 2015. UAV photogrammetry for topographic monitoring of coastal areas. ISPRS J. Photogramm. Remote Sens. 104, 101–111. https://doi.org/10.1016/j.isprsjprs.2015.02.009

Graham, D.J., Reid, I., Rice, S.P., 2005a. Automated sizing of coarse-grained sediments: Image-processing procedures. Math. Geol. 37, 1–28. https://doi.org/10.1007/s11004-005-8745-x

Graham, D.J., Rice, S.P., Reid, I., 2005b. A transferable method for the automated grain sizing of river gravels. Water Resour. Res. 41, 1–12. https://doi.org/10.1029/2004WR003868

Grant, U.S., 1948. Influence of the water table on beach aggradation and degradation. J. Mar. Res. 7, 655–660.

Guest, T.B., Hay, A.E., 2021. Small-scale morpho-sedimentary dynamics in the swash zone of a megatidal mixed sand–gravel beach. J. Mar. Sci. Eng. 9. https://doi.org/10.3390/jmse9040413

Guest, T.B., Hay, A.E., 2019. Timescales of beach cusp evolution on a steep, megatidal, mixed sand-gravel beach. Mar. Geol. 416, 105984. https://doi.org/10.1016/J.MARGEO.2019.105984

Guza, R.T., Thornton, E.B., 1982. Swash oscillations on a natural beach. J. Geophys. Res. Ocean. 87, 483–491.

Hack, J.T., 1960. Interpretation of erosional topography in humid temperate regions.

Hammons, T.J., 1993. Tidal Power. Proc. IEEE 81, 419–433. https://doi.org/10.1109/5.241486

Hanson, H., 1989. GENESIS - a generalized shoreline change numerical model. J. Coast. Res. 5, 1–27.

Hapke, C.J., Plant, N.G., Henderson, R.E., Schwab, W.C., Nelson, T.R., 2016. Decoupling processes and

scales of shoreline morphodynamics. Mar. Geol. 381, 42–53. https://doi.org/10.1016/j.margeo.2016.08.008

Harley, M.D., Turner, I.L., Short, A.D., 2015. New insights into embayed beach rotation: The importance of wave exposure and cross-shore processes. J. Geophys. Res. F Earth Surf. 120, 1470–1484. https://doi.org/10.1002/2014JF003390

Hay, A.E., Zedel, L., Stark, N., 2014. Sediment dynamics on a steep, megatidal, mixed sand-gravel-cobble beach. Earth Surf. Dyn. 2, 443–453. https://doi.org/10.5194/esurf-2-443-2014

Hayes, M.O., Michel, J., Betenbaugh, D. V., 2010. The intermittently exposed, coarse-grained gravel beaches of Prince William Sound, Alaska: Comparison with open-ocean gravel beaches. J. Coast. Res. 26, 4–30. https://doi.org/10.2112/08-1071.1

He, K., Gkioxari, G., Dollar, P., Girshick, R., 2017. Mask R-CNN. Proc. IEEE Int. Conf. Comput. Vis. 2017-Octob, 2980–2988. https://doi.org/10.1109/ICCV.2017.322

Heikkila, J., Silven, O., 1997. A four-step camera calibration procedure with implicit image correction, in: Proceedings of Ieee Computer Society Conference on Computer Vision and Pattern Recognition. IEEE, pp. 1106–1112.

Hine, Al.C., 1979. Mechanisms of berm development and resulting beach growth along a barrier spit complex. Sedimentology 26, 333–351. https://doi.org/10.1111/J.1365-3091.1979.TB00913.X

Holman, R., Plant, N., Holland, T., 2013. CBathy: A robust algorithm for estimating nearshore bathymetry. J. Geophys. Res. Ocean. 118, 2595–2609. https://doi.org/10.1002/jgrc.20199

Holman, R.A., 2018. Edge waves and the configuration of the shoreline, in: Handbook of Coastal Processes and Erosion. CRC Press, pp. 21–34.

Holman, R.A., Lippmann, T.C., O'Neill, P. V., Hathaway, K., 1991. Video estimation of subaerial beach profiles. Mar. Geol. 97, 225–231. https://doi.org/10.1016/0025-3227(91)90028-3

Holman, R.A., Stanley, J., 2007. The history and technical capabilities of Argus. Coast. Eng. 54, 477–491. https://doi.org/10.1016/j.coastaleng.2007.01.003

Holmes, P., Baldock, T.E., Chan, R.T.C., Neshaei, M.A.L., 1997. Beach evolution under random waves, in: Coastal Engineering 1996. pp. 3006–3019.

Horn, D., Li, L., 2006. Measurement and modelling of gravel beach groundwater response to wave run-up: effects on beach profile changes. J. Coast. Res. 22, 1241–1249.

Horn, D.P., 2002. Beach groundwater dynamics. Geomorphology 48, 121–146. https://doi.org/10.1016/S0169-555X(02)00178-2

Horn, D.P., Walton, S.M., 2007. Spatial and temporal variations of sediment size on a mixed sand and gravel beach. Sediment. Geol. 202, 509–528. https://doi.org/10.1016/j.sedgeo.2007.03.023

Hoyez, B., Girard, J., Cottard, N., 2020. The Cenomanian of the Normandy coast between the Valleuse d'Antifer and the Capde La Hève. https://doi.org/10.2110/carnets.2020.0001

Huang, Z., Huang, L., Gong, Y., Huang, C., Wang, X., 2019. Mask scoring r-cnn, in: Proceedings of the IEEE Conference on Computer Vision and Pattern Recognition. pp. 6409–6418.

Hughes, M.G., Cowell, P.J., 1987. Adjustment of Reflective Beaches to Waves. Source J. Coast. Res. 3, 153–167.

Ibbeken, H., Schleyer, R., 1986. Photo-sieving: A method for grain-size analysis of coarse-grained, unconsolidated bedding surfaces. Earth Surf. Process. Landforms 11, 59–77. https://doi.org/10.1002/esp.3290110108

Isla, F.I., 1993. Overpassing and armouring phenomena on gravel beaches. Mar. Geol. 110, 369–376. https://doi.org/10.1016/0025-3227(93)90094-C

Isla, F.I., Bujalesky, G.G., 2000. Cannibalisation of Holocene gravel beach-ridge plains, northern Tierra del Fuego, Argentina. Mar. Geol. 170, 105–122. https://doi.org/10.1016/S0025-3227(00)00069-4

Isla, F.I., Bujalesky, G.G., 1993. Saltation on gravel beaches, Tierra del Fuego, Argentina. Mar. Geol. 115, 263–270. https://doi.org/10.1016/0025-3227(93)90055-Z

Ivamy, M.C., Kench, P.S., 2006. Hydrodynamics and morphological adjustment of a mixed sand and gravel beach, Torere, Bay of Plenty, New Zealand. Mar. Geol. 228, 137–152. https://doi.org/10.1016/J.MARGEO.2006.01.002

Jara, M.S., González, M., Medina, R., 2015. Shoreline evolution model from a dynamic equilibrium beach profile. Coast. Eng. 99, 1–14. https://doi.org/10.1016/j.coastaleng.2015.02.006

Jennings, R., Shulmeister, J., 2002. A field based classification scheme for gravel beaches. Mar. Geol. 186, 211–228. https://doi.org/10.1016/S0025-3227(02)00314-6

Jongejan, R., Ranasinghe, R., Wainwright, D., Callaghan, D.P., Reyns, J., 2016. Drawing the line on coastline recession risk. Ocean Coast. Manag. 122, 87–94.

https://doi.org/10.1016/j.ocecoaman.2016.01.006

Karunarathna, H., Horrillo-Caraballo, J., Ranasinghe, R., Short, A., Reeve, D., 2012. An analysis the of cross-shore beach morphodynamics of a sandy and a composite gravel beaches. Coast. Eng. Proc. 1, 18. https://doi.org/10.9753/icce.v33.sediment.18

Karunarathna, H., Pender, D., Ranasinghe, R., Short, A.D., Reeve, D.E., 2014. The effects of storm clustering on beach profile variability. Mar. Geol. 348, 103–112. https://doi.org/10.1016/j.margeo.2013.12.007

Kellerhals, R., Bray, D.I., 1971. Sampling Procedures for Coarse Fluvial Sediments. J. Hydraul. Div. 97, 1165–1180.

Kikkert, G.A., Pokrajac, D., O'Donoghue, T., Steenhauer, K., 2013. Experimental study of bore-driven swash hydrodynamics on permeable rough slopes. Coast. Eng. 79, 42–56. https://doi.org/10.1016/J.COASTALENG.2013.04.008

Kingston, K.S., 2003. Applications of complex adaptive systems approaches to coastal systems. University of Plymouth.

Kirillov, A., Wu, Y., He, K., Girshick, R., 2020. Pointrend: Image segmentation as rendering, in: Proceedings of the IEEE/CVF Conference on Computer Vision and Pattern Recognition. pp. 9799–9808.

Klingeman, P.C.., Emmett, W.W., 1982. Gravel bedload transport processes, in: Hey, R.D., Bathurst, J.C., Thorne, C.R. (Eds.), Gravel Bed Rivers. Wiley, Chichester, UK, pp. 141–179.

Kondolf, G.M., Wolman, M.G., 1993. The sizes of salmonid spawning gravels. Water Resour. Res. 29, 2275–2285. https://doi.org/10.1029/93WR00402

Kopp, M., Tuo, Y., Disse, M., 2019. Fully automated snow depth measurements from time-lapse images applying a convolutional neural network. Sci. Total Environ. 697, 134213. https://doi.org/10.1016/j.scitotenv.2019.134213

Krumbein, W.C., Monk, G.D., 1943. Permeability as a Function of the Size Parameters of Unconsolidated Sand. Trans. AIME 151, 153–163. https://doi.org/10.2118/943153-g

Kuenen, H., 1948. The Formation of Beach Cusps. J. Geol. 56, 34–40. https://doi.org/10.1086/625475

Laboratoire Central d'Hydraulique de France (LCHF), 1972. Étude de la production des galets sur le littoral haut-normand (Study of the pebble production on the shorelines of High-Normandy).

Sitecmo, Dieppe, France.

Lacey, E.M., Peck, J.A., 1998. Long-term beach profile variations along the south shore of Rhode Island, U.S.A. J. Coast. Res. 14, 1255–1264.

Laporte-Fauret, Q., Marieu, V., Castelle, B., Michalet, R., Bujan, S., Rosebery, D., 2019. Low-Cost UAV for High-Resolution and Large-Scale Coastal Dune Change Monitoring Using Photogrammetry. J. Mar. Sci. Eng. 2019, Vol. 7, Page 63 7, 63. https://doi.org/10.3390/JMSE7030063

Larson, M., Kraus, N.C., 1994. Temporal and spatial scales of beach profile change, Duck, North Carolina. Mar. Geol. 117, 75–94. https://doi.org/10.1016/0025-3227(94)90007-8

Le Cozannet, G., Bulteau, T., Castelle, B., Ranasinghe, R., Wöppelmann, G., Rohmer, J., Bernon, N., Idier, D., Louisor, J., Salas-y-Mélia, D., 2019. Quantifying uncertainties of sandy shoreline change projections as sea level rises. Sci. Rep. 9, 1–11. https://doi.org/10.1038/s41598-018-37017-4

Le, Q. V., 2013. Building high-level features using large scale unsupervised learning. ICASSP, IEEE Int. Conf. Acoust. Speech Signal Process. - Proc. 8595–8598. https://doi.org/10.1109/ICASSP.2013.6639343

Lee, J.-M., Park, J.-Y., Choi, J.-Y., 2013. Evaluation of Sub-aerial Topographic Surveying Techniques Using Total Station and RTK-GPS for Applications in Macrotidal Sand Beach Environment. J. Coast. Res. 65, 535–540. https://doi.org/10.2112/si65-091.1

Lemke, L., Miller, J.K., 2017. EOF analysis of shoreline and beach slope variability at a feeder beach constructed within a groin field at Long Branch, New Jersey. Coast. Eng. 121, 14–25. https://doi.org/10.1016/j.coastaleng.2016.11.001

Lemos, C., Floc'h, F., Yates, M., Le Dantec, N., Marieu, V., Hamon, K., Cuq, V., Suanez, S., Delacourt, C., 2018. Equilibrium modeling of the beach profile on a macrotidal embayed low tide terrace beach. Ocean Dyn. 68, 1207–1220. https://doi.org/10.1007/s10236-018-1185-1

Leont'yev, I.O., 2018. Changes in shoreline contour due to cross-shore structure in the Sea Coastal Zone. Geomorfologiya 2018-Janua, 32–39. https://doi.org/10.7868/S0435428118030033

Leont'yev, I.O., 2007. Changes in the shoreline caused by coastal structures. Oceanology 47, 877–883. https://doi.org/10.1134/S0001437007060124

Leopold, L.B., 1970. An Improved Method for Size Distribution of Stream Bed Gravel. Water Resour. Res. 6, 1357–1366. https://doi.org/10.1029/WR006i005p01357

Letortu, P., 2013. Le recul des falaises crayeuses haut-normandes et les inondations par la mer en Manche centrale et orientale: de la qualification de l'aléa à la caracterisation des risques induits (Retreat of the High-Normandy chalk cliffs and flooding by the sea in the . University of Caen Normandy.

Levoy, F., Anthony, E.J., Monfort, O., Larsonneur, C., 2000. The morphodynamics of megatidal beaches in Normandy, France. Mar. Geol. 171, 39–59. https://doi.org/10.1016/S0025-3227(00)00110-9

López de San Román-Blanco, B., Coates, T.T., Holmes, P., Chadwick, A.J., Bradbury, A., Baldock, T.E., Pedrozo-Acuña, A., Lawrence, J., Grüne, J., 2006. Large scale experiments on gravel and mixed beaches: Experimental procedure, data documentation and initial results. Coast. Eng. 53, 349–362. https://doi.org/10.1016/J.COASTALENG.2005.10.021

Lorang, M.S., 2000. Predicting threshold entrainment mass for a boulder beach. J. Coast. Res. 16, 432–445.

Loureiro, C., Ferreira, Ó., 2020. Mechanisms and timescales of beach rotation, Sandy Beach Morphodynamics. Elsevier Ltd. https://doi.org/10.1016/b978-0-08-102927-5.00024-2

Mason, D.C., Gurney, C., Kennett, M., 2000. Beach topography mapping - a comparison of techniques. J. Coast. Conserv. 6, 113–124. https://doi.org/10.1007/BF02730475

Mason, T., Coates, T.T., 2001. Sediment transport processes on mixed beaches: A review for shoreline management. J. Coast. Res. 17, 645–657.

Mason, T., Voulgaris, G., Simmonds, D.J., Collins, M.B., 1997. Hydrodynamics and sediment transport on composite (mixed sand/shingle) and sand beaches: A comparison, in: Coastal Dynamics' 97. ASCE, pp. 48–57.

Masselink, G., Evans, D., Hughes, M.G., Russell, P., 2006. Suspended sediment transport in the swash zone of a dissipative beach 216, 169–189. https://doi.org/10.1016/j.margeo.2005.02.017

Masselink, G., Hughes, M., Knight, J., 2014a. Introduction to coastal processes and geomorphology. Routledge.

Masselink, G., Li, L., 2001. The role of swash infiltration in determining the beachface gradient: a numerical study. Mar. Geol. 176, 139–156. https://doi.org/10.1016/S0025-3227(01)00161-X

Masselink, G., Poate, T., McCall, R., van Geer, P., 2014b. Modelling storm response on gravel beaches using XBeach-G. Proc. Inst. Civ. Eng. Marit. Eng. 167, 173–191.

https://doi.org/10.1680/maen.14.00020

Masselink, G., Russell, P., Blenkinsopp, C., Turner, I., 2010. Swash zone sediment transport, step dynamics and morphological response on a gravel beach. Mar. Geol. 274, 50–68. https://doi.org/10.1016/j.margeo.2010.03.005

Masselink, G., Short, A.D., 1993. The effect of tide range on beach morphodynamics and morphology: a conceptual beach model. J. Coast. Res. 9, 785–800.

Masselink, G., Turner, I.L., 2012. Large-scale laboratory investigation into the effect of varying back-barrier lagoon water levels on gravel beach morphology and swash zone sediment transport. Coast. Eng. 63, 23–38. https://doi.org/10.1016/J.COASTALENG.2011.12.007

Maxwell, A.E., Pourmohammadi, P., Poyner, J.D., 2020. Mapping the topographic features of mining-related valley fills using mask R-CNN deep learning and digital elevation data. Remote Sens. https://doi.org/10.3390/rs12030547

McCall, R., Masselink, G., Roelvink, D., Russel, P., Davidson, M., Poate, T., 2012. MODELLING OVERWASH AND INFILTRATION ON GRAVEL BARRIERS. Coast. Eng. 33, 1–15. https://doi.org/doi.org/10.9753/icce.v33.currents.34

McCall, R.T., 2015. Process-based modelling of storm impacts on gravel coasts. University of Plymouth.

McCall, R.T., Masselink, G., Poate, T.G., Roelvink, J.A., Almeida, L.P., 2015. Modelling the morphodynamics of gravel beaches during storms with XBeach-G. Coast. Eng. 103, 52–66. https://doi.org/10.1016/j.coastaleng.2015.06.002

McCall, R.T., Masselink, G., Poate, T.G., Roelvink, J.A., Almeida, L.P., Davidson, M., Russell, P.E., 2014. Modelling storm hydrodynamics on gravel beaches with XBeach-G. Coast. Eng. 91, 231–250. https://doi.org/10.1016/j.coastaleng.2014.06.007

McCarroll, R.J., Masselink, G., Wiggins, M., Scott, T., Billson, O., Conley, D., 2019. Gravel Beach Cross- and Alongshore Response To an Extreme Event: Beach Length and Headland Proximity Controls 2735–2745. https://doi.org/10.1142/9789811204487_0234

Medina, R., Losada, M.A., Losada, I.J., Vidal, C., 1994. Temporal and spatial relationship between sediment grain size and beach profile. Mar. Geol. 118, 195–206. https://doi.org/10.1016/0025-3227(94)90083-3

Medina, R., Vidal, C., Losada, M.A., Roldan, A.J., 1993. Three-mode principal component analysis of

bathymetric data, applied to" Playa de Castilla"(Huelva, Spain), in: Coastal Engineering 1992. pp. 2265–2278.

Medjkane, M., Maquaire, O., Costa, S., Roulland, T., Letortu, P., Fauchard, C., Antoine, R., Davidson, R., 2018. High-resolution monitoring of complex coastal morphology changes: cross-efficiency of SfM and TLS-based survey (Vaches-Noires cliffs, Normandy, France). Landslides 15, 1097–1108. https://doi.org/10.1007/S10346-017-0942-4/FIGURES/11

Mendoza, E.T., Trejo-Rangel, M.A., Salles, P., Appendini, C.M., Lopez-Gonzalez, J., Torres-Freyermuth, A., 2013. Storm characterization and coastal hazards in the Yucatan Peninsula. J. Coast. Res. 65, 790–795. https://doi.org/10.2112/si65-134.1

Meur-Férec, C., Deboudt, P., Morel, V., 2008. Coastal risks in France: An integrated method for evaluating vulnerability. J. Coast. Res. 24, 178–189. https://doi.org/10.2112/05-0609.1/28786/COASTAL-RISKS-IN-FRANCE-AN-INTEGRATED-METHOD-FOR

Michaud, H., Pasquet, A., Baraille, R., Leckler, F., Aouf, L., Dalphinet, A., Huchet, M., Roland, A., Dutour-Sikiric, M., Ardhuin, F., others, Dutour Sikirić, M., Ardhuin, F., Filipot, J.-F., 2015. Implementation of the new French operational coastal wave forecasting system and application to a wave-current interaction study, in: 14th International Workshop on Wave Hindcasting and Forecasting, and 5 Coastal Hazard Symposium.

Miller, J.K., Dean, R.G., 2007. Shoreline variability via empirical orthogonal function analysis: Part I temporal and spatial characteristics. Coast. Eng. 54, 111–131. https://doi.org/10.1016/j.coastaleng.2006.08.013

Molina, R., Manno, G., Re, C. Lo, Anfuso, G., Ciraolo, G., 2019. Storm energy flux characterization along the mediterranean coast of Andalusia (Spain). Water (Switzerland) 11, 1–14. https://doi.org/10.3390/w11030509

Montaño, J., Coco, G., Antolínez, J.A.A., Beuzen, T., Bryan, K.R., Cagigal, L., Castelle, B., Davidson, M.A., Goldstein, E.B., Ibaceta, R., Idier, D., Ludka, B.C., Masoud-Ansari, S., Méndez, F.J., Murray, A.B., Plant, N.G., Ratliff, K.M., Robinet, A., Rueda, A., Sénéchal, N., Simmons, J.A., Splinter, K.D., Stephens, S., Townend, I., Vitousek, S., Vos, K., 2020. Blind testing of shoreline evolution models. Sci. Rep. 10, 1–10. https://doi.org/10.1038/s41598-020-59018-y

Morton, R.A., Leach, M.P., Paine, J.G., Cardoza, M.A., Mortont, R.A., Leacht, M.P., Painet, J.G., Car, M.A., 1993. Monitoring Beach Changes Using GPS Surveying Te stability and rates of shoreline movement , which. J. Coast. Res. 9, 702–720.

Munk, W.H., 1950. Origin and Generafion of Waves, in: Proceedings of First Conference on Coastal Engineering. Long Beach, California, pp. 51–57.

Nadler, S., 2012. Comportement d ’ un milieu granulaire soumis ` a des vibrations horizontales : Etudes num ´ eriques et exp ´ erimentales ebastien Nadler To cite this version : Ecole Nationale Supérieure des Mines de Saint-Etienne.

Napier City Concil, 2007. The dynamics of mixed sand-and-gravel beaches and the Hawke’s Bay monitoring programme.

Neumann, B., Vafeidis, A.T., Zimmermann, J., Nicholls, R.J., 2015. Future Coastal Population Growth and Exposure to Sea-Level Rise and Coastal Flooding - A Global Assessment. PLoS One 10, e0118571. https://doi.org/10.1371/JOURNAL.PONE.0118571

Nex, F., Remondino, F., 2014. UAV for 3D mapping applications: A review. Appl. Geomatics 6, 1–15. https://doi.org/10.1007/s12518-013-0120-x

Nicholls, R.J., Wong, P.P., Burkett, V.R., Codignotto, J.O., Hay, J.E., McLean, R.F., Ragoonaden, S., Woodroffe, C.D., 2007. Coastal systems and low-lying areas, Cambridge. ed, Climate Change 2007: Impacts, Adaptation and Vulnerability. Contribution ofWorking Group II to the Fourth Assessment Report of the Intergovernmental Panel on Climate Change. Cambridge, UK.

Nie, S., Jiang, Z., Zhang, H., Cai, B., Yao, Y., 2018. Inshore ship detection based on mask r-cnn. Int. Geosci. Remote Sens. Symp. 2018-July, 693–696. https://doi.org/10.1109/IGARSS.2018.8519123

Nolan, T.J., Kirk, R.M., Shulmeister, J., 1999. Beach cusp morphology on sand and mixed sand and gravel beaches, South Island, New Zealand. Mar. Geol. 157, 185–198. https://doi.org/10.1016/S0025-3227(98)00150-9

Odezulu, C.I., Lorenzo-Trueba, J., Wallace, D.J., Anderson, J.B., 2018. Follets Island: A case of unprecedented change and transition from rollover to subaqueous shoals. Barrier Dyn. Response to Chang. Clim. 147–174. https://doi.org/10.1007/978-3-319-68086-6_5

Ojeda, E., Appendini, C.M., Mendoza, E.T., 2017. Storm-wave trends in Mexican waters of the Gulf of Mexico and Caribbean Sea. Nat. Hazards Earth Syst. Sci. 17, 1305–1317. https://doi.org/10.5194/nhess-17-1305-2017

Orford, J., Anthony, E., 2022. Coastal Gravel Systems, Second Edi. ed, Treatise on Geomorphology. Elsevier. https://doi.org/10.1016/b978-0-12-818234-5.00072-9

Orford, J., Jennings, S.C., Forbes, D.L., 2001. Origin, development, reworking and breakdown of gravel-dominated coastal barriers in Atlantic Canada: future scenarios for the British coast., in: Packham, J.R., Randall, R.E., Barnes, R.S.K., Neal, A. (Eds.), British Shingles. Westbury Academic and Scientific Publishing, pp. 23–55.

Orford, J.D., 2020. Early (1973-4) Experiments on Gravel Beach Morphodynamics. J. Coast. Res. 62–68. https://doi.org/10.2307/48639082

Orford, J.D., 1975. Discrimination of particle zonation on a pebble beach. Sedimentology 22, 441–463. https://doi.org/10.1111/j.1365-3091.1975.tb01640.x

Osorio, A.F., Medina, R., Gonzalez, M., 2012. An algorithm for the measurement of shoreline and intertidal beach profiles using video imagery: PSDM. Comput. Geosci. 46, 196–207. https://doi.org/10.1016/j.cageo.2011.12.008

Pasquet, A., Michaud, H., Aouf, L., Baraille, R., Bru, C., Correard, S., Gouillon, F., Jourdan, D., Morvan, G., Ohl, P., Paradis, D., 2014. Implémentation d'un nouveau modèle opérationnel de prévision des vagues et surcotes marines, in: Acte Des XIIIiemes Journées Nationales Génie Côtier-Génie Civil, Dunkerque, France. Dunkerque, France. https://doi.org/10.5150/jngcgc.2014.017

Perez, L., Wang, J., 2017. The Effectiveness of Data Augmentation in Image Classification using Deep Learning. arXiv Prepr.

Pintado-Patiño, J.C., Torres-Freyermuth, A., Puleo, J.A., Pokrajac, D., 2015. On the role of infiltration and exfiltration in swash zone boundary layer dynamics. J. Geophys. Res. Ocean. 120, 6329–6350. https://doi.org/10.1002/2015JC010806

Pitman, S.J., Jol, H.M., Shulmeister, J., Hart, D.E., 2019. Storm response of a mixed sand gravel beach ridge plain under falling relative sea levels: A stratigraphic investigation using ground penetrating radar. Earth Surf. Process. Landforms 44, 1610–1617. https://doi.org/10.1002/ESP.4598

Plant, N.G., Aarninkhof, S.G.J., Turner, I.L., Kingston, K.S., 2007. The performance of shoreline detection models applied to video imagery. J. Coast. Res. 23, 658–670. https://doi.org/10.2112/1551-5036(2007)23[658:TPOSDM]2.0.CO;2

Plant, N.G., Holman, R.A., 1997. Intertidal beach profile estimation using video images. Mar. Geol. 140, 1–24. https://doi.org/10.1016/S0025-3227(97)00019-4

Poate, T., Masselink, G., Davidson, M., McCall, R., Russell, P., Turner, I., 2013. High frequency in-situ

field measurements of morphological response on a fine gravel beach during energetic wave conditions. Mar. Geol. 342, 1–13. https://doi.org/10.1016/j.margeo.2013.05.009

Poate, T.G., McCall, R.T., Masselink, G., 2016. A new parameterisation for runup on gravel beaches. Coast. Eng. 117, 176–190. https://doi.org/10.1016/j.coastaleng.2016.08.003

Pollard, J.A., 2020. Gravel barrier dynamics , coastal erosion and flooding risk.

Pollard, J.A., Spencer, T., Brooks, S.M., Christie, E.K., Möller, I., 2020. Understanding spatio-temporal barrier dynamics through the use of multiple shoreline proxies. Geomorphology 354, 107058. https://doi.org/10.1016/J.GEOMORPH.2020.107058

Pontee, N.I., Pye, K., Blott, S.J., 2004. Morphodynamic Behaviour and Sedimentary Variation of Mixed Sand and Gravel Beaches, Suffolk, UK. Source J. Coast. Res. 20, 256–276.

Powell, K.A., 1990. Predicting short term profile response for shingle beaches. Hydraulics Research Wallingford.

Purinton, B., Bookhagen, B., 2019. Introducing PebbleCounts: A grain-sizing tool for photo surveys of dynamic gravel-bed rivers. Earth Surf. Dyn. 7, 859–877. https://doi.org/10.5194/esurf-7-859-2019

Qiao, Y., Truman, M., Sukkarieh, S., 2019. Cattle segmentation and contour extraction based on Mask R-CNN for precision livestock farming. Comput. Electron. Agric. 165, 104958. https://doi.org/10.1016/j.compag.2019.104958

Ranasinghe, R., Callaghan, D., Stive, M.J.F., 2012. Estimating coastal recession due to sea level rise: Beyond the Bruun rule. Clim. Change 110, 561–574. https://doi.org/10.1007/s10584-011-0107-8

Ratliff, K.M., Murray, A.B., 2014. Modes and emergent time scales of embayed beach dynamics. Geophys. Res. Lett. 41, 7270–7275. https://doi.org/10.1002/2014GL061680

Reeve, D., Li, Y., Lark, M., Simmonds, D., 2007. An investigation of the multi-scale temporal variability of beach profiles at Duck using wavelet packet transforms. Coast. Eng. 54, 401–415. https://doi.org/10.1016/j.coastaleng.2006.11.008

Ren, S., He, K., Girshick, R., Sun, J., 2016. Faster R-CNN: Towards Real-Time Object Detection with Region Proposal Networks. arXiv1506.01497 [cs] 39, 1137–1149. https://doi.org/10.1109/TPAMI.2016.2577031

Roberts, T.M., Wang, P., Puleo, J.A., 2013. Storm-driven cyclic beach morphodynamics of a mixed sand and gravel beach along the Mid-Atlantic Coast, USA. Mar. Geol. 346, 403–421. https://doi.org/10.1016/J.MARGEO.2013.08.001

Robinet, A., Castelle, B., Idier, D., Harley, M.D., Splinter, K.D., 2020. Controls of local geology and cross-shore/longshore processes on embayed beach shoreline variability. Mar. Geol. 422, 106118. https://doi.org/10.1016/j.margeo.2020.106118

Roelvink, D., Reniers, A., Van Dongeren, A., Van Thiel de Vries, J., Lescinski, J., McCall, R., 2010. XBeach model description and manual. Unesco-IHE Inst. Water Educ. Deltares Delft Univ. Tecnhology. Rep. June 21, 2010.

Roelvink, D., Reniers, A., van Dongeren, A., van Thiel de Vries, J., McCall, R., Lescinski, J., 2009. Modelling storm impacts on beaches, dunes and barrier islands. Coast. Eng. 56, 1133–1152. https://doi.org/10.1016/j.coastaleng.2009.08.006

ROL, 2019. Réseau d'observation du littoral de Normandie et des Hauts-de-France [WWW Document]. URL www.rolnp.fr

Román-Rivera, M.A., Ellis, J.T., 2019. A synthetic review of remote sensing applications to detect nearshore bars. Mar. Geol. 408, 144–153. https://doi.org/10.1016/j.margeo.2018.12.003

Rubin, D.M., 2004. A simple autocorrelation algorithm for determining grain size from digital images of sediment. J. Sediment. Res. 74, 160–165. https://doi.org/10.1306/052203740160

Ruiz de Alegria-Arzaburu, A., Masselink, G., 2010. Storm response and beach rotation on a gravel beach, Slapton Sands, U.K. Mar. Geol. 278, 77–99. https://doi.org/10.1016/j.margeo.2010.09.004

Salameh, E., Frappart, F., Almar, R., Baptista, P., Heygster, G., Lubac, B., Raucoules, D., Almeida, L.P., Bergsma, E.W.J., Capo, S., De Michele, M.D., Idier, D., Li, Z., Marieu, V., Poupardin, A., Silva, P.A., Turki, I., Laignel, B., 2019. Monitoring Beach Topography and Nearshore Bathymetry Using Spaceborne Remote Sensing: A Review. Remote Sens. 11. https://doi.org/10.3390/rs11192212

Sarti, G., Bertoni, D., 2007. Monitoring backshore and foreshore gravel deposits on a mixed sand and gravel beach (Apuane-Versilia coast, Tuscany, Italy). GeoActa 6, 73–81.

She, K., Road, L., House, G., Water, A., 2007. Effect of permeability on the performance of mixed sand-gravel beaches. Coast. Sediments '07, Am. Soc. Civ. Eng. 1–11. https://doi.org/10.1061/40926(239)39

Shelhamer, E., Long, J., Darrell, T., 2017. Fully Convolutional Networks for Semantic Segmentation. IEEE Trans. Pattern Anal. Mach. Intell. 39, 640–651. https://doi.org/10.1109/TPAMI.2016.2572683

SHOM, 2015. MNT Bathymétrique de façade Atlantique (Projet Homonim), Descriptif de contenu du produit externe. https://doi.org/doi.org/10.17183/MNT_ATL100m_HOMONIM_WGS84

Short, A.D., 2012. Coastal processes and beaches. Nat. Educ. Knowl. 3, 15.

Short, A.D., 1999. Handbook of Beach and Shoreface Morphodynamics. Willey, Chichester.

Short, A.D., Trembanis, A.C., Turner, I.L., 2000. Beach oscillation, rotation and the Southern Oscillation, Narrabeen Beach, Australia. Coast. Eng. 2000 - Proc. 27th Int. Conf. Coast. Eng. ICCE 2000 276. https://doi.org/10.1061/40549(276)191

Short, A.D., Woodroffe, C.D., 2009. The coast of Australia. Cambridge University Press.

Silva, A.N., Taborda, R., Catalão, J., Freire, P., 2009. DTM extraction using video-monitoring techniques: Application to a fetch limited beach. J. Coast. Res. I, 203–207.

Sime, L.C., Ferguson, R.I., 2003. Information on Grain Sizes in Gravel-Bed Rivers By Automated Image Analysis. J. Sediment. Res. 73, 630–636. https://doi.org/10.1306/112102730630

Simon, B., 2007. La marée océanique côtière, Institut O. ed. Concours financier du Gouvernement de Monaco, Paris.

Small, C., Nicholls, R.J., 2003. A global analysis of human settlement in coastal zones. J. Coast. Res. 19, 584–599.

Solano, C.L., Turki, E.I., Hamdi, Y., Soloy, A., Costa, S., Laignel, B., Barceló, Á.D.G., Abcha, N., Jacono, D., Lafite, R., 2022. Dynamics of Nearshore Waves during Storms: Case of the English Channel and the Normandy Coasts. Water (Switzerland) 14. https://doi.org/10.3390/w14030321

Soloy, A., Grottoli, E., Lorang, M.S., De Graffenried, B., Pascal, I., Bertoni, D., Turki, I., Lecoq, N., Jackson, D.W., Guisado-Pintado, E., Ancey, C., Trembanis, A.C., Laignel, B., 2021a. Mapping the size and shape of coarse clasts using Mask R-CNN: spatial and temporal variability over six different study sites including sea shores, and lake and river banks, in: EP34A - Grains to Satellites: Sediment and Hydrological Processes Across Scales II Oral. New Orleans, USA.

Soloy, A., Turki, I., Fournier, M., Costa, S., Peuziat, B., Lecoq, N., 2020. A deep learning-based method for quantifying and mapping the grain size on pebble beaches. Remote Sens. 12, 1–23.

https://doi.org/10.3390/rs12213659

Soloy, A., Turki, I., Lecoq, N., Gutiérrez Barceló, Á.D., Costa, S., Laignel, B., Bazin, B., Soufflet, Y., Le Louargant, L., Maquaire, O., 2021b. A fully automated method for monitoring the intertidal topography using Video Monitoring Systems. Coast. Eng. 103894. https://doi.org/10.1016/j.coastaleng.2021.103894

Soloy, A., Turki, I., Lecoq, N., Solano, C.L., Laignel, B., 2022. Spatio-temporal variability of the morpho-sedimentary dynamics observed on two gravel beaches in response to hydrodynamic forcing. Mar. Geol. 106796. https://doi.org/https://doi.org/10.1016/j.margeo.2022.106796

Stark, N., Hay, A.E., 2016. Pebble and cobble transport on a steep, mega-tidal, mixed sand and gravel beach. Mar. Geol. 382, 210–223. https://doi.org/10.1016/j.margeo.2016.10.012

Stark, N., Hay, A.E., Cheel, R., Lake, C.B., 2014. The impact of particle shape on the angle of internal friction and the implications for sediment dynamics at a steep, mixed sand-gravel beach. Earth Surf. Dyn. 2, 469–480. https://doi.org/10.5194/esurf-2-469-2014

Steers, J.A., 1965. The Coastline of England and Wales. Cambridge University Press, New York.

Strunz, G., Post, J., Zosseder, K., Wegscheider, S., Mück, M., Riedlinger, T., Mehl, H., Dech, S., Birkmann, J., Gebert, N., Harjono, H., Anwar, H.Z., Sumaryono, Khomarudin, R.M., Muhari, A., 2011. Tsunami risk assessment in Indonesia. Nat. Hazards Earth Syst. Sci. 11, 67–82. https://doi.org/10.5194/nhess-11-67-2011

Sutherland, J., Peet, A.H., Soulsby, R.L., 2004. Evaluating the performance of morphological models. Coast. Eng. 51, 917–939. https://doi.org/https://doi.org/10.1016/j.coastaleng.2004.07.015

Talavera, L., Río, L. Del, Benavente, J., Barbero, L., López-Ramírez, J.A., 2018. UAS & SfM-based approach to Monitor Overwash Dynamics and Beach Evolution in a Sandy Spit. J. Coast. Res. 85, 221–225. https://doi.org/10.2112/SI85-045.1

Tolman, H.L., 2009. User manual and system documentation of WAVEWATCH-IIITM version 3.14. Tech. note 220.

Turki, I., Medina, R., Gonzalez, M., Coco, G., 2013. Natural variability of shoreline position: Observations at three pocket beaches. Mar. Geol. 338, 76–89. https://doi.org/10.1016/j.margeo.2012.10.007

Turner, I., Leyden, V., Symonds, G., McGRATH, J., Jackson, A., Jancar, T., Aarninkhof, S.G.J., Elshoff, I.E., 2001. Comparison of observed and predicted coastline changes at the gold coast artificial

(surfing) reef, Sydney, Australia, in: Proceedings of the International Conference on Coastal Engineering.

Turner, I.L., Aarninkhof, S.G.J., Dronkers, T.D.T., McGrath, J., 2004. CZM applications of argus coastal imaging at the Gold Coast, Australia. J. Coast. Res. 20, 739–752. https://doi.org/10.2112/1551-5036(2004)20[739:caoaci]2.0.co;2

Turner, I.L., Harley, M.D., Short, A.D., Simmons, J.A., Bracs, M.A., Phillips, M.S., Splinter, K.D., 2016. A multi-decade dataset of monthly beach profile surveys and inshore wave forcing at Narrabeen, Australia. Sci. Data 3, 1–13. https://doi.org/10.1038/sdata.2016.24

Ulrich, S., Schröter, M., Swinney, H.L., 2007. Influence of friction on granular segregation. Phys. Rev. E 76, 24–26. https://doi.org/10.1103/physreve.76.042301

Uunk, L., Wijnberg, K.M., Morelissen, R., 2010. Automated mapping of the intertidal beach bathymetry from video images. Coast. Eng. 57, 461–469. https://doi.org/10.1016/j.coastaleng.2009.12.002

Valentini, N., Saponieri, A., Molfetta, M.G., Damiani, L., 2017. New algorithms for shoreline monitoring from coastal video systems. Earth Sci. Informatics 10, 495–506. https://doi.org/10.1007/s12145-017-0302-x

Van Rijn, L.C., 2007. Unified view of sediment transport by currents and waves. III: Graded beds. J. Hydraul. Eng. 133, 761–775.

Van Rijn, L.C., Wasltra, D.J.R., Grasmeijer, B., Sutherland, J., Pan, S., Sierra, J.P., 2003. The predictability of cross-shore bed evolution of sandy beaches at the time scale of storms and seasons using process-based profile models. Coast. Eng. 47, 295–327. https://doi.org/10.1016/S0378-3839(02)00120-5

Van Wellen, E., Chadwick, A.J., Mason, T., 2000. A review and assessment of longshore sediment transport equations for coarse-grained beaches. Coast. Eng. 40, 243–275. https://doi.org/10.1016/S0378-3839(00)00031-4

Verdú, J.M., Batalla, R.J., Martínez-Casasnovas, J.A., 2005. High-resolution grain-size characterisation of gravel bars using imagery analysis and geo-statistics. Geomorphology 72, 73–93. https://doi.org/10.1016/j.geomorph.2005.04.015

Vos, K., Harley, M.D., Splinter, K.D., Walker, A., Turner, I.L., 2020. Beach Slopes From Satellite-Derived Shorelines. Geophys. Res. Lett. 47, 0–2. https://doi.org/10.1029/2020GL088365

Wadell, H., 1932. Volume, shape, and roundness of rock particles. J. Geol. 40, 443–451.

Wainwright, D.J., Roshanka, R., Callaghan, D.P., Woodroffe, C.D., Jongejan, R., Dougherty, A.J., Rogers, K., Cowell, P.J., 2015. Moving from deterministic towards probabilistic coastal hazard and risk assessment : development of a modelling framework and application to. Coast. Eng. 92–99.

Wang, X., Zhang, R., Kong, T., Li, L., Shen, C., 2020. SOLOv2: Dynamic, Faster and Stronger. arXiv Prepr. arXiv2003.10152.

Wentworth, C.K., 1922. A scale of grade and class terms for clastic sediments. J. Geol. 30, 377–392.

Westoby, M.J., Brasington, J., Glasser, N.F., Hambrey, M.J., Reynolds, J.M., 2012. "Structure-from-Motion" photogrammetry: A low-cost, effective tool for geoscience applications. Geomorphology 179, 300–314. https://doi.org/10.1016/j.geomorph.2012.08.021

Williams, A.T., Caldwell, N.E., 1988. Particle size and shape in pebble-beach sedimentation. Mar. Geol. 82, 199–215. https://doi.org/10.1016/0025-3227(88)90141-7

Winant, C.D., Inman, D.L., Nordstrom, C.E., 1975. Description of seasonal beach changes using empirical eigenfunctions. J. Geophys. Res. 80, 1979–1986. https://doi.org/https://doi.org/10.1029/JC080i015p01979

Wolf, J., Woolf, D., Bricheno, L., 2020. Impacts of climate change on storms and waves relevant to the coastal and marine environment around the UK. MCCIP Sci. Rev. 2020, 132–157. https://doi.org/doi.org/10.14465/2020.arc07.saw

Wolman, M.G., 1954. A method of sampling coarse river-bed material. Trans. Am. Geophys. Union 35, 951–956.

Wright, L.D., Short, A.D., 1984. Morphodynamic variability of surf zones and beaches: A synthesis. Mar. Geol. 56, 93–118. https://doi.org/10.1016/0025-3227(84)90008-2

Yang, F., Feng, T., Xu, G., Chen, Y., 2020. R-CNN, Applied method for water-body segmentation based on mask. J. Appl. Remote Sens. 14, 014502. https://doi.org/https://doi.org/10.1117/1.JRS.14.014502

Yates, M.L., Guza, R.T., O'Reilly, W.C., 2009. Equilibrium shoreline response: Observations and modeling. J. Geophys. Res. Ocean. 114, 1–16. https://doi.org/10.1029/2009JC005359

Zhao, K., Kang, J., Jung, J., Sohn, G., Street, K., Drive, M., York, N., Mb, O.N., 2018. Building Extraction

from Satellite Images Using Mask R-CNN with Building Boundary Regularization. CVPR Work. 247–251.

Zhao, S., Zhang, D.M., Huang, H.W., 2020. Deep learning–based image instance segmentation for moisture marks of shield tunnel lining. Tunn. Undergr. Sp. Technol. 95, 103156. https://doi.org/10.1016/j.tust.2019.103156

Zingg, T., 1935. Beitrag zur schotteranalyse. ETH Zurich.

APPENDICES

A. Wavelet spectrums

A.1. Morphodynamics

A.1.1. Beach width (BW)

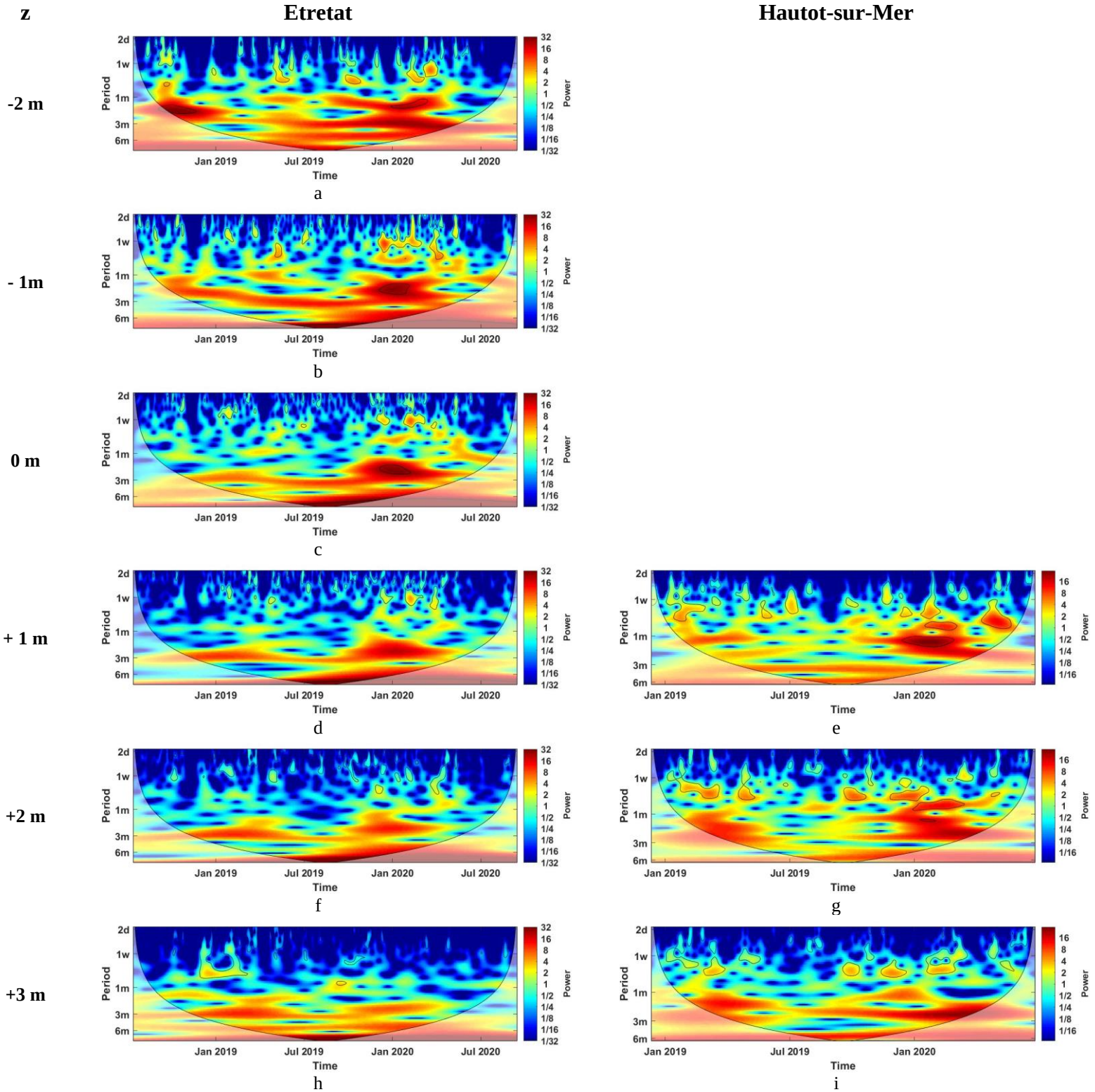

Figure 72 - Wavelet spectrums of beach width (BW) at various elevations in Etretat (left) and Hautot-sur-Mer (right)

A.1.1. Beach orientation angle (BOA)

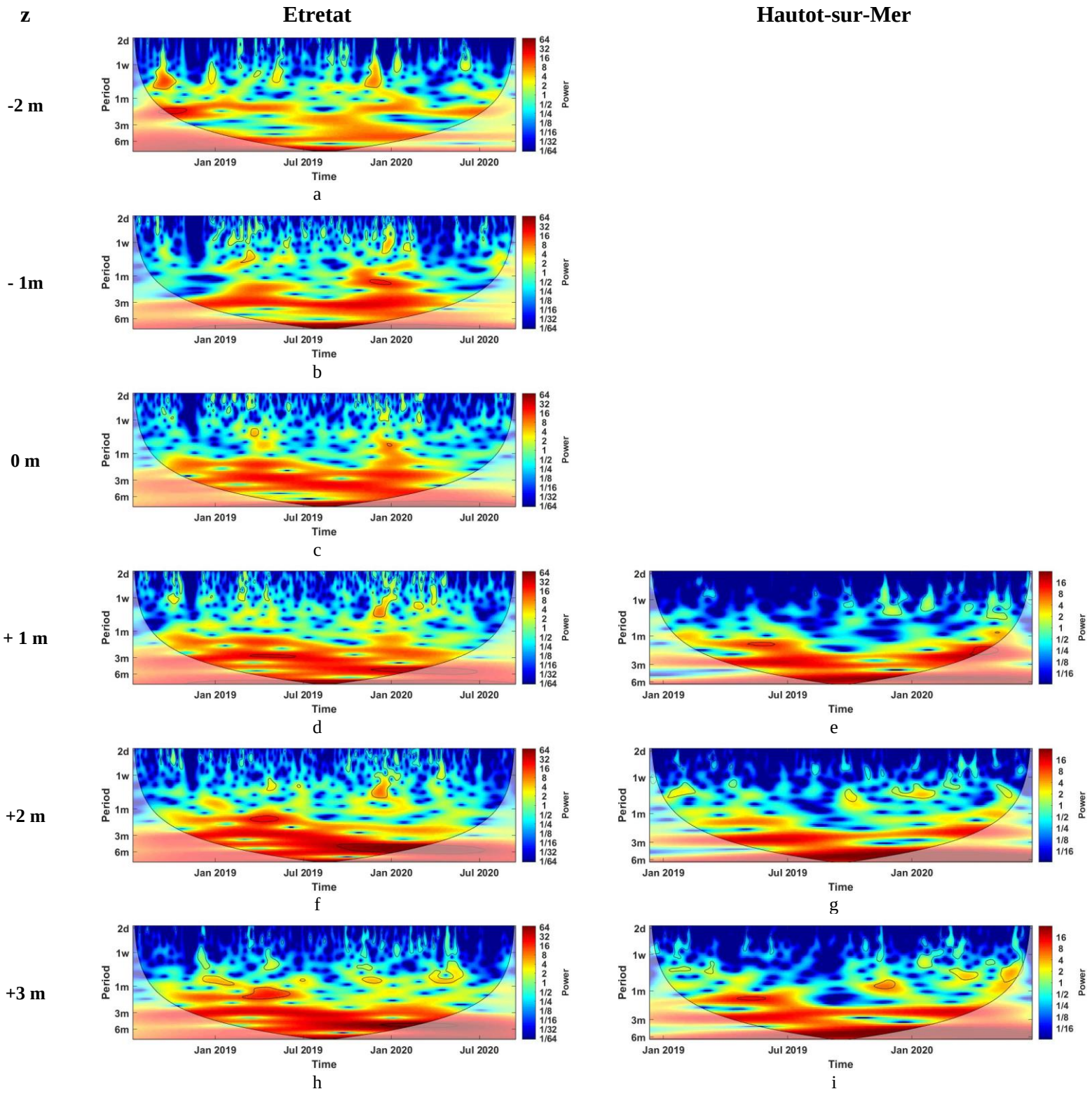

Figure 73 - Wavelet spectrums of beach orientation angle (BOA) at various elevations (z) in Etretat (left) and Hautot-sur-Mer (right)

A.1.1. Beach slope (BS)

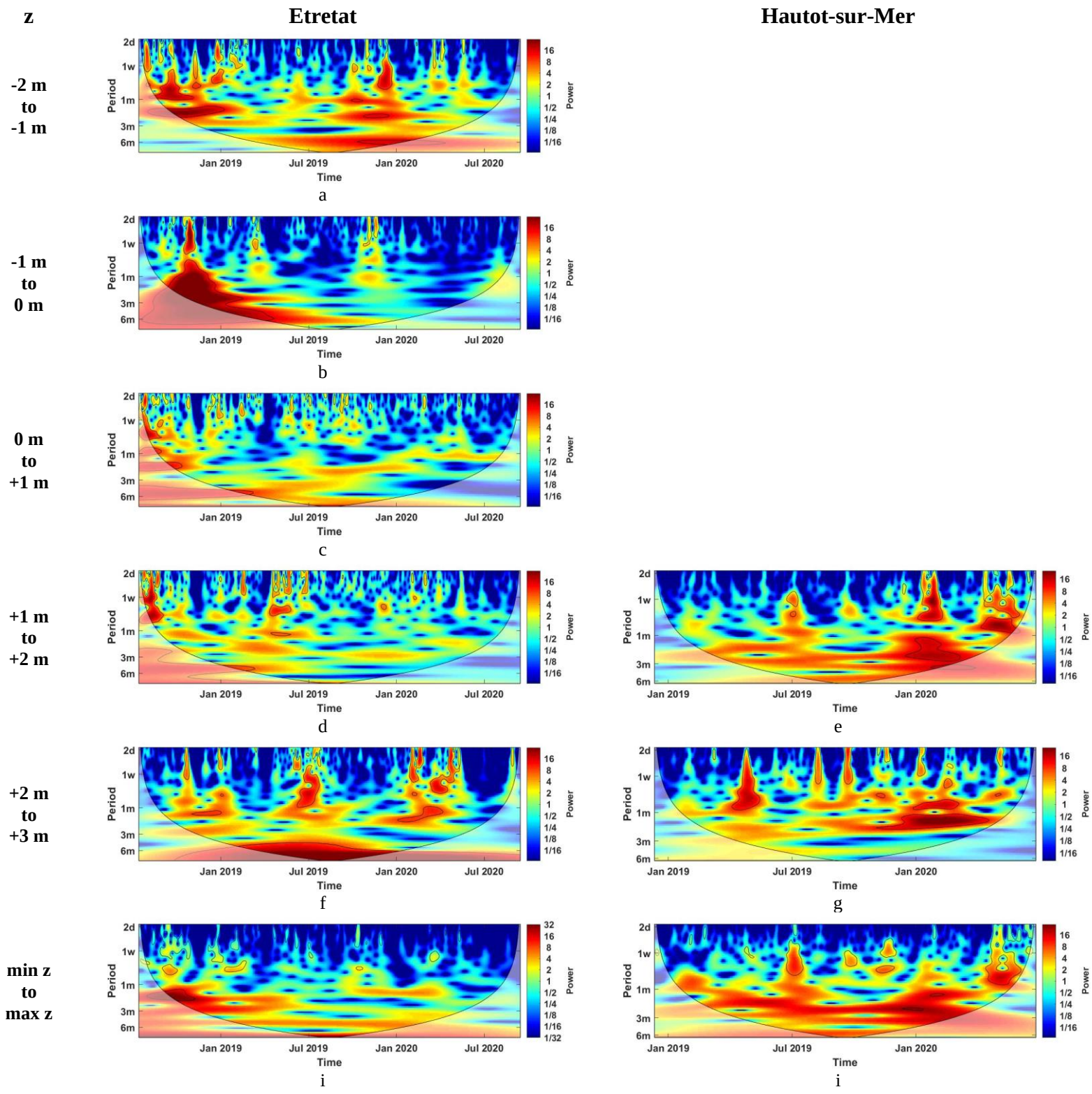

Figure 74 - Wavelet spectrums of beach slope (BS) between various elevations (z) in Etretat (left) and Hautot-sur-Mer (right)

A.1.1. EOF principal components (PC)

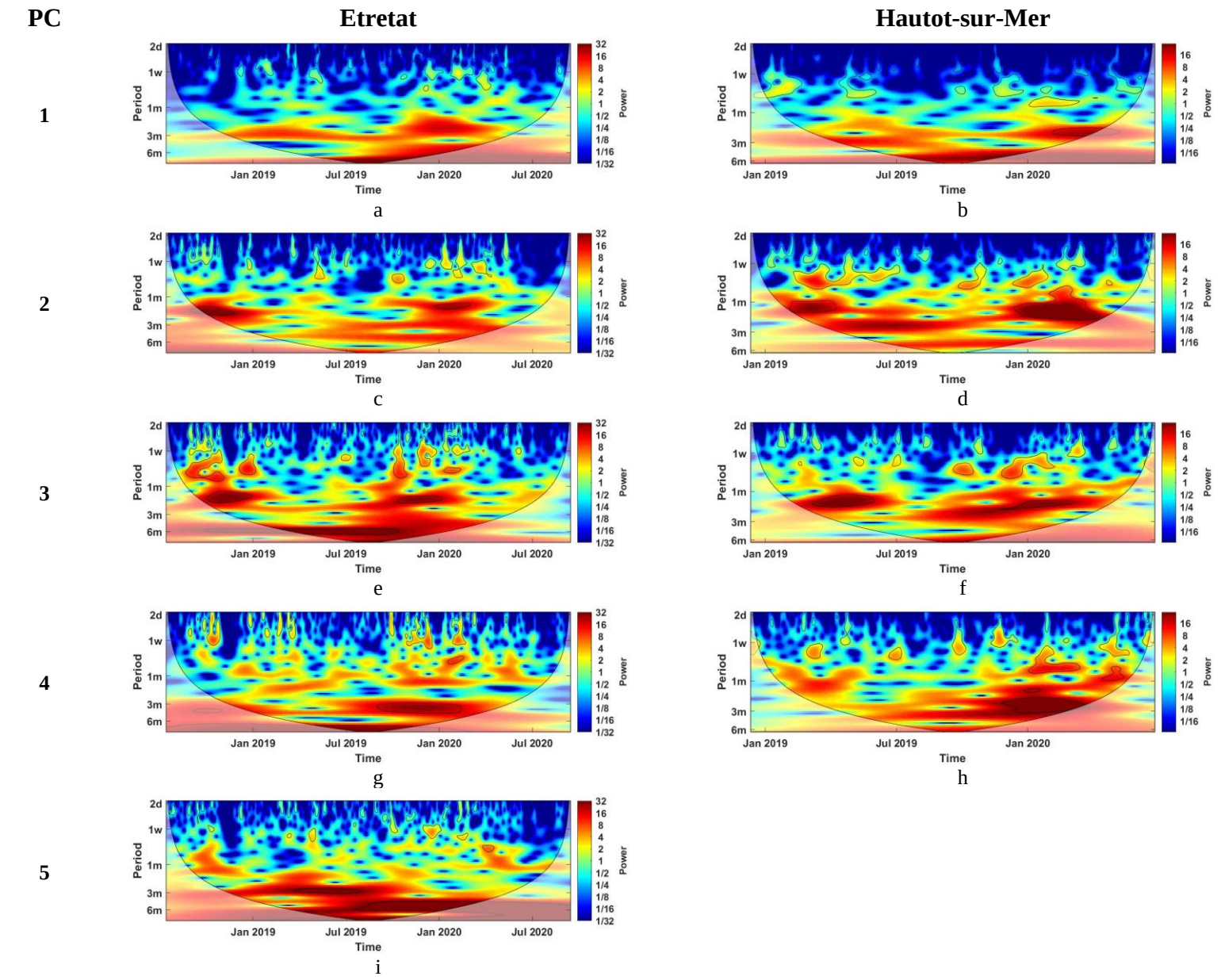

Figure 75 - Wavelet spectrums of the temporal eigenfunctions $C_k(t)$ resulting from the EOF analysis applied to a dataset of 3D daily shoreline position in Etretat (left) and Hautot-sur-Mer (right). Each row corresponds to a specific principal component (PC).

A.2. Hydrodynamics

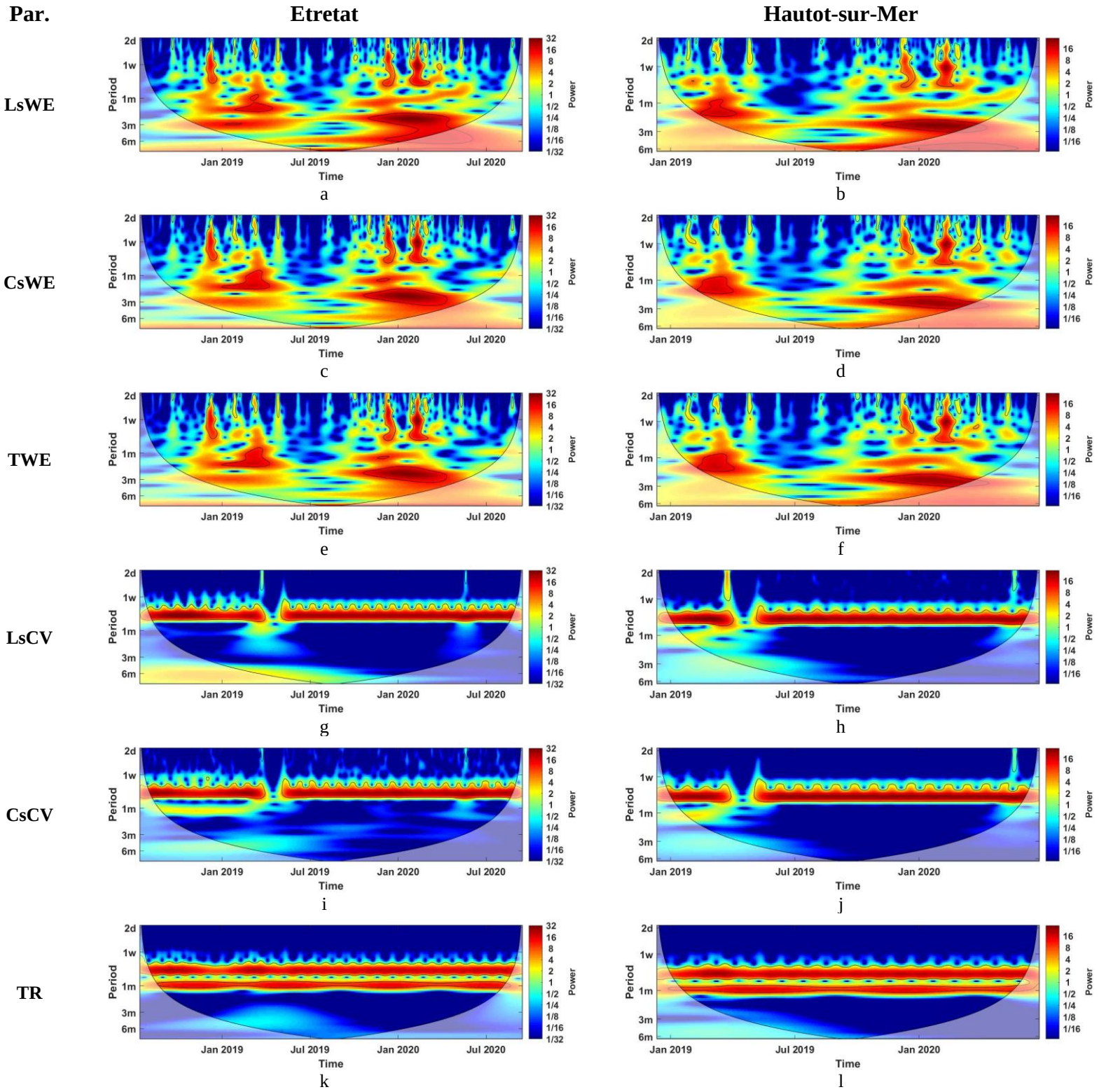

Figure 76 - Wavelet spectrums of hydrodynamic parameters in Etretat (left) and Hautot-sur-Mer (right). Parameters include longshore wave energy (LsWE) (a, b), cross-shore wave energy (CsWE) (c, d), total wave energy (TWE) (e, f), longshore current velocity (LsCV) (g, h), cross-shore current velocity (CsCV) (i, j), tidal range (TR) (k, l).

B. Gravel size maps

B.1. Etretat – 2020/06/10

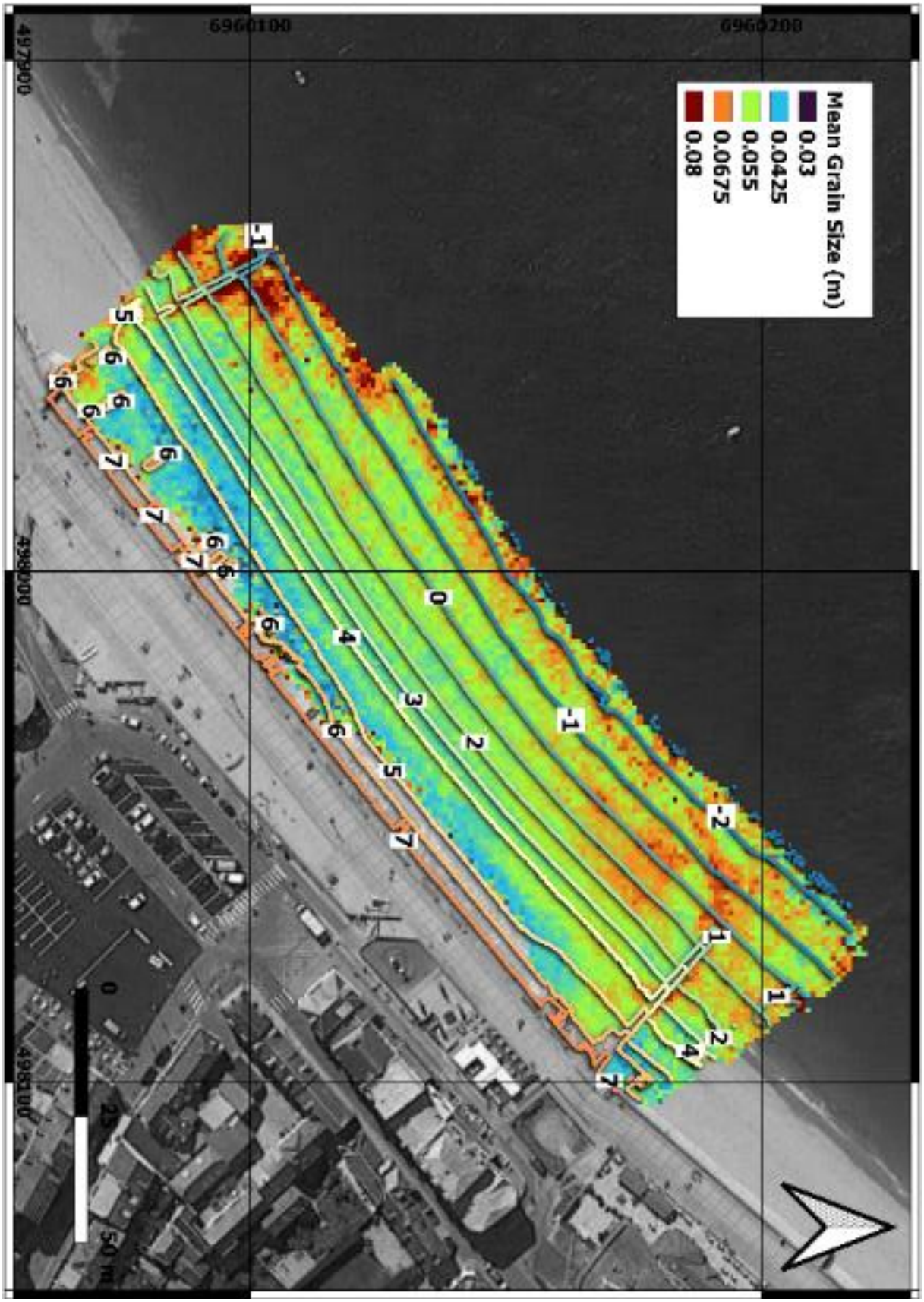

Figure 77 - Map of the mean clast length measured in Etretat on 2020/06/10. Contour lines of elevation are indicated for each round elevation with a vertical separation of 1 m.

B.2. Hautot-sur-Mer – 2019/04/09

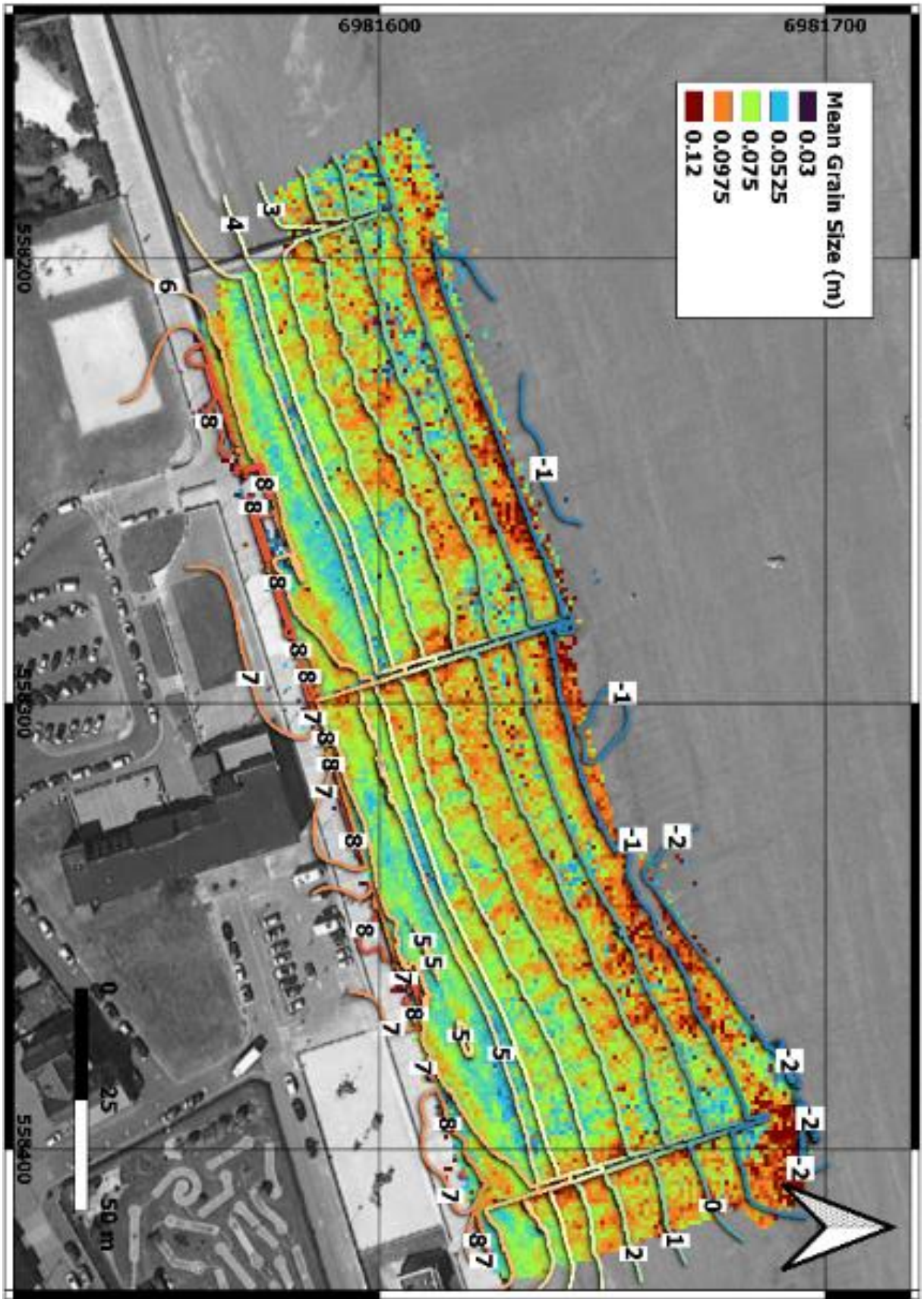

Figure 78 – Map of the mean clast length measured in Hautot-sur-Mer on 2019/04/09. Contour lines of elevation are indicated for each round elevation with a vertical separation of 1 m.

B.3. Hautot-sur-Mer – 2019/06/04

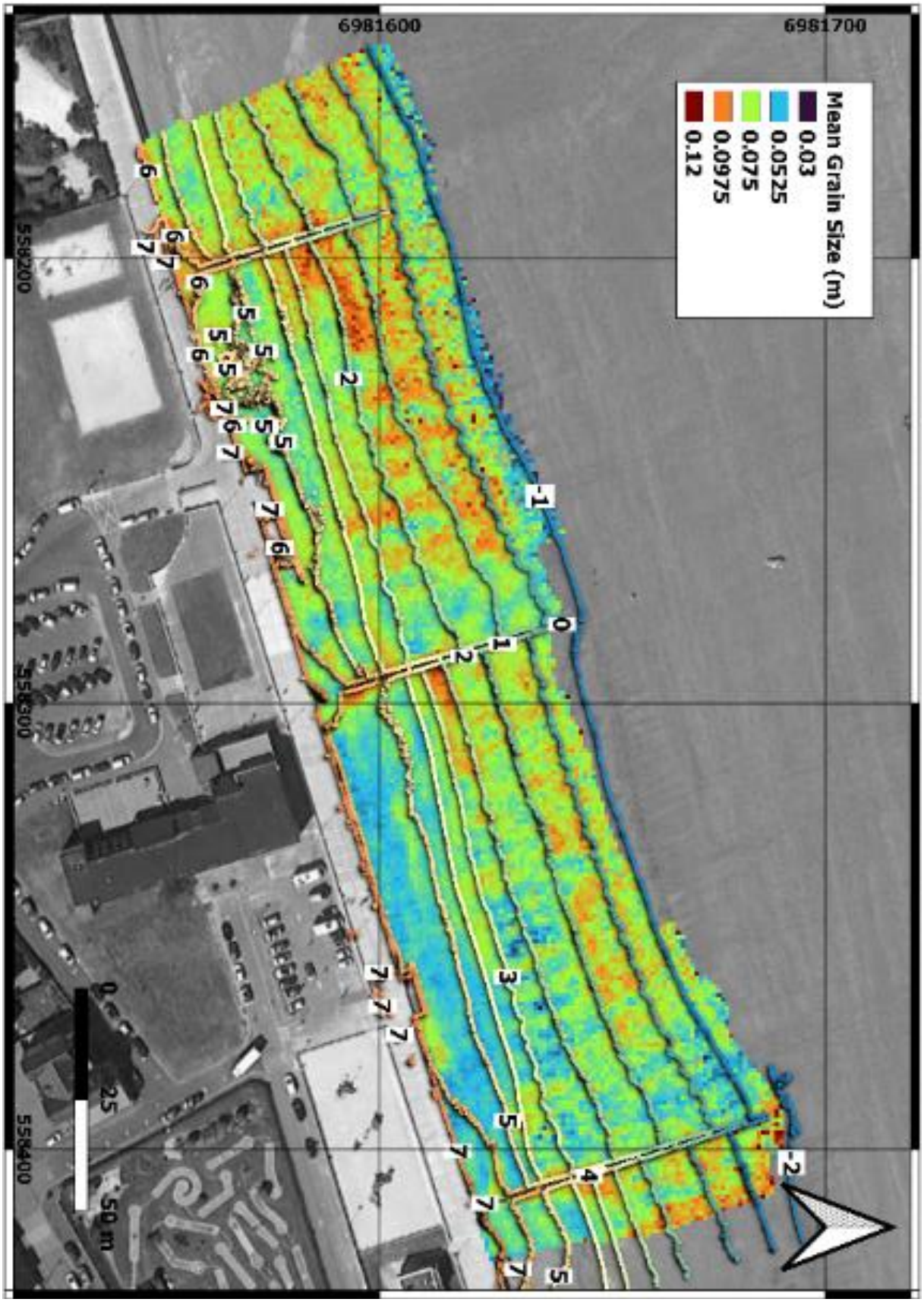

Figure 79 - Map of the mean clast length measured in Hautot-sur-Mer on 2019/06/04. Contour lines of elevation are indicated for each round elevation with a vertical separation of 1 m.

B.4. Hautot-sur-Mer – 2020/06/09

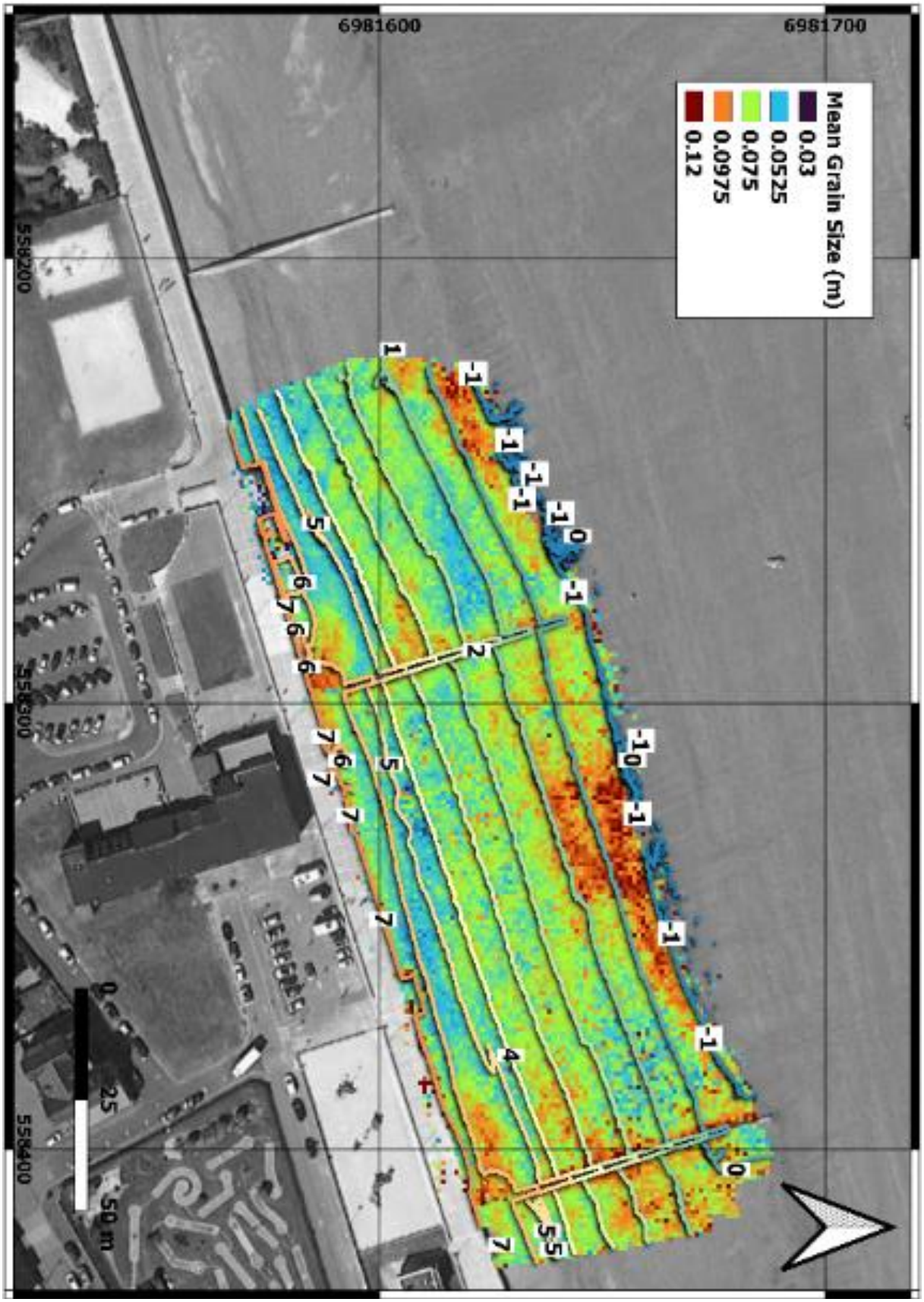

Figure 80 - Map of the mean clast length measured in Hautot-sur-Mer on 2020/06/09. Contour lines of elevation are indicated for each round elevation with a vertical separation of 1 m.

C. XBeach-G Model results

C.1. Storm 5

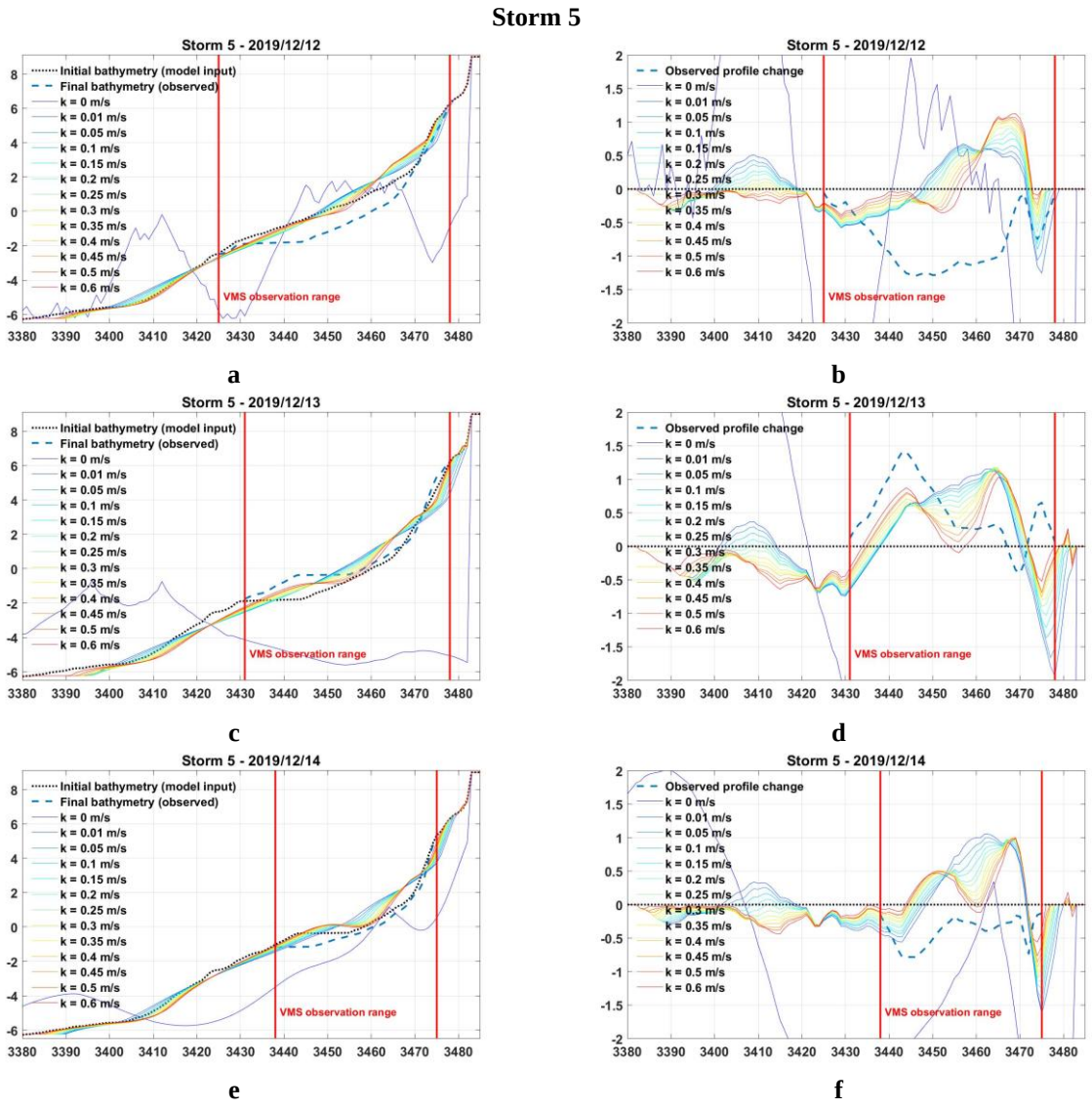

Figure 81 - Comparison between observed (black dotted and blue dashed lines) and modeled cross-shore profiles of Etretat using Xbeach-G (colored solid lines, one color per value of permeability k). Each row presents results after one day of observation/modeling during storm 5 (2019/12/12 to 2019/12/15). Figures on the left side present the initial and final profiles, figures on the right show the associated elevation change. The red vertical lines present the extent of the area monitored daily through video monitoring system (i.e., the section of the profile that was observed at the model's beginning and ending dates).

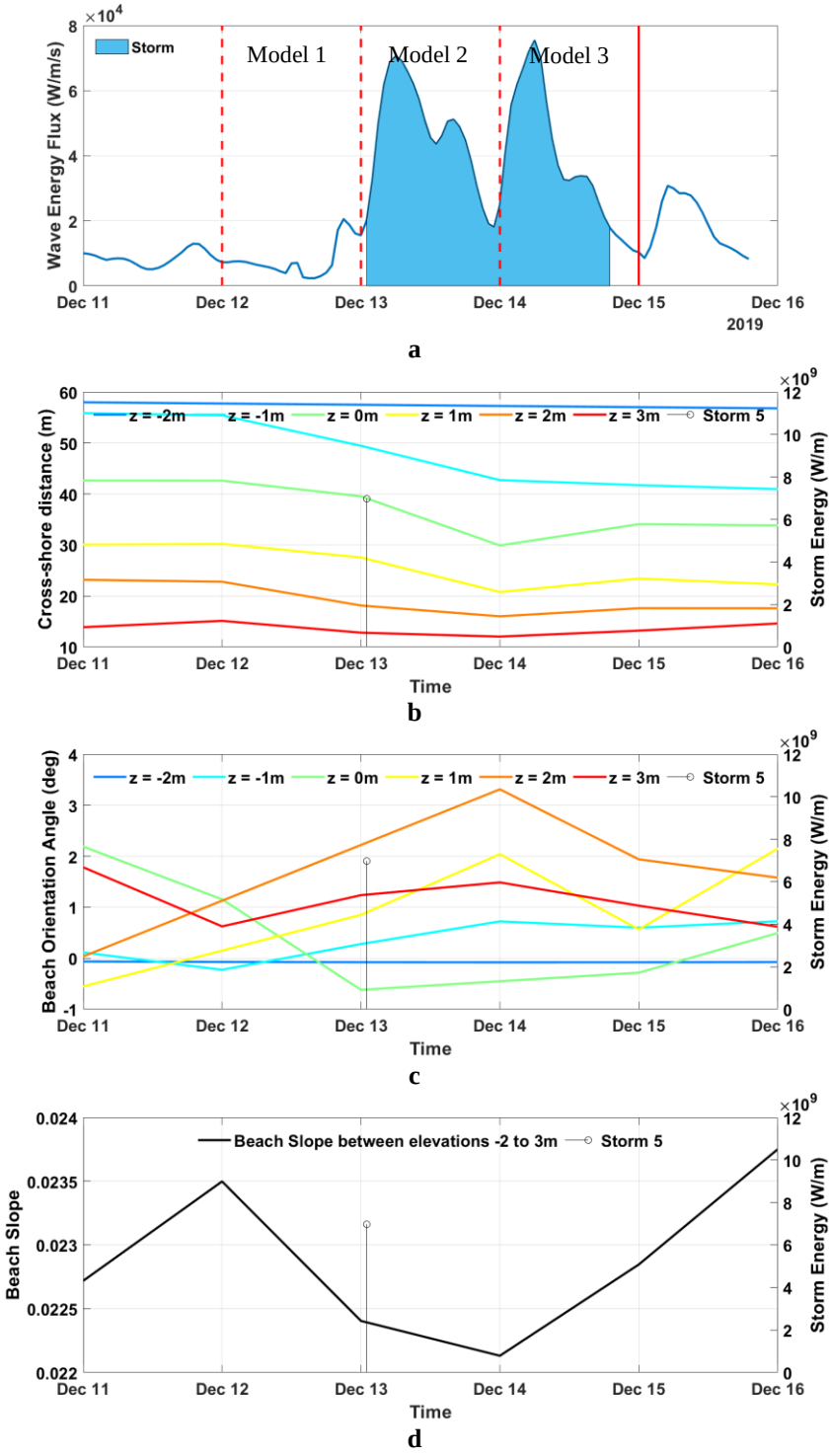

Figure 82 – Wave Energy Flux (a), Beach Width (BW, b), Beach Orientation Angle (BOA, c) and Beach Slope (BS, d) observed using VMS during storm 5, at various elevations from -2 m to +3 m. The storm starting date is presented as a vertical bar, its height relates to the cumulated wave energy. Vertical red lines (both dashed and solid) indicate the dates at which VMS-derived intertidal DEMs were available, the dashed ones specifically correspond to model starting dates while the solid lines indicate the last date with data available for model performance assessment.

C.2. Storm 7

Storm 7

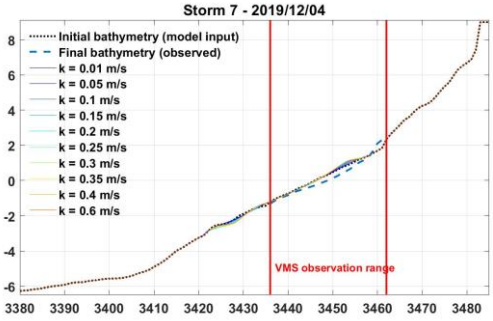

a

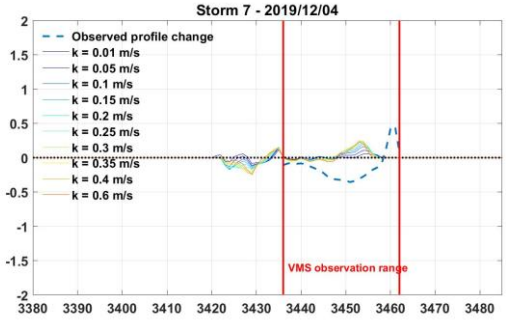

b

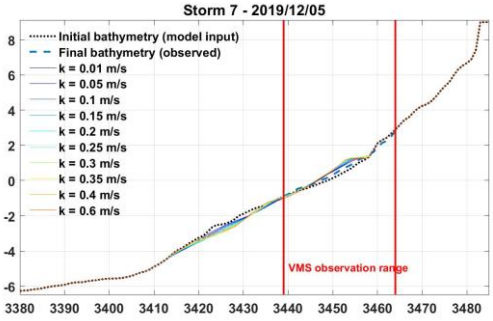

c

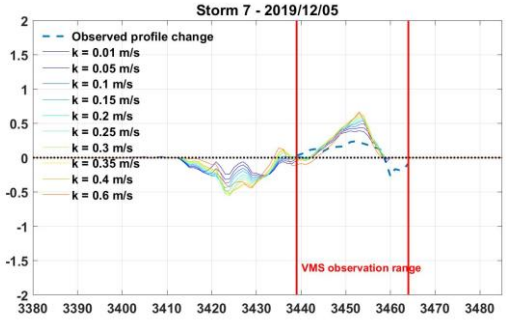

d

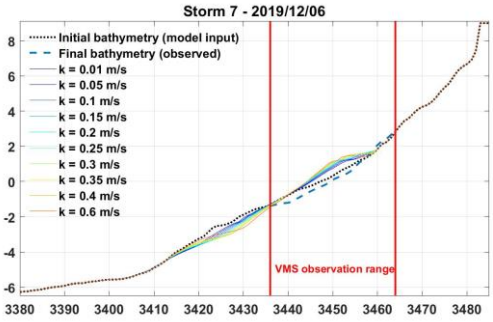

e

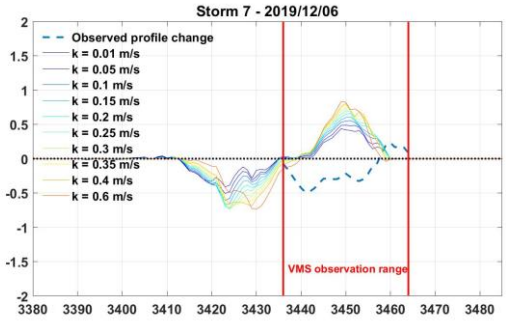

f

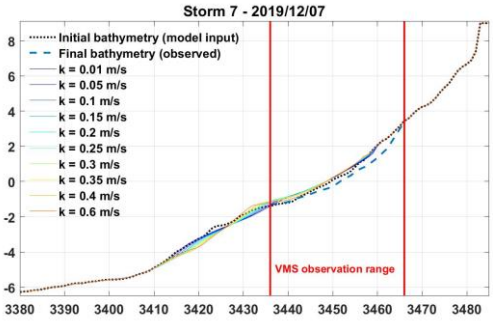

g

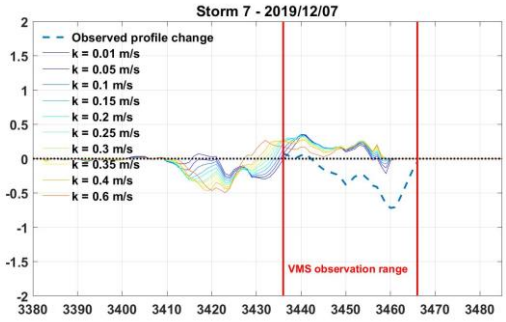

h

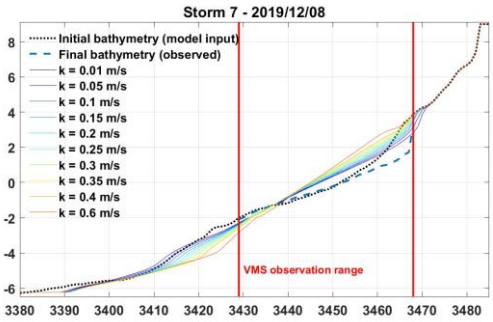

i

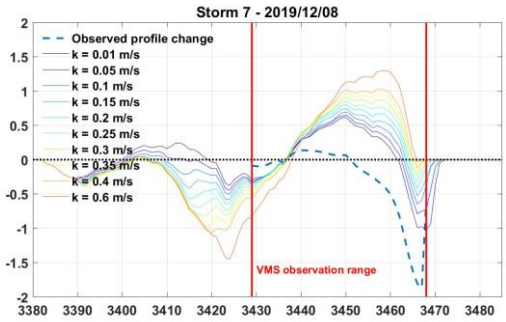

j

Figure 83 - Comparison between observed (black dotted and blue dashed lines) and modeled cross-shore profiles of Etretat using Xbeach-G (colored solid lines, one color per value of permeability k). Each row presents results after one day of observation/modeling during storm 7 (2019/12/04 to 2019/12/09). Figures on the left side present the initial and final profiles, figures on the right show the associated elevation change. The red vertical lines present the extent of the area monitored daily through video monitoring system (i.e., the section of the profile that was observed at the model's beginning and ending dates).

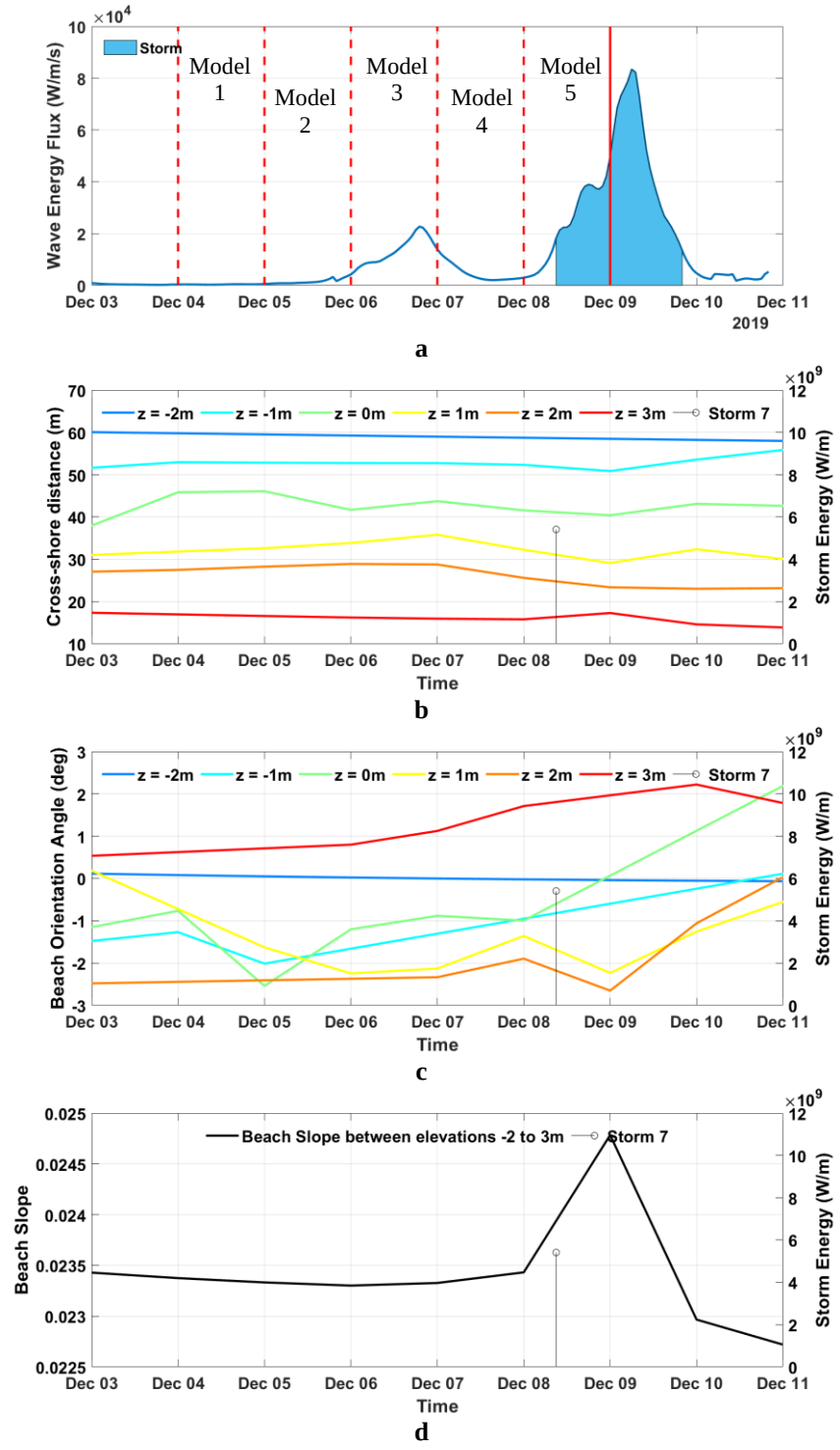

Figure 84 - Wave Energy Flux (a), Beach Width (BW, b), Beach Orientation Angle (BOA, c) and Beach Slope (BS, d) observed using VMS during storm 7, at various elevations from -2 m to +3 m. The storm starting date is presented as a vertical bar, its height relates to the cumulated wave energy. Vertical red lines (both dashed and solid) indicate the dates at which VMS-derived intertidal DEMs were available, the dashed ones specifically correspond to model starting dates while the solid lines indicate the last date with data available for model performance assessment

Title (titre): Study of the Hydro-Morpho-Sedimentary dynamics on pebble beaches

Keywords (mots clefs): coastal dynamics; gravel beaches; grain size mapping; remote sensing; deep learning

French abstract (résumé en français):

Les plages de galets sont des environnements côtiers très repandus sur les côtes de la Manche. Elles offrent une protection efficace aux structures côtières contre lesquelles elles reposent en absorbant une part significative de l'énergie des vagues, et sont par conséquent des environnements particulièrement dynamiques. Cependant, bien que la dynamique des plages de sable soit aujourd'hui bien comprise, celle des plages de galets reste à ce jour relativement peu documentée. Le consensus scientifique actuel décrit la dynamique complexe des plages de galets comme étant le résultat d'interactions rétroactives entre la morphodynamique, l'hydrodynamique et la dynamique sédimentaire. Plus particulièrement, il est admis que les variabilités spatiale et temporelle de la granulométrie jouent un rôle important dans la régulation de ces interactions. Ainsi, notre manque de compréhension vis-à-vis de la dynamique des plages de galet serait en grande partie dû à la difficulté de mesurer ces trois aspects simultanément.

Le présent manuscrit rapporte le travail réalisé dans l'objectif d'étudier la dynamique hydro-morpho-sédimentaire des plages de galets à des échelles multiples, en analysant un couplage de données provenant de plateforme multiple : drone (Unmaned Aerial Vehicle, UAV), et Système de surveillance par caméras vidéo (Video Monitoring System, VMS). Pour ce faire, deux méthodes innovantes basées sur des techniques de deep learning ont été développées afin de (1) cartographier la taille, la forme et l'orientation des galets à la surface d'une plage à partir d'une ortho-image drone, et (2) de produire un ensemble de Modèles Numériques de Terrain (MNT, ou DEM pour Digital Elevation Model) journaliers de plages à partir d'images VMS. A cet effet, deux sites comportant chacun une plage de galets ont été instrumentés et sont surveillés de façon continue depuis 2018 en Normandie. Les deux plages sont situées sur les côtes de la Manche, à proximité l'une de l'autre (64 km), et rencontrent des conditions de marée et de vagues considérées comme similaires. Cependant leur organisation spatiale et leurs caractéristiques granulométriques diffèrent : Etretat est une plage de galets pure située dans le creux d'une baie, et Hautot-sur-Mer est une plage composite de sable et galets située sur une côte semi-ouverte.

Les données recueillies ont permis l'analyse la dynamique morphologique des plages en réponse aux forçages marins entre les échelles journalière et biannuelle. Différents mécanismes du mouvement des plages ont été mis en évidence (e.g. translation, rotation, rollover and breathing), et certains ont pu être reliés à des processus physiques. Les résultats concernant la variabilité de la granulométrie ont également mis en évidence la présence de motifs sédimentaires spatiaux en lien avec l'altitude comme un gradient cross-shore systématique, et avec la présence d'épis comme la périodicité des assemblages de clastes triés par taille. Enfin, l'évolution temporelle de la perméabilité au cours d'évènements de tempêtes a été analysée en utilisant une stratégie de calibration du modèle numérique XBeach-G, lui-même nourrit avec les données de morphologie et de granulométrie mesurées depuis les plateformes VMS et UAV, respectivement.

English abstract (résumé en anglais):

Gravel beaches are very common coastal environments on the English Channel coasts. They offer an effective protection to the coastal structures against which they rest by absorbing a significant part of the wave energy and are therefore particularly dynamic environments. However, although the dynamics of sandy beaches are well documented, the dynamics of gravel beaches remain relatively poorly understood. The current scientific consensus describes the complex dynamics of gravel beaches as the result of feedback interactions between morphodynamics, hydrodynamics and sediment dynamics. Spatial and temporal variabilities in grain size are expected to play an important role in these interactions. Thus, the lack of understanding of pebble beach dynamics is related to the difficulty of measuring these three aspects simultaneously.

The present manuscript reports the work done with the aim to investigate the hydro-morpho-sedimentary dynamics of gravel beaches at multiple timescales, by coupling data from multiple platforms: Unmanned Aerial Vehicle (UAV) and Video Monitoring System (VMS). For this purpose, two innovative methods based on deep learning techniques were developed (1) to map the size, shape and orientation of gravel on the surface of a beach using UAV-derived ortho-imagery, and (2) to produce a dataset of daily digital elevation models (DEM) of a beach morphology using VMS images. For this purpose, two pebble beach sites have been instrumented and monitored since 2018 in Normandy, France: Etretat and Hautot-sur-Mer. Both beaches are located on the French coasts of the English Channel, they are close to each other (64 km), and thus face tidal and wave conditions that are considered similar. However, they differ in their spatial organization and granulometric characteristics: Etretat is a pure gravel beach located in the hollow of a bay, and Hautot-sur-Mer is a composite sand and gravel beach located on a semi-open coast.

The data collected allowed the analysis of the morphological dynamics of the beaches in response to marine forcing from daily to biannual scales. Different mechanisms of shoreline movement were highlighted (e.g., translation, rotation, rollover and breathing), some of which were linked to physical processes. The results on grain size variability also highlighted the presence of spatial sedimentary patterns related to elevation such as a systematic cross-shore gradient, and to the presence of groin structures such as the periodic repetition of size-sorted clast assemblages. Finally, the temporal evolution of permeability during storm events was analyzed with a calibration strategy using the XBeach-G numerical model that was fed with measured morphology and gravel size data.